

NUMERICAL MODELING OF ESTUARINE GEOCHEMISTRY

Tamara Michelle Wood

S. M., Physical Oceanography, Massachusetts Institute of Technology, 1987

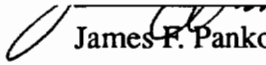
B.S., Mechanical Engineering, Union College, 1982

A dissertation submitted to the faculty of the
Oregon Graduate Institute of Science & Technology
in partial fulfillment of the
requirement for the degree of
Doctor of Philosophy
in
Environmental Science and Engineering

July, 1993

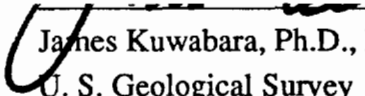
The dissertation "Numerical Modeling of Estuarine Geochemistry" by Tamara Michelle Wood has been examined and approved by the following examination committee:

António M. Baptista, Ph.D., Thesis Advisor



James F. Pankow, Ph.D., Professor

William Fish, Ph.D., Associate Professor



James Kuwabara, Ph.D., Hydrologist
U. S. Geological Survey

DEDICATION

To Rachel,

in the hope that she will find joy in asking questions and seeking answers.

ACKNOWLEDGEMENTS

I wish to express my sincere thanks to my advisor, Antonio Baptista, who always gave generously of his time, and who had enough faith in me to provide financial support. I have benefited greatly from his scientific insights, and I have learned a great deal from his bold approach to infusing the science establishment with new and rebellious ideas. When I was inclined to be timid, he would always push me to be a little less safe and a little more provocative in my scientific discourse.

To the rest of my committee I am also greatly indebted. Bill Fish has provided many hours of stimulating conversation, much of it having nothing whatsoever to do with science, and has always understood that my recalcitrant nature really has more to do with my East Coast upbringing than anything else, and has never taken it personally. Jim Pankow has always been patient with my sometimes naive approach to joining chemistry and fluid dynamics, and always took me seriously in spite of my protestations that I don't do lab work. Jim Kuwabara at the USGS provided a much-needed real-world perspective to my work. To all of these guys I would like to say thank you for your time, and your thoughtful commentary.

This work was greatly aided by the excellent programming efforts of Paul Turner. His software has been a real joy to work with. It seems that I could always come up with some new, really nice way to display my data, and Paul always did his best to comply. The library staff at OGI was also immensely helpful. They always did a great job of finding things in a timely fashion, even when I would sneak into the library after hours because I felt so guilty about leaving a stack of 30 inter-library loan requests at once.

I would also like to express my sincere gratitude to my three mentors at Atmospheric and Environmental Research in Cambridge: Dave Gutzler, Rick Rosen, and Dave Salstein. They believed in me and encouraged me when I was quite discouraged, and without them I probably would have left science altogether and done something really rash like go to law school.

I have been lucky to have been surrounded by other students (you know who you are) who have also been good friends. They provided diversion when the work became

drudgery, perspective when the difficulties seemed all-consuming, and a friendly ear when I felt alone.

My parents, Jane and Gary, who always encouraged me to excel, created the foundation that I would need to bring this work to fruition and accomplish other things in my life. At times they may wonder how in the world they managed to raise a child with my political bent, but my love of science and interest in the way the natural world works is no surprise at all. They always encouraged me to ask questions, lively discussions with them honed my powers of analytical thinking and debate, and most importantly of all, they NEVER told me girls shouldn't do science.

The most important and heartfelt thanks of all goes to Scott Hahn. He has been there through thick and thin, and I have always known how proud he is of me. He has been a friend and confidant, and he has kept me going when I would have quit were I on my own. He has also provided us a sound financial base at no small sacrifice to himself. And since our daughter Rachel came along, he has been not only a good husband, but a good father, sometimes when her mother was a little preoccupied.

And to Rachel, thank you for making me take the time to stop and smell the diapers (oops! I mean roses).

TABLE OF CONTENTS

DEDICATION.....	iii
ACKNOWLEDGEMENTS.....	iv
LIST OF FIGURES.....	ix
LIST OF TABLES.....	xiv
ABSTRACT.....	xv
CHAPTER 1: Introduction.....	1
Opening Remarks.....	1
Objectives.....	3
Reader's Guide to the Thesis.....	4
References.....	5
CHAPTER 2: A Model for Diagnostic Analysis of Estuarine Geochemistry.....	6
Abstract.....	6
Introduction.....	6
Conceptual Formulation.....	13
Aqueous Complexation.....	14
Slow reactions.....	14
Fast reactions.....	15
Adsorption Reactions.....	17
Surface complexation.....	17
Non-site-specific adsorption.....	18
Summary of Equations.....	19
Mathematical Formulation.....	21
Overview.....	21
Solution of Chemical Reaction Equations.....	24
Solution of hydraulic transport.....	32
Numerical Verification.....	32
Application: Introduction to Diagnostic Modeling.....	34
Test System.....	35
Effect of Symmetrical and Asymmetrical Sources.....	36
Effect of Reaction Kinetics.....	38
Effect of Sediment Deposition.....	39
Final Comments.....	40
Notation.....	41
References.....	43
CHAPTER 3: Modeling the Pathways of Nonconservative Substances in Estuaries.....	68

Abstract.....	68
Introduction.....	68
Formulation of Transformation Equations.....	71
Solution of the Transformation Equations.....	74
Decoupling of the Transformation and Diffusion Time Step	77
Future Developments	79
References.....	83
CHAPTER 4: Diagnostic Modeling of Trace Metal Partitioning in South San Francisco Bay	84
Abstract.....	84
Introduction.....	85
Review of Field Data	86
Experimental Design.....	90
Circulation	91
Mixing Characteristics.....	92
Chemical Equations	94
Source Scenarios.....	98
Suspended Solids	100
Aqueous Ligands	101
Experimental Results	102
Conclusions.....	106
Final Remarks	108
References.....	110
CHAPTER 5: User's Manual	147
Introduction.....	147
Governing Equations and Numerical Discretization	148
Development of Weighted Residual Statement for Dispersion	149
Development of Transformation Equations.....	153
Secondary Equations	155
Primary Equations	156
Description of Input Files	158
Description of the ".min" file.....	159
Format of Other Input Files	167
Flow Field Input.....	168
File Unit Numbers	168
Running ELAmet.....	168
Output File Description	169
Example Applications.....	169
1D Carbonate System	169

1D Copper System	171
1D Zinc System	172
1D Tin System	176
San Francisco Bay	180
References.....	185
CHAPTER 6: Conclusions	205
Contributions	205
Directions for Further Research.....	206
VITA.....	208
Publications.....	209

LIST OF FIGURES

Figure 1.1.	Schematic illustrating the feedback that connects the three components of the most effective approach to understanding complex natural systems.	3
Figure 2.1	Schematic diagram of the phases and processes that distribute mass between phases included in ELAmet.	47
Figure 2.2	Profiles of $[MeX_2]$ and $[MeX_{2(s)}]$ along the channel at 5 different times during the simulation.	48
Figure 2.3	Profiles of $[Me^{2+}]$ and $[MeO^+]$ along the channel at 5 different times during the simulation.	49
Figure 2.4	Profiles of $[Me^{2+}]$, $[MeO^+]$ and $[MeX^+]$ along the channel at 5 different times during the simulation.	50
Figure 2.5	Profiles of 15 species at time $t=100$ hrs.	51
Figure 2.6	A schematic of the 1-dimensional mixing plot.	52
Figure 2.7	Numerical grid corresponding to the test system.	53
Figure 2.8	Lagrangian pathways of numerical drogues.	54
Figure 2.9	Eulerian time series of salinity sampled at 5 locations as indicated in Figure 2.7.	55
Figure 2.10	Contours of the salinity plume after 43 days.	56
Figure 2.11	Contours of the metal plume resulting from a symmetrical source located at x_0	57
Figure 2.12	Mixing plot for the metal plume shown in Figure 2.11.	58
Figure 2.13	Contours of the metal plume resulting from an assymetrical source located at (x_0, y_0)	59
Figure 2.14	Mixing plot for the metal plume shown in Figure 2.13. Also shown are the sampled mixing plots, using the schemes shown in Figure 2.15.	60
Figure 2.15	Three sampling schemes for the grid, each designed with 10 sample points.	61
Figure 2.16	Contours of the plumes of particulate and aqueous metal, corresponding to a symmetric source and a first-order desorption process.	62
Figure 2.17	Mixing plot corresponding to the particulate and aqueous metal plumes shown in Figure 2.16.	63
Figure 2.18	Plot of "apparent K_p " for the metal plumes of Figure 2.16.	64
Figure 2.19	Outline of numerical grid showing the region chosen for a constant, nonzero deposition rate.	65
Figure 2.20	Plume of particulate metal resulting from a symmetric source and a nonuniform deposition as shown in Figure 2.19.	66
Figure 2.21	Mixing plot corresponding to the metal plume of Figure 2.20.	67

Figure 3.1	Time series of concentration at the top of the gauss hill (at $x=5$ km).	77
Figure 3.2	Time series of concentration at $x=5$ km.	79
Figure 3.3.	The numerical grid used for simulations in San Francisco Bay (3.3a), and the conservative tracer plume (3.3b) generated by the source shown in 3.3a.	80
Figure 3.4	Time series of concentration for substances (a), (b), and (c) at a sample point close to the source shown in Figure 3.3.	82
Figure 3.5	Scatter plot showing the relationship between variability at the M2 frequency in a conservative tracer and in two different nonconservative tracers.....	82
Figure 4.1	Plot of observed partition coefficient, K_d^a , for 1985 and 1989 copper data.....	115
Figure 4.2	Plot of observed partition coefficient, K_d^a , for 1985 and 1989 cadmium data.....	116
Figure 4.3	Plot of observed partition coefficient, K_d^a , for 1985 and 1989 zinc data.....	117
Figure 4.4	Outline of the numerical grid used in simulations.....	118
Figure 4.5	A comparison of the M2 amplitude and phase of elevations from the TEA-NL generated circulation used in the model simulations and USGS tide gage data.	119
Figure 4.6	A comparison of the mean salinity and M2 (semi-diurnal) amplitude of salinity from ELAmet and USGS salinity data.	120
Figure 4.7	Outline of South Bay showing the locations of 5 POTWs located within the basin.	121
Figure 4.8	Tidally-averaged profiles of total concentration, percent mass in the solid phase, and apparent distribution coefficient for copper, experiment P4.	122
Figure 4.9	Tidally-averaged profiles of total concentration, percent mass in the solid phase, and apparent distribution coefficient for cadmium, experiment P4.	123
Figure 4.10	Tidally-averaged profiles of total concentration, percent mass in the solid phase, and apparent distribution coefficient for zinc, experiment P4.	124
Figure 4.11	Profiles of α for copper, cadmium and zinc, experiment P4. The bars represent the limits of tidal variability at each station.	125
Figure 4.12	Tidally-averaged profiles of K_d^e for copper, cadmium and zinc, same conditions as experiment P4.	126
Figure 4.13	Tidally-averaged profiles of percent mass in the solid phase and apparent distribution coefficient for copper, experiment P3.....	127

Figure 4.14	Tidally-averaged profiles of percent mass in the solid phase and apparent distribution coefficient for zinc, experiment P3.	128
Figure 4.15	Tidally-averaged profiles of concentration of suspended solids, experiment P3.	129
Figure 4.16	Tidally-averaged profiles of total concentration, percent mass in the solid phase, and apparent distribution coefficient for copper, experiment B4.	130
Figure 4.17	Tidally-averaged profiles of total concentration, percent mass in the solid phase, and apparent distribution coefficient for cadmium, experiment B4.	131
Figure 4.18	Tidally-averaged profiles of total concentration, percent mass in the solid phase, and apparent distribution coefficient for zinc, experiment B4.	132
Figure 4.19	Tidally-averaged profiles of percent mass in the solid phase and apparent distribution coefficient for copper, experiment B3.	133
Figure 4.20	Tidally-averaged profiles of percent mass in the solid phase and apparent distribution coefficient for zinc, experiment B3.	134
Figure 4.21	Scatterplot of apparent distribution coefficient of copper as a function of salinity.	135
Figure 4.22	Scatterplot of apparent distribution coefficient of cadmium as a function of salinity.	136
Figure 4.23	Scatterplot of apparent distribution coefficient of zinc as a function of salinity.	137
Figure 4.24	Scatterplot of apparent distribution coefficient of copper as a function of suspended solids concentration.	138
Figure 4.25	Scatterplot of apparent distribution coefficient of cadmium as a function of suspended solids concentration.	139
Figure 4.26	Scatterplot of apparent distribution coefficient of zinc as a function of suspended solids concentration.	140
Figure 4.27	Plot of distance from equilibrium as a function of time for copper.	141
Figure 4.28	Plot of distance from equilibrium as a function of time for cadmium.	142
Figure 4.29	Plot of distance from equilibrium as a function of time for zinc.	143
Figure 4.30	Schematic dependence of K_d^a on salinity for all cruises.	144
Figure 4.31	Schematic dependence of K_d^a on concentration of suspended solids for all cruises.	144
Figure 4.32	Plot of percent mass in the solid phase as a function of suspended solids concentration for 1985 data.	145

Figure 4.33	Plot of percent mass in the solid phase as a function of suspended solids concentration for 1989 data.	146
Figure 5.1	Schematic of the grouping of different types of species in ELAmet.	154
Figure 5.2	Schematic depiction of the order in which species are stored in ELAmet, with an indication of the type of equation used to solve for each type of species.....	155
Figure 5.3	Profile of concentration along the 1-dimensional domain for the carbonate system after 50 1-hour time steps.....	187
Figure 5.4	Comparison of the concentration of $[CO_3^{2-}]$ using the single-valued constants as in the ELAmet carbonate example with concentration computed using the salinity-dependent constants given in Mook and Koene [1975].	188
Figure 5.5	Profile of concentration along the 1-dimensional domain for the copper system after 50 1-hour time steps.	189
Figure 5.6	Profiles of concentration of the dominant copper species, showing the exchange of mass with increasing concentration of humic material.	190
Figure 5.7	Profile of concentration along the 1-dimensional domain for the zinc system after 50 1-hour time steps; adsorption rate proportional to Zn_T	191
Figure 5.8	Profile of concentration along the 1-dimensional domain for the zinc system after 50 1-hour time steps; adsorption rate proportional to $[Zn^{2+}]$	192
Figure 5.9	Profile of measured distribution coefficient along the domain for the two different adsorption rates depicted in Figure 5.7 and Figure 5.8.	193
Figure 5.10	Profile of concentration along the 1-dimensional domain for the cadmium system after 50 1-hour time steps; adsorption rate proportional to Cd_T	194
Figure 5.11	Profile of concentration along the 1-dimensional domain for the cadmium system after 50 1-hour time steps; adsorption rate proportional to $[Cd^{2+}]$...	195
Figure 5.12	Profile of measured distribution coefficient along the domain for the two different adsorption rates depicted in Figure 5.10 and Figure 5.11.	196
Figure 5.13	Profile of concentration along the 1-dimensional domain for the tin system after 100 1-day time steps.....	197
Figure 5.14	Location of five POTWs used as point sources.	198
Figure 5.15	Outline of the numerical grid used in San Francisco Bay simulations, with sampling transect.....	199

Figure 5.16	Profile along the transect shown in Figure 5.15 of Cd(II) species.....	200
Figure 5.17	Profile along the transect shown in Figure 5.15 of Cu(II) species.....	201
Figure 5.18	Profile along the transect shown in Figure 5.15 of Zn(II) species.....	202
Figure 5.19	Profile along the transect shown in Figure 5.15 of apparent distribution coefficient.	203
Figure 5.20	Profile along the transect shown in Figure 5.15 of departure from equilibrium as measured by the apparent distribution coefficient normalized by the distribution coefficient at equilibrium.....	204

LIST OF TABLES

Table 2.1	Comparison of Selected Models	8
Table 4.1	Measured Distribution Coefficients	88
Table 4.2	Measured Rate Constants.....	91
Table 4.3	Preliminary Speciation.....	94
Table 4.4	Model Transformation Equations	94
Table 4.5	Summary of Metal Sources.....	100
Table 4.6	Model Runs.....	103
Table 5.1	Summary of Required Input Information	165
Table 5.2	Template of “.min” File	169
Table 5.3	Equations for Carbonate System.....	176
Table 5.4	Test111.min.....	177
Table 5.5	Test112.min.....	178
Table 5.6	Equations for Copper System	178
Table 5.7	Test113.min.....	182
Table 5.8	Equations for Zinc System.....	182
Table 5.9	Equations for Cadmium System	182
Table 5.10	Equations for Tin System.....	182
Table 5.11	Test116.min.....	186
Table 5.12	Species in San Francisco Bay System	189
Table 5.13	Sfba472.min.....	190

ABSTRACT

Numerical Modeling of Estuarine Geochemistry

Tamara M. Wood, Ph.D.

Oregon Graduate Institute of Science & Technology, 1993

Supervising Professor: António M. Baptista

A spatially and temporally explicit numerical model for the fate and transport of nonconservative metals in an estuarine environment was developed, tested, and applied. This model, known as ELAmet, solves the depth-averaged advection/dispersion/transformation equation on a 2-dimensional grid using a finite element formulation in an Eulerian-Lagrangian framework. The model incorporates aqueous speciation and adsorption/desorption, and accommodates chemical equilibria and kinetics simultaneously.

Application of the model was done in two phases. A preliminary application was used to illustrate the concept of diagnostic modeling for a synthetic estuarine system. The possible effects of source location, chemical kinetics, and sediment deposition on the observed mixing plot (concentration as a function of salinity) was examined. The results indicate that the “true” mixing plot can occupy a 2-dimensional region in concentration-salinity space, and that sparse field sampling may result in an incomplete representation of the mixing plot.

In a more extensive application, ELAmet was used to investigate the effect of adsorption kinetics on the apparent distribution coefficients of copper, cadmium and zinc in South San Francisco Bay, California. The numerical experiments were designed with three goals in mind: 1) to use a spatially and temporally explicit modeling approach to extrapolate laboratory partitioning data to an environmental setting, 2) to establish that adsorption kinetics can control the basin-scale variability of the observed partitioning and therefore the apparent dependencies of partitioning on salinity and suspended solids, and 3) to define the conditions under which adsorption kinetics could account for strong inter-annual variability in partitioning.

The numerical results indicate that aqueous speciation will control the profile of the apparent distribution coefficient K_d^a if the system is close to equilibrium. However, if the system is far from equilibrium the profile of K_d^a and its apparent dependencies on salinity and suspended solids will be determined by the location of the sources of metal, and the suspended solids concentration of the receiving water. The results also indicate that the further the basin as a whole is from equilibrium, the greater the basin-scale variability in K_d^a that would likely be observed during a single sampling cruise. This work has interesting implications for the interpretation of field data from San Francisco Bay. Apparent distribution coefficients from two different years exhibit strong dissimilarities; K_d^a values for copper, cadmium, and zinc during 1989 are generally higher and more variable than those observed during 1985.

CHAPTER 1

Introduction

Opening Remarks

This work was guided, sometimes explicitly and always implicitly, by two fundamental principles. The first was that estuaries, like all natural systems, are fundamentally interdisciplinary. The second was that numerical models can and will be an invaluable tool in advancing the understanding of these complex natural systems.

It is, in principle, well-recognized that the study of environmental systems must be approached at the ecosystem level; in the case of an estuarine system this requires the expertise of fluid dynamicists, geologists, marine chemists, marine biologists and numerical modelers, to name a few. The interdisciplinary approach, however, remains more principle than fact, as evidenced, for example, by the difficulty we encountered in finding a journal to which some of this work could logically be submitted for publication. On a personal level, the crossing of disciplinary boundaries was both a professional goal and a personal challenge. Having come from a physical oceanography background, the mastery of the concepts and the language of environmental chemistry that was required to create and apply the model ELAmet was a painstaking process, at times difficult but ultimately rewarding. It is my hope that this work will be useful and accessible to scientists from many different backgrounds. Clearly my experience will not be unique; environmental scientists will continue to cross disciplinary boundaries, as the systems we seek to understand do not respect the divisions convenient for academic departments and professional journals.

The investigation of a natural system like an estuary does not lend itself to a strictly reductionist approach, in which processes believed to be important are isolated under controlled and highly simplified laboratory conditions for individualized study. Because of the multitude of temporal and spatial scales involved and their interactions, an extrapolation from a set of such reduced systems to the real system quickly becomes

impossible. The study of estuaries carries the additional complication that the collection of field data is hampered by the considerable expense involved in gathering samples. Thus the information available for validating conclusions is usually inadequate.

Given the intractability of this situation, the time is clearly right for numerical models to play a larger role in helping scientists advance the understanding of estuarine and other environmental systems. However, if numerical models are to fulfill their potential as a useful tool in the study of complex natural systems, the focus must be realigned to emphasize their *diagnostic* capabilities rather than their *prognostic* capabilities. The term *diagnostic*, in this case, is meant to imply a procedure closely analogous to the way in which laboratory experiments are used to attack a problem. Environmental conditions are controlled, and experiments are designed to illuminate a particular process, through direct measurement or deduction. In a similar manner, numerical experiments can be controlled, and designed specifically to illuminate the effects of a particular underlying process. The structure of Chapter 4, for example, which is the presentation of an application of ELAmet to South San Francisco Bay, is parallel to the presentation that would be expected for a series of laboratory experiments.

While there are strong analogies between laboratory and numerical experimentation, the latter provides some capabilities that the former cannot. Numerical experimentation allows experimentation in a domain which is representative of the actual physical domain, rather than a constructed (and simpler) domain that could be used in a laboratory. In addition, numerical experiments allow a level of complexity, in terms of the mixing of various physical process and temporal and spatial scales, that laboratory experiments cannot.

Just as laboratory experiments must be continuously checked for consistency with field measurements, diagnostic modeling is only effective as part of an iterative process in which it is part of an ongoing program of laboratory and numerical experimentation and field surveys (see Figure 1.1). Without this context of checks and balances, there is a danger that model results can be taken too literally. Ultimately this leads to a distrust of models, as model results which are not properly calibrated and validated are bound to be inadequate for predictive purposes. And for the foreseeable future it is clear that the data required to properly calibrate and validate models does not exist. However, numerical models still constitute a very powerful tool *if* they are used with the proper expectation.

Objectives

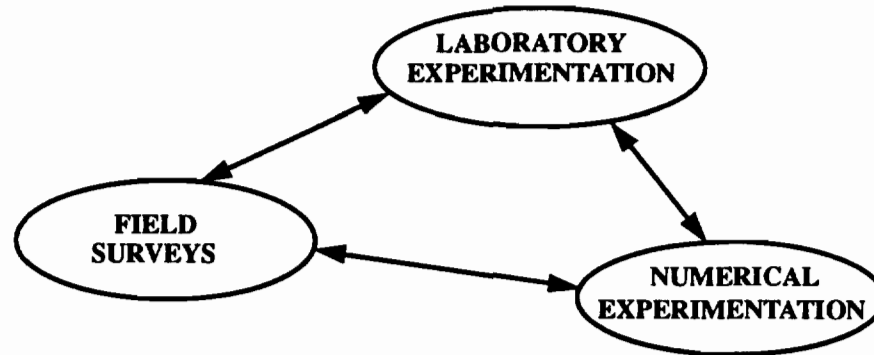


Figure 1.1. Schematic illustrating the feedback that connects the three components of the most effective approach to understanding complex natural systems.

The objectives of this work were basically two: to produce a numerical model which sets a new standard for the state-of-the art in nonconservative surface water transport modeling, and to demonstrate an application of the model that significantly alters the expectations of what can be learned from the use of such models.

The first step, therefore, was to create a computer code (designated ELAmet) which combines spatially and temporally explicit numerical modeling of tidally-dominated hydraulic transport with chemical transformation equations that describe the chemistry of trace elements in more detail than existing models. Surface water quality models have tended to emphasize *either* hydraulic transport *or* chemical transformations, but not both. As a result, 2D and 3D numerical models have been developed which provide good descriptions of hydraulic transport, but which are only appropriate for conservative substances or substances with a very simple chemistry. Our current understanding of estuaries shows that very many trace materials of interest have a complicated chemistry, involving aqueous speciation, partitioning between the aqueous and solid phases, oxidation/reduction reactions, and biologically-mediated reactions. Thus the accurate description of the fate and transport of these materials requires a description of the chemistry at the level of the mathematical equations that goes well beyond just total water column concentrations, or even total dissolved and total particulate concentrations. ELAmet incorporates aqueous speciation, and equilibrium- or rate-controlled adsorption. With minor modifications, the model can also be expanded to incorporate redox chemistry.

The next objective was to apply ELAmet in a way that demonstrates the diagnostic function of numerical models. To this end, ELAmet was used to investigate the contribution of adsorption kinetics to the variability observed in the partitioning between the aqueous and solid phases in South San Francisco Bay. Thus this example illustrates the unique contribution that numerical models can make to estuarine studies; in this case ELAmet allows us to look at the interaction of adsorption kinetics and a dynamic, tidally-dominated hydraulic transport in a way that cannot be done by any other means.

Reader's Guide to the Thesis

Each of the succeeding chapters was written at a different time and as a stand-alone contribution; consequently, each chapter can be read alone without difficulty. The purposes of each chapter are as follows. Chapter 2 is a detailed presentation of the mathematical formulation, especially in terms of the chemical transformation equations; this chapter appeared in virtually the same form in the January, 1993 issue of *Water Resources Research* [Wood and Baptista, 1993]. In addition, included in this paper is an introduction to the concept of diagnostic modeling, as illustrated by some preliminary experimentation with a synthetic estuary. This early experimentation focussed on the effects of source location, sediment deposition, and simple chemical kinetics on the 2-dimensional representation of the mixing plot, which is the format often used to present observational data.

Chapter 3 is derived from a paper given at the 2nd International ASCE Conference on Estuarine and Coastal Modeling, held in Tampa in November, 1992, and is published in the *Proceedings* of that conference [Wood and Baptista, 1992]. The purpose of this paper was primarily to present in detail the solution of the chemical transformation equations that is incorporated into ELAmet. Aspects of the equations that were not appropriate to be included in either this paper or the above paper are included in the *Governing Equations and Numerical Discretization* section of the Users Manual (Chapter 5). Thus Chapters 2, 3, and 5 taken together provide a detailed, comprehensive presentation of the mathematical equations making up the model, as well as their solution.

Chapter 4 presents an application of ELAmet to a "real" system. South San Francisco Bay was chosen because of the availability of observational metal data, the lack of vertical stratification, and the narrow range of salinity variations. In this application,

ELAmet has been used to perform experiments designed to study how adsorption kinetics might be manifested in the observed partitioning data.

Chapter 5 is a User's Manual for ELAmet, and is part of the Software Documentation Series of the Center for Coastal and Land Margin Research [Wood and Baptista, 1993b]. This Manual was designed to be more than a set of instructions for model users. The example applications are very important, as they were carefully chosen to demonstrate different aspects of the capabilities of ELAmet. However, ELAmet is a relatively flexible code, and the examples certainly do not cover all of the possibilities. The Manual was also designed to provide the user with some intuition about how the model works, in the hope that this will be helpful in cases not explicitly covered by the examples.

References

- Wood, T. M. and A. M. Baptista, Modeling the pathways of nonconservative substances in estuaries, in *Estuarine and Coastal Modeling, proceedings of the 2nd International conference*, edited by M.L. Spaulding et al., pp. 280-291, 1992.
- Wood, T. M. and A. M. Baptista, A Diagnostic Model for Estuarine Geochemistry, *Water Resources Research*, 29(1), pp. 51-71, 1993.
- Wood, T. M. and A. M. Baptista, *ELAmet: User's Manual. An Eulerian-Lagrangian model for estuarine geochemistry*, OGI-CCALMR Software Documentation Series SDS#5-93/1, 1993b.

CHAPTER 2

A Model for Diagnostic Analysis of Estuarine Geochemistry

Abstract

A new numerical model for the fate and transport of nonconservative metals in an estuarine environment is introduced. ELAmet solves the depth-averaged advection/dispersion/transformation equation on a 2-dimensional grid using a finite element formulation in an Eulerian-Lagrangian framework. The model incorporates aqueous speciation and adsorption/desorption. Adsorption to any number of solid types can take place through linear (partitioning) reactions or nonlinear (complexation) reactions. The model accommodates chemical equilibria and kinetics simultaneously. Rate constants can span any range of time scales, as the computational time step for solving the chemical transformation equations has been decoupled from that dictated by the circulation. Verification of the model is included for a 1-dimensional channel and up to 15 chemical species. Preliminary applications are included which illustrate the concept of diagnostic modeling for a synthetic estuarine system in which the effects of source location, chemical kinetics, and sediment deposition on the mixing plot are examined.

Introduction

The fate and transport of nonconservative trace substances in estuaries and coastal embayments has been a topic of interest for several decades. Interest in this subject has been based on issues of water quality, as well as on the role of estuaries in the global geochemical cycles of many elements. Most numerical models of surface water transport have focused on improving the description of hydraulic transport, but have done little to improve the description of nonconservative chemical behavior. In this paper we introduce the numerical model ELAmet, designed to model the fate and transport of trace metals in estuarine environments. ELAmet couples 2-dimensional advective/dispersive mass trans-

port with complexation and adsorption processes that distribute mass among the various species in the aqueous and solid phase.

The coupling of transport with reactive chemical behavior has been investigated much more extensively as a groundwater problem than as a surface water problem; therefore a discussion of the capabilities of ELAmet would be incomplete without referring to some of the groundwater literature describing coupled transport models. A comprehensive review of hydrogeochemical modeling in groundwater is given by *Mangold and Tsang* [1991], and we will mention only a few notable examples here. *Valocchi, et al.* [1981] incorporated the single chemical process of ion exchange adsorption into the solution of the equations of mass transport. *Miller and Benson* [1983], in their model CHEMTRN, expanded the number of chemical processes to include aqueous complexation and the determination of pH as a dependent quantity. In both of these cases, the chemical reaction equations were substituted directly into the equations governing transport, resulting in a system of nonlinear partial differential equations (PDEs) to be solved directly by numerical techniques. Alternatively, the chemical reaction equations can remain a separate system of equations, and be incorporated into the total mass transport problem by iterating sequentially between the chemical reaction equations and the hydraulic transport equations. This was the approach taken by *Cederburg, et al.* [1985] in the model TRANQL, which included aqueous complexation and sorption via surface complexation. The advantages of the latter approach for problems of realistic size and complexity are discussed by *Yeh and Tripathi* [1989]; these authors have recently developed the model HYDRO-GEOCHEM [*Yeh and Tripathi*, 1991] which uses the same approach. HYDRO-GEOCHEM includes the chemical processes of aqueous complexation, precipitation/dissolution, redox, adsorption via surface complexation and ion exchange, and acid/base reactions.

Table 1 summarizes salient properties of some numerical surface water transport models appropriate for estuaries and coastal embayments that have appeared in the literature over the last decade. This list is not intended to be exhaustive, and includes only models supported by at least a two-dimensional grid, but it establishes a context for ELAmet by comparing its features with those of other estuarine transport models. While there has been steady improvement in the modeling of physical processes, little effort has been devoted to improving the modeling of the other half of the coupled problem: the chemical

Table 2.1. Comparison of Selected Models

	Dimen- sions	Solution Technique	Reaction Rate	Chemical Pro- cesses	Speciation
FETRA Onishi (1981)	2D	finite ele- ment	limited by transport time step	linear adsorp- tion, linear decay	total dis- solved, total particulate
FLESCOT Onishi and Trent (1982)	3D	finite differ- ence	limited by transport time step	linear adsorp- tion, linear decay	total dis- solved, total particulate
Hauser, et al. (1983)	3D	finite vol- ume	limited by transport time step	linear adsorp- tion	total dis- solved, total particulate
ELA Baptista, et al. (1984)	2D	finite ele- ment, Eule- rian- Lagrangian		linear decay	none
CONTAM -3D Hayter & Pakala (1989)	3D	finite ele- ment	limited by transport time step	linear adsorp- tion	total dis- solved, total particulate
CH3D Sheng, et al. (1990)	3D	finite vol- ume on cur- vilinear grid		none	none
Dortsch, et al. (1992)	3D	integrated compart- ment method		none	none
ELAmet	2D	finite ele- ment, Eule- rian- Lagrangian	not limited by transport time step	adsorption (lin- ear, nonlinear), aqueous com- plexation	any number dissolved and particu- late species

transformation terms. To date, surface water models have dealt with total dissolved and total particulate forms of sorptive substances, they have employed a non-site-specific sorption mechanism similar to hydrophobic partitioning, and they have failed to take into account aqueous speciation, which can vary dramatically with environmental factors such as pH, salinity and the availability of aqueous ligands. The treatment of the chemical transformation terms in ELAmet is general enough to accommodate many of the reactions likely to be important in determining the fate and transport of nonconservative substances in estuaries: adsorption via surface complexation or partitioning, aqueous complexation, and acid-base reactions (by considering the proton as an aqueous species). As in the previously mentioned subsurface models TRANQL and HYDROGEOCHEM, the chemical transformation equations are not substituted directly into the equations for hydraulic transport, but rather are kept as a separate system.

While there are many problems that are common to surface and subsurface modeling, one of the aspects of estuarine modeling that distinguishes it from groundwater modeling is the highly dynamic nature of the flow. Subsurface flows are comparatively slow, and transport models generally assume thermodynamic equilibrium; a few exceptions are noted in the review by *Mangold and Tsang* [1991]. However, circulation considerations in estuaries dictate a computational time step no longer than about an hour, which is sufficient to resolve the extremely important tidal frequencies. While many important chemical reactions will take place on a time scale short compared with an hour, we would like to consider as well reactions which take place on time scales of the same order or longer. Therefore, ELAmet has been designed to accommodate both chemical equilibria and kinetics. Each reaction in the system can be specified as rate-controlled, or can reach thermodynamic equilibrium in a time which is short compared to the computational time step required to resolve the circulation. This is done by dividing the chemical transformation equations into a system of mass action equations and a system of kinetic rate equations.

Another aspect which distinguishes estuarine transport from subsurface transport is that there is no fixed solid matrix. Instead, an estuarine geochemical model should generally be used in conjunction with a model designed to solve for transport of cohesive sediments. Because most organic and inorganic trace materials have at least some affinity for the solid phase, these sediments play a fundamental role in the transport of nearly all substances of interest. Thus a great deal of effort has been put into generating a satisfactory

model for cohesive sediment transport. *Onishi* [1981] and *Onishi and Trent* [1982] incorporated several sediment types into their models, recognizing that sediments comprise different size and compositional fractions, each with distinct sorptive and depositional characteristics. These models incorporate 2-dimensional representations of the physics of flocculation, erosion, and settling. ELAsed [Barros and Baptista, 1990] also uses 2-dimensional physics, and solves the problem in an Eulerian-Lagrangian framework. Most recently, three-dimensional models have been developed by *Sheng* [1983], and by *Hayter and Pakala* [1989]. *Hayter and Pakala* have also included a high-density near-bed suspension. We note, however, that all of these sediment transport models contain a limitation which may be serious in terms of fate and transport of adsorptive trace substances. In particular, they do not consider the colloidal fraction of the sediments, which can carry a substantial portion of the total nonfilterable concentration [Pankow and McKenzie, 1991, Eadie, et al., 1990].

Also unique to estuarine transport is the role of salinity, particularly in determining the ionic strength of the solution. Due to the mixing of freshwater and seawater in combination with a dynamic circulation, salinity, and therefore ionic strength, are functions of space and time. In geochemical speciation problems, this makes the calculation of the activity corrections to reactant concentrations a difficult matter, both because of the high ionic strengths involved (up to $I = 0.7M$) and because of the continuum of ionic strength to be found in a single system. Equations such as Debye-Hückel and Davies [Stumm and Morgan, 1981] provide a consistent means to calculate activity coefficients up to ionic strengths of $0.5M$, but become unsatisfactory at ionic strengths approaching that of seawater. In ELAmet we have taken the approach of using apparent constants, based on concentrations, rather than activities. This is based on the realization that, while explicit functions such as Debye-Hückel will be useful for extending thermodynamic constants over the lower range in salinity, there is at present no satisfactory alternative at higher salinities to using apparent constants obtained in seawater, or in solutions at high ionic strength.

In this paper we do not include a discussion of the details of the numerical solution technique used to solve the governing equations on a computational grid. As can be seen in Table 1, transport models have successfully employed finite elements, finite differences, and finite volumes; each technique has its supporting arguments. ELAmet uses a finite element technique, but the important aspects of the model and its application are not depen-

dent on this choice of solution technique. However, one aspect of how the entire advection/dispersion/transformation problem is reduced to tractable pieces is noteworthy. As will be discussed further below, the Eulerian-Lagrangian methods introduced by ELA [Baptista, *et al.* 1984] and expanded by ELAmet to include geochemical transformations [Wood and Baptista, 1992] have a distinct advantage in the solution of the advection/dispersion/transformation equation, as they overcome some severe Courant number limitations by decoupling advection and dispersion. These methods can be used, however, in either a finite element or finite difference context.

An obvious limitation of ELAmet is its use of depth-averaged equations, given that transport in estuarine environments is, in general, fully 3-dimensional. This dimensionality arises from the nature of the bottom sediments, and the stratification that occurs when saline ocean water meets fresh water. Several contributions to 3-dimensional transport modeling have been made [Onishi and Trent, 1982, Hauser, *et al.*, 1983, Hayter and Pakala, 1989, Sheng, *et al.*, 1990, Dortch *et al.*, 1992, Dimou, 1992]. The treatment of the chemical transformation terms in ELAmet is independent of dimensionality, and could therefore be incorporated in a straightforward way into a model for 3-dimensional transport. However, the development and use of 3-dimensional numerical models is limited by three things: 1) as in 2 dimensions, the lack of a basic understanding of processes, resulting in excessive use of parameterizations, 2) the lack of adequate field data to validate and calibrate models in three dimensions, and 3) the computing requirements for any realistic 3-dimensional problem. The third of these, while often given the most attention, is the least daunting, as available computing power is constantly increasing. In the case of ELAmet, the nonconservative terms that we introduce have not yet been examined in two dimensions, and there is much to be learned before taking the problem to three dimensions. Clearly, nonconservative transport is a 3-dimensional problem and should ultimately be modeled as such. We emphasize, however, that the limitations in field data cannot be trivialized in attacking this problem, and modifications in sampling strategies must occur if 3-dimensional modeling is to be successful.

Along with the presentation of the model, we wish to emphasize the intended mode of application, which is the subject of ongoing research. Numerical models have not fulfilled their potential to contribute to our understanding of fundamental estuarine processes. This is because the “diagnostic” function of numerical models has been underuti-

lized in favor of the “predictive” function, largely because the latter provides a basis for decision-making. Given that there is an acknowledged lack of measured equilibrium and rate constant data under environmentally relevant conditions, it is inappropriate to use a numerical model for which the input parameters are not well-known with the intent of “predicting” fate and transport. On the other hand, more advantage should be taken of the ability of models to aid our attempts to better understand natural processes. They are a means to extrapolate the information that can be obtained from laboratory experiments, representing small scales and hydrodynamically simple systems, to large-scale and hydrodynamically complex natural systems. As an example, consider the case of adsorption kinetics. This is a highly intractable problem if one is attempting to *predict* the fate of an adsorptive metal ion in an estuary. In order to accurately simulate the fate and transport of an adsorptive metal ion, one would need at the very least an accurate characterization of suspended sediments, including composition and surface area, and experimentally-determined rate constants obtained over the environmentally relevant ranges in salinity and pH. This type of information is not generally available as yet. However, we can look at the role of the numerical model differently. While rate constants can be measured under controlled conditions in the laboratory, it is difficult under these conditions to simulate the dynamic conditions of an estuary in which concentrations vary over the tidal cycle. A numerical model is a useful means of determining how the time scale of reaction kinetics interacts with the dominant time scale of the circulation. It is legitimate to use the model in this way to understand a small piece of the larger problem, even though the experimental data that would be needed to treat the problem completely is not available. It is this function of a numerical model, which we designate “diagnostic modeling”, that we want to emphasize with the introduction of ELAmet.

In the next two sections we present the basic features of ELAmet. The conceptual formulation section establishes a process-oriented interpretation of the chemical transformations that have been included in this model. The mathematical formulation section more rigorously defines the mathematical structure that results from the definition of the physical processes. A numerical verification follows to demonstrate the integrity of the algorithm used to solve the chemical transformations within the model. Finally, we present some examples of the diagnostic application of ELAmet to a simplified, prototype estuary. We have included an application in which ELAmet is used in a diagnostic mode to re-examine the interpretation of estuarine mixing plots. While this example does not fully

explore either the capabilities of ELAmet or the potential of diagnostic numerical modeling, it demonstrates that numerical models can provide additional insight into processes which are believed to be well-understood.

Conceptual Formulation

ELAmet integrates advective/dispersive transport with a description of the chemical transformations that affect the fate and transport of a metal in a way that represents a significant improvement over current state-of-the-art in numerical nonconservative estuarine transport models. Three significant contributions of ELAmet include: incorporation of aqueous speciation, the use of both linear and nonlinear reactions, and incorporation of both chemical equilibria and chemical kinetics.

The definition of the phases among which a given metal in the water column is distributed, and the processes that distribute mass among phases and among species within a single phase are shown schematically in Figure 2.1. Also indicated are the processes that remove mass from or add mass to the water column. Aqueous complexation reactions transfer mass between the various aqueous species. Adsorption reactions transfer mass between the aqueous and solid phase; the various solids represent, for example, distinct types of suspended particles. Adsorption can occur through site-specific reactions at the solid surface, analogous to aqueous complexation reactions, or through non-site-specific partitioning, analogous to hydrophobic partitioning. Depositional and erosional fluxes can remove mass from or add mass to the various solid phases. Sources and sinks internal to the system can contribute to mass changes in any of the water column phases.

One of the primary goals of ELAmet is to simultaneously accommodate reaction time scales which span several orders of magnitude, from minutes to days or longer. The model therefore allows for the assumption of thermodynamic equilibrium or the specification of a rate-controlled process, as the particular reaction requires. This is accomplished by separating the solution of the system of “fast” reaction equations from the solution of the system of “slow” reaction equations. Fast reaction equations are algebraic mass-action equations, independent of time, while slow reaction equations are time-dependent partial differential rate equations. We will also refer to “fast” species and “slow” species, the former being those species which enter into reactions assumed to equilibrate rapidly, and

the latter being those species which enter into reactions that must be described by rate equations.

The processes included in ELAmet are most easily understood through an example of a simple physical system. For the purposes of demonstration, we define a system which contains the following component species: a divalent metal ion, denoted Me^{2+} , two different fast aqueous ligands, denoted A^- and B^- , and another slow aqueous ligand denoted X^- ; in addition, suspended solids are present, which have two distinct site types available for complexation, a fast site denoted S^- and a slow site denoted O^- . Component and derived species must be defined within the context of the fast reactions and slow reactions; within each set of reactions a component species is defined as a species with a total mass that remains reaction invariant and a derived species is defined as a unique combination of component species. In this system Me^{2+} and all derived species are dependent variables, while A^- , B^- , O^- and S^- are independent variables. Dependent and independent variables are distinguished by whether their hydraulic transport is part of the model solution (dependent variables), or their values are supplied to ELAmet at each time step and grid node (independent variables). Generally, any concentration of surface sites would be an independent variable since sediment concentration is solved separately in a sediment transport model. The concentrations of non-metal-containing species such as aqueous ligands can be solved for as dependent variables in ELAmet, or they can be treated as independent variables.

Aqueous Complexation

Slow reactions

In this system, aqueous complexes can be formed between the divalent metal ion and one or two equivalents of the slow species X^- . This reaction is slow, in that it does not achieve thermodynamic equilibrium over the computational time step. Furthermore, it occurs in a two-part process with independent rate constants controlling each step. This type of rate-controlled reaction may represent, for example, a biologically-mediated methylation or butylation process. If we represent the first part of this reaction as



then the evolution of the reaction in time is represented by the second order rate equation:

$$\frac{d}{dt}[MeX^+] = \kappa_f[Me^{2+}][X^-] - \kappa_b[MeX^+] \quad (2.2)$$

where κ_f and κ_b are the forward and backward reaction rate constants, respectively. These rate constants have been modified to incorporate the activity coefficients of the species involved, so that the rate equation can be written in terms of concentrations, rather than activities. It follows from the form of reaction (2.1) that the rate of change in concentration of the dependent reactant species Me^{2+} is determined by:

$$\frac{d}{dt}[Me^{2+}] = -\frac{d}{dt}[MeX^+] = -\kappa_f[Me^{2+}][X^-] + \kappa_b[MeX^+] \quad (2.3)$$

The right-hand-side of reaction (2.1) contains the derived species which is a product of the reactants, or component species, on the left-hand-side. In the second part of the total reaction, another derived species is obtained by using the derived species in (2.1) as a component species, along with the component species X^- :



The rate equations associated with the dependent variables in reaction (2.4) are:

$$\frac{d}{dt}[MeX_2] = \kappa'_f[MeX^+][X^-] - \kappa'_b[MeX_2] \quad (2.5)$$

$$\frac{d}{dt}[MeX^+] = -\kappa'_f[MeX^+][X^-] + \kappa'_b[MeX_2] \quad (2.6)$$

The total rate of change in MeX^+ is therefore the sum of (2.2) and (2.6), illustrating that the rate of change in any dependent variable will be the cumulative effect of the reactions involving the variable as a product and as a reactant.

Fast reactions

In addition to complexation with the slow ligand X^- , the divalent metal ion will form complexes with the fast ligands A^- and B^- . The complexes involving Me^{2+} , A^- , and B^- form and dissociate quickly and it is reasonable to assume that thermodynamic equilibrium is reached in a time short compared to the computational time step. This type of

behavior is common in seawater, for example, in complexes involving the inorganic ligands OH^- and Cl^- . The reactions for the possible complexes are:



Because we can assume thermodynamic equilibrium, the adjustment in the speciation resulting from these reactions is not time dependent, and the defining relation becomes a simple ratio of products to reactants, the stability constant. For (2.7) the stability constant K is:

$$K = \frac{[\text{MeA}^+]}{[\text{Me}^{2+}] [\text{A}^-]} \quad (2.10)$$

This stability constant has been modified to incorporate the activity coefficients in a manner analogous to what was done for the rate constants above. A mass action equation is formed from this expression by solving for the product species.

Reaction (2.9) involves only component species as reactants. However, a fast complex can be derived from component species in combination with species derived from slow reactions such as (2.1). For example, in this system the inorganic ligand A^- will also form a complex with the charged molecule MeX^+ according to the reaction:



Since the adjustment to equilibrium is instantaneous, the total mass of $\text{MeX}_T = \text{MeXA} + \text{MeX}^+$ does not change during the course of the fast reaction. In this sense, species such as MeX^+ which are derived from slow reactions act as components within the context of the fast reactions.

ELAmet simultaneously handles fast reactions of the type (2.7), (2.8), (2.9) and (2.11), and slow reactions of the type (2.1) and (2.4) by defining two systems of equations that are solved separately and iterating between the two solutions. These two systems cannot be entirely independent, as some species are “shared”. For example, as illustrated by

the reactions above, free metal ions and complexes formed through rate-controlled reactions are available for further complexation through fast *and* slow reactions.

Adsorption Reactions

The adsorption of a metal ion or a metal complex onto the surface of a natural particle such as a suspended sediment is not well-understood. Given the uncertainties in defining the characteristics of natural particles and the various simultaneous mechanisms that combine under environmental conditions to make up “total” adsorption, our attempt in ELAmet is not to rely on one of the several *microscopic* descriptions of the solid/solution interface. Variations of the Gouy-Chapman-Stern model which are used to describe the electrostatic attraction between a charged surface and ions in solution, for example, have little, if any, relevance to natural particles which rarely have flat surfaces and for which there is no direct evidence regarding the nature of the binding sites [Westall, 1987]. Rather, we have tried to provide the mathematical framework to describe the adsorption process on a *macroscopic* level. In this context, the surface complexation conceptual model is a macroscopic description of adsorption for which the rate and the concentrations at equilibrium are observed to depend on the concentration of the sorbent (and therefore the concentration of sites) as well as the concentration of the solute. The binding site concentration in this case is a mathematically convenient quantity which is a function of the concentration of suspended sediments. The non-site-specific partitioning conceptual model is a macroscopic description of adsorption for which the rate and concentrations at equilibrium are independent of the concentration of sorbent. Furthermore, we can combine chemical equilibria and kinetics to describe the effect of the heterogeneities in the solid phase which manifest themselves in the bulk state as varying rates of uptake [Cameron and Klute, 1977]. Clearly the use of macroscopic representations in ELAmet implies that rate and equilibrium constants used in the model should be measured under environmentally relevant conditions and using natural particles, in order to duplicate as closely as possible the *bulk* properties of the natural system.

Surface complexation

Experimental adsorption data which exhibit Langmuir isotherm behavior indicate that the rate of the reaction depends upon the concentration of available sorbent sites. Surface complexation can be used to describe this type of site-specific adsorption. In this con-

ceptual model, adsorption onto the surface of a solid occurs as an aqueous species forms a complex with a charged surface site in a manner analogous to the formation of aqueous complexes. We carry the analogy further by representing fast surface sites as S^- and slow surface sites as O^- , but this does not imply any particular structure for the binding site. The adsorption of the free metal ion to the two sites is then represented by the following reactions:



where the subscript (s) emphasizes that the derived species is in the solid phase.

Reaction (2.12) achieves instantaneous equilibrium, and the time-independent ratio of the derived solid-phase species to the product of the reactants is given by a stability constant:

$$K'' = \frac{[MeS_{(s)}^+]}{[Me^{2+}][S^-]} \quad (2.14)$$

The evolution of the reaction (2.13) in time is described by a rate equation:

$$\frac{d}{dt}[MeO_{(s)}^+] = \kappa''_f [Me^{2+}][O^-] - \kappa''_b [MeO_{(s)}^+] \quad (2.15)$$

The corresponding rate equation describing the change in concentration of the dependent variable Me^{2+} is:

$$\frac{d}{dt}[Me^{2+}] = -\kappa''_f [Me^{2+}][O^-] + \kappa''_b [MeO_{(s)}^+] \quad (2.16)$$

Thus we have a fast and slow system for adsorption through complexation with surface sites, which is analogous to the fast and slow system developed for aqueous complexation.

Non-site-specific adsorption

In addition to the surface complexation mechanism for adsorption, non-site-specific adsorption is a means for conversion from the aqueous to the solid phase. Experimen-

tal data which show a linear isotherm for adsorption of a metal or metal complex indicate that the adsorption does not depend on the concentration of sorbent sites, and can be described by a linear type of reaction, analogous to the partitioning of hydrophobic molecules into the solid phase. The partitioning of the nonpolar compound MeX_2 is assumed to occur through a fast and slow reaction of the form:



and



respectively. Reaction (2.17) adjusts to equilibrium instantaneously, resulting in a ratio of the solid to aqueous phase called the partition coefficient:

$$K_p = \frac{[MeX_{2(s)}^{(fast)}]}{[MeX_2]} \quad (2.19)$$

whereas the evolution of the reaction (2.18) is determined by the first-order rate equations:

$$\frac{d}{dt}[MeX_{2(s)}^{(slow)}] = \kappa_f''' [MeX_2] - \kappa_b''' [MeX_{2(s)}^{(slow)}] \quad (2.20)$$

$$\frac{d}{dt}[MeX_2] = -\kappa_f''' [MeX_2] + \kappa_b''' [MeX_{2(s)}^{(slow)}] \quad (2.21)$$

Summary of Equations

We can now summarize the equations used to solve for the speciation in this system. The fast equations are the nonlinear algebraic mass action equations for the derived species in the fast system: MeA^+ , MeB^+ , $MeAB$, $MeXA$, $MeS_{(s)}^+$, and $MeX_{2(s)}^{(fast)}$. In order to have enough information to solve for all unknowns, this system of equations must be complemented with a mass balance equation for each of the component species. The species that act as components for the fast system are Me^{2+} , A^- , B^- , S^- , and MeX^+ and MeX_2 . Noting that the totals Me_T , MeX_T , and MeX_{2T} refer to the total mass only within the context of the fast system, the required mass balances are:

$$Me_T = [Me^{2+}] + [MeAB] + [MeA^+] + [MeB^+] + [MeS_{(s)}^+] \quad (2.22)$$

$$MeX_T = [MeX^+] + [MeXA] \quad (2.23)$$

$$MeX_{2T} = [MeX_2] + [MeX_{2(s)}^{(fast)}] \quad (2.24)$$

$$A_T = [A^-] + [MeAB] + [MeA^+] + [MeXA] \quad (2.25)$$

$$B_T = [B^-] + [MeAB] + [MeB^+] \quad (2.26)$$

$$S_T = [S^-] + [MeS_{(s)}^+] \quad (2.27)$$

The slow equations of this system are ordinary differential equations for the species Me^{2+} , MeX^+ , MeX_2 , $MeO_{(s)}^+$, and $MeX_{2(s)}^{(slow)}$ formed by combining source/sink terms for the same species from (2.2), (2.3), (2.5), (2.6), (2.15), (2.16), (2.20) and (2.21). The resulting equations for the aqueous phase species are:

$$\frac{d}{dt}[Me^{2+}] = -\kappa_f[Me^{2+}][X^-] + \kappa_b[MeX^+] - \kappa''_f[Me^{2+}][O^-] + \kappa''_b[MeO_{(s)}^+] \quad (2.28)$$

$$\frac{d}{dt}[MeX^+] = \kappa_f[Me^{2+}][X^-] - \kappa_b[MeX^+] - \kappa'_f[MeX^+][X^-] + \kappa'_b[MeX_2] \quad (2.29)$$

$$\frac{d}{dt}[MeX_2] = \kappa'_f[MeX^+][X^-] - \kappa'_b[MeX_2] - \kappa'''_f[MeX_2] + \kappa'''_b[MeX_{2(s)}^{(slow)}] \quad (2.30)$$

Equations (2.15), (2.20) and (2.21) are the required solid phase species equations. An additional equation is needed for the components X^- , and O^- in order to solve for all of the unknowns. Mass balance equations are written for X^- and O^- :

$$O_T = [O^-] + [MeO_{(s)}^+] \quad (2.31)$$

$$X_T = [X^-] + [MeX^+] + 2[MeX_2] \quad (2.32)$$

An iteration between the fast system and the slow system is required to converge on a speciation. The two systems are linked because the species Me^{2+} , MeX^+ , and MeX_2 are shared. In practice, it is convenient to substitute the fast system totals Me_T , MeX_T , and

MeX_{2T} , which are proportional to these three species, as dependent variables in the slow system.

The physical system we have described is sufficiently complex to demonstrate the important features ELAmet's treatment of aqueous speciation and fast and slow reactions. Additional constraints such as linear decay, internal sources and sinks, and fluxes due to sediment deposition/erosion can be placed on any of the variables in the model system. Also, we have demonstrated the use of first and second order reactions, but any stoichiometry is allowed. Adsorption via ion exchange can also be accommodated. Redox reactions can, in principle, be handled within ELAmet's mathematical framework by treating the activity of the electron as a component species. However, because the activity of the electron can span a range covering tens of orders of magnitude, the solution technique that ELAmet uses to solve the matrix equations for the chemical reactions may have to be modified before redox reactions can really be accommodated [Yeh and Tripathi, 1991]. A major limitation in the geochemistry of ELAmet is that the model cannot accommodate the precipitation of solids.

Mathematical Formulation

In this section we provide a precise and comprehensive description of the mathematical equations making up ELAmet. A list of symbols used in this section is found in the Appendix.

Overview

We begin with the depth-averaged equation for conservation of mass of a passive, nonconservative tracer. Derivation of this equation will not be included here, as it is readily available in the literature [e.g., Adams and Baptista, 1986]. Every species in our system has a conservation of mass equation of the general form

$$\frac{\partial c_i}{\partial t} + \Lambda(c_i) = \Theta_i^c + Q_i^c \quad (2.33)$$

where c_i is any species concentration (mass/volume), Q_i^c represents any internal sources or sinks, Θ_i^c includes all nonconservative chemical transformation terms, and Λ is the depth-averaged advection/dispersion operator

$$\Lambda = u_k \frac{\partial}{\partial x_k} - \frac{1}{h} \frac{\partial}{\partial x_k} (D_{kj} h \frac{\partial}{\partial x_j}) \quad (2.34)$$

In the above expression D_{kj} is the dispersion coefficient, h is the depth of the water column, and u_k is the depth-averaged velocity. Thus the $\Lambda(c_i)$ term on the left-hand-side of equation (2.33) describes the change in mass concentration due to an imbalance between mass in and out of a control volume through hydraulic transport processes. The right-hand-side term Θ_i^c describes changes in mass concentration due to chemical transformations that convert mass of one species to mass of another; also included in this term are linear decay terms which represent a net loss of mass, and deposition/erosion terms which transfer mass to the bed sediments. In general, this term will be highly nonlinear and will involve several species c_i , making the equations of the system interdependent. Solving a system consisting of an equation of the form (2.33) for each species is a formidable prospect. Consequently, much effort has been put into devising ways of breaking the problem up into more manageable pieces.

In ELAmet, the first step is to decouple the advection portion of the hydraulic transport from the dispersion and the chemical transformation portions of the problem using an Eulerian-Lagrangian method [Baptista, 1987]. This method incorporates advection by tracking backward along a characteristic originating from each grid node. Conditions at the intersection of the characteristic line with the last time step are used as the initial conditions for the rest of the problem. These methods are well-established for solving advection/dispersion problems, and it is a logical extension to also solve the chemical transformation part of the problem along the same characteristic.

The next step is to separate the solution of the chemical transformation equations from the solution of dispersion. This is not a new concept, and as it is done in ELAmet it is similar to the choice of primary governing equations (PGEs) and secondary governing equations (SGEs) as discussed by Yeh and Tripathi [1989]. We significantly expand this concept, however, in that we allow for both equilibrium-type and kinetic-type chemical reactions to take place, and in doing so we break up the solution of the chemical reaction equations into a fast system of nonlinear algebraic equations and a slow system of linear partial differential equations.

There are several advantages of breaking up the complete advection/dispersion/transformation problem as we have done here, all of which translate into greater computational efficiency. However, it is also conceptually satisfying to recognize the increased ability to tailor the specifics of the solution directly to the portion of the problem being solved. As an example, consider the computational time step. The solution of the advection/dispersion equation using strictly Eulerian methods is highly constrained by a limitation on the Courant number. However, when tracking is separated from dispersion, this constraint on the dispersion portion of the problem is relaxed and the tracking, while requiring a small computational time step, is efficient as it involves solving an extremely simple equation at only one computational grid node at a time. In ELAmet this is taken a step further, as the chemical reaction equations are also solved along the characteristic lines. This allows the choice of a computational time step which is appropriate for the chemical time scales under consideration, independent of the time steps chosen for advection and dispersion. Thus the original equation (2.33) is now broken into three simpler equations of the form:

$$u_i = \frac{dx_i}{dt} , \quad (2.35)$$

$$\frac{dc_i}{dt} = \Theta_i^c , \quad (2.36)$$

$$\frac{\partial c_i}{\partial t} = Q_i^c + \frac{1}{h} \frac{\partial}{\partial x_k} \left(D_{kj} h \frac{\partial c_i}{\partial x_j} \right) . \quad (2.37)$$

As noted above, equation (2.35) has no spatial gradients and can therefore be done at one computational grid node at a time. Furthermore, the tracking itself (locating the feet of the characteristics) will be identical for each chemical species, and therefore need only be done once at each grid node. Equation (2.36) will, in general, be a dependent system of equations, but since it contains no spatial gradients, it can be solved at one computational grid node at a time. The form of this equation also means that the solution of chemical transformations in ELAmet is independent of the dimensionality of the problem. Equation (2.37) has spatial gradients and therefore must be solved simultaneously over the entire domain, but since each equation only involves one chemical species, the solution can be done independently for each of the species in the system. This distinction between field equations containing spatial gradients and point equations which do not has also been used

to advantage by *Yeh and Tripathi*, [1991]. In addition to substantially decreasing the size of the matrices that must be stored and inverted, this approach allows many computations to be done concurrently, and therefore is especially suited to solution on parallel computers.

Solution of Chemical Reaction Equations

Any chemically-reactive system can be described in terms of component and derived species. The component species form a set of "basis functions" for the derived species. Each component is made up only of itself, whereas each derived species is a unique combination of component species. This distinction is important conceptually because we associate with each component species a mass balance equation, and with each derived species a mass action or a kinetic rate equation, depending on whether it is a fast or slow reaction. A general surface water system will be made up of aqueous metal-containing components, aqueous ligand components, and sorbent components. The sorbent components represent sites available for participation in adsorption reactions. The aqueous ligand components are non-metal-containing dissolved species which participate in the formation of aqueous complexes. Derived species are aqueous complexes which are combinations of aqueous metal-containing and ligand components, and adsorbed species which are combinations of aqueous metal-containing and sorbent components.

ELAmet accommodates a range of reaction time scales by defining two systems for the determination of speciation: a fast system governed by the assumption of equilibrium, and a slow system made up of rate-controlled processes. We can write the following mass balance equations, one for each component species in the fast system (system I):

$$C_j = c_j + \sum_{i=1}^{M_d} a_{ij}c'_i + \sum_{i=1}^{M_s} b_{ij}c''_i \quad j = 1, 2, \dots, N_c \quad (2.38)$$

$$L_j = l_j + \sum_{i=1}^{M_d} d_{ij}c'_i \quad j = 1, 2, \dots, N_l \quad (2.39)$$

$$S_j = s_j + \sum_{i=1}^{M_s} e_{ij}c''_i \quad j = 1, 2, \dots, N_s \quad (2.40)$$

where C_j , L_j , and S_j are the total analytical concentrations of the j^{th} aqueous metal-containing component, the j^{th} aqueous non-metal-containing component, and the j^{th} sorbent component, respectively; c'_i is the concentration of the i^{th} complexed species; N_c , N_l , N_s are the number of aqueous metal-containing components, aqueous ligand components, and sorbent components, respectively; M_d is the number of aqueous complexed derived species; M_s is the number of solid-phase derived species; a_{ij} is the stoichiometric coefficient of the j^{th} aqueous component in the i^{th} complexed species; c''_i is the concentration of the i^{th} sorbed species; b_{ij} is the stoichiometric coefficient of the j^{th} aqueous component in the i^{th} sorbed species; d_{ij} is the stoichiometric coefficient of the j^{th} aqueous ligand in the i^{th} complexed species, and e_{ij} is the stoichiometric coefficient of the j^{th} sorbent component in the i^{th} sorbed species. The mass balance equations associated with the component species of the slow system (system II) are:

$$\bar{C}_j = \bar{c}_j + \sum_{i=1}^{\bar{M}_d} \bar{a}_{ij} \bar{c}'_i + \sum_{i=1}^{\bar{M}_s} \bar{b}_{ij} \bar{c}''_i \quad j = 1, 2, \dots, \bar{N}_c \quad (2.41)$$

$$\bar{L}_j = \bar{l}_j + \sum_{i=1}^{\bar{M}_d} \bar{d}_{ij} \bar{c}'_i \quad j = 1, 2, \dots, \bar{N}_l \quad (2.42)$$

$$\bar{S}_j = \bar{s}_j + \sum_{i=1}^{\bar{M}_s} \bar{e}_{ij} \bar{c}''_i \quad j = 1, 2, \dots, \bar{N}_s \quad (2.43)$$

where the symbols with overbars have definitions analogous to those without the overbar.

These two systems are connected in that they share metal-containing aqueous species. All of the metal-containing aqueous components and the aqueous complexes from the slow system are available as metal-containing aqueous components in the fast system. In other words, each of the c_j in the fast system corresponds to a particular \bar{c}_j or a particular \bar{c}'_j in the slow system. It follows that $N_c = \bar{N}_c + \bar{M}_d$. In the notation introduced above, we have:

$$\begin{aligned} c_j &= \bar{c}_j & j &= 1, 2, \dots, \bar{N}_c \\ c_j &= \bar{c}'_k & k &= 1, 2, \dots, \bar{M}_d & j &= \bar{N}_c + 1, \dots, \bar{N}_c + \bar{M}_d \end{aligned} \quad (2.44)$$

This corresponds to a situation such as that described in the previous section in which the divalent metal ion Me^{2+} acts as a component species in both fast reactions and slow reactions. Thus, this ion is represented by c_j in the fast system and by \bar{c}_j in the slow system. Similarly, in the previous section it was shown that a species such as MeX^+ derived from a slow reaction could act as a component in a fast complexation reaction along with another complexing ligand. Using the current notation, MeX^+ is represented by \bar{c}_j in the slow system and by c_j in the fast system.

Associated with each derived species in both systems is an equation which describes how the component species combine to create the derived species. The form that this equation takes depends on whether the time scale of the reaction is very short compared to the computational time step being used in the time-stepping algorithm. A “fast” reaction relative to the computational time step will be described by a mass action equation, whereas a “slow” reaction will be described by a kinetic rate equation. In our formulation, the derived species c'_i and c''_i of system I are described by mass action equations of the form:

$$c'_i = \alpha_i \left(\prod_{j=1}^{N_l} l_j^{d_{ij}} \right) \left(\prod_{k=1}^{N_c} c_k^{a_{ik}} \right) \quad i = 1, 2, \dots, M_d \quad (2.45)$$

$$c''_i = \beta_i \left(\prod_{j=1}^{N_s} s_j^{e_{ij}} \right) \left(\prod_{k=1}^{N_c} c_k^{b_{ik}} \right) \quad i = 1, 2, \dots, M_s \quad (2.46)$$

where α_i is the stability constant of the i^{th} complexed species, and β_i is the stability constant of the i^{th} sorbed species.

All stability and rate constants have been modified to incorporate activity coefficients of the species concentrations, and therefore are *apparent* constants, based on concentrations rather than activities. For example, in equation (2.45):

$$\alpha_i = \alpha'_i \left(\prod_{j=1}^{N_l} \gamma_{l_j}^{d_{ij}} \right) \left(\prod_{k=1}^{N_c} \gamma_{c_k}^{a_{ik}} \right) \gamma_{c'_i}^{-1} \quad (2.47)$$

where γ_{c_i} is the activity coefficient of species c_i and α'_i is the thermodynamic stability constant based on activities referenced to the infinite dilution state. ELAmet makes use of apparent constants in the chemical transformation equations. However, the major seawater ions and/or salinity can be solved for within the model, providing ionic strength values as a function of space and time. Activity corrections to thermodynamic constants can then be calculated at low salinities (ionic strengths up to $I = 0.1M$) using the Debye-Hückel equation and its extension, and a further modification, the Davies equation, for ionic strengths up to $0.5M$ [Stumm and Morgan, 1981]. At salinities approaching that of seawater ($I = 0.7M$), this means of making activity corrections becomes unsatisfactory. Theories based on sound thermodynamic principles, such as ion interaction theory, are available for calculating activity corrections at higher salinities [Stumm and Morgan, 1981]. However, it is useful to recognize that very precise calculations of activity corrections are probably not very worthwhile when one considers that the uncertainties in the thermodynamic constants themselves are very high. Differences in values taken from the literature for stability constants are likely to produce differences in the resultant speciation that swamp any differences attributed to errors in activity corrections. Our viewpoint is that in the application of ELAmet to real systems, the most satisfactory solution to this problem is to use apparent constants from the literature, valid for a particular ionic strength, whenever possible, and to avoid the necessity of making activity corrections.

The components of system II combine through slow reactions to form new derived species \bar{c}'_i and \bar{c}''_i . If we denote by \bar{r}'_i the rate of production of the complexed species \bar{c}'_i and by \bar{r}''_i the rate of production of the sorbed species \bar{c}''_i , then:

$$\bar{r}'_i = \kappa_i^f \left(\prod_{j=1}^{\bar{N}_i} \bar{l}_j^{d_{ij}} \right) \left(\prod_{k=1}^{\bar{N}_c} \bar{c}_k^{a_{ik}} \right) \left(\prod_{n=1}^{\bar{M}_d} \bar{c}_n^{\bar{g}_{in}} \right) - \kappa_i^b \bar{c}'_i \quad i = 1, 2, \dots, \bar{M}_d \quad n \neq i \quad (2.48)$$

$$\bar{r}''_i = \kappa_i^{f''} \left(\prod_{j=1}^{\bar{N}_i} \bar{s}_j^{e_{ij}} \right) \left(\prod_{k=1}^{\bar{N}_c} \bar{c}_k^{b_{ik}} \right) \left(\prod_{n=1}^{\bar{M}_d} \bar{c}_n^{\bar{h}_{in}} \right) - \kappa_i^{b''} \bar{c}''_i \quad i = 1, 2, \dots, \bar{M}_s \quad n \neq i \quad (2.49)$$

where κ_i^f and κ_i^b are the forward and backward reaction rate constants, respectively, for the i^{th} complexation reaction; $\kappa_i^{f''}$ and $\kappa_i^{b''}$ are the forward and backward reaction rate constants, respectively, for the i^{th} adsorption reaction. As with the stability constants, these reaction rate constants must be modified to incorporate the products of the activity coefficients of the reactant species concentrations. The exponents \bar{g}_{in} and \bar{h}_{in} are the sto-

stoichiometric coefficients of the n^{th} aqueous complex in the i^{th} aqueous complex and the i^{th} sorbed species, respectively. Nonzero values of these coefficients indicate that we allow derived species to be built up from other derived species, as well as directly from components.

We are now in a position to construct the advection/dispersion/transformation equation (2.33) for each of the species in our two systems. The chemical transformation term for system II species must include the rate-of-change information in equations (2.48) and (2.49) for every reaction in which the species appears as either a reactant or a product. Therefore, the general form of the equation (2.33) for each of the system II species has a right-hand-side chemical transformation term defined as (note that the Einstein convention for the summation of repeated indices is not being used):

$$\bar{\Theta}_i^c = - \sum_{k=1}^{\bar{M}_d} \bar{a}_{ki} \bar{r}'_k - \sum_{k=1}^{\bar{M}_s} \bar{b}_{ki} \bar{r}''_k - \bar{F}_i^c \bar{c}_i \quad i = 1, 2, \dots, \bar{N}_c \quad (2.50)$$

$$\bar{\Theta}_i^l = - \sum_{k=1}^{\bar{M}_d} \bar{d}_{ki} \bar{r}'_k - \bar{F}_i^l \bar{l}_i \quad i = 1, 2, \dots, \bar{N}_l \quad (2.51)$$

$$\bar{\Theta}_i^s = - \sum_{k=1}^{\bar{M}_s} \bar{e}_{ki} \bar{r}''_k - \bar{F}_i^s \bar{s}_i \quad i = 1, 2, \dots, \bar{N}_s \quad (2.52)$$

$$\bar{\Theta}_i^v = \bar{r}'_i - \sum_{k=1}^{\bar{M}_d} \bar{g}_{ki} \bar{r}'_k - \sum_{k=1}^{\bar{M}_s} \bar{h}_{ki} \bar{r}''_k - \bar{F}_i^v \bar{c}'_i \quad i = 1, 2, \dots, \bar{M}_d \quad k \neq i \quad (2.53)$$

$$\bar{\Theta}_i'' = \bar{r}''_i - \bar{F}_i'' \bar{c}''_i \quad i = 1, 2, \dots, \bar{M}_s \quad (2.54)$$

where F_i is a flux which can include a linear decay or a loss/gain of mass due to sediment deposition/erosion in the case of a solid-phase species. In system I, the chemical transformation information is decoupled from the time-dependent hydraulic transport, so that the Θ_i term in general has a simpler form:

$$\Theta_i^c = \bar{\Theta}_i^c \quad i = 1, 2, \dots, \bar{N}_c \quad (2.55)$$

$$\Theta_i^c = \bar{\Theta}_j^v \quad j = 1, 2, \dots, \bar{M}_d \quad i = \bar{N}_c + 1, \dots, \bar{N}_c + \bar{M}_d \quad (2.56)$$

$$\Theta_i^z = -F_i^z z_i \quad z = (l, s, c', c'') \quad i = 1, 2, \dots, (N_l, N_s, M_d, M_s) \quad (2.57)$$

The equations resulting from substituting (36) and (37) into (2.33) represent a formidable set of nonlinear partial differential equations. However, it is not necessary to solve the system as is. In order to proceed, we introduce the concept of primary variables and secondary variables. This terminology is similar to that used by *Yeh and Tripathi* [1989], and we use a definition which is roughly equivalent to that used in their paper. Our primary variables are defined as those variables which we solve for directly by solving the advection/dispersion/transformation equations. Thus the equations making up the system that is solved for the primary variables are partial differential equations of the form (2.33). Secondary variables are those variables which are solved for through a mass action or mass balance equation once the primary variables are known.

The following are the unknowns in the two systems: $C_j, L_j, S_j, c_j, c'_j, l_j, s_j, c''_j$ in the "fast" system, and $\bar{C}_j, \bar{L}_j, \bar{S}_j, \bar{c}_j, \bar{c}'_j, \bar{l}_j, \bar{s}_j, \bar{c}''_j$ in the slow system. Because the mass balance equations (2.38), (2.39), and (2.40) and the mass action equations (2.45) and (2.46) relate the concentrations in system I independently of time, the eight unknowns in this system can be reduced to only three. We do this by using equations (2.38), (2.39), and (2.40) to linearly combine the transport equations as follows:

$$\frac{\partial C_j}{\partial t} + \Lambda(C_j) = \Theta_j^c + \sum_{i=1}^{M_d} a_{ij} \Theta'_i + \sum_{i=1}^{M_s} b_{ij} \Theta''_i \quad j = 1, 2, \dots, N_c \quad (2.58)$$

$$\frac{\partial L_j}{\partial t} + \Lambda(L_j) = \Theta_j^l + \sum_{i=1}^{M_d} d_{ij} \Theta'_i \quad j = 1, 2, \dots, N_l \quad (2.59)$$

$$\frac{\partial S_j}{\partial t} + \Lambda(S_j) = \Theta_j^s + \sum_{i=1}^{M_s} e_{ij} \Theta''_i \quad j = 1, 2, \dots, N_s \quad (2.60)$$

In general, the concentration of surface sites will not be treated as an unknown, but rather will be input at each node and time step as an independent variable. In this case, equation (2.60) will not be needed, and will be replaced by a mass balance equation of the form (2.40). The total aqueous ligand concentration may also be treated as an independent variable, in which case system I has only 1 primary variable, which is C_j .

Because the transformation information for system II is contained in the \bar{r}'_i and \bar{r}''_i terms, the hydraulic transport equations cannot be combined as in system I, as this would result in too few equations to solve for the complete speciation. However, since \bar{L}_j and \bar{S}_j are, in general, independent variables, the mass balance equations (2.42) and (2.43) can be used to solve for \bar{l}_j and \bar{s}_j , reducing the number of primary variables to three for this system. Of these three- $\bar{c}_j, \bar{c}'_j, \bar{c}''_j$ -two are not independent because of the correspondence between c_j and \bar{c}_j, \bar{c}'_j . This correspondence means that the fast system variable C_j is proportional to one of the slow system variables \bar{c}_j or \bar{c}'_j , and only C_j need be considered an independent variable. This leaves only the solid phase species in system 2 as independent primary variables. Therefore, the final set of governing equations (without the requisite mass balances) for primary variables from the two systems is:

$$\frac{\partial C_j}{\partial t} + \Lambda(C_j) = \Theta_j^c + \sum_{i=1}^{M_d} a_{ij} \Theta_i' + \sum_{i=1}^{M_s} b_{ij} \Theta_i'' \quad i = 1, 2, \dots, N_c \quad (2.61)$$

$$\frac{\partial \bar{c}''_j}{\partial t} + \Lambda(\bar{c}''_j) = \bar{\Theta}''_j \quad i = 1, 2, \dots, \bar{M}_s \quad (2.62)$$

At this point it is useful to recognize that the left-hand-side of (2.61) and (2.62) is dependent on only one variable, so that by separating the solution of advection and dispersion from the solution of chemical transformation, we can gain a significant advantage by solving the advection/dispersion portion of the problem separately for each primary variable. As indicated by equations (2.35), (2.36), and (2.37), this is how the solution proceeds.

The chemical reaction portion of the problem consists of two systems of equations and requires an iterative procedure to converge on a speciation of system I and II variables to within a prescribed error criterion [Wood and Baptista, 1992]. System I equations are the mass balance equations (2.38), (2.39), and (2.40) and the mass action equations (2.45) and (2.46). System II equations are the mass balance equations (2.41), (2.42), and (2.43) and the ordinary differential kinetic rate equations which result from (2.61) and (2.62) when the advection/dispersion operator Λ is set to zero. At the beginning of each time step, the initial condition for the iteration is obtained from the last time step by interpolating to the foot of the characteristic line which results from tracking backward from each node. A Newton-Raphson technique is used to solve the set of nonlinear algebraic equations which make up system I. These results are then used as initial conditions in solving

the differential equations which make up system II. System II equations are linearized by using values from the previous iteration. The solution of system II results in a modified value of C_j , which must be substituted back into system I. The iteration proceeds until convergence is reached.

In addition to the distribution of mass of the metal within the water column, if sediment deposition and erosion are present, there is a transfer of mass to the bed sediments. The evolution of the concentration in the bed sediments is governed by an equation of the form:

$$\frac{dc_j^{bed}}{dt} = F_j'' c_j \quad \text{or} \quad \frac{d\bar{c}_j^{bed}}{dt} = \bar{F}_j'' \bar{c}_j \quad (2.63)$$

in the case of deposition, and by an equation of the form:

$$\frac{dc_j^{bed}}{dt} = F_j'' c_j^{bed} \quad \text{or} \quad \frac{d\bar{c}_j^{bed}}{dt} = \bar{F}_j'' \bar{c}_j^{bed} \quad (2.64)$$

in the case of erosion, where c_j and \bar{c}_j represent solid-phase species only, as the total mass in the aqueous phase in the bed sediments is assumed to be small. The flux F_j'' is positive in the case of sediment deposition, and negative in the case of sediment erosion. Equations (2.63) and (2.64) constitute a third set of equations that is included in the iterative loop with the first two.

As these equations indicate, the bed sediments are treated as a single well-mixed layer in terms of chemical speciation, with all diagenetic processes neglected. This is clearly a simplistic description of the structure of the bottom sediments, for several reasons. First, the near-bed high-density sediment suspension is not included in this formulation. Second, while bioturbation processes might be expected to mix the sediments through the first few centimeters, the time-dependent layering of the sediments would be expected to give them a distinctly 3-dimensional nature [Berner, 1980]. Finally, all chemical transformations taking place within the sediments themselves are ignored. For some estuarine metal cycles, these diagenetic transformations are thought to be very important, especially when the reducing environment of the deeper sediments becomes involved.

However, for the purposes of exploring the nature of the nonconservative behavior in the water column, this treatment of the sediments is adequate, and is a precursor to a more comprehensive study of nonconservative behavior, which will eventually take into account depth-dependent sediments and diagenetic behavior.

Solution of hydraulic transport

The solution of tracking and dispersion (equations (2.35) and (2.37)) for each of the primary variables is obtained using an Eulerian-Lagrangian method (ELM). These methods are well-established in the literature, so a detailed development is not included here (see, e.g., *Baptista*, 1987). In short, ELMs take their name from the fact that the advection portion of the transport equation is solved by tracking backward along characteristic lines, which is a Lagrangian formulation, while the dispersion part of the transport equation is solved on a fixed grid, which represents an Eulerian formulation. The initial conditions for dispersion are provided by the intersection of the backward tracking with the previous time step. In ELAmet, the dispersion equation is solved on a quadratic triangular finite element grid using a Galerkin formulation. The tracking is done using a fifth-order Runge Kutta scheme. Interpolation at the feet of the characteristic lines is done using the same quadratic shape functions as are used in the finite element formulation of the dispersion equation.

Numerical Verification

To demonstrate the integrity of the numerical algorithm, we include here a 1-dimensional channel problem. The channel is of constant depth, width 200 m and length 10 km. A spatially uniform, constant along-channel velocity of 0.02 m s^{-1} is imposed.

The problems we discuss use specifically some of the various reactions discussed for the hypothetical system in the *Conceptual Formulation* section of this paper. In each case, the initial conditions for metal ion concentration are zero throughout the domain. Metal is introduced into the domain through a constant boundary concentration of aqueous metal imposed at the upstream end of the channel. The metal concentration is then advected down the channel as a front, undergoing chemical transformations along the way. There is no dispersion in this problem, as our primary goal is to test the numerical algo-

rithm for mass conservation, and where possible, to compare with an analytical solution. The time step used to solve the chemical transformations is 1 hour.

The first demonstration problem is a simple linear partitioning of the aqueous into the solid phase, as described by equations (2.20) and (2.21). We use $\kappa'''_f = \kappa'''_b = (25hr)^{-1}$. For simplicity, all concentrations are nondimensional. A constant concentration of $[MeX_2]=1.0$ is imposed at the upstream end of the channel. Thus, as the front is advected down the channel, the concentration of $[MeX_2]$ is depleted and $[MeX_{2(s)}^{(slow)}]$ increases as the sorption process proceeds. Figure 2.2 shows the front at several different times during the simulation. Especially at early times during the simulation, there are small oscillations at the edge of the front. These are due to the fact that the transport algorithm advects the highest frequencies at a slightly different speed than the lower frequencies. In this case, there is an analytical expression for the evolution of the reaction in time, so that by equating the distance along the front to the time since entering the domain, we can calculate the theoretical shape of the aqueous metal concentration along the channel for comparison. This analytical solution is plotted in Figure 2.2 at $t=100$ hrs, and the agreement is excellent. Also shown is the profile of total metal, as calculated at $t=100$ hrs, which shows only minor distortions in the theoretical step function shape, due to the previously mentioned problems with the solution of advection.

The second problem involves a complexation-type of adsorption, as described by equations (2.15), and (2.16). In this case, we use the same values as above for the rate constants. A constant unit concentration of metal ion $[Me^{2+}]$ is imposed at the end of the channel. The total concentration of surface sites $[O^-]$ is initially set to the nondimensional value of 1.0 throughout the domain, so that as the adsorption process proceeds, the free surface sites are depleted, and the concentration of $[MeO^+]$ increases. The results for several time steps are shown in Figure 2.3. A comparison of this figure with Figure 2.2 shows that a second-order adsorption in which the surface sites are available in concentrations comparable to the adsorbing metal ion will lead to a steady-state in which less of the metal is adsorbed than in the linear partitioning case. An analytical solution is available for this problem, and is included in the figure for comparison with time $t=100$ hrs. The comparison is excellent. The profile of total metal preserves very well the step-function shape of the front, and the total of free and complexed surface sites remains uniform over the domain, as it should.

The third problem is a variation on the second, in that we introduce competition with an aqueous ligand into the problem. The ligand A^- competes with the surface sites for the free metal ion through a rapid reaction as in Equation (2.7), with an equilibrium constant $K = 10$. The ligand is initially present at a nondimensional concentration of 0.1 throughout the domain, and therefore this represents the concentration of free plus complexed ligand at all subsequent times. The results are plotted in Figure 2.4, and show that, as expected, the competition from the aqueous ligand further limits the extent of adsorption with respect to either of the first two problems. An analytical solution is not available for this problem; however, we show the total mass of metal, surface sites, and ligand at time $t=100$ hrs. Again, the total metal concentration preserves the step-function shape of the front very well, and the total ligand and total surface sites remain uniform over the domain, as they should.

As a final demonstration, the entire system as described in the *Conceptual Formulation* section was used in this 1-dimensional channel. The initial conditions include surface site concentrations $[O^-]$ and $[S^-]$ equal to 1.0 throughout the domain, and ligand concentrations $[A^-]$, $[B^-]$, and $[X^-]$ equal to 0.1 throughout the domain. The free metal ion is imposed at a constant concentration $[Me^{2+}]=1.0$ at the channel end. The values chosen for rate and equilibrium constants are as follows: $\kappa_f = \kappa_b = (25hr)^{-1}$, $\kappa'_f = \kappa'_b = (50hr)^{-1}$, $\kappa''_f = \kappa''_b = (25hr)^{-1}$, and $\kappa'''_f = \kappa'''_b = (50hr)^{-1}$; $K_1 = 1.0$, $K_2 = 5.0$, $K_3 = 1.0$, $K'' = 1.0$ and $K_p = 0.1$, where the notation is as defined in the *Conceptual Formulation*, and K_1 , K_2 , and K_3 are the equilibrium constants for $[MeA^+]$, $[MeB^+]$, and $[MeXA]$, respectively. These values do not represent a particular real situation, but they do allow us to test the algorithm for a problem with a large number (15) of independent species. In Figure 2.5 we show the profiles of all of the species at $t=100$ hr. We have computed the total metal, total surface sites, and total aqueous ligands. These totals behave as they should, with minor deviations in the total metal at the edge of the front due to the differential advection of high and low frequencies.

Application: Introduction to Diagnostic Modeling

A routine procedure in the interpretation of field data is to plot the concentration of trace metals against salinity, the latter representing a substance known to be conserved in the system. If the data plotted in this way fall along a straight line connecting the riverine

and oceanic end members, is taken to indicate that the trace metal is mixed conservatively (see Figure 2.6). If the data fall on a curve tending toward a concave upward form, this indicates some type of internal sink, while a tendency toward a concave downward form indicates an internal source.

In this section we use simple applications of ELAmet in a diagnostic mode to examine the mixing process in a prototype estuary, and consider the implications for field sampling of this system. We demonstrate that 1) in two or more dimensions, the mixing curve will not be a single-valued function of salinity if the system cannot be described as the mixing of two end-members, and 2) that limited field sampling can fail to capture important features of the mixing curve. The three examples that we have chosen use the placement of the source, reaction kinetics, and sediment deposition to show that the traditional 1-dimensional interpretation of the sampled mixing plot can be deceiving.

Test System

Our test system has the advantage of being relatively simple, while capturing the features of one type of realistic system in terms of circulation and basin geometry. Our prototype estuarine system is characterized by a long (length much greater than width), straight, symmetric channel emptying into the coastal zone, and a strong freshwater flow. The numerical grid corresponding to this system is shown in Figure 2.7. The depth contours are parallel to the coastline. The depth increases from 3 m at the river end of the grid to 20 m at the deepest extent of the coastal zone.

The flow field for this system was generated using the frequency-domain model TEA-NL (Westerink, et al. 1988). Forcing includes a zero frequency and a single semi-diurnal tidal component. Zero frequency forcing is a combination of a river flow of $500 \text{ m}^3 \text{ s}^{-1}$ and a pressure gradient parallel to the coastline which forces an alongshore current of approximately 1 cm/s. An M_2 tidal wave propagates alongshore with an amplitude of approximately 0.25 m at the farthest extent of the coastal zone. Sea level boundary conditions at the ocean boundary were generated using the inverse tidal method (Nuñez, 1990).

The behavior of a conservative substance in this system is demonstrated using salinity. A simulation of salinity was generated using initial conditions of 35 ppt everywhere in the system, representing the oceanic end member, while a constant riverine end

member concentration of 0 ppt was applied at the river end of the channel. Examination of Lagrangian pathways, shown in Figure 2.8, indicate that a front of salinity deficit passes rapidly through the channel. Upon nearing the channel mouth, the front begins to undergo considerable periodic back-and-forth movement due the M_2 tidal forcing, and spreading of the frontal gradients. After leaving the estuary, the plume is swept northward out of the domain by the low-frequency alongshore coastal current.

For all of the ELAmet simulations shown in this section, the time step chosen for dispersion and chemical transformation was one twelfth of an M_2 tidal cycle, or slightly more than an hour. This time step represented an acceptable compromise between the need to resolve the smallest important time scales of the system (the M_2 period), and the need for a time step large enough to allow long-term simulations.

It is intuitively appealing to assume that natural systems exist very close to a dynamic steady-state condition, and therefore this is the condition of the system which we would like to capture with our modeled simulations. However, there is no guarantee that the system will ever reach a true dynamic steady state, as there is no inherent constraint that the mass of salinity leaving the system be equal to the mass entering. Nonetheless, our model simulations lead to a condition close to a dynamic steady state. In Figure 2.9, we show the Eulerian time series of salinity, sampled at the locations indicated in Figure 2.7. Based on examination of this type of plot, we feel that a run of 1035 hours, or approximately 43 days, is enough to bring the system very close to a dynamic steady state. At the end of this time, the front has passed through each of the sampled points, and any residual low-frequency trend in Eulerian concentrations does not significantly affect our results. Therefore, all runs for this section have been taken out to 43 days. Figure 2.10 shows the contours of the salinity deficit plume at the end of the simulation.

For all the ELAmet simulations discussed in this section, the dispersion coefficient is set to $5 \text{ m}^2 \text{ s}^{-1}$, and is constant over the domain. The assumption of spatial invariance in the dispersion is not necessary, but it is adequate for the present applications.

Effect of Symmetrical and Asymmetrical Sources

We introduce a metal into the domain through a source located in the channel, centered on a point x_0 that is 3 km from the channel mouth as indicated in Figure 2.7. The

source Q has the form of a gauss hill in the direction parallel to the channel, and has no variation perpendicular to the channel:

$$Q = Ae^{-\frac{(x-x_0)^2}{\sigma^2}} \quad (2.65)$$

with $\sigma=1$ km. The value of A is chosen to be $3 \times 10^{-5} \text{ s}^{-1}$, which gives a nondimensional concentration at the center of the source of approximately 1.0. The initial condition is zero metal concentration over the domain. Figure 2.11 is a plot of the resulting metal plume.

The grid was then sampled at every node for metal concentration and salinity. In Figure 2.12 we show the resulting mixing plot. Since all of the channel water passes through the metal source, we have essentially one well-defined end member coming out of the channel and one well-defined oceanic end member on the outside. Since there are two end members of the mixing curve in this case, and no other internal sinks or chemical transformations, subsequent dilution occurs along a straight line in a manner consistent with conservative mixing.

We now look at the same problem, with the difference that the source, instead of being even across the channel, is weighted to one side according to the equation:

$$Q = Ae^{-\frac{-(x-x_0)^2 + (y-y_0)^2}{\sigma^2}} \quad (2.66)$$

where y_0 is a point along the southern edge of the channel (indicated in Figure 2.7), and the rest of the constants have the same values as above. The resulting concentration plume is shown in Figure 2.13. Once again the entire grid was sampled for metal concentration and salinity, and the result is shown in Figure 2.14. Clearly the concentration vs. salinity plot no longer approximates a single-valued function. This occurs primarily because we no longer have two well-defined end members which are mixed; rather, because of the asymmetry in the problem, the channel represents a range of end members which mix with the oceanic waters. The effect on the mixing curve is not unlike the effect of a time-varying end member, as shown by *Loder and Reichard* [1981]. However, *Loder and Reichard* use a 1-dimensional prototype; this example demonstrates that in two dimensions many different end members can be present simultaneously.

The logistical difficulties associated with field sampling necessarily reduce the observable mixing curve to a relatively few points. Using the model diagnostically, we can determine a priori what features of the mixing curve a given sampling scheme can capture. In Figure 2.15 we show three different schemes representing samples taken parallel to the channel, parallel to the coastline, and across the channel mouth, respectively; ten sample points were used in each case. In Figure 2.14 we show the results of sampling the concentration vs. salinity plot using these three schemes. The conclusions that would be drawn if only the sampled information were available are clearly dependent on the scheme used. In each case, some degree of upward concavity is evident in the sampled data. This would indicate a source, which is, in the broadest terms, correct. However, each of these sampling schemes, if interpreted with a 1-dimensional mixing model in mind, would give very different quantitative estimates of the source, and none by itself adequately captures the range of concentration associated with each salinity.

Effect of Reaction Kinetics

We now examine the effect on the mixing plot of rate-controlled nonconservative behavior. We use a simple case of a metal ion that partitions into the solid phase in a manner described by a first-order or pseudo first-order reaction. This reaction is of the general form:

$$\frac{dc_s}{dt} = \kappa_f c_a - \kappa_b c_s. \quad (2.67)$$

We let $\kappa_f = \kappa_b = \kappa$, with κ^{-1} effectively equal to the time scale of the reaction, and we choose $\kappa = (24 \text{ hr})^{-1}$. The source concentration is assumed to be made up entirely of metal in the particulate phase, so that as water “ages” away from the source, a desorption reaction proceeds until the equilibrium condition of equal concentrations of particulate and dissolved phase is reached. A symmetrical source of particulate metal as described in equation (2.65) was used. The simulation was run for 43 days, with zero concentration initial conditions for both phases. Figure 2.16 shows the resulting plumes of the two metal phases.

In this case, the entire grid was sampled for both dissolved and particulate concentration, and these are plotted against salinity in Figure 2.17. This figure indicates that some water parcels leave the source and come into thermodynamic equilibrium before much

mixing occurs; these water parcels then mix conservatively along the line connecting a concentration of 0.5 and 0 ppt salinity with a concentration of 0 and 35 ppt salinity. However, other water parcels begin to mix before the desorption has been completed, and these are represented by points which deviate from the straight line. In this case, the combination of mixing and rate-controlled desorption causes a 20-30% spread in metal concentration at low salinities.

For each grid point, an “apparent” partition coefficient K_p was constructed by dividing the particulate by the dissolved concentration. These apparent K_p values are plotted against salinity in Figure 2.18, along with the points representing samples taken according to the three sampling schemes discussed above. All three of these sampling schemes indicate a dependence of the partition coefficient on salinity; however, this is only an *apparent* dependence, and is really caused by the kinetic nature of the desorption process. As the reaction is speeded up, approaching an instantaneous equilibrium, all mixing would occur along the straight line as described above, and all of the K_p values would fall along $K_p=1$.

Effect of Sediment Deposition

As a final demonstration of the effects of sampling on interpretation of the mixing plot, we consider a simplified example of the removal of particulate phase through sediment deposition. The metal in this case undergoes nonconservative solid partitioning as was described in the previous example, except that the reaction has been speeded up so as to be essentially instantaneous, thereby removing the kinetic effects on the mixing plot that were shown above. A simplified geographical dependence in the depositional flux was created by designating a portion of the grid surrounding the mouth of the channel as having a constant, nonzero deposition as indicated in Figure 2.19. The magnitude of the flux chosen for this example is the flux that would be required to remove all of the particulate metal from the water column in a time scale of 2 days; i.e., referring to Equation (2.54), $\bar{F}''=(2 \text{ days})^{-1}$.

Figure 2.20 shows the resulting plume of dissolved metal, while Figure 2.21 shows the mixing plot and the points sampled according to the three sampling schemes discussed above. In this case, the sediment deposition acts as an internal sink of metal, and indeed, the sampled points generally show a concave downward trend. However, depending on

the sampling scheme used, a 1-dimensional interpretation of these results would yield different conclusions about the location of the sink and its strength.

Final Comments

A new numerical model for fate and transport of nonconservative metals in an estuarine environment, known as ELAmet, has been introduced. This model incorporates nonconservative aqueous complexation and adsorption processes that distribute mass among aqueous and solid-phase species into the equations for hydraulic transport. ELAmet can simultaneously accommodate rate-controlled chemical reactions and reactions that reach thermodynamic equilibrium on a time scale short compared to the computational time step. Any range of rate constants is allowed, and the time step used to solve for the chemical transformations has been decoupled from that used for solving dispersion. With the introduction of this model, we urge the consideration of a new mode of use for geochemical numerical models which is diagnostic, rather than predictive, in nature. Current field data limitations preclude a meaningful use of numerical models for prediction of metal fate, even though the demand for predictive capabilities is very high.

We have included examples of ELAmet used in a diagnostic mode to examine some synthetic mixing plots, and to show that numerical models can add insight even into processes that are thought to be well-understood. Clearly these examples do not fully explore either the capabilities of ELAmet or the concept of diagnostic modeling. Applications under more “realistic” conditions are needed, and such work is in progress. However, we feel that it is important not to judge the utility of the model solely on its ability to be used under realistic conditions and produce apparently realistic simulation results. This would set unrealistically high expectations, since in all likelihood the field data do not currently exist to validate this model correctly for any particular estuary being studied. Given this limitation, the most “realistic” approach is to accept the notion that we can use a numerical model in conjunction with existing field and experimental data, however sparse, to better understand small pieces of the bigger nonconservative transport problem.

Of course, this understanding is always subject to further testing. This suggests that perhaps one of the most appropriate uses of diagnostic modeling is in an iterative cycle in which the modeling suggests sampling strategies to better sample for particular

estuarine processes; field data will in turn either validate the model, or suggest the need to modify it.

Notation

C_i, \bar{C}_i	total analytical concentration of the i^{th} aqueous metal-containing component species in system I, system II
L_i, \bar{L}_i	total analytical concentration of the i^{th} aqueous non-metal-containing component species in system I, system II
S_i, \bar{S}_i	total analytical concentration of the i^{th} sorbent component species in system I, system II
c_i, \bar{c}_i	concentration of the i^{th} aqueous metal-containing component species in system I, system II
c'_i, \bar{c}'_i	concentration of the i^{th} aqueous derived species in system I, system II
c''_i, \bar{c}''_i	concentration of the i^{th} solid-phase derived species in system I, system II
l_j, \bar{l}_j	concentration of the i^{th} aqueous non-metal-containing component species in system I, system II
s_j, \bar{s}_j	concentration of the i^{th} sorbent component species in system I, system II
a_{ij}, \bar{a}_{ij}	stoichiometric coefficient of the j^{th} metal-containing aqueous component in the i^{th} aqueous derived species in system I, system II
b_{ij}, \bar{b}_{ij}	stoichiometric coefficient of the j^{th} metal-containing aqueous component in the i^{th} solid-phase derived species in system I, system II
d_{ij}, \bar{d}_{ij}	stoichiometric coefficient of the j^{th} non-metal-containing aqueous component in the i^{th} aqueous derived species in system I, system II
e_{ij}, \bar{e}_{ij}	stoichiometric coefficient of the j^{th} sorbent component in the i^{th} solid-phase derived species in system I, system II

M_d, \bar{M}_d	number of aqueous derived species in system I, system II
M_s, \bar{M}_s	number of solid-phase derived species in system I, system II
N_c, \bar{N}_c	number of aqueous metal-containing components in system I, system II
N_l, \bar{N}_l	number of aqueous non-metal-containing components in system I, system II
N_s, \bar{N}_s	number of sorbent components in system I, system II
\bar{h}_{ij}	stoichiometric coefficient of the j^{th} aqueous derived species in the i^{th} solid-phase derived species in system II
\bar{g}_{ij}	stoichiometric coefficient of the j^{th} aqueous derived species in the i^{th} aqueous derived species in system II
α_i	stability constant of the i^{th} aqueous derived species (system I)
β_i	stability constant of the i^{th} solid-phase derived species (system I)
κ_i^f	forward rate constant for the i^{th} complexation reaction (system II)
κ_i^b	backward rate constant for the i^{th} complexation reaction (system II)
$\kappa_i^{f'}$	forward rate constant for the i^{th} adsorption reaction (system II)
$\kappa_i^{b'}$	backward rate constant for the i^{th} complexation reaction (system II)
\bar{r}'_i	rate of production of the i^{th} aqueous derived species (system II)
\bar{r}''_i	rate of production of the i^{th} solid-phase derived species (system II)
$\Theta_i^c, \bar{\Theta}_i^c$	chemical transformation term for the i^{th} aqueous metal-containing component in system I, system II
$\Theta'_i, \bar{\Theta}'_i$	chemical transformation term for the i^{th} aqueous derived species in system I, system II

$\Theta''_i, \bar{\Theta}''_i$	chemical transformation term for the i^{th} solid-phase derived species in system I, system II
$\Theta^s_i, \bar{\Theta}^s_i$	chemical transformation term for the i^{th} sorbent species in system I, system II
$\Theta^l_i, \bar{\Theta}^l_i$	chemical transformation term for the i^{th} aqueous non-metal-containing component species in system I, system II
F^c_i, \bar{F}^c_i	linear flux for the i^{th} aqueous metal-containing component species in system I, system II
F'_i, \bar{F}'_i	linear flux for the i^{th} aqueous derived species in system I, system II
F''_i, \bar{F}''_i	linear flux, including sediment deposition/erosion, for the i^{th} solid-phase derived species in system I, system II
F^s_i, \bar{F}^s_i	linear flux, including sediment deposition/erosion, for the i^{th} sorbent species in system I, system II
F^l_i, \bar{F}^l_i	linear flux for the i^{th} aqueous non-metal-containing component species in system I, system II

References

- Adams, E.E. and A.M. Baptista, Ocean dispersion modeling, in *Encyclopedia of Fluid Mechanics, Vol. 6, Complex Flow Phenomena and Modeling*, edited by N.P. Chermisinoff, pp. 865-895, 1986.
- Baptista, A.M., Solution of advection-dominated transport by Eulerian-Lagrangian methods using the backwards method of characteristics, Ph.D. Dissertation, Massachusetts Institute of Technology, Cambridge, Mass, 1987.
- Baptista, A.M., E.E. Adams, and K.D. Stolzenbach, Eulerian-Lagrangian analysis of pollutant transport in shallow water, *Technical Report no. 296*, MIT R.M. Parsons Laboratory, Cambridge, Mass, 1984.

- Barros, A.P. and A.M. Baptista, An Eulerian-Lagrangian model for sediment transport in estuaries, in *Estuarine and Coastal Modeling, proceedings of the ASCE conference*, edited by M.L. Spaulding, pp. 102-112, 1990.
- Berner, R.A., *Early diagenesis: a theoretical approach*, 241 pp., Princeton University Press, Princeton, NJ, 1980.
- Cameron, D. R., and A. Klute, Convective-dispersive solute transport with a combined equilibrium and kinetic adsorption model, *Water Resour. Res.*, 13(1), 183-188, 1977.
- Cederberg, G.A., R.L. Street, and J.O. Leckie, A groundwater mass-transport and equilibrium chemistry model for multicomponent systems, *Water Resour. Res.*, 21(8), 1095-1104, 1985.
- Dimou, K., 3-D Hybrid Eulerian-Lagrangian / particle tracking model for simulating mass transport in coastal water bodies, Ph.D. Dissertation, Massachusetts Institute of Technology, Cambridge, Ma., 1992.
- Dortch, M. S., R. S. Chapman, and S. R. Abt, Application of three-dimensional lagrangian residual transport, *Journal of Hydraulic Engineering*, 118(6), 831-848, 1992.
- Eadie, B. J., N.R. Morehead and P. F. Landrum, Three-phase partitioning of hydrophobic organic compounds in great lakes waters, *Chemosphere*, 20(1-2), pp. 161-178, 1990.
- Hauser, J.,D. Eppel, M. Lobmeyr, and A. Muller, A Mathematical Simulation Model for Environmental Transport Processes in Tidal Rivers and Estuaries. *Report No. DE84-751505*, Nat. Tech. Inform. Serv., Springfield, Va., 1983.
- Hayter, E. J. and C. V. Pakala, Transport of inorganic contaminants in estuarial waters, *Jnl. of Coastal Research*, SI (5), pp. 217-230, 1989.
- Loder, T. C. and R. P. Reichard, The dynamics of conservative mixing in estuaries, *Estuaries*, 4(1), pp. 64-69, 1981.

- Mangold, D. C. and C. F. Tsang, A summary of subsurface hydrological and hydrochemical models, *Reviews of Geophysics*, 29(1), 51-97, 1991.
- Miller, C. W. and L. V. Benson, Simulation of solute transport in a chemically reactive heterogeneous system: model development and application, *Water Resources Research*, 19(2), pp. 381-391, 1983.
- Nuñez, R. H., Prediction of tidal propagation and circulation in Chilean inland seas using a frequency domain model, M.S. Thesis, Oregon State University, Corvallis, Or., 1990.
- Onishi, Y. and D.S. Trent, Mathematical simulation of sediment and radionuclide transport in estuaries, *Rep. PNL-4109*. Battelle Pacific Northwest Laboratory, Richland, Wa., 1982.
- Onishi, Y., Sediment-contaminant transport model. *J. Hydraul. Div. ASCE*, 107(HY9), 1981.
- Pankow, J.F. and S.W. McKenzie, Parameterizing the equilibrium distribution of chemicals between the dissolved, solid particulate matter, and colloidal matter compartments in aqueous systems, *Environmental Science and Technology*, 25(12), pp. 2046-2053, 1991.
- Sheng, Y. P., Mathematical modeling of three-dimensional coastal currents and sediment dispersion: Model development and application, *Technical Report CERC-83-2*, US Army Corps of Engineers Waterways Experimental Station, Vicksburg, MS, 1983.
- Sheng, Y. P., J.-K. Choi, and A. Y. Kuo, Three-dimensional numerical modeling of tidal circulation and salinity transport in James River Estuary, in *Estuarine and Coastal Modeling, proceedings of the 1st ASCE conference*, edited by M.L. Spaulding, pp. 209-218, 1990.
- Stumm W. and J.J. Morgan, *Aquatic Chemistry, An Introduction Emphasizing Chemical Equilibria in Natural Waters*, 780 pp., W. Stumm, editor, Wiley-Interscience, New York, 1981.

- Valocchi, A. J., R. L. Street, and P. V. Roberts, Transport of ion-exchanging solutes in groundwater: chromatographic theory and field simulation, *Water Resour. Res.*, 17(5), pp. 1517-1527, 1981.
- Westall, J. C., Adsorption mechanisms in aquatic surface chemistry, in *Aquatic Surface Chemistry: Chemical Processes at the Particle-Water Interface*, edited by W. Stumm, John Wiley, New York, 1987.
- Westerink, J.J., J.J. Connor and K.D. Stolzenbach, A frequency-time domain finite element model for tidal circulation based on the least-squares harmonic analysis method, *International Journal for Numerical Methods in Fluids*, vol. 8, pp. 813-843, 1988.
- Wood, T. M. and A. M. Baptista, Modeling the pathways of nonconservative substances in estuaries, in *Estuarine and Coastal Modeling, proceedings of the 2nd International conference*, edited by M.L. Spaulding et al., pp. 280-291, 1992.
- Yeh, G. T. and V.S. Tripathi, A model for simulating transport of reactive multispecies components: model development and demonstration, *Water Resour. Res.*, 27(12), pp. 3075-3094, 1991.
- Yeh, G.T. and V.S. Tripathi, A critical evaluation of recent developments in hydro-geochemical transport models of reactive multichemical components, *Water Resour. Res.*, 25(1), pp. 93-108, 1989.

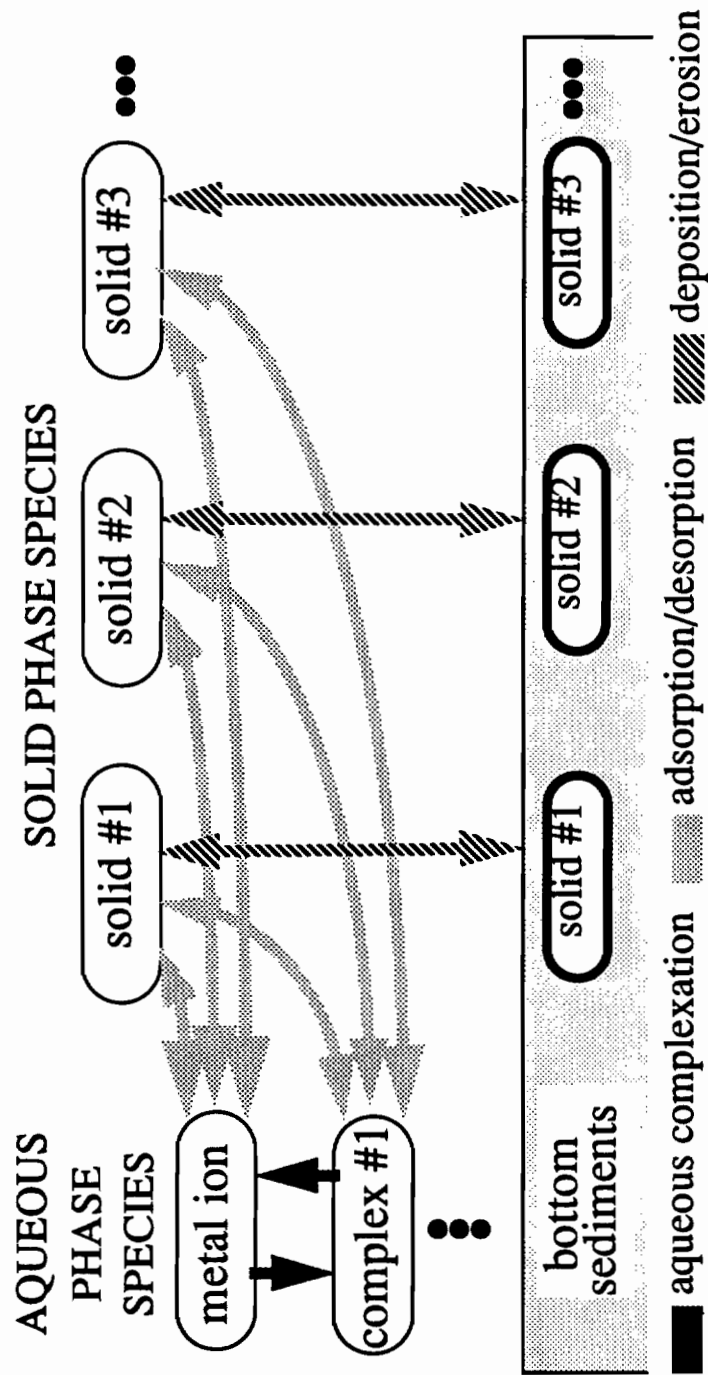


Figure 2.1. Schematic diagram of the phases and processes that distribute mass between phases included in ELAmet.

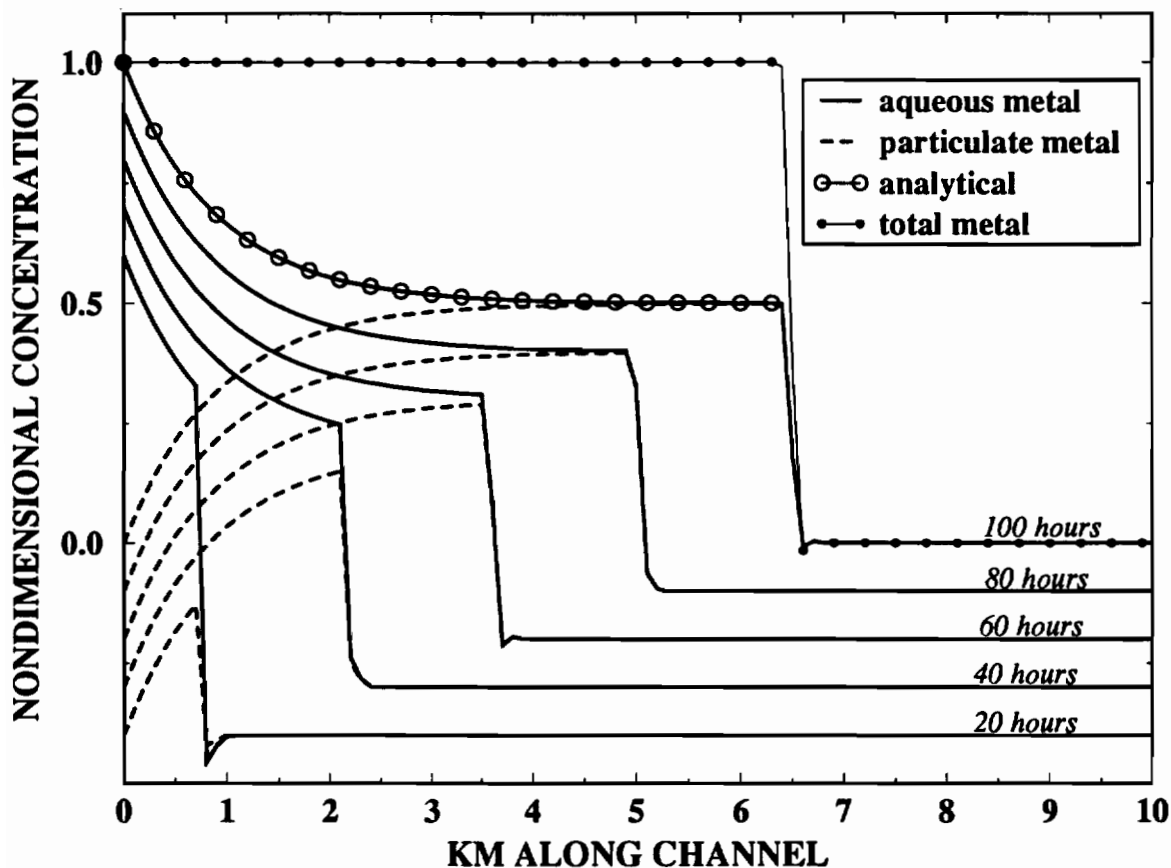


Figure 2.2. Profiles of $[MeX_2]$ and $[MeX_{2(s)}]$ along the channel at 5 different times during the simulation. For clarity, only profiles at $t=100$ hrs are placed correctly with respect to the y axis; previous profiles are displaced sequentially by -0.2 along the y axis. Also plotted is the profile of $[MeX_2] + [MeX_{2(s)}]$ as calculated at $t=100$ hrs. The analytical solution at $t=100$ hrs is given by

$$[MeX_2] = \frac{[MeX_2]_0 \kappa_f'''}{\kappa_f''' + \kappa_b'''} \left[\frac{\kappa_b'''}{\kappa_f'''} + e^{-(\kappa_f''' + \kappa_b''') \tau} \right]$$

where $[MeX_2]_0$ is the initial value of $[MeX_2]$. Note that in this expression, τ is the time since entering the domain, as determined by distance along the front.

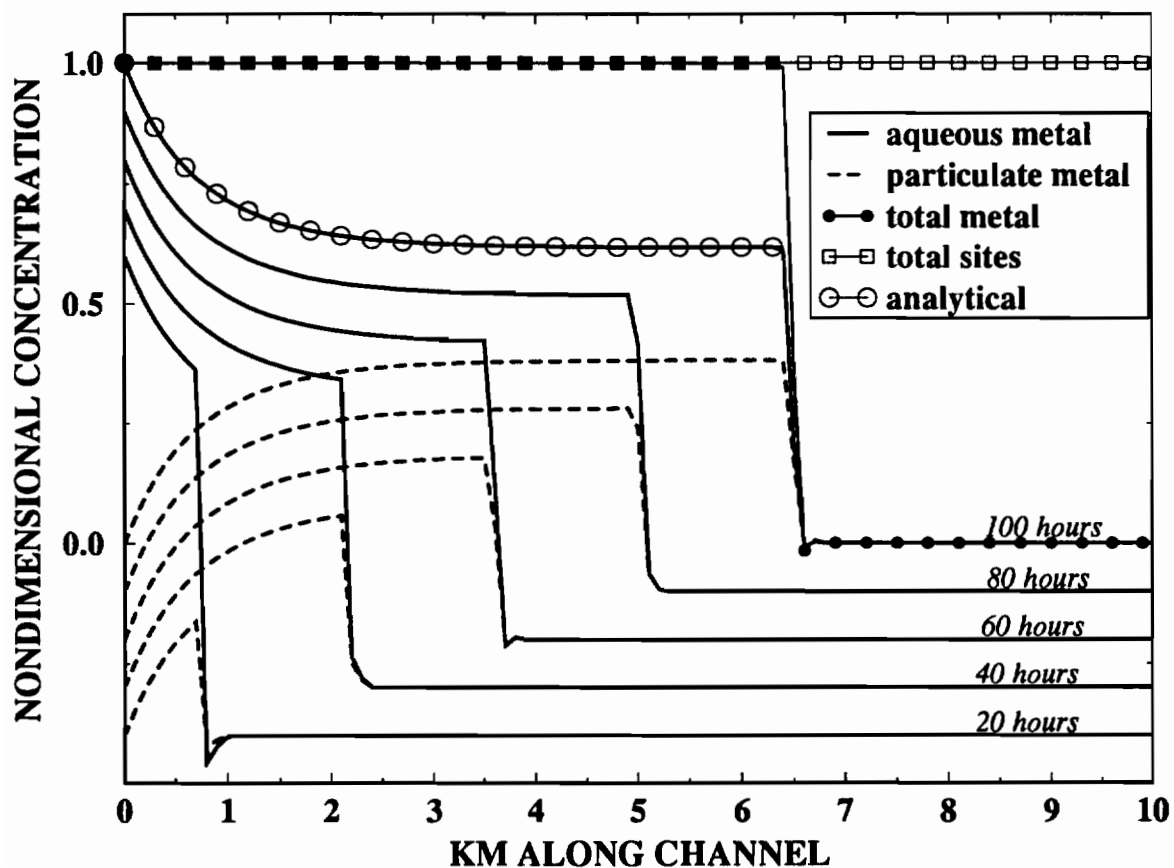


Figure 2.3. Profiles of $[Me^{2+}]$ and $[MeO^+]$ along the channel at 5 different times during the simulation. Profiles are displaced as in Figure 2.2. The profiles of $[Me^{2+}] + [MeO^+]$ and $[O^-] + [MeO^+]$ are calculated at $t=100$ hrs. The analytical solution at $t=100$ hrs is given by

$$[Me^{2+}] = 1 - \left\{ \frac{\sqrt{-q}}{2\kappa''_f} \left[\frac{1+r_0 e^{\sqrt{-q}\tau}}{1-r_0 e^{-\sqrt{-q}\tau}} \right] - \frac{\beta}{2\kappa''_f} \right\}, \text{ where } q = 4\alpha\kappa''_f - \beta, r_0 = \frac{\beta - \sqrt{-q}}{\beta + \sqrt{-q}},$$

$\alpha = \kappa''_f [Me^{2+}]_0 [O^-]_0$, and $\beta = \kappa''_f [Me^{2+}]_0 + \kappa''_f [O^-]_0 + \kappa''_b$. As in Figure 2.2, τ is time since entering the domain.

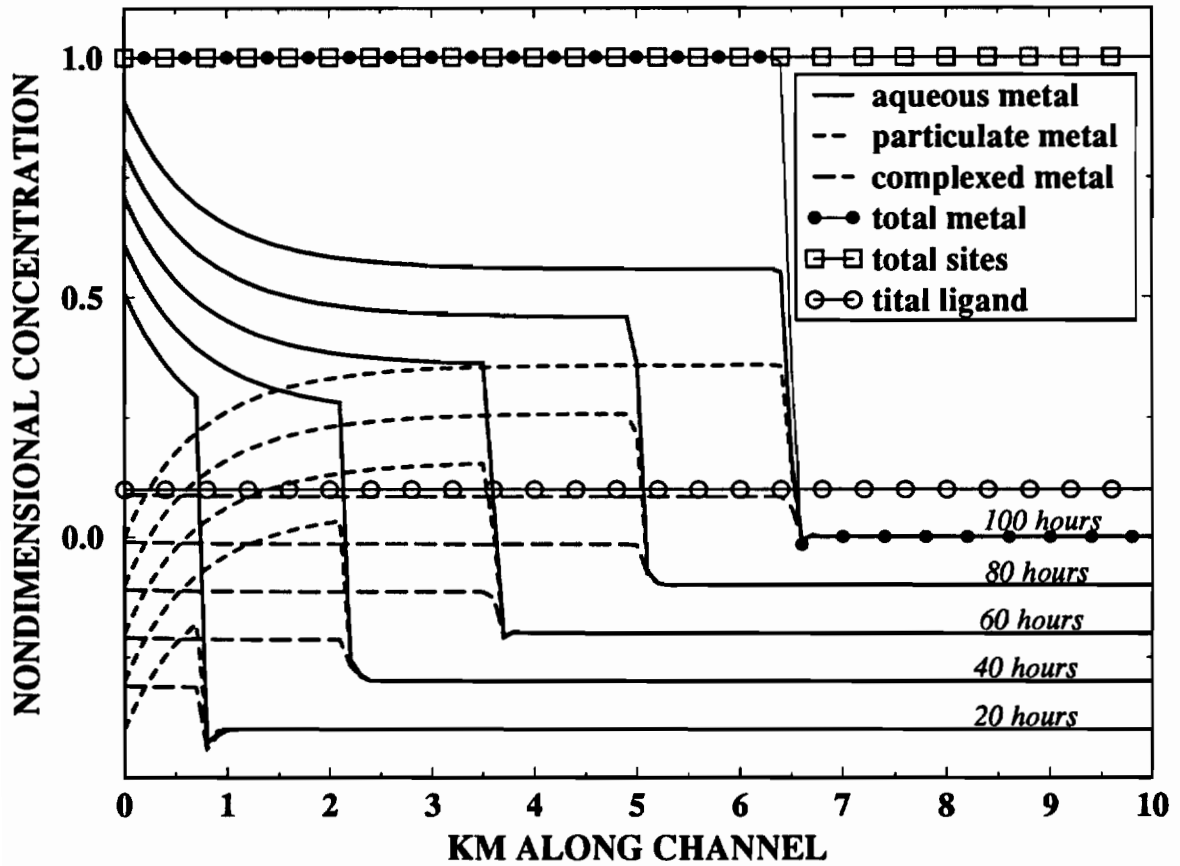


Figure 2.4. Profiles of $[Me^{2+}]$, $[MeO^+]$ and $[MeX^+]$ along the channel at 5 different times during the simulation. Profiles are displaced as in Figure 2.2. Also plotted are the profiles of $[Me^{2+}] + [MeO^+] + [MeX^+]$, $[X^-] + [MeX^+]$ and $[O^-] + [MeO^+]$ as calculated at $t=100$ hrs.

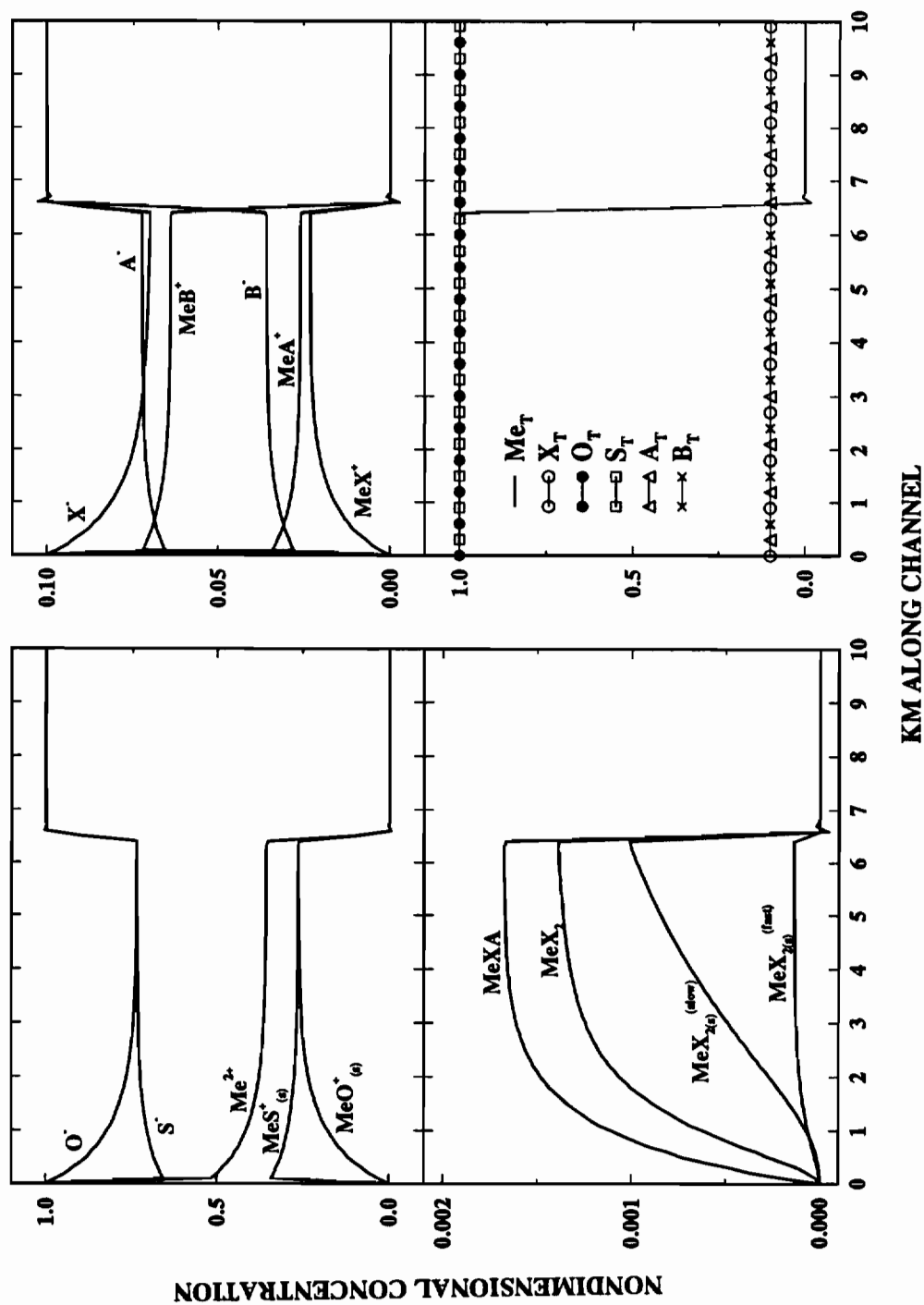


Figure 2.5. Profiles of 15 species at time $t=100$ hrs. Also included are the following calculated totals at $t=100$ hrs: $Me_T = [Me^{2+}] + [MeX^+] + [MeX_2] + [MeA^+] + [MeB^+] + [MeXA] + [MeS^+] + [MeX_{2(s)}^{(fast)}] + [MeX_{2(s)}^{(slow)}] + [MeO^+]$, $X_T = [X^-] + [MeX^+] + 2[MeX_2] + [MeXA] + 2[MeX_{2(s)}^{(fast)}] + 2[MeX_{2(s)}^{(slow)}]$, $O_T = [O^-] + [MeO^+]$, $S_T = [S^-] + [MeS^+]$, $A_T = [A^-] + [MeA^+] + [MeXA]$, $B_T = [B^-] + [MeB^+]$.

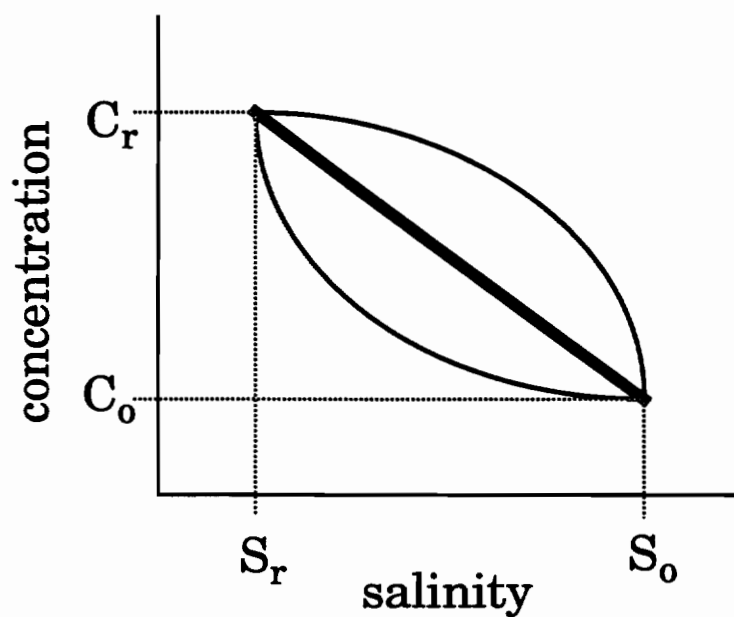


Figure 2.6. A schematic of the 1-dimensional mixing plot. C_o and S_o are the concentration and salinity, respectively, of the oceanic end member. C_r and S_r are the concentration and salinity, respectively, of the riverine end member. The bold line indicates conservative mixing along a straight line connecting riverine and oceanic end members. The concave upward line indicates the presence of an internal sink of substance C ; the concave downward line indicates the presence of an internal source.

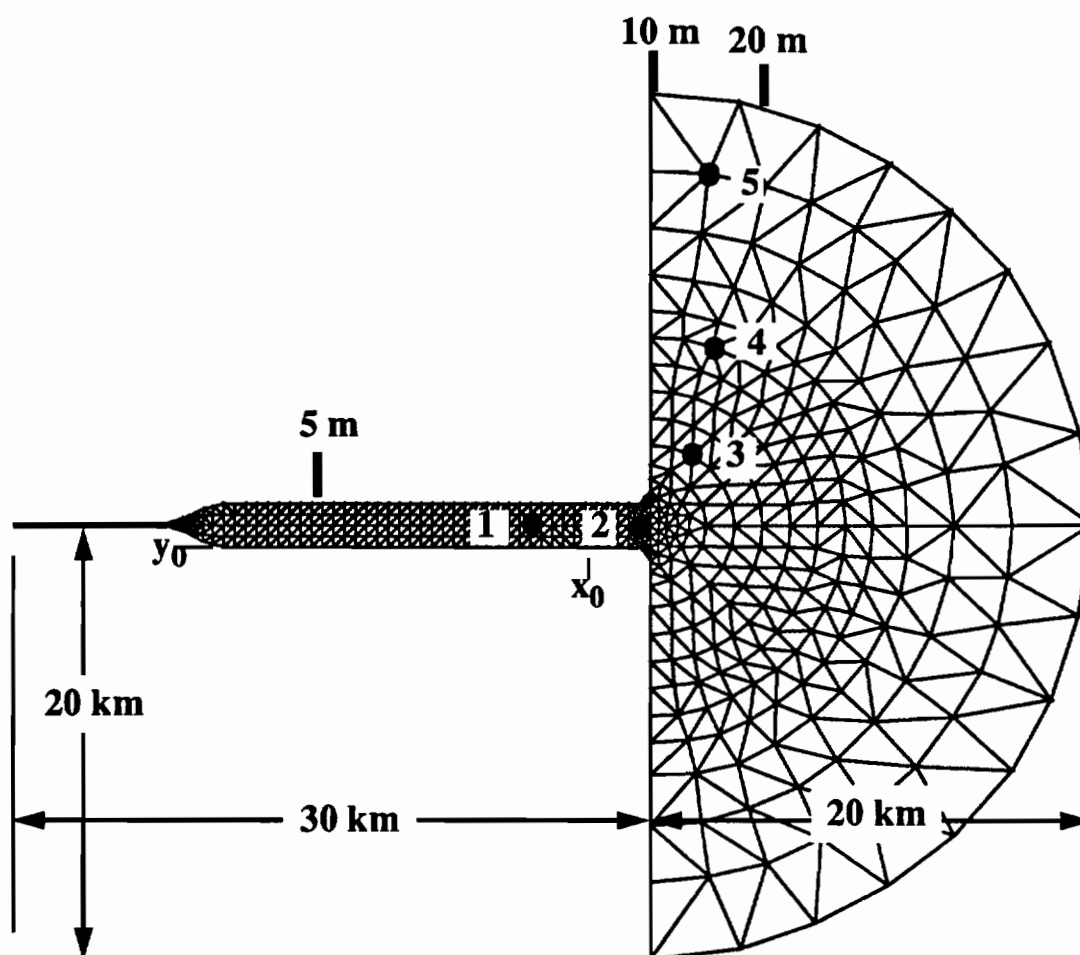


Figure 2.7. Numerical grid corresponding to the test system. The 5, 10, and 20 m depth contours are indicated. Also shown are the five sampling stations for the Eulerian concentrations in Figure 2.9, and the position (x_0, y_0) of the sources used in the example simulations.

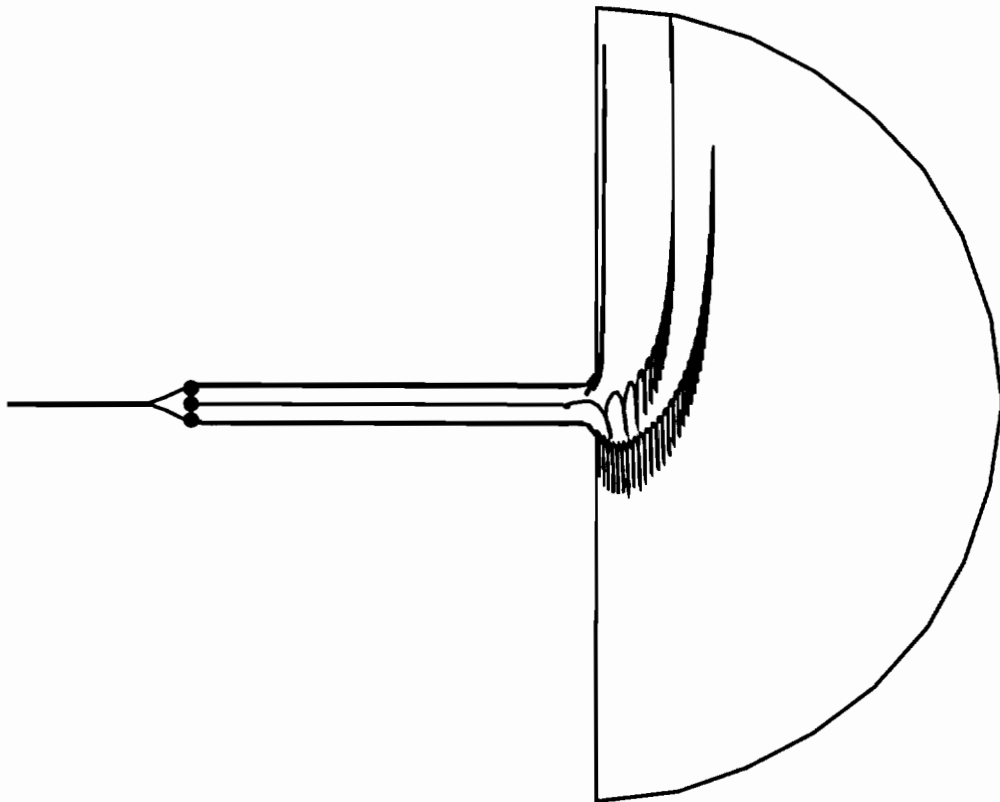


Figure 2.8. Lagrangian pathways of numerical drogues.

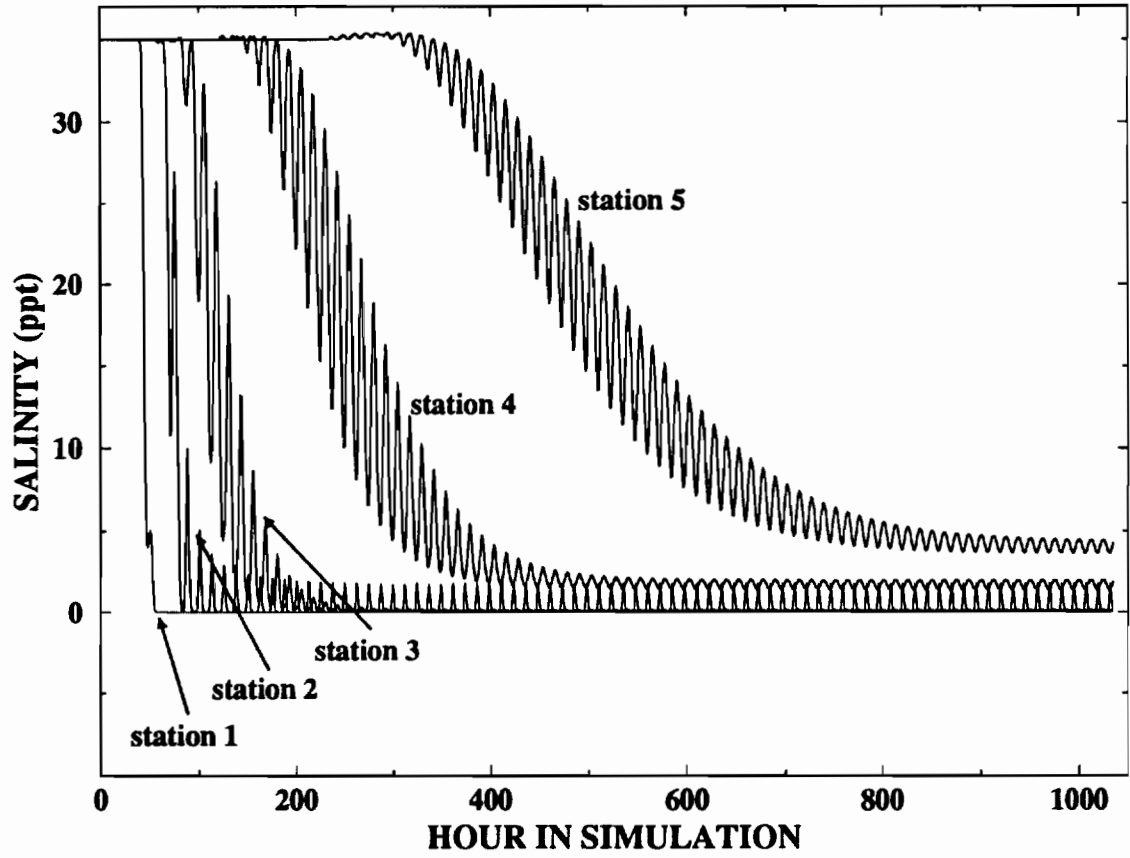


Figure 2.9. Eulerian time series of salinity sampled at 5 locations as indicated in Figure 2.7.

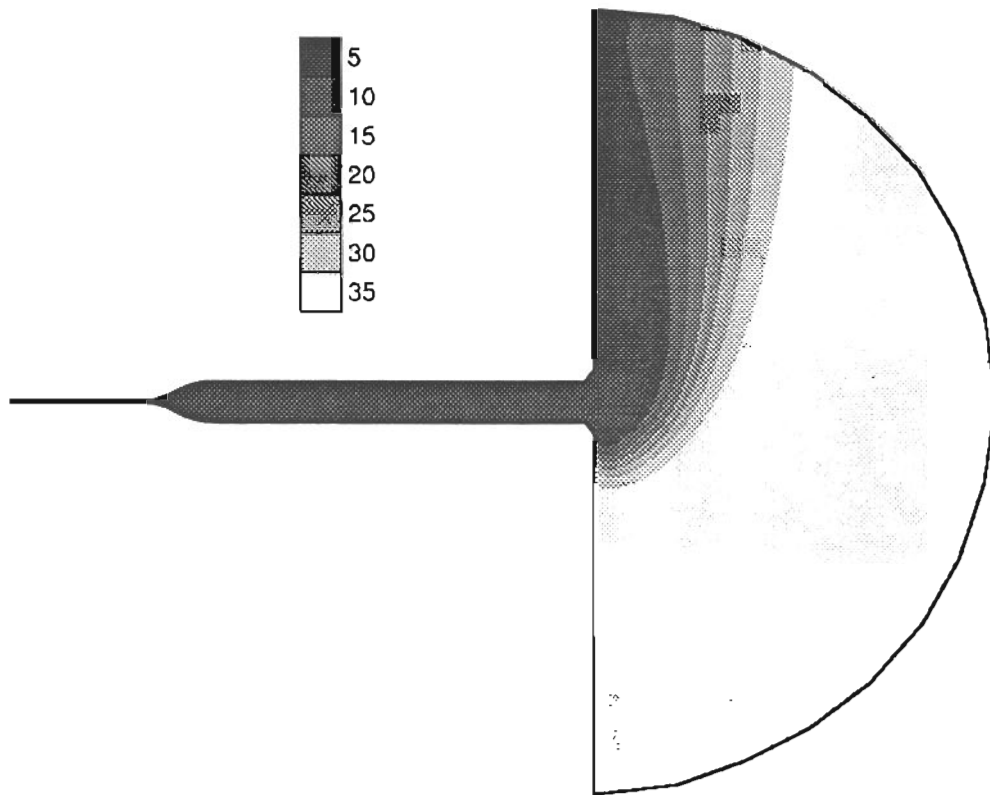


Figure 2.10. Contours of the salinity plume after 43 days. Contour interval is 5 ppt. The numbers in the legend indicate the upper limit of the range of values covered by the corresponding shade value.

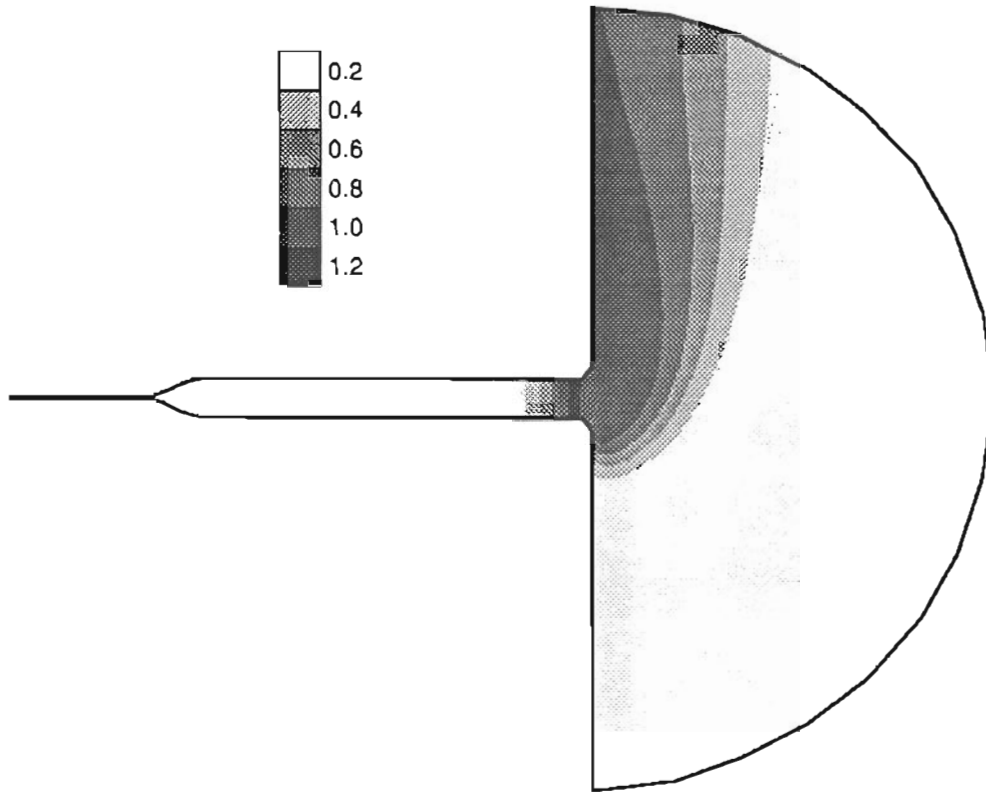


Figure 2.11. Contours of the metal plume resulting from a symmetrical source located at x_0 .

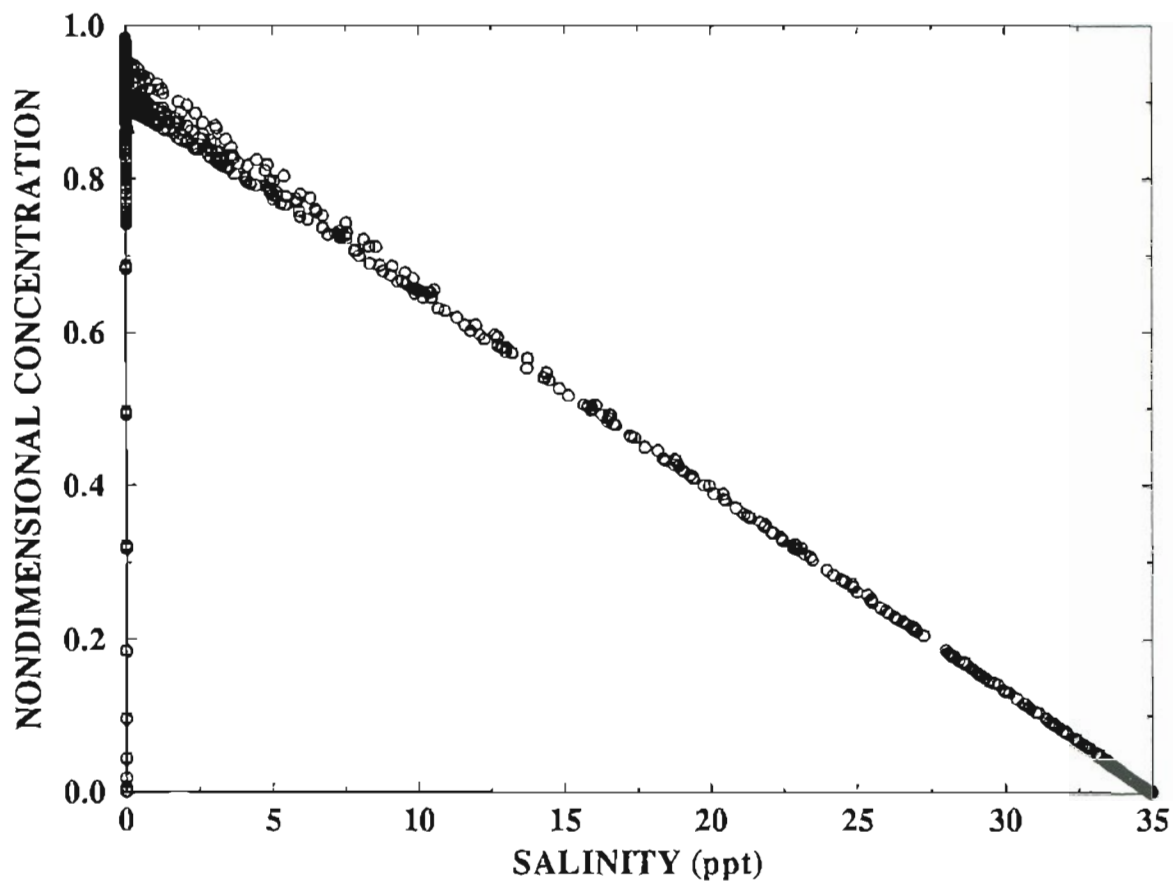


Figure 2.12. Mixing plot for the metal plume shown in Figure 2.11.

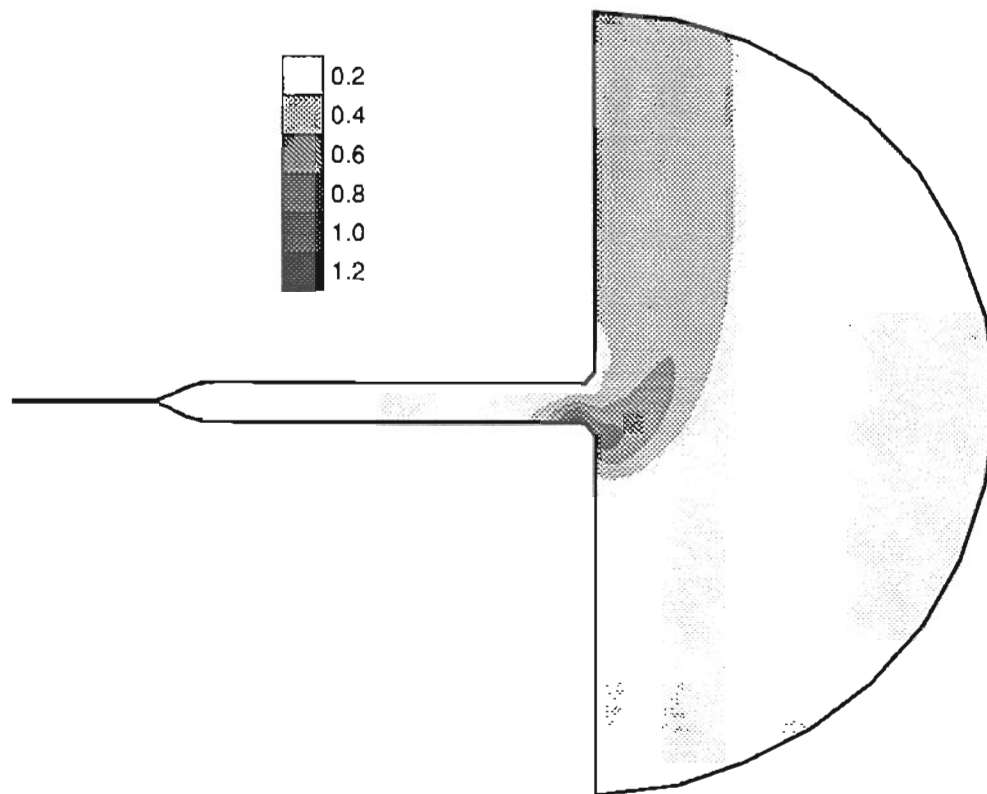


Figure 2.13. Contours of the metal plume resulting from an asymmetrical source located at (x_0, y_0) .

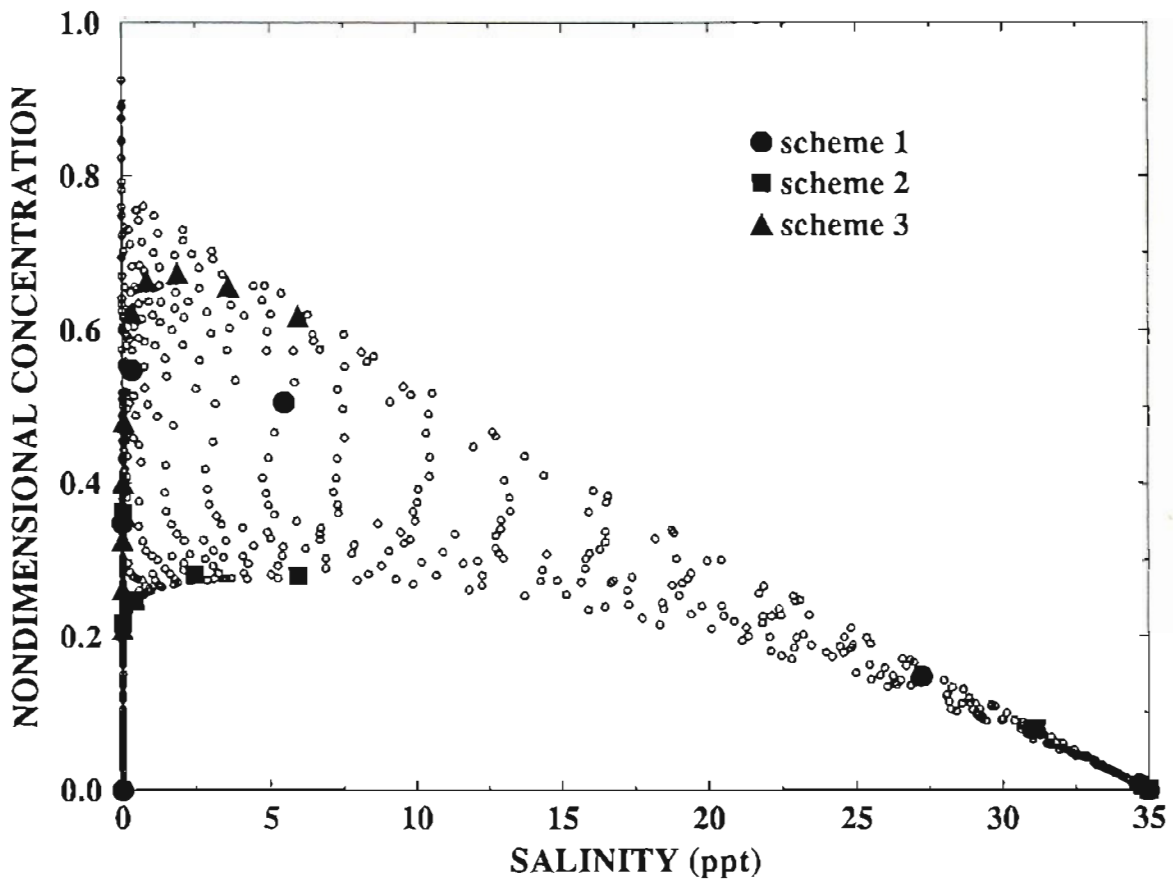


Figure 2.14. Mixing plot for the metal plume shown in Figure 2.13. Also shown are the sampled mixing plots, using the schemes shown in Figure 2.15.

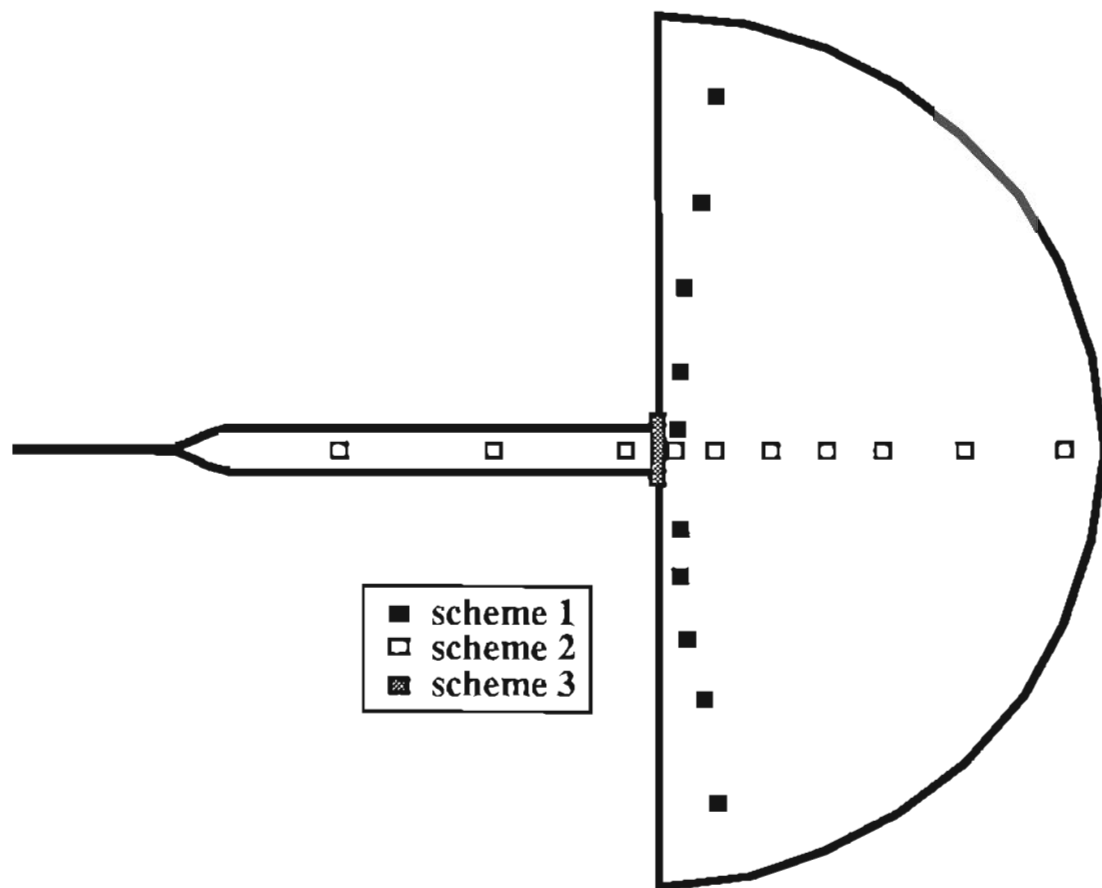


Figure 2.15. Three sampling schemes for the grid, each designed with 10 sample points.

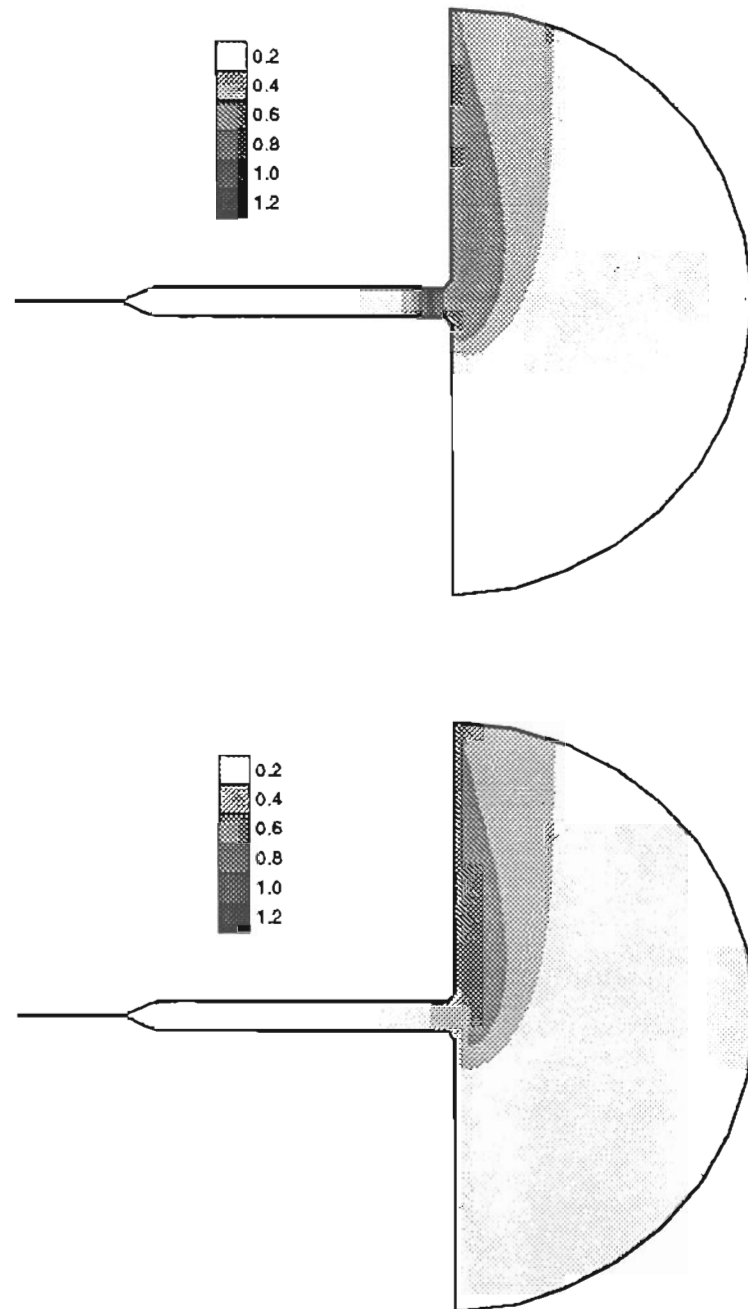


Figure 2.16. Contours of the plumes of particulate (top) and aqueous (bottom) metal, corresponding to a symmetric source and a first-order desorption process.

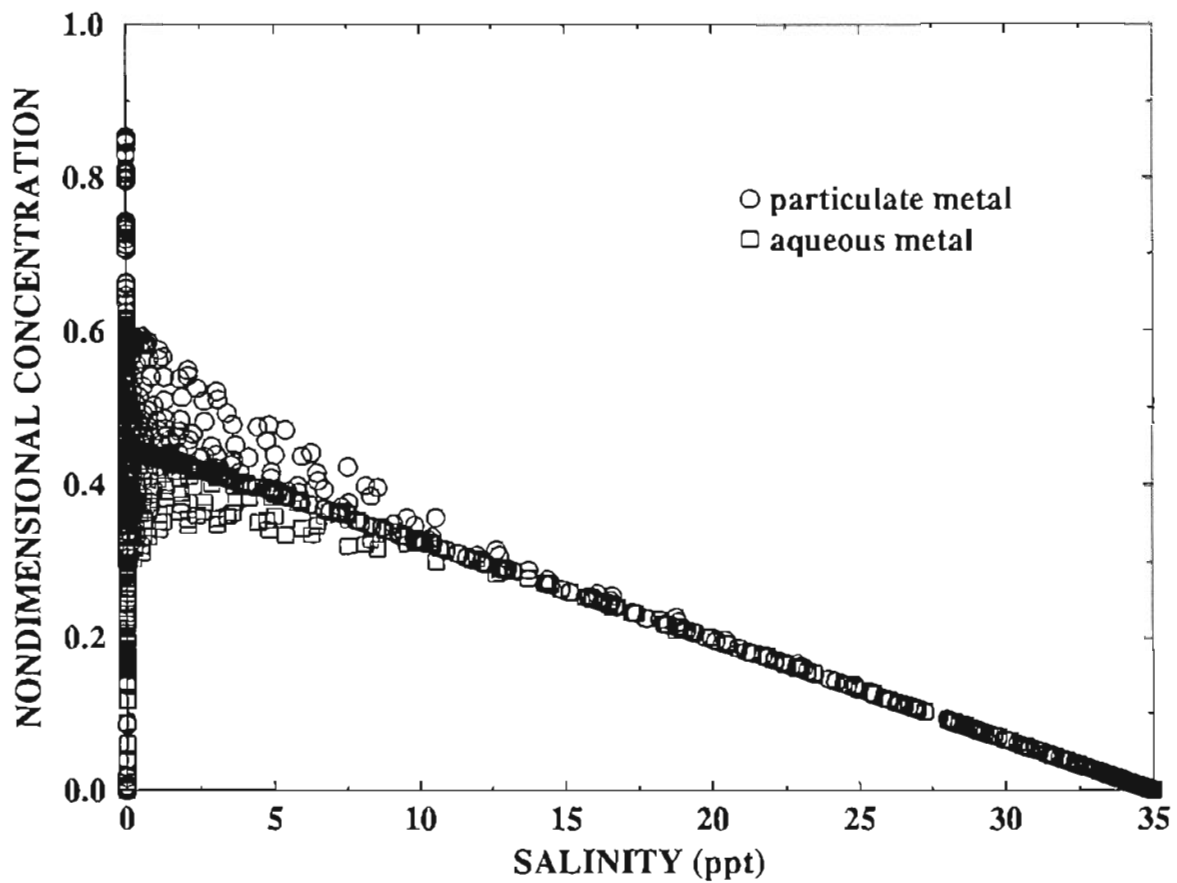


Figure 2.17. Mixing plot corresponding to the particulate and aqueous metal plumes shown in Figure 2.16.

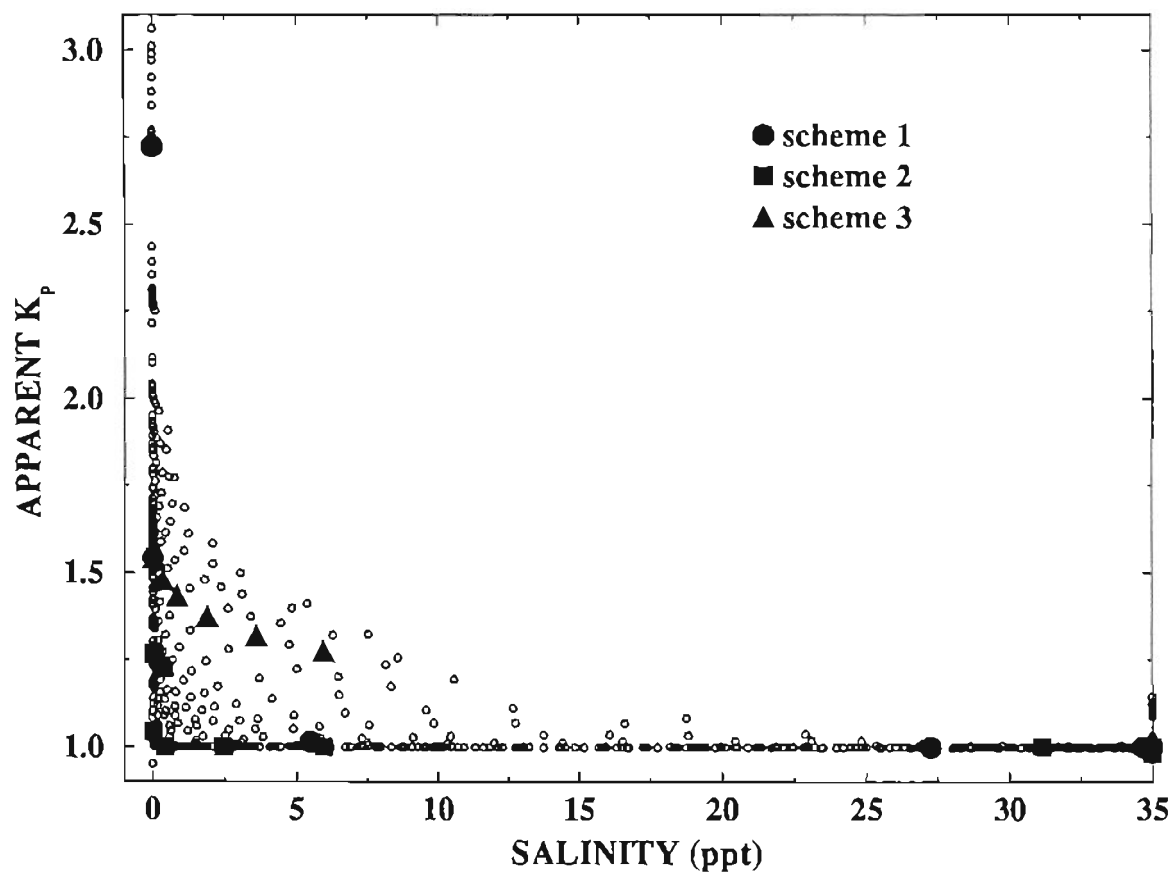


Figure 2.18. Plot of “apparent K_p ” (particulate metal concentration divided by aqueous metal concentration) for the metal plumes of Figure 2.16. The plot is also sampled using the three schemes of Figure 2.15.

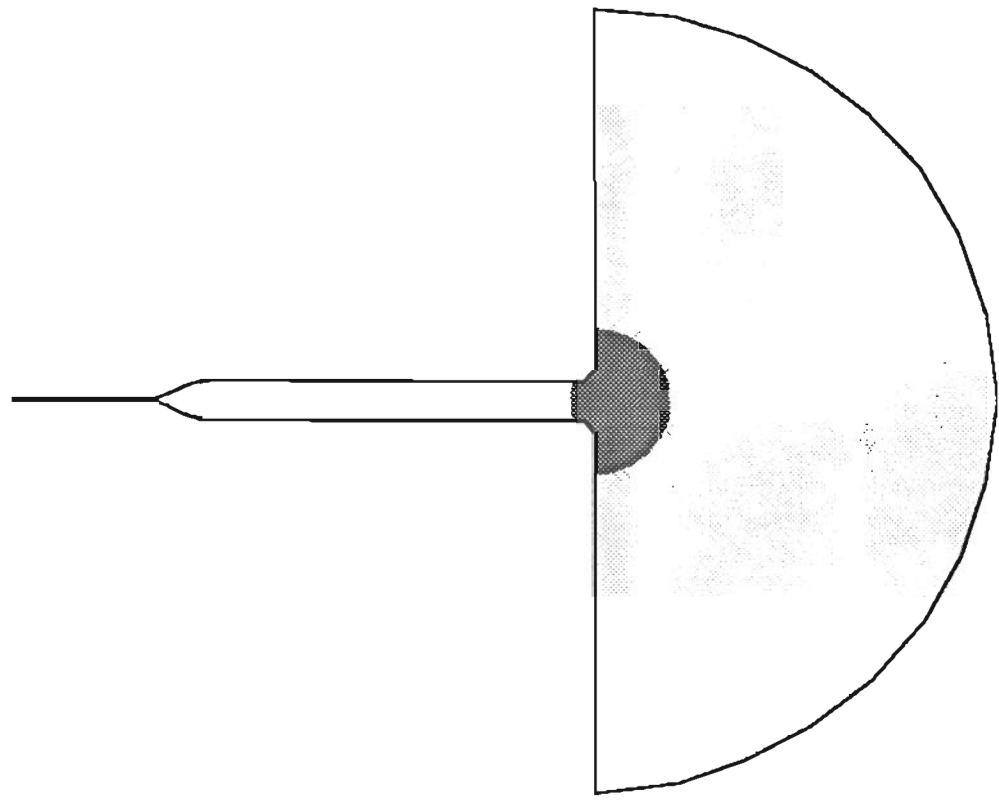


Figure 2.19. Outline of numerical grid showing the region chosen for a constant, nonzero deposition rate.

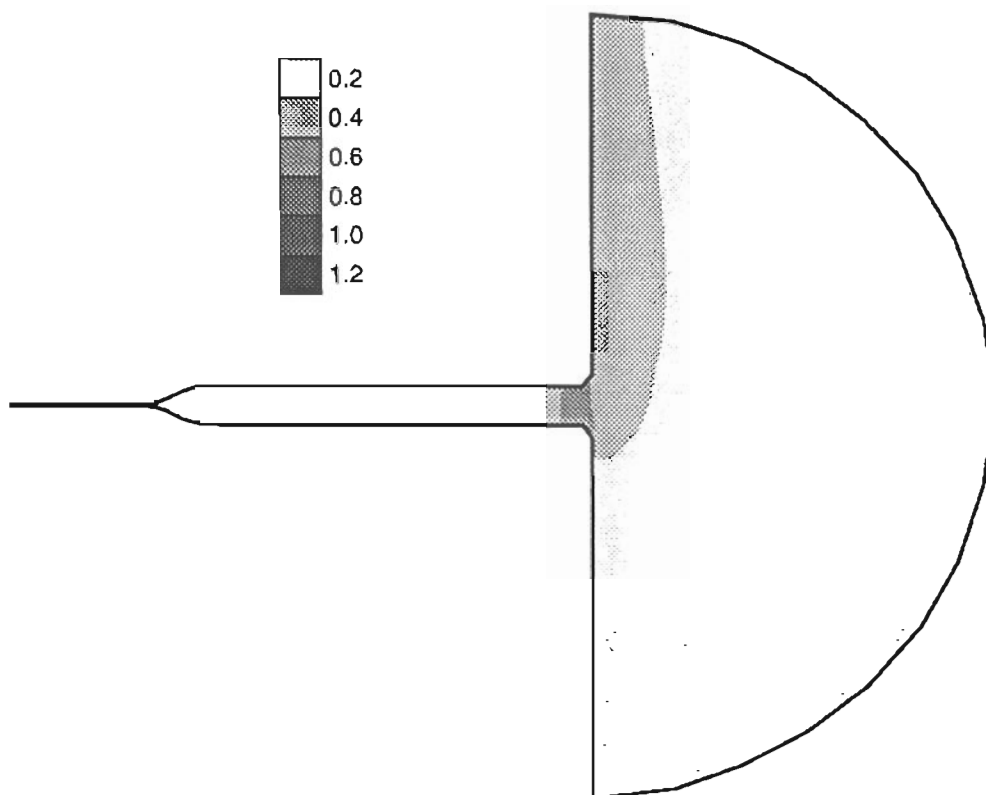


Figure 2.20. Plume of particulate metal resulting from a symmetric source and a nonuniform deposition as shown in Figure 2.19.

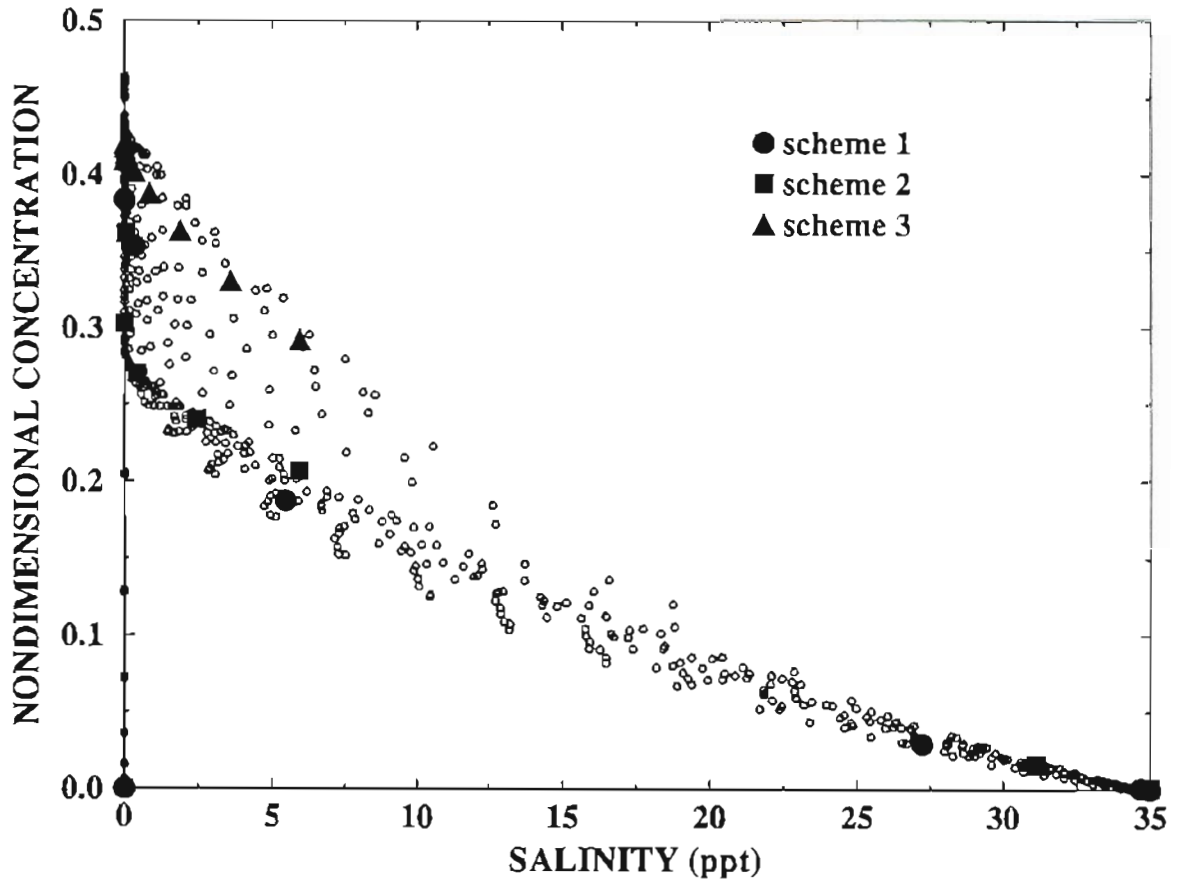


Figure 2.21. Mixing plot corresponding to the metal plume of Figure 2.20. The plot has been sampled using the three schemes of Figure 2.15.

CHAPTER 3

Modeling the Pathways of Nonconservative Substances in Estuaries

Abstract

ELAmet is a model for nonconservative chemical transport which solves the advection/dispersion/transformation equation using a modification of Eulerian-Lagrangian methods. In this paper we isolate the chemical transformation portion of the problem, present the equations that represent nonconservative chemical behavior in their general form, and discuss the method of solution. ELAmet decouples the time step used for solving diffusion from that used for solving the chemical transformations; some implications of this decoupling are discussed, with examples in a 1-dimensional domain.

Introduction

The incorporation of realistic nonconservative chemical behavior into the equations for conservative transport has been hampered by several factors, among them the fact that the resulting equations form a highly nonlinear, interdependent set of equations that are extremely difficult to solve. We have developed a way to get around this problem by using a modification of the Eulerian-Lagrangian methods (ELMs) that have become well-established as efficient methods of solving the advection/diffusion problem. We have incorporated this treatment of nonconservative behavior into a new model for the fate and transport of metals, known as ELAmet. ELAmet solves the depth-averaged transport equation for nonconservative substances using ELMs in a finite element framework; however, the discussion presented here in no way depends on the use of finite elements.

In a general, nonconservative estuarine system the metal of interest is present in the form of several different chemical species, distributed among the solid and aqueous

phases. The concentration of each species is governed by a conservation of mass equation of the general form

$$\frac{\partial c_i}{\partial t} + \Lambda(c_i) = \Theta_i^c + Q_i^c \quad (3.1)$$

where c_i is any species concentration (mass/volume), Q_i^c represents any internal sources or sinks, Θ_i^c includes all nonconservative chemical transformation terms, and Λ is the depth-averaged advection/dispersion operator

$$\Lambda = u_k \frac{\partial}{\partial x_k} - \frac{1}{h} \left(\frac{\partial}{\partial x_k} (D_{kj} h) \frac{\partial}{\partial x_j} \right) \quad (3.2)$$

In the above expression D_{kj} is the dispersion coefficient, h is the depth of the water column, and u_k is the depth-averaged velocity. Thus the $\Lambda(c_i)$ term on the left-hand-side of the equation describes the change in mass concentration due to an imbalance between mass in and out of a control volume through hydraulic transport processes. The term Θ_i^c on the right-hand-side describes changes in mass concentration due to chemical transformations that convert mass of one species to mass of another; also included in this term are linear decay terms which represent a net loss of mass and deposition/erosion terms which transfer mass to the bed sediments. In general, this term will be highly nonlinear and will involve several species c_i , making the equations of the system interdependent. In ELAmet, we deal with this problem by first decoupling the advection portion of the hydraulic transport from the dispersion and the chemical transformation portions of the problem using an ELM [Baptista, 1987].

The basic premise of an ELM is that the substantial derivative in equation (1) can be replaced by a simple time derivative. The method incorporates advection by “mapping” the location of each grid node at the current time step onto the previous time step using the characteristic line originating from each grid node. The characteristic line is the pathway in time and space along which conditions remain unchanged in the case of a simple wave equation, and its location at previous time steps is found by solving the tracking equation, shown below as equation (3.3). Conditions at the intersection of the characteristic line with the last time step (known as the “foot” of the characteristic line) are used as the initial conditions for the dispersion and transformation equations at the current time step. These methods are well-established for solving advection/dispersion problems, and it is a logical

extension to solve the chemical transformation part of the problem along the same characteristic.

The next step is to separate solution of the chemical transformation equations from solution of dispersion. As done in ELAmet, this step is similar to creating primary governing equations and secondary governing equations as discussed by *Yeh and Tripathi* [1989]. We significantly expand this concept, however, in that we allow for both equilibrium-type and kinetic-type chemical reactions to take place, and in doing so we break up the solution of the chemical reaction equations into a system of nonlinear algebraic equations and a system of linear differential equations. The solution of both of these systems of equations is the focus of this paper.

The effect of this modified ELM is to break down the original equation (3.1) into three simpler equations of the form:

$$u_i = \frac{dx_i}{dt}, \quad (3.3)$$

$$\frac{dc_i}{dt} = \Theta_i^c, \quad (3.4)$$

$$\frac{\partial c_i}{\partial t} = Q_i^c + \frac{1}{h} \frac{\partial}{\partial x_k} \left(D_{kj} h \frac{\partial c_i}{\partial x_j} \right). \quad (3.5)$$

Equation (3.3) is the tracking equation, which has no spatial gradients and can therefore be done at one computational grid node at a time. Furthermore, the tracking itself (locating the feet of the characteristics) will be identical for each chemical species, and therefore need only be done once at each grid node. Equation (3.4) will, in general, be a dependent system of equations, but since it contains no spatial gradients, it can be solved at one computational grid node at a time. Equation (3.5) has spatial gradients and therefore must be solved simultaneously over the entire domain, but since each equation only involves one chemical species, the solution can be obtained independently for each of the species in the system.

A consequence of converting equation (3.1) into equations (3.3), (3.4), and (3.5) is that the computational time step becomes tailored to the portion of the problem being solved. When tracking is separated from dispersion, the Courant number constraint on the

dispersion portion of the problem is relaxed and the tracking, while requiring a small time step which is computationally expensive, involves solving a relatively simple equation at only one grid node at a time. In ELAmet this is taken a step further, as the chemical reaction equations are also solved along the characteristic lines. This allows the choice of a computational time step which is appropriate for the chemical time scales under consideration, and independent of the time steps chosen for advection and dispersion.

The tracking is done using a fourth-order Runge-Kutta technique. The tracking time step is continually adjusted to assure that the tracking error does not exceed a specified maximum. The dispersion portion of the problem is solved using a Galerkin weighted residual method on a quadratic, triangular, finite element grid. Interpolation at the foot of the characteristic lines is done using the quadratic shape functions associated with the element containing the foot. The mechanics of the solution of advection and dispersion are not discussed further in this paper; rather we go directly to the chemical transformation equations and discuss in detail the solution of those.

Formulation of Transformation Equations

The construction of the transformation equations as given here is simplified, since the purpose is to derive a general, representative form of the equations and discuss the solution technique in detail. A more detailed and precise account of how the equations are constructed is given in *Wood and Baptista* [1992].

In formulating the chemical transformation equations, we presume that the metal of interest is distributed among several different species; these species may exist in the aqueous or the solid phase. In general, these species are divided into two broad types- composite species which are “building blocks” in the sense that they are not broken down further through any reactions, and derived species which are unique combinations of the component species as determined by the chemical reactions. Furthermore, the reactions affecting the metal of interest can occur over a very wide range of time scales. In the most general case it is therefore important to divide the derived species into two additional categories- those which are formed in a time scale short compared to the computational time step chosen for the chemical transformations, and those which are formed in a time scale long compared to the same time step.

Associated with each of these three distinct types of species is a particular type of equation. Composite species, which do not appear as products in a reaction, are associated with a mass balance equation, since the total mass of a component species will remain invariant when added up over the entire system. The first type of derived species, which can be assumed in instantaneous equilibrium with its component species, is governed by a mass action equation. The second type of derived species is governed by a kinetic rate equation. If we denote the concentration of the species by c_j , then the most general form of each of these equations is as follows. The mass balance equation for a component species is:

$$C_j = c_j + \sum_{i=1}^M a_{ij} c_i \quad i \neq j \quad (3.6)$$

where C_j is the total analytical concentration of the j^{th} species, a_{ij} is the stoichiometric coefficient of the j^{th} species in the i^{th} species, and M is the total number of species. For the first type of derived species the mass action equation is of the general form:

$$c_j = \beta_j \prod_{i=1}^M c_i^{a_{ji}} \quad (3.7)$$

where β_j is the stability constant of the j^{th} species. Finally, the most general form of the rate equation for the second type of derived species is:

$$\frac{dc_j}{dt} = \kappa_j^f \prod_{i=1}^M c_i^{a_{ji}} - \kappa_j^b c_j - \sum_{i=1}^M \left(\kappa_i^f \prod_{n=1}^M c_n^{a_{in}} - \kappa_i^b c_i \right) \alpha_{ij} - \kappa_j c_j - F_j (\delta_j c_j + (1 - \delta_j) c_j^{bed}) \quad (3.8)$$

where κ_j^f and κ_j^b are the forward and backward rate constants, respectively, of the reaction producing c_j ; κ_j is the linear decay constant for c_j ; F_j is the flux due to sediment deposition or erosion; c_j^{bed} represents the concentration of species c_j in the bed sediments; $\alpha_{ij} = 0$ if $a_{ij} = 0$ and $\alpha_{ij} = 1$ if $a_{ij} > 0$, and $\delta_j = 1$ in the case of sediment deposition ($F_j > 0$), and $\delta_j = 0$ in the case of sediment erosion ($F_j < 0$). The first two terms on the right-hand-side of equation (3.8) represent the rate of production of c_j due to the reaction in which it appears as a product; the next $2M$ terms represent the loss of c_j due to all reactions in which it appears as a reactant; the next term represents the loss of c_j due to linear decay, and the final term represents a loss or gain of mass due sediment deposition or erosion. It should be apparent from the form of this equation that the derived species are not limited in this

formulation to being products in a reaction; they can also combine with composite species as reactants to form another derived species as a product.

A simple environmental system serves to demonstrate the definition of the three different species and the use of the corresponding equations. Suppose the sample system contains the following species concentrations: $[Me^{2+}]$, $[L^-]$, $[O^-]$, $[MeL^+]$, and $[MeO^+]_{(s)}$. The concentration of divalent aqueous metal ion is denoted $[Me^{2+}]$; it could represent, for example, Cd^{2+} , Pb^{2+} , or Zn^{2+} . An aqueous ligand such as OH^- or Cl^- is denoted by $[L^-]$. The concentration of surface sites available for surface complexation reactions is denoted by $[O^-]$, $[MeL^+]$ is the aqueous complex formed between the free metal ion and the aqueous ligand, and $[MeO^+]_{(s)}$ is the solid phase species formed by a surface complexation reaction between the aqueous metal ion and surface sites. This system contains three component species which cannot be broken into smaller units. There are three mass balance equations associated with $[Me^{2+}]$, $[L^-]$, and $[O^-]$:

$$Me_T = [Me^{2+}] + [MeL^+] + [MeO^+]_{(s)} , \quad (3.9)$$

$$L_T = [MeL^+] + [L^-] , \quad (3.10)$$

$$O_T = [O^-] + [MeO^+]_{(s)} , \quad (3.11)$$

where Me_T , L_T , and O_T are the total analytical concentrations of $[Me^{2+}]$, $[L^-]$, and $[O^-]$, respectively. The aqueous complex $[MeL^+]$ is formed and dissociated so rapidly that it is always in equilibrium with its component species. Associated with this species is a mass action equation:

$$[MeL^+] = \beta [Me^{2+}] [L^-] . \quad (3.12)$$

The solid phase species $[MeO^+]_{(s)}$ is formed relatively slowly, and therefore a rate equation is required to describe the time dependence of its concentration. The rate equations associated with the complexation reaction are:

$$\frac{d}{dt}[MeO^+] = \kappa^f [Me^{2+}] [O^-] - \kappa^b [MeO^+] , \quad (3.13)$$

$$\frac{d}{dt}[Me^{2+}] = -\kappa^f [Me^{2+}] [O^-] + \kappa^b [MeO^+] . \quad (3.14)$$

As is discussed below for the general case, the total speciation of this system would now be solved by breaking the set of equations (3.9) through (3.14) into two smaller sets. The first set consists of the mass action equations, in this case (3.12), along with the mass balance equations required to complete the set, (3.10) and (3.11). The second set consists of the rate equations, in this case (3.13) and (3.14), and the required mass balance equation (3.9).

Solution of the Transformation Equations

The equations (3.6), (3.7), and (3.8) are of three distinct types, (3.6) being a linear algebraic equation, (3.7) being a nonlinear algebraic equation, and (3.8) being a nonlinear differential equation. It is extremely difficult to solve this entire system of dissimilar equations simultaneously; therefore, we instead use a method which separates the system into two smaller subsystems (I and II) which are solved separately. However, because the two systems are not generally independent, this requires an iteration between them in order to converge on a consistent speciation of the metal. Note that because the transformation equations are solved on a node-by-node basis, the solution algorithm is independent of the dimensionality of the problem.

System I consists of all of the mass action equations, and the mass balance equations for the component species that are required to generate enough equations to solve for the concentration of all species appearing in the mass action equations. System I equations are then solved using a Newton-Raphson technique. This is an iterative technique, so that in addition to an iteration between system I and system II, system I requires its own iteration to converge on a solution. The procedure is to first write all of the system I equations in the form $\psi_j(c_1, c_2, \dots, c_M) = 0$. In the case of a component species,

$$\psi_j = C_j - c_j - \sum_{i=1}^M a_{ij} c_i, \quad (3.15)$$

and in the case of derived species,

$$\psi_j = c_j - \left(\beta_j \prod_{i=1}^M c_i^{a_{ji}} \right). \quad (3.16)$$

A Taylor series expansion is used to expand ψ_j around chosen values of (c_1, c_2, \dots, c_M) . In this way, using the first iteration as an example, $\psi_j(c_1^o, c_2^o, \dots, c_M^o)$ is approximated by

$$\psi_j(c_1^o, c_2^o, \dots, c_M^o) \approx - \left[\frac{\partial \psi_j}{\partial c_1} (c_1 - c_1^o) + \frac{\partial \psi_j}{\partial c_2} (c_2 - c_2^o) + \dots + \frac{\partial \psi_j}{\partial c_M} (c_M - c_M^o) \right] \quad (3.17)$$

where only the highest-order terms are kept in the approximation. At any particular loop k in the iteration the simultaneous set of equations making up system I can be written in matrix form as:

$$\begin{bmatrix} \frac{\partial \psi_1}{\partial c_1} & \frac{\partial \psi_1}{\partial c_2} & \dots & \frac{\partial \psi_1}{\partial c_M} \\ \frac{\partial \psi_2}{\partial c_1} & \frac{\partial \psi_2}{\partial c_2} & \dots & \frac{\partial \psi_2}{\partial c_M} \\ \vdots & \vdots & \ddots & \vdots \\ \frac{\partial \psi_M}{\partial c_1} & \frac{\partial \psi_M}{\partial c_2} & \dots & \frac{\partial \psi_M}{\partial c_M} \end{bmatrix} \begin{bmatrix} \Delta c_1 \\ \Delta c_2 \\ \vdots \\ \Delta c_M \end{bmatrix} = - \begin{bmatrix} \psi_1 \\ \psi_2 \\ \vdots \\ \psi_M \end{bmatrix} \quad (3.18)$$

where $\Delta c_n = c_n - c_n^k$. An iteration is required to converge on a set of c_n . At the beginning of the process, values from the last time step are used as c_n^o , and the matrix equation (3.18) is solved for the vector $\{\Delta c_n\}$. A new estimate of c_n is calculated from $c_n^1 = c_n^o + \Delta c_n$. This new estimate is used to calculate new values of the jacobian matrix and the right-hand-side vector, and the process is repeated until an error criterion of the form $\max(\Delta c_n / c_n^k) < \epsilon$ is satisfied. A sparse solver is used to solve the matrix equation [e.g. Zlatev, et al., 1981].

System II consists of all of the partial differential rate equations, again complemented by the mass balance equations necessary to complete the system. In order to solve this system we employ a linearization technique and solve the resulting linear system explicitly using standard matrix inversion techniques.

The linearization of (3.8) proceeds as follows. We first employ the general time-stepping method described by:

$$\frac{dc}{dt} = f(c, t) \quad \Rightarrow \quad \frac{c^{[p+1]} - c^{[p]}}{\Delta t} = \theta f^{[p+1]} + (1 - \theta) f^{[p]} \quad (3.19)$$

where θ can take on any value between 0 (Euler-forward) and 1 (Euler-backward). A value of $\theta=0.5$ corresponds to a Crank-Nicholson time-stepping. The superscripts $[p]$ and $[p+1]$ denote the value at time step p and $p+1$, respectively. When this general θ -method is applied to equation (3.8), the result is:

$$c_j^{[p+1]} - \Delta t \theta \lambda_j^{[p+1]} = c_j^{[p]} + \Delta t (1 - \theta) \lambda_j^{[p]} \quad (3.20)$$

where

$$\lambda_j = \kappa_j^f \prod_{i=1}^M c_i^{a_{ji}} - \kappa_j^b c_j - \sum_{i=1}^M \left(\kappa_i^f \prod_{n=1}^M c_n^{a_{in}} - \kappa_i^b c_i \right) \alpha_{ij} - \kappa_j c_j - F_j (\delta_j c_j + (1 - \delta_j) c_j^{bed}) \quad (3.21)$$

The right-hand-side of (3.20) is calculated explicitly using values at the previous time step.

Nonlinearities in λ_j arise when $\sum_i a_{ji} > 1$ or $\sum_n a_{in} > 1$. In this case we linearize

the relevant terms on the left-hand-side of (3.20) by using values from the last iteration to calculate a coefficient for a modified linear term. Thus these terms are approximated by:

$$\begin{aligned} \left\{ \kappa_j^f \prod_{i=1}^M c_i^{a_{ji}} \right\}^{[p+1]} &\approx \left\{ \kappa_j^f \left(\prod_{i \neq i'} c_i^{a_{ji}} \right) c_i^{(a_{ji} - 1)} \right\}^{[p']} c_i^{[p+1]} \\ \left\{ \kappa_i^f \prod_{n=1}^M c_n^{a_{in}} \right\}^{[p+1]} &\approx \left\{ \kappa_i^f \left(\prod_{n \neq n'} c_n^{a_{in}} \right) c_n^{(a_{in} - 1)} \right\}^{[p']} c_n^{[p+1]} \end{aligned} \quad (3.22)$$

where the superscript $[p']$ indicates the value at the last iteration. In the case of the first iteration, we use instead the value at the end of the last time step. Note that “iteration” refers to the last iteration with the system I equations; no iteration is required to solve the system II equations themselves. As the coefficients of all terms on the left-hand-side of (3.20) can now be calculated explicitly, we can combine all of the system II equations into a linear matrix equation of the form:

$$\Phi^{[p+1]} \mathcal{C}^{[p+1]} = \Lambda^{[p]} \quad (3.23)$$

where Φ is a square matrix with dimensions $m \times m$, where m is the total number of equations (rate equations plus required mass balance equations) in system II, \mathcal{C} is a column

vector with dimensions $m \times 1$ containing the unknown concentrations c_j , and \mathbf{A} is the known right-hand-side vector with dimensions $m \times 1$. As indicated, Φ will in general have to be calculated and inverted at each time step. The coefficient matrix is not generally symmetric, but a sparse solver can be used.

The dependence of the system I and II equations arises because the two systems share some species; in particular, the same component species can participate in reactions in either system, and derived species from system II can act as component species in system I. This can be seen in the example provided at the end of the last section. In this simple system, $[Me^{2+}]$ acts as a component in both equilibrium and rate-controlled reactions, and is therefore an unknown in both system I and system II equations. An iteration between system I and II equations would be required to converge on a value for $[Me^{2+}]$.

Decoupling of the Transformation and Diffusion Time Step

The advantage in being able to choose independent chemical and diffusive time steps can be demonstrated with two simple examples. The first involves no advection. In this example, we begin with a gauss hill of initial aqueous metal concentration centered on a 1-dimensional domain 10 km long. The aqueous metal undergoes a linear transformation into the solid phase, as given by the rate expression:

$$\frac{dc_a}{dt} = \kappa^f c_s - \kappa^b c_a \quad (3.24)$$

where c_a is the aqueous phase concentration, c_s is the solid phase concentration, κ^f and κ^b are the forward and backward rate constants, respectively, for this particular partitioning reaction. For this simulation, we choose equal values for the forward and backward rate constants: $\kappa^f = \kappa^b = (1 \text{ hr})^{-1}$. Equilibrium at any point in the domain will therefore be characterized by equal concentrations of the aqueous and solid phases. The maximum initial concentration of c_a at the top of the gauss hill is 10 nondimensional units.

Simultaneously, the concentration profile of both c_a and c_s are subject to diffusion; in this case the diffusivity is set to $D = 5 \text{ m}^2 \text{ sec}^{-1}$. The time step for solving the diffusion is set to 1 hour, while the time step for solving the chemical reaction is varied from one per diffusion time step (a reaction time step of 1 hour) to ten per diffusion time step (a reaction time step of 6 minutes).

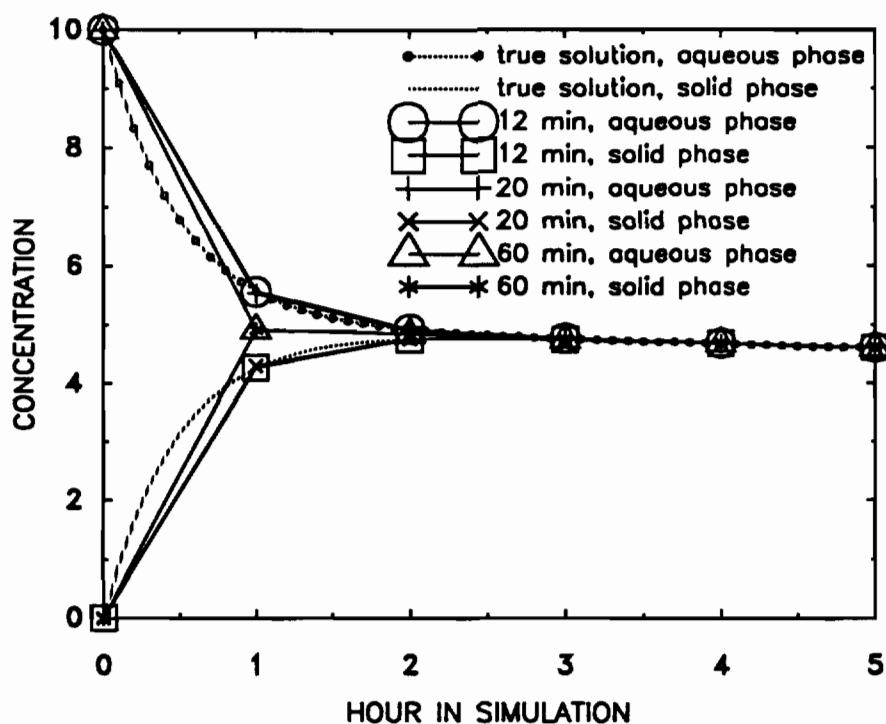


Figure 3.1. Time series of concentration at the top of the gauss hill (at $x=5$ km). The heavy lines are the “true” solution, as computed using small chemical and diffusion time steps. The light lines connect points at the diffusion time steps for 5 (open circles), 3 (solid circles), and 1 (triangles) chemical time steps per diffusion time step.

Figure 3.1 shows the evolution of concentration in time at the center point of the domain, corresponding to the top of the gauss hill. The “true” time series of concentration shown in the figure was calculated numerically using both a small diffusion and a small reaction time step, and very closely approximates the real problem solution. The test simulations use a 1 hour diffusion time step and therefore sample the true solution at 1 hour intervals. During the first few hours of the simulation, while the concentrations of aqueous and solid phase at this point in the domain are still quite far from equilibrium, a chemical time step of about 20 minutes seems adequate to sample the series accurately. After equilibrium is reached, all of the simulations eventually converge on the correct solution. This problem demonstrates that in a system in which equilibrium is eventually obtained, the ratio of chemical time step to diffusion time step is likely to be important only at initial times during which the system is not in an equilibrium state.

However, in a dynamic environment which more closely simulates estuarine conditions, there is no reason to assume that chemical equilibrium at a given point is ever achieved. In this case, the choice of chemical time step may be important at all times. To demonstrate this situation, we use the same domain as in the last problem, and we consider the same linear chemical transformation. In this case we impose a flow field such that the domain is continually being flushed with fluid in a nonequilibrium state, and with a time-varying concentration. The flow field has two components: a steady current of -1 m/s, and an oscillatory current with a period of 12 hours and a phase difference of 2π from one end of the domain to the other. The oscillatory current has a maximum amplitude of approximately .3 m/s, so that the velocity is always into the domain at the $x=10\text{km}$ boundary where steady boundary conditions of $c_a=1$ and $c_s=0$ are imposed.

In Figure 3.2 we again show the time series of concentration at $x=5\text{ km}$; as in Figure 3.1 the “true” solution is computed numerically using a small chemical and diffusion time step. In this case, the state of chemical equilibrium, characterized by equal c_a and c_s concentrations, is never achieved. Once again the test simulations use a 1 hour diffusion time step. In this case the error associated with a particular chemical to diffusion time step ratio does not decrease as the simulation progresses. The error associated with 1 chemical time step per diffusion time step is relatively large, but in this case splitting the diffusion time step into only two chemical time steps can reduce the error substantially. The simulation using a chemical time step of 6 minutes reproduces the true solution almost exactly.

Future Developments

Our interest in applying ELAmet is largely in exploring the notion of “diagnostic” modeling; i.e., using numerical models as a research tool to aid in the understanding of complex estuarine systems, rather than emphasizing the predictive function of modeling. In a simple example of this diagnostic function of numerical modeling, ELAmet has been applied to a stylized estuarine system in order to discuss some implications of relatively sparse sampling in the interpretation of the salinity vs. concentration plots which are the form often used to present observational data. In particular we showed that the salinity vs. concentration plot for a 2-dimensional domain is not likely to be a single-valued function of salinity. Features such as asymmetry in the source and loss terms such as deposition cause the water properties of a 2-dimensional system to occupy an area, rather than a line,

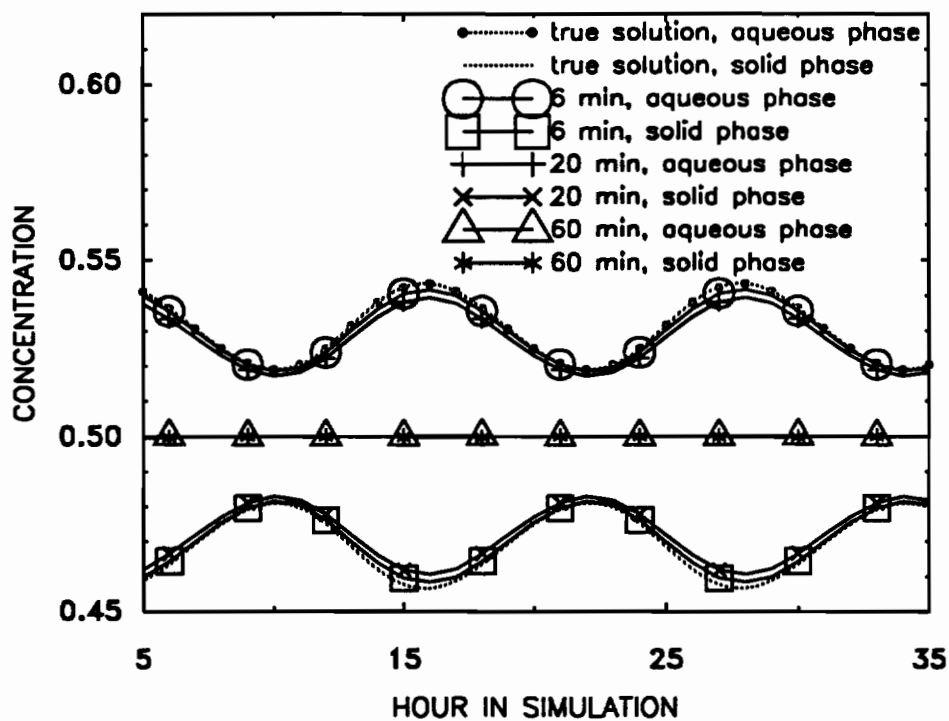


Figure 3.2. Time series of concentration at $x=5$ km. The heavy lines are the “true” solution, as computed using small chemical and diffusion time steps. The light lines connect points at the diffusion time steps for 10 (open circles), 3 (solid circles), and 1 (triangles) chemical time steps per diffusion time step.

in the salinity vs. concentration plane. We also found that kinetically-controlled adsorption reactions can create an apparent dependence on salinity in the partition coefficient where none exists [Wood and Baptista, 1992].

Preliminary work is underway in applying ELAmet to the San Francisco Bay System. As a first step, we are investigating how different types of nonconservative behavior will alter the spectral characteristics of the concentration field, as compared to a conservative substance with the same source properties. We have looked at, for example, how the amplitude of the M2 variability changes with different chemical behavior. Suppose we define three substances (a), (b), and (c), with the following chemical behavior:

$$\frac{dc_a}{dt} = 0 \quad , \quad (3.25)$$

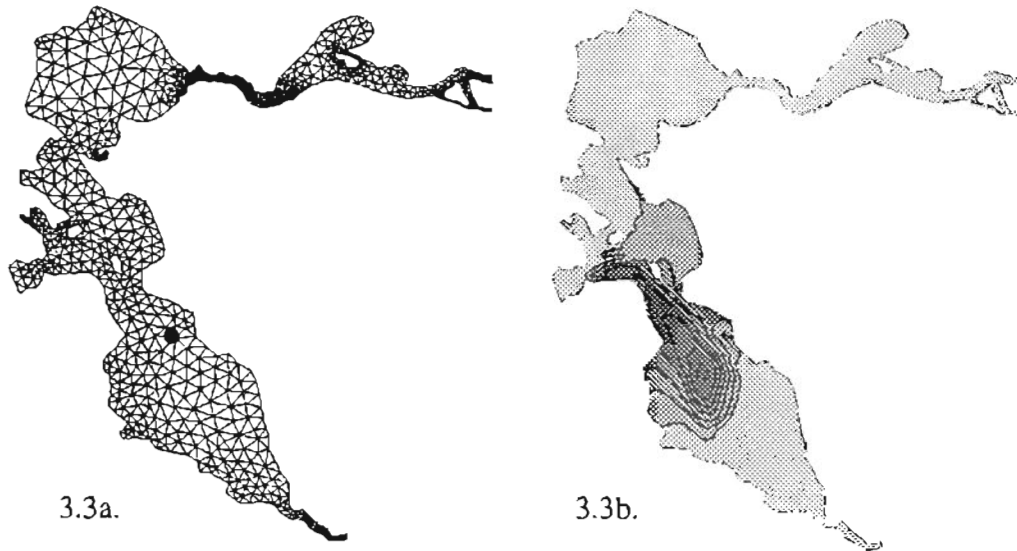


Figure 3.3. Figure 3.3a shows the numerical grid used for simulations in San Francisco Bay. The black dot marks the approximate location of the source for the plume shown in Figure 3.3b and the sample point where time series shown in Figure 3.4 are taken. Figure 3.3b is a snapshot of the conservative tracer plume generated by the source shown in 3.3a. Note that the plume moves with the tidal cycle and therefore the maximum in the plume does not necessarily coincide with the source location.

$$\frac{dc_b}{dt} = -\kappa_b(S) c_b, \text{ and} \quad (3.26)$$

$$\frac{dc_c}{dt} = -\kappa_c(c_c) c_c, \quad (3.27)$$

respectively, all of which have the same source location and strength (Figure 3.3). The decay coefficient κ_b varies linearly with the salinity S such that $\kappa_b=0$ for a salinity of 25 ppt and κ_b is a maximum at maximum salinity. The decay coefficient κ_c varies linearly with concentration such that $\kappa_c=0$ when $c_c=0$ and κ_c reaches a maximum at maximum concentration. If salinity is out of phase with concentration, equation (3.26) requires that substance (b) has a maximum loss rate at the point in the tidal cycle when concentration is at a minimum. The effect is that the nonconservative behavior of substance (b) has the ability to enhance tidal oscillations as compared to the conservative substance (a), even while the mean value of the nonconservative substance is lower. Equation (3.27), on the other hand, requires that substance (c) has a maximum loss rate at the point in the tidal cycle when concentration is at a maximum. Therefore, the nonconservative behavior of

substance (c) will tend to diminish the tidal oscillations as compared to the conservative substance. These effects can be seen in the time series plots shown in Figure 3.4. These effects are most easily seen near the source, therefore the time series were taken at a sample point very close to the source shown in Figure 3.3. A scatter plot which plots the M2 amplitude of substance (a) against that of substances (b) and (c) for all of the grid nodes in the South and Central Bay is shown in Figure 3.5. The plot suggests that there are some regions of the domain where the two types of nonconservative behavior are distinct in their relationship to the conservative substance. If distinctive spectral relationships between salinity, conservative tracers, and various nonconservative tracers exist and can be defined, then sampling strategies for the estuary could be designed to distinguish between substances with differing chemical behavior.

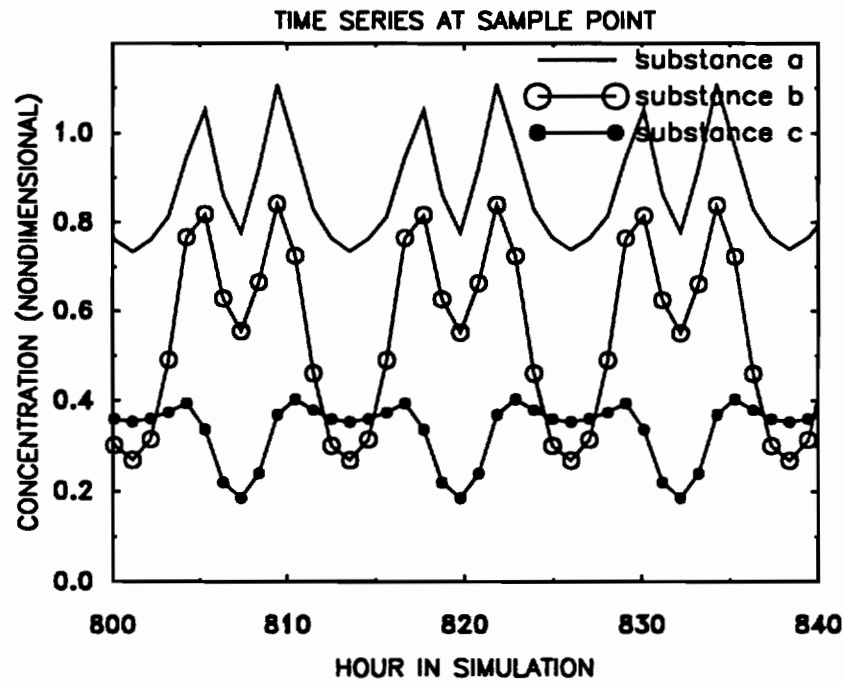


Figure 3.4. Time series of concentration for substances (a), (b), and (c) at a sample point close to the source shown in Figure 3.3.

The most useful contribution of this model will be in a diagnostic mode, to yield insight into how the Bay system works, and to suggest optimal ways of sampling the Bay system in order to better isolate geochemical pathways of interest. In general, diagnostic modeling will be most successful if it is part of a feedback loop in which modeling suggests sampling strategies, sampling in turn yields new information, new information is used to improve the models, and so on.

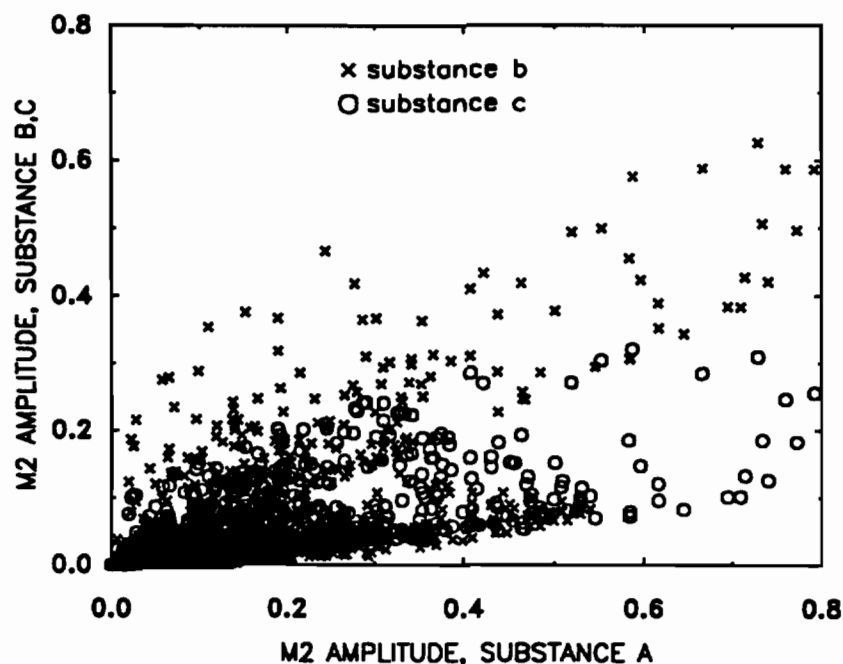


Figure 3.5. Scatter plot showing the relationship between variability at the M2 frequency in a conservative tracer (substance (a)) and in two different nonconservative tracers (substances (b) and (c)).

References

- Baptista, A.M., 1987: Solution of advection-dominated transport by Eulerian-Lagrangian methods using the backwards method of characteristics, *Ph.D. Thesis, MIT, Cambridge, Mass.*
- Wood, T.M. and A.M. Baptista, 1993: A model for diagnostic analysis of estuarine geochemistry, *Water Resources Research*, 29(1), pp. 51-71.
- Yeh, G.T. and V.S. Tripathi, 1989: A critical evaluation of recent developments in hydro-geochemical transport models of reactive multichemical components, *Water Resources Research*, vol. 25, pp. 93-108.
- Zlatev, Z. , J. Wasniewski, and K. Schaumburg, 1981: Y12M: Solution of large and sparse systems of linear algebraic equations (Lecture notes in computer science 121). Berlin, NY: Springer-Verlag.

CHAPTER 4

Diagnostic Modeling of Trace Metal Partitioning in South San Francisco Bay

Abstract

A spatially and temporally explicit numerical model ELAmet was used to investigate the effect of adsorption kinetics on the apparent distribution coefficients of copper, cadmium and zinc in South San Francisco Bay, California. The numerical experiments were designed with three goals in mind: 1) to use a spatially and temporally explicit modeling approach to extrapolate laboratory partitioning data to an environmental setting, 2) to establish that adsorption kinetics can control the basin-scale variability of the observed partitioning and therefore the apparent dependencies of partitioning on salinity and suspended solids, and 3) to define the conditions under which adsorption kinetics could account for strong interannual variability in partitioning.

The numerical results indicate that aqueous speciation will control the profile of the apparent distribution coefficient K_d^a if the system is close to equilibrium. However, if the system is far from equilibrium the profile of K_d^a and its apparent dependencies on salinity and suspended solids will be determined by the location of the sources of metal, and the suspended solids concentration of the receiving water. The results also indicate that the further the basin as a whole is from equilibrium, the greater the basin-scale variability in K_d^a that would likely be observed during a single sampling cruise.

This work has interesting implications for the interpretation of field data from San Francisco Bay. Apparent distribution coefficients from two different years exhibit strong dissimilarities; K_d^a values for copper, cadmium, and zinc during 1989 are generally higher and more variable than those observed during 1985. Our modeling work implies that South Bay was, on the whole, much closer to equilibrium during 1985 than during 1989.

The reason for this appears to be an unexplained, strong influx of particulate metal during 1989.

Introduction

San Francisco Bay is a highly urbanized estuary on which the anthropogenic impact is undeniable. One direct result of this impact has been an increase in the concentration of several trace metals with respect to the surrounding coastal waters [Gordon, 1980], and a consequent interest in understanding the effects of these increased concentrations on the Bay ecosystem. An important factor in determining a trace metal's bioavailability and its residence time in the Bay is the extent to which it will partition between the dissolved and particulate phases.

Field surveys in the Bay have raised as many questions as they have answered regarding trace metal partitioning. The observational data reveal that trace metal partitioning is a highly complex phenomenon, that observed distribution coefficients vary on several spatial and temporal scales, and that making any connection between laboratory data and field measurements is difficult at best. One aspect of trace metal partitioning that may explain some of the inconsistencies in the data is adsorption kinetics, which remains a largely unexplored aspect of estuarine geochemical cycling.

We have used the numerical transport model ELAmet [Wood and Baptista, 1993], which has the capability to combine aqueous speciation with adsorption kinetics, to investigate the effect of adsorption kinetics on the measured values of distribution coefficients in South San Francisco Bay. Our goals were three: 1) to use a spatially and temporally explicit modeling approach to extrapolate laboratory partitioning data to an environmental setting, 2) to establish that adsorption kinetics can control the basin-scale variability of the observed partitioning and therefore the apparent dependencies of partitioning on salinity and suspended solids, and 3) to define the conditions under which adsorption kinetics could account for the observed interannual variability in partitioning in South Bay. We did not attempt to precisely duplicate prevailing environmental conditions and observations. Rather, the intent was to design numerical experiments that lead to a greater understanding of the adsorption process in South Bay and how it is manifested in observations, and to encourage further modeling studies, laboratory experiments, and observational surveys of

the Bay by highlighting some of the important remaining uncertainties. We call this approach diagnostic modeling.

Review of Field Data

A presentation of some pertinent field data serves to motivate the modeling work that follows. In Figure 4.1, Figure 4.2, and Figure 4.3 we show the observed apparent distribution coefficient, K_d^a , for copper, cadmium and zinc from two different surveys in South San Francisco Bay which looked at the distribution of these metals between the dissolved and particulate phases. The first survey consisted of 5 cruises between March and September of 1985, each sampling 4 stations along the axis of the South Bay [Kuwabara, *et al.*, 1989]. The second consisted of three cruises in April, August and December of 1989. Eight of the 27 stations sampled were located in the South Bay [Flegal, *et al.*, 1991]. A comparison of these two data sets must be done with care, as they have not been intercalibrated, and different sampling techniques were used. Nonetheless, the figures suggest that interpreting partitioning data is not a simple matter, and that there can be significant interannual changes in both the mean values of K_d^a and its variability. The 1989 data have higher mean values for each of the metals, and display significantly more variation around that mean than the data from 1985. While we cannot rule out the possibility that the differences between the two data sets are due to sampling artifacts, there are physical and chemical processes that might plausibly induce interannual variability of this magnitude in K_d^a .

In Table 4.1 we have compiled laboratory measurements of the distribution coefficient K_d for a variety of adsorbents, all done in seawater or at high ionic strengths (with the exception of Glegg, *et al.*, 1988, who looked at the desorption of estuarine bottom sediments in freshwater). Several of these values are also displayed in Figure 4.1, Figure 4.2, and Figure 4.3 for purposes of comparison. The huge variation in measured K_d values complicates the South Bay data even more, as it is evident that partitioning to different types of particles occurs over a range covering several orders of magnitude for each of these metals. There is very little information on the temporal variability in the chemical composition of the suspended particles of the South Bay between sampling cruises, or the spatial variability during any given cruise. An analysis of the inorganic suspended sediments at two stations during two separate 1985 cruises showed little variation in the weight percent of major elements; however, the cruises used for this comparison were

both during the summer, which might mask variations in particle composition during the algal bloom period [Kuwabara, *et al.*, 1989].

Interannual variability in suspended sediments may be of more importance, especially if, as in the case of 1985 and 1989, a comparison is being made between a non-drought and drought year. *Thomson-Becker and Luoma* [1985] found interannual differences in the percentage of fine-grained sediment in bottom deposits which could be correlated with year-to-year differences in wind and precipitation. Higher surface runoff during late fall and winter carries a larger percentage of fine-grained material to the water column where it is subsequently deposited; as runoff tapers off in summer, winds become stronger and the bottom sediments become relatively depleted in fine-grained material. These seasonal variations could be extrapolated to some extent to interannual differences, as year-to-year differences in the grain size distributions were to some extent predictable from year-to-year differences in wind and precipitation.

Seasonal and interannual variations in the size distribution of sediments are accompanied by variations in composition. *Thomson-Becker and Luoma* [1985] found that total organic carbon, extractable organic material, and extractable iron were all correlated with an increase in the percentage of fine particles; the latter relationship, however, had a distinct seasonal dependence. Their work also indicated that years of anomalously high runoff resulted in a relatively high percentage of humic material in the surface sediments; for example, the absorbance of extractable organic matter reached a maximum of $\sim 10 \text{ g}^{-1}$ during the high-flow years of 1981-82, whereas it reached a maximum of only $\sim 4 \text{ g}^{-1}$ during the low-flow year of 1980-81. Iron levels in the sediment also exhibited interannual variability, although the relationship to yearly precipitation and runoff was less clear. Iron extractable by hydroxylamine hydrochloride and ammonium oxalate reached maximums of 4500 and 14000 $\mu\text{g g}^{-1}$, respectively, in 1987, as compared to maximums of only 2500 and 8000 $\mu\text{g g}^{-1}$, respectively, in 1980. Thus the inherent variability in the nature of the suspended sediments in South Bay may be responsible for some of the observed variability in trace metal partitioning, but to an extent that we cannot predict. However, one aspect of the work of *Thomson-Becker and Luoma* [1985] argues against particle variability being a major factor- their work indicated that seasonal fluctuations in the composition of surficial sediment were generally as strong or stronger than year-to-year fluctuations, and seasonal fluctuations in the 1985 and 1989 partitioning data are not obvious, and in any

event appear to be secondary to the interannual variability. For the moment, we leave the question of how much variability in metal partitioning can be attributed to particle variability open, and explore other possible sources.

The data from individual cruises during both 1985 and 1989 exhibit basin-scale variability (substantially greater during 1989) which is not easily explained, and exhibit ambiguous dependencies on salinity and the concentration of suspended solids. A negative correlation with salinity can be attributed to a change in the aqueous speciation of the metal, as more metal is held in solution at higher salinities by increased complexation with major seawater ions [Comans and van Dijk, 1988; Gonzalez-Davila, et al., 1990; Li, et al., 1984]. Kuwabara, et al. [1989] found that the combined partitioning data from all five 1985 cruises was significantly and negatively correlated with salinity (several environmental parameters were correlated with salinity, making it difficult to separate true from spurious correlations), but the aggregate data for the 1989 cruises do not show a similarly high negative correlation with salinity. Furthermore, if one examines individual cruises from both data sets, a negative correlation of distribution coefficient with salinity is found to be the exception rather than the rule. It appears, therefore, that over the limited salinity range covered by a single cruise, other factors control the relationship between K_d and salinity.

Assuming for the moment that particle variability is not a major factor, the distribution coefficient should not, in theory, depend on the concentration of solids at the low solids concentrations typical of estuarine water columns. Nonetheless, apparent constants often show a marked decrease with an increase in the concentration of the solid phase. This effect can be attributed to the existence of colloids which act as a solid phase in the adsorption process but which are not separated with the solid phase when measurements are taken [Pankow and McKenzie, 1991; Morel and Gschwend, 1987]. However, analysis of both the aggregate and the individual cruise data during 1985 and 1989 for copper, cadmium and zinc does not reveal any consistent relationship between partitioning and total suspended solids concentration. In fact, in only one case (April 1989) do the data show an exponential decrease in partitioning with solids concentration that could be attributed to the colloidal phase. Clearly the relationship between K_d^a and suspended solids concentration is not a simple one. Changes in the surface composition of suspended particles with seasonal fluctuations in DOC, for example, might mask any contribution of the colloids in

Table 4.1. Measured Distribution Coefficients

Cu	Cd	Zn	adsorbent	ref
	8.5×10^{-5}	1.2×10^{-3}	Narragansett Bay sediments	1
	4.7×10^{-5}	1.1×10^{-3}	San Clemente sediments	1
	9.5×10^{-5}	0.14	MANOP site H sediments	1
		3.6×10^{-3}	sediment trap sediments	1
		9.4×10^{-3}	fecal pellets	1
		0.045	Puget Sound sediments	2
1.15		2.1	Tamar seds (freshwater)	3
	0.22		pyrite	4
0.48	6×10^{-3}	0.15	MANOP site H sediments	5
		0.051	MANOP site H sediments	6
22.	1.1×10^{-3}	0.035	goethite	6
	1×10^{-3}	0.014	zooplankton fecal pellets	7
	0.016	0.14	zooplankton fecal pellets	7
	3.7×10^{-3}	1.7×10^{-3}	riverine suspended particles	8
0.043	1.1×10^{-3}		bentonite clay	9
0.21	4.4×10^{-3}		Fe(OH) ₃	9
7.3	0.015		MnO ₂	9
0.37	2×10^{-4}		humic acid	9
3.2×10^{-3}			chitin	10

All units are $l \text{ mg}^{-1}$.

¹ Nyfeller, et al. (1984); Table 2.

² Jannasch, et al. (1988); Table 4.

³ Glegg, et al. (1988); Table 2.; computed as k_1^*/k_{-1} .

⁴ Kornicker and Morse (1991) Table 1.; site concentration converted to weight [FeS₂].

⁵ Balistrieri and Murray (1984); Table 2.; site concentration converted to weight.

⁶ Balistrieri and Murray (1983); approximate values from Figures 3&5; site concentration converted to weight.

⁷ Fisher, et al. (1991); Table 2.

⁸ Li, et al. (1984); Table 2.

⁹ Oakley, et al. (1981); Table 1.

¹⁰ Gonzalez-Davila and Millero (1990); estimated from Figure 9.

the aggregate data. Within a single cruise, spatial variations in particle composition over the South Bay could produce variations in K_d^a . However, the complicated relationship between K_d^a and both salinity and suspended solids concentration could also be a manifestation of adsorption kinetics at the basin scale.

Thus there are two distinct types of variability in South Bay that are largely unexplained: basin-scale variability that is seen during a single cruise, and interannual variability seen in the difference between data sets from two different years. The extent to which adsorption kinetics can be a controlling factor in this variability remains largely unexplored, due to the lack of adequate tools for studying the problem. A numerical model can make an important contribution in this regard. Numerical experiments that incorporate adsorption kinetics can be used to better understand how rate-controlled adsorption in the estuarine environment is likely to be manifested in field data.

Experimental Design

Consistent with a diagnostic modeling approach, the ELAmet experiments were designed to produce plausible experimental scenarios, rather than to duplicate any particular set of conditions. Any attempt to recreate the environment of a particular sampling period in detail is bound to be unsuccessful, as the detailed spatial and temporal information that would be needed is not available. For example, metal and sediment loadings are generally available in terms of daily or even annual averages to the basin as a whole, whereas measured concentrations of metal and sediment are dependent on the time-history of metal and sediment loadings leading up to that point, as well as on spatial variability in these loadings. Nonetheless, we can use available information to construct simulations that capture enough important characteristics of the system that it is possible to gain significant new insight into the nonconservative transport of trace metals in the Bay.

All circulation and salinity simulations were done using the finite element grid shown in Figure 4.4. In order to appropriately define the boundary values using oceanic and Delta conditions, it was necessary to include the entire Bay in the simulations. However, we restrict our analysis to the South Bay which provides sufficient complexity to test the validity of using ELAmet to understand metal transport. The reasons for not expanding the analysis beyond the South Bay at this point are two: first, the use of a 2-dimensional model to evaluate transport in the northern reach is more questionable, as stratification plays a dominant role, and second, expanding the analysis into portions of the Bay with lower salinities than those in South Bay will require the incorporation of variable thermodynamic constants, as discussed further below.

Circulation

The circulation used in the ELAmet simulations presented in this paper was calculated using the frequency-domain model TEA-NL [Westerink, *et al.* 1988]. Boundary conditions in the form of elevation and phase of the M_2 tide were applied to the grid at the Delta, at the southernmost point of the South Bay, and at the ocean boundary. These boundary conditions were obtained from tidal analysis of USGS tide gages [Cheng and Gartner, 1984]; the oceanic boundary condition was obtained by extrapolating current meters near the Golden Gate to the ocean boundary using the inverse tidal method [Nuñez, 1990]. Calibration of the circulation was done by comparing the modeled elevation amplitude and phase with 34 USGS tide gages located throughout the Bay. A Manning friction coefficient of 0.02 gave the best comparison to the observations. The results of the comparison with USGS data (station locations shown in Figure 4.4) are shown in Figure 4.5. The comparisons at several stations throughout the Bay are certainly not as good as could be obtained if our goal were to calibrate the model to obtain the best possible simulation of the circulation; this would likely require substantial refinement of the numerical grid. However, our goal was to obtain a reasonable approximation to the circulation in San Francisco Bay, capturing the dominant features of the tidal variability for the purposes of our transport modeling.

Consistent with this approach, we restricted the frequencies included in the frequency-domain model to two: the M_2 and Z_0 . This allowed long ELAmet simulations (~45 days) to be made. Because ELAmet is based on Eulerian-Lagrangian methods, the advection portion of the process is solved by tracking backward in time along characteristics of the flow originating from each node [Baptista, 1987]. By including only these two frequencies, the tracking information in ELAmet could be done for one tidal cycle, and saved for the rest of the simulation. While the use of a single tidal constituent results in reduced tidal mixing, the trade-off in being able to do long simulations is a good one, as it allows us to run a computationally-intensive model long enough to see the partitioning between solid and aqueous phases approaching a steady-state value. The Z_0 component of the circulation is determined by a flux of $265 \text{ m}^3/\text{s}$ at the Delta outflow and $16 \text{ m}^3 \text{ s}^{-1}$ into the South Bay, which is representative of low-flow conditions. As explained below, only low-flow conditions could reasonably be considered with a depth-averaged model.

Table 4.2. Measured Rate Constants

K'	k_1	k_{-1}	k_2	κ_f	ref	c_p	adsorbent
Copper:							
1.14	2.5×10^{-3}	2.2×10^{-3}		2.5	4	1500.	riverine sediments
Cadmium:							
8.5×10^{-5}	3.5×10^{-6}	0.042		9.4×10^{-5}	1	100.	Narragansett Bay sediments
4.7×10^{-5}	2.0×10^{-6}	0.042		5.2×10^{-5}	1	100.	San Clemente Basin sediments
9.5×10^{-5}	1.2×10^{-4}	0.013	1.7×10^{-3}	3.2×10^{-3}	1	100.	MANOP site H sediments
Zinc:							
1.2×10^{-3}	1.6×10^{-5}	0.013		3.4×10^{-5}	1	100.	Narragansett Bay sediments
1.1×10^{-3}	2.8×10^{-5}	0.025		6.0×10^{-5}	1	100.	San Clemente Basin sediments
0.14	4.2×10^{-4}	2.9×10^{-3}	1.7×10^{-3}	8.9×10^{-4}	1	100.	MANOP site H sediments
3.6×10^{-3}	3.0×10^{-4}	0.083		6.4×10^{-4}	1	27.5	sediment trap
9.4×10^{-3}	3.9×10^{-4}	0.042		8.3×10^{-4}	1	100.	fecal pellets
0.045	2.0×10^{-3}	0.079	6.7×10^{-3}	4.3×10^{-3}	2	1.49	Puget Sound sediments
2.1	2.7×10^{-3}	1.3×10^{-3}		5.8×10^{-3}	3	1500.	riverine sediments

Units of K' are $l \text{ mg}^{-1}$; units of k_1 and κ_f are $l \text{ mg}^{-1} \text{ hr}^{-1}$; units of k_{-1} and k_2 are hr^{-1} ; units of c_p are mg l^{-1} .

¹ Nyfeller, et al. (1984).

² Jannasch, et al. (1988).

³ Glegg, et al. (1988); natural particles used in freshwater.

Mixing Characteristics

As ELAmet is a depth-averaged model, the most important parameter that determines the mixing characteristics of ELAmet is the dispersion parameter. Two means were used to calibrate ELAmet with regard to this parameter, resulting in the dispersion coefficient of $200 \text{ m}^2 \text{ s}^{-1}$ that has been used in the simulations presented. The first was to ensure

that resulting residence times are appropriate to the South Bay. The estimates of low-flow residence time in the South Bay reported by *Walters, et al.* [1985] is 160 days, although this is based on freshwater replacement time. In the South Bay where the freshwater inflow is very small, residence times based on these values are likely to be high, especially under high flow conditions when mixing with the Central Bay across the northern boundary may be important. Our estimate of residence time is based on a numerical experiment in which an initial uniform concentration of tracer was allowed to dissipate due to mixing and replacement with “clean” water from the freshwater inflow. The time to reduce the concentration in the central part of South Bay to 10% of its original concentration is approximately 160 days.

In addition, we used ELAmet in a conservative mode to simulate salinity for comparison with USGS salinity data [*Cheng and Gartner, 1984*]. This comparison was hampered by the fact that the time series of salinity do not generally overlap for large periods of time; consequently we were forced to choose time series for comparison which are not coincident, although all are representative of relatively low-flow conditions. Boundary conditions for the salinity simulations were 0 ppt salinity at the Delta, 35 ppt salinity at the ocean boundary, and 20 ppt at the inflow to South Bay. In Figure 4.6 we show the comparison of computed salinities (mean salinity and “M₂ amplitude”) with USGS data, at the station locations indicated in Figure 4.4. The “M₂ amplitude” of the USGS data was determined by a Fourier transform, not a tidal analysis for specific frequencies, and thus incorporates other semi-diurnal variability.

The use of a depth-averaged model quickly highlights the dominance of the delta-outflow on the mixing in the Bay, and in determining the salinity in the South Bay [*Conomos, 1979*]. Under high-flow conditions ($>1000 \text{ m}^3 \text{ s}^{-1}$), it was determined that, because the model does not contain the mixing induced by the greatly increased stratification in the northern reach, the flux of fresh water into the southern reach from the Delta was far greater than it should be. This could only be counter-acted with the use of an unacceptably large dispersion coefficient, on the order of $1000 \text{ m}^2 \text{ s}^{-1}$. Therefore, we concluded that a 2-D model is inadequate for the simulation of high-flow conditions, and restricted our ELAmet simulations to low-flow conditions.

Chemical Equations

The mass action and rate equations used in the ELAmet simulations are summarized in Table 4.4. There is an incentive to keep the problem as small as possible, as the savings in computer run-time are significant. Therefore, preliminary simulations were done on a smaller, one-dimensional grid. The upstream "riverine" boundary conditions and the downstream "oceanic" boundary conditions of this grid were defined so as to encompass the range of environmental conditions in the larger San Francisco Bay simulations. From these preliminary runs only species contributing more than 1 percent to the total mass of the metal were retained for the SFB simulations. Table 4.3 summarizes the larger speciation which was taken into account for the preliminary simulations.

Table 4.3. Preliminary Speciation

Copper Species:	Cu^{2+} , $\text{Cu}_{(s)}$, CuSO_4 , CuHCO_3^+ , CuCO_3 , CuOH^+ , $\text{Cu}(\text{OH})_2$, CuHu
Cadmium Species:	Cd^{2+} , $\text{Cd}_{(s)}$, CdCl^+ , CdCl_2 , CdCl_3^- , CdSO_4 , CdHCO_3^+ , CdHu
Zinc Species:	Zn^{2+} , $\text{Zn}_{(s)}$, ZnCl^+ , ZnCl_2 , ZnCl_3^- , ZnCl_4^{2-} , ZnSO_4 , ZnCO_3 , ZnHCO_3^+ , ZnOH^+ , ZnHu

Conditional constants obtained at high ionic strength were used whenever possible; however, in the cases that activity corrections were required, they were made to an ionic strength of 0.7M using the Davies equation. The use of the Davies equation outside of its range of validity, which is up to 0.5M (about 25 ppt salinity) is a concern, but there is no satisfactory alternative and the errors introduced into the constants are probably not larger than the uncertainties in the constants themselves. A larger problem is the use of a single thermodynamic constant for a system in which the salinity covers the entire range from fresh- to seawater. In this case, we can justify the use of a single constant because we are only interested in results in the South Bay, where variations in salinity are limited to the range of about 25 to 35 ppt salinity. However, future applications of ELAmet will need to resolve this issue and incorporate variable coefficients, probably by using an extended form of the Debye-Hückel equation in conjunction with a database of parameters specific to each of the ions in the system [Truesdell and Jones, 1974].

Table 4.4. Model Transformation Equations

Mass Action Equation	K	Ref	
$[CuCO_3] = K [Cu^{2+}] [CO_3^{2-}]$	$10^{5.75} M^{-1}$	3	
$[CuHu] = K [Cu^{2+}] [Hu]$	$10^{9.22} M^{-1}$	2	
$[CdCl^+] = K [Cd^{2+}] [Cl^-]$	$10^{1.35} M^{-1}$	4	
$[CdCl_2] = K [Cd^{2+}] [Cl^-]^2$	$10^{1.7} M^{-2}$	4	
$[CdCl_3] = K [Cd^{2+}] [Cl^-]^3$	$10^{1.5} M^{-3}$	4	
$[CdSO_4] = K [Cd^{2+}] [SO_4^{2-}]$	$10^{1.3} M^{-1}$	1	
$[ZnCl^+] = K [Zn^{2+}] [Cl^-]$	$10^{0.11} M^{-1}$	4	
$[ZnSO_4] = K [Zn^{2+}] [SO_4^{2-}]$	$10^{1.3} M^{-1}$	1	
$[ZnHu] = K [Zn^{2+}] [Hu]$	$10^{4.8} M^{-1}$	2	
$[CO_3^{2-}] = K [OH^-]^2$	$10^{7.7} M^{-1}$	5	
$[HCO_3^-] = K [OH^-]$	$10^{2.97}$	5	
Rate Equation	κ_f	κ_b	Ref
$[Cu_{(s)}]_t = \kappa_f [Cu^{2+}] [TSS] - \kappa_b [Cu_{(s)}]$	$10^{0.28} \text{ l mg}^{-1} \text{ hr}^{-1}$	$10^{-1.4} \text{ hr}^{-1}$	6
$[Cd_{(s)}]_t = \kappa_f [Cd^{2+}] [TSS] - \kappa_b [Cd_{(s)}]$	$10^{-4.3} \text{ l mg}^{-1} \text{ hr}^{-1}$	$10^{-1.4} \text{ hr}^{-1}$	7
$[Zn_{(s)}]_t = \kappa_f [Zn^{2+}] [TSS] - \kappa_b [Zn_{(s)}]$	$10^{-4.2} \text{ l mg}^{-1} \text{ hr}^{-1}$	$10^{-1.6} \text{ hr}^{-1}$	7

¹ Zirino and Yamamoto (1972), as reported in Mantoura, et al. (1978), corrected to an ionic strength of $I=0.7M$ using the Davies equation.

² Mantoura, et al. (1978), uncomplexed metal ion activity coefficient calculated using the Davies equation.

³ Sunda and Hanson (1979), corrected to an ionic strength of $I=0.7M$, activity coefficients calculated using the Davies equation.

⁴ Smith and Martell (1976), conditional constant measured at an ionic strength of $I=1.0M$.

⁵ Stumm and Morgan (1981), Tables 4.7-4.9, seawater at 19ppt chlorinity and $20^\circ C$.

⁶ Oakley, et al. (1981), see text.

⁷ Nyfeller, et al. (1984).

It is difficult to obtain reasonable estimates of rate constants for use in simulating the rate-controlled metal adsorption, as they are limited and the measured values that are available, like the distribution coefficient data, show a great deal of variability. A summary of measured values, concentrating on experiments done in seawater, is given in Table 4.2. The forward and backward rate constants are denoted k_1 and k_{-1} , respectively. In some cases a better fit to the data was found by postulating two reactions in sequence; in these cases a forward constant for the second reaction, denoted k_2 , is supplied. The column labeled κ_f contains the forward rate constant k_1 corrected for adsorbate speciation. The use of measured constants in ELAmet required a “correction” to the forward rate constant because in laboratory experiments the rate constants k_1 and k_{-1} are measured with respect to total dissolved and total solid-phase concentration. However, at the high salinities of these experiments it is unlikely that the primary adsorbing species, presumably the uncomplexed metal ion, dominates the aqueous speciation. When simulating adsorption in ELAmet, if aqueous speciation is included, the sorbing species must be specified, and the forward rate constant must be adjusted accordingly. This can be demonstrated with a simple problem to which there is an analytical solution.

Suppose a system consists of total dissolved-phase metal $c_{(d)}$, total solid-phase metal $c_{(s)}$, and suspended particle concentration c_p , and is governed by the equations:

$$\frac{d}{dt} \left(\frac{c_{(s)}}{c_p} \right) = k_1 c_{(d)} - k_{-1} \frac{c_{(s)}}{c_p} \quad , \quad (4.1)$$

$$c_T = c_{(s)} + c_{(d)} \quad .$$

Under the conditions of zero initial conditions of solid-associated metal and constant particle concentration, the analytical solution is

$$c_{(s)} = \frac{k_1 c_p c_T}{k_1 S + k_{-1}} (1 - e^{-(k_1 c_p + k_{-1})t}) \quad . \quad (4.2)$$

At equilibrium, the distribution coefficient is given by:

$$K_d^e = \frac{c_{(s)}}{c_{(d)} c_p} = \frac{k_1}{k_{-1}} \quad . \quad (4.3)$$

If the concentration in the dissolved phase at equilibrium is given by $c_{(d)}^e$, then at any time t

$$\frac{c_{(d)} - c_{(d)}^e}{c_T - c_{(d)}^e} = e^{-(k_1 c_p + k_{-1})t}, \quad (4.4)$$

and a plot of $\ln\{c_{(d)} - c_{(d)}^e / c_T - c_{(d)}^e\}$ against time has a slope equal to the inverse time scale of the reaction, $\{k_1 c_p + k_{-1}\}$. If we now suppose that the total dissolved phase can be broken up into the sorbing dissolved phase, $c'_{(d)}$, and the remaining aqueous concentration, $c''_{(d)}$, then the governing equations become

$$\frac{d}{dt} \left(\frac{c_{(s)}}{c_p} \right) = \kappa_f c'_{(d)} - \kappa_b \frac{c_{(s)}}{c_p}, \quad (4.5)$$

$$c_T = c_{(s)} + c'_{(d)} + c''_{(d)}.$$

Under the assumption that the ratio $c'_{(d)} / c_{(d)}$ remains constant (probably a good assumption for a batch experiment) and equal to α , the analytical solution is

$$c_{(s)} = \frac{\kappa_f c_p \alpha c_T}{\kappa_f c_p \alpha + \kappa_b} (1 - e^{-(\kappa_f \alpha c_p + \kappa_b)t}), \quad (4.6)$$

so that the plot of $\ln\{c_{(d)} - c_{(d)}^e / c_T - c_{(d)}^e\}$ against time has a slope equal to $\{\kappa_f \alpha c_p + \kappa_b\}$. Equating the time scales in these two cases shows that the appropriate forward constant to use is $\kappa_f = k_1 / \alpha$, while the backward constant needs no modification (i.e. $\kappa_b = k_{-1}$).

It is impossible to know the correct value of α to apply to a given laboratory experiment, since detailed information on the aqueous speciation is not known. However, the accuracy of α is certainly not a greater limiting factor than the uncertainty in the estimates of the constants themselves, based on the variability seen in the measured data. Based on our simulations, we used estimates of $\alpha=0.47$, 0.038 for zinc and cadmium, respectively, and these compare favorably with, for example, the graphical data of *Mantoura, et al.* [1978] at high salinities. It is more difficult to get a good estimate of α for copper, since the speciation of copper is more dependent on the amount and composition of organic ligand in solution than on salinity. We used a value of $\alpha=10^{-3}$ for copper, which is approximately the value estimated by *Van Den Berg and Kramer* [1979] at pH 8 for Lake Ontario water. It is at the high end of the range in values ($\sim 10^{-3}$ to 10^{-6}) found by *van den Berg* [1984], but it is substantially higher than the average value of $\sim 10^{-7}$ found by *van den Berg, et al.* [1987], demonstrating the difficulty in accurately defining α values. It should

be noted that while we have assumed that the uncomplexed metal ion is the primary adsorbing species, there is no direct evidence of this. Indirect evidence is provided by the fact that increasing the available aqueous ligands, either inorganic in the case of zinc and cadmium, or organic in the case of copper, tends to decrease the partitioning to the solid phase [Comans and van Dijk, 1988; Gonzalez-Davila, et al., 1990; Li, et al., 1984; Laxen, 1985].

We chose to use the rate constants of Nyfeller, et al. [1984], obtained using San Clemente Basin surface sediments as an adsorbent, for cadmium and zinc. This choice is somewhat arbitrary, but it provides a necessary starting point for our modeling work and our conclusions can be evaluated in light of the uncertainties of these constants. The only rate information for copper [Glegg, et al., 1988] was judged to be inadequate as it employed very high particle concentrations and freshwater. Therefore, for copper we used the equilibrium information obtained from Oakley, et al. [1981] for bentonite clay. We then assumed that the backward rate constant was equal to that of cadmium, based on the fact that backward rate constants of many metals have been shown to vary by relatively little [Honeyman and Santschi, 1988; Jannasch, et al., 1988]. The forward rate constant for copper was then calculated accordingly.

Source Scenarios

Two different source scenarios were used in modeling the metals: a “POTW” scenario, and a “benthic” scenario. The POTW scenario is based on the minimum daily loads from the six largest Publicly Owned Treatment Works that release effluent directly into the Bay, as given in Tables 9, 11 and 13 of Gunther, et al. [1987]. The location of the sources that are within South Bay are shown in Figure 4.7. In addition to these, there is a POTW located in Suisun Bay with a flux of 2.66, 0.65, and 6.6 kg d⁻¹ for copper, cadmium, and zinc, respectively; however, we found that this source contributed relatively little to the levels in South Bay. The result of all of the POTW sources is a total average loading of 29.25 kg d⁻¹, 3.98 kg d⁻¹, and 88.5 kg d⁻¹ for copper, cadmium and zinc, respectively. The total loading of each metal is distributed between the particulate and dissolved phases such that the ratio of particulate metal to total metal, denoted $c_{(s)}^0/c_T^0$, is either 0.1 or 0.2.

A benthic source scenario has been included in order to compare the POTW scenario with a more distributed source, and also to determine the fluxes that would be

required if benthic fluxes were the primary source of metal to the water column. There is some evidence that benthic fluxes play an important role in South Bay. Benthic sources of cadmium and zinc, although not for copper, were inferred by *Flegal, et al.* [1991], based on the correlation between elevated levels of these metals in South Bay with elevated levels of silica. Fluxes for the benthic scenario were determined through numerical experimentation, as there have been no measurements of benthic metal fluxes in South Bay. However, *Hammond, et al.* [1985] measured benthic fluxes of nutrients and silica at a shoal and a channel station. Under the assumption that the primary source of metal to the South Bay was benthic, and that the benthic fluxes in areas deeper and shallower than 10 m were in the same ratio as the benthic fluxes of silicate from the channel and shoal station as measured by *Hammond, et al.* [1985], we found that fluxes of 318, 9, and 298 kg d⁻¹ for copper, cadmium, and zinc, respectively, resulted in water column concentrations of total metal comparable to those measured during 1989 [*Flegal, et al.*, 1990]. As with the POTW loadings, the total benthic loadings are distributed between the particulate and dissolved phases in the ratio $c_{(s)}^0/c_T^0 = 0.1$ or 0.2. The fluxes from the two source scenarios are summarized in Table 4.5.

The numerical experiments were run for about 43 days, starting from initial conditions of zero metal concentration. The length of the simulations was chosen to be long enough for the partitioning in the system to approach a steady-state. Concentration profiles of total metal under the POTW scenario are shown in Figure 4.8, Figure 4.9, and Figure 4.10, which are discussed further below. These concentrations are likely to be an upper limit for POTW discharges into the South Bay, as no removal mechanisms within the Bay itself have been considered. A portion of the metal input due to the POTWs is almost certainly removed from the water column within the South Bay itself, presumably through the settling of particulates, and probably in close proximity to the various outfalls. This has been deduced from the patchiness of sediment concentrations of various metals [*Luoma and Phillips, 1988*], and from the fact that localized enrichments in sediments and bivalves that have been associated with nearby discharges [*Thomson, et al. 1984*]. An additional limitation on our characterization of the POTW scenario is that point source discharges, while probably the most consistent source of trace metals to the Bay, are not constant over a 45-day period, and vary on a weekly and monthly basis [*Davis, et al. 1991*].

Concentration profiles of total metal under the benthic scenario are shown in Figure 4.16, Figure 4.17, and Figure 4.18 below. The benthic fluxes required to bring the water column to observed concentrations over a 45-day period are larger than the POTW fluxes estimated under the “minimum” loading scenario. On a yearly basis, our benthic fluxes (116×10^3 , 3.3×10^3 , and 108×10^3 kg yr⁻¹ for copper, cadmium and zinc, respectively) are greater than the upper range of anthropogenic inputs to the South Bay from point source discharges estimated by *Davis, et al.* [1991] (17×10^3 , 2.2×10^3 , and 36×10^3 kg yr⁻¹, for copper, cadmium and zinc, respectively). This contrasts with *Smith and Flegal* [1993], who made estimates of benthic fluxes of silver in the South Bay that amounted to approximately 10% of the anthropogenic input. These authors also estimated that benthic fluxes could replace all of the dissolved silver in the water column in about 22 days. In contrast, our benthic fluxes take 45 days to reach the total concentration levels shown in Figure 4.16, Figure 4.17, and Figure 4.18. The differences are explained in part by the fact that *Smith and Flegal* [1993] considered only dissolved silver and we are using total copper, cadmium, and zinc. A large increase in the population of *Potamocorbula amurensis* starting in 1986, with concomitant changes (presumably increases) in the fluxes of particulate and dissolved metal, is another complicating factor, the effects of which are not well-understood. Even so, the benthic fluxes that we are using are probably an upper limit. Under normal conditions point source discharges and several other sources, most notably urban and nonurban runoff, should be contributing to the levels of total metal in the water column [*Gunther, et al.*, 1987].

Table 4.5. Summary of Metal Sources

	copper	cadmium	zinc
channel benthic ($\mu\text{mol m}^{-2} \text{d}^{-1}$)	9	0.14	8.2
shallow benthic ($\mu\text{mol m}^{-2} \text{d}^{-1}$)	12	0.19	11
cumulative benthic (kg d ⁻¹)	318	9.1	298
cumulative point (kg d ⁻¹)	29.25	3.98	88.5

Suspended Solids

The source of suspended solids to the model is a benthic flux at an average rate of $0.8 \text{ g m}^{-2} \text{ day}^{-1}$, which when integrated over the entire embayment yields a total of 345×10^3 kg/day. This magnitude was determined by adjusting the fluxes such that a rea-

sonable concentration of suspended solids was obtained over the course of the 43-day simulations, as seen in Figure 4.15. If this flux is used as a daily average to compute the annual contribution of the substrate to the total sediment budget of South Bay, the resultant 0.13×10^6 metric tons per year compares favorably with the 0.2×10^6 metric tons per year estimated by *Conomos, et al.* [1979].

Conomos, et al. [1979] estimated an additional 0.5×10^6 metric tons per year into South Bay due to riverine input, and 78.3 metric tons per day ($\sim 0.03 \times 10^6$ metric tons per year) of suspended solids due to waste-water treatment loadings. Our POTW source scenario contributes an additional 13 metric tons per day of suspended solids, but this contribution is small in comparison to the benthic contribution. Under the low-flow conditions of the model, adding a significant contribution due to riverine sources results in unrealistically high suspended solids concentration in the water column, so we have not included this source.

Aqueous Ligands

As can be inferred from the chemical equations used in the model experiments, the aqueous ligands of concern are the major seawater ions Cl^- and SO_4^{2-} , the carbonate ion, and dissolved humic material. The concentration of major seawater ions was specified at the ocean boundary as the concentration in seawater at 35 ppt [*Brewer, 1975*], and at the delta as the concentration in average river water, as defined in *Livingstone* [1963]. Alkalinity boundary conditions were used to model the carbonate ion concentration. Freshwater alkalinity at the Delta was specified as 10^{-3} M, corresponding to average river water [*Livingstone, 1963*], and at the ocean boundary alkalinity was specified as 2.4×10^{-3} M, corresponding to seawater at 35 ppt [*Brewer, 1975*]. The inflow to the South Bay was estimated at an alkalinity of 1.8×10^{-3} M, reflecting the same mix of fresh and salt water values as the salinity. These boundary conditions ignore the significant alkalinity inputs from waste-water treatment plants [*Conomos, et al., 1979; Spiker and Schemel, 1979*]; while this is believed to be unimportant for our purposes, it will be important in the case that a closer scrutiny of the carbon cycle in the Bay is desired. Concentration of dissolved organic ligand (denoted Hu) was determined by boundary conditions of zero at the ocean boundary and Delta, and 4.4 mg C l^{-1} at the inflow to the South Bay. The concentration of Hu was converted to an available site concentration using 10^{-6} mol per mg dissolved C [*McKnight, et al. 1983; Cabaniss and Shuman, 1988; Davis, 1984*]. These boundary con-

ditions result in a tidally-averaged concentration which varies smoothly from $\sim 2.5 \text{ mg C l}^{-1}$ ($2.5 \text{ }\mu\text{M}$ of dissolved organic ligand) at Dumbarton Bridge to $\sim 1 \text{ mg C l}^{-1}$ ($1 \text{ }\mu\text{M}$ of dissolved organic ligand) at the north end of South Bay, and is negatively correlated with salinity. Therefore, while the boundary conditions do not realistically portray the sources and sinks of dissolved organic carbon in the Bay, they result in reasonable water column concentrations, and a negative correlation of H_u with salinity such as observed by *Kuwabara, et al.* [1989], which was sufficient for our purposes. As with alkalinity, these boundary conditions will need to be modified in future studies which seek to describe the carbon cycle in the Bay more accurately.

Experimental Results

The results of the numerical experiments were strongly dependent on three factors: the source scenario for metal input, the mass ratio of particulate to dissolved metal in the source, and the concentration of total suspended solids. The designations for the runs discussed and their characteristics are compiled in Table 4.6. All runs start from zero initial metal concentration. Under “variable” suspended solids conditions, initial conditions are also zero for suspended solids; particles are added to the water column through a benthic source as described above. Under “constant” suspended solids conditions, initial concentrations of suspended particles are 10 mg l^{-1} everywhere, and this concentration is maintained throughout the numerical simulation. The source ratio of mass associated with the particulate phase to total mass was held constant at either 10% or 20%; this quantity is designated by $c_{(s)}^0 / c_T^0$ in the table. The simulations were sampled at 5, 9, 18, 26, 35, and 44 days along the 19-station transect shown in Figure 4.4. The quantities plotted are averages over the tidal cycle, unless otherwise noted.

The results of a single experiment show some marked differences in the partitioning behavior of the three metals. In Figure 4.8, Figure 4.9, and Figure 4.10 we show for copper, cadmium, and zinc transects of the total metal concentration, the percentage in the solid phase, and the apparent distribution coefficient, for experiment P4. The apparent distribution coefficient K_d^a is the sampled value of $c_{(s)} / (c_{(d)} c_p)$. The total concentration profiles for all three metals is similar, reflecting the location of the POTWs. In terms of partitioning, however, cadmium and zinc behave similarly, while copper is quite distinct. The most important reason for this can be seen in Figure 4.11, where we plot the values of

$\alpha = c^{2+}/c_{(d)}$, where c^{2+} is the concentration of the uncomplexed divalent metal ion, for the three metals. Because of the high concentration of dissolved organic ligand (ranging from about 2.5 mg C l⁻¹ at station 1 to 1 mg C l⁻¹ at station 19), most of the copper is held in the dissolved phase and is unavailable for adsorption. Cadmium and zinc also undergo significant aqueous complexation, but the α values associated with these two metals are greater than that associated with copper by two and three orders of magnitude, respectively. As a result, copper enters the water column very close to equilibrium, whereas cadmium and zinc enter the water column quite far from equilibrium, and undergo subsequent desorption as the simulation progresses. The profile of K_d^a for the three metals mirrors that of the percentage of mass in the solid phase, $c_{(s)}/c_T$, which follows from the definition of K_d^a and the condition that c_p is held constant. In the case of cadmium and zinc, the shape of this profile is determined primarily by the location of the “point” sources associated with the POTW scenario. A higher percentage of solid phase indicates closer proximity to a source, and therefore a higher percentage of “new” material. As the simulation progresses and the water column concentration becomes dominated by “old” material, the profile of K_d^a tends to flatten out, while at the same time the mean value over the transect decreases as the desorption proceeds. In contrast, the profile of K_d^a for copper shows some adsorption taking place, but in general very little change over the course of the simulation. The profile of $c_{(s)}/c_T$ and K_d^a both show a distinct upward trend northward in the Bay. This reflects the controlling influence of the speciation, with more copper being held in the dissolved phase at the southern end of the Bay.

Table 4.6. Model Runs

Run Code	Source Scenario	Suspended Solids	$c_{(s)}^0/c_T^0$
P1	POTW	variable	0.1
P3	POTW	variable	0.2
P4	POTW	constant	0.2
B1	benthic	variable	0.1
B3	benthic	variable	0.2
B4	benthic	constant	0.2

In the absence of kinetically-controlled adsorption, the profile of the equilibrium distribution coefficient, K_d^e , reflects the aqueous speciation of all three metals to varying

degrees. In Figure 4.12 we show the profiles of K_d^e for all three metals from an ELAmet simulation in which adsorption was assumed to reach thermodynamic equilibrium instantaneously, with $K_d^e = \kappa_f \alpha / \kappa_b$. These profiles mirror the behavior of α in Figure 4.11. Copper, with the lowest overall α values, shows the greatest range in K_d^e , increasing by more than 100% from south to north over the transect. The distribution coefficient increases northward in the basin, as the concentration of dissolved organic ligands decreases. Cadmium has a speciation controlled by the major seawater ions; consequently its distribution coefficient decreases northward in the basin, although the total range in K_d^e is much less than for copper, decreasing by only about 20% from station 1 to 19. The distribution coefficient of zinc reflects aqueous complexation by both dissolved organic ligands and major seawater ions, but for practical purposes it is constant.

In experiment P4, which uses a constant suspended solids concentration, the dominant influence on the partitioning of copper is the aqueous speciation, and the dominant influence on the partitioning of cadmium and zinc is the percentage of material in the solid phase. A comparison of experiment P4 with an experiment using “variable” suspended solids (P3) illustrates the influence of a variable suspended solids concentration on the profile of K_d^a . In Figure 4.13 and Figure 4.14 we show the results, in terms of $c_{(s)}/c_T$ and K_d^a , for experiment P3. The profiles of total concentration are the same as in experiment P4. Cadmium is not included because, as in experiment P4, its behavior mimics that of zinc. In Figure 4.15 we show the evolution of the concentration of suspended solids, c_p , in time. In this case, the apparent distribution coefficient starts out at a higher value, as the concentration of suspended solids is lower than the 10 mg l^{-1} used in experiment P4. The partitioning decreases through time due to both desorption and the increasing concentration of suspended solids. The profile of K_d^a now reflects the influence of both $c_{(s)}/c_T$ and the variation in c_p from higher to lower values south to north in the Bay. The increase in $c_{(s)}/c_T$ for copper reflects a progressive adsorption of metal as the overall concentration of suspended solids increases with time.

The results from experiment B4, employing the benthic source scenario and constant suspended solids, are shown in Figure 4.16, Figure 4.17, and Figure 4.18, and are compared with results for copper and zinc for variable suspended solids (experiment B3) in Figure 4.19 and Figure 4.20. The interpretation of these plots is analogous to that discussed above for the POTW experiments. The primary difference is that the benthic sce-

nario is a much more distributed source, so that the ratio of “new” to “old” mass over the length of the Bay remains relatively constant as compared to the POTW scenario. This is reflected in the flatter profiles of $c_{(s)}/c_T$ and K_d^a .

In these simulations, in which there is no monthly or seasonal variation in sources or salinity, the salinity increases monotonically from north to south in the South Bay, and the suspended solids concentration (in the case of variable concentration), decreases monotonically with salinity. It follows that K_d^a will, in general, show an increase with salinity, and a corresponding decrease with suspended solids. This can be seen in Figure 4.21, Figure 4.22, and Figure 4.23, where we plot K_d^a against salinity, and in Figure 4.24, Figure 4.25, and Figure 4.26, where we plot K_d^a against the concentration of suspended solids. These scatterplots were made by sampling each station in the transect 12 times over the tidal cycle, so that the points encompass the variability due to the tides. The greatest change in K_d^a over the transect is found in experiments which use variable suspended solids concentration. In experiments P1, P3 and B3, the relatively lower concentration of suspended solids at the north end of South Bay, coupled with a rate-controlled desorption process, results in a strong increase in K_d^a with salinity, and with decreasing suspended solids concentration.

As a measure of how the distance from equilibrium varies with time for each of the metals, we have plotted K_d^a/K_d^e against sampling time for each metal in Figure 4.27, Figure 4.28, and Figure 4.29. The symbol represents the tidally-averaged value at station 10 (mid-transect), and the bars around the symbol indicate the highest and lowest values that were sampled across the entire transect over the tidal cycle (thus the bars represent a particular sampled value, not an average). The distance from equilibrium was calculated as:

$$\frac{K_d^a}{K_d^e} = K_d^a \left\{ \frac{\kappa_f}{\kappa_b} \alpha \right\}^{-1} \quad (4.7)$$

These figures indicate that the basin as a whole approaches a steady-state, in terms of the partitioning, with a time scale on the order of 25 days. The variation in K_d^a/K_d^e across the transect is greatest when the basin as a whole is farthest from equilibrium; as the entire basin approaches a steady-state, the mean value of apparent distribution coefficient across the entire basin is much closer to the equilibrium value, and the variation around that mean is greatly reduced as well. This is true for all of the experiments,

although the POTW scenario produces greater basin-scale variability than the benthic scenario, and the variable suspended solids concentration enhances variability as compared to the constant suspended solids concentration.

Conclusions

The numerical results indicate that adsorption kinetics can be responsible for the basin-scale variability in the observed partitioning in South Bay. If the adjustment to equilibrium between the solid and aqueous phase were instantaneous, neither the location of the sources nor the concentration of suspended solids would have any effect on the observed values of the distribution coefficient. This would leave aqueous speciation as the primary factor determining the dependency of partitioning on salinity, or more likely in the case of copper, on the concentration of dissolved organic ligands. Therefore, two of the three factors that we found to control the basin-scale variability of K_d^a are dependent on kinetically-controlled adsorption.

In addition, the numerical results indicate that the further the basin as a whole is from equilibrium, the greater is the basin-scale variability in K_d^a . This may be a key to understanding the difference between the 1985 and 1989 field data presented in the introduction. Extrapolating our results to the observations would suggest that the higher mean K_d^a values and the stronger intra-cruise variability in K_d^a during 1989 is indicative of a basin that is on the whole much farther from an equilibrium state than was the South Bay during 1985.

Based on our results, we would also conclude that the factors controlling the dependence of K_d^a on salinity and suspended solids concentration would be different between the two years. In Figure 4.30 and Figure 4.31 we present an analysis of the dependence of K_d^a on salinity and c_p on a cruise-by-cruise basis for the two observational years. There are not enough data during any individual cruise to do rigorous statistical analyses (8 stations during 1989 and 4 during 1985 if all provided good data, otherwise less), but we have instead subjectively evaluated data from each cruise for salinity and c_p dependence. No definitive conclusions can be made from this figure in light of the sparsity of data points; however, it does provide a few interesting comparisons. First, the 1989 data are more likely to exhibit a positive correlation with salinity and a negative correlation

with suspended solids than the 1985 data, which are more likely to exhibit the opposite correlation with each variable. To the extent that a negative correlation with salinity indicates a control of K_d^a by speciation (due to aqueous complexation by major seawater ions), the correlations with salinity are consistent with the hypothesis that the 1985 data are close to an equilibrium state, while the 1989 data are not. In addition, the negative correlations with suspended solids during 1989 are consistent with the result that the same $c_{(s)}/c_T$ ratio, in a system far from equilibrium, will result in a partitioning coefficient that decreases as c_p decreases.

Additional evidence of the difference between 1985 and 1989 data is found in Figure 4.32 and Figure 4.33, in the form of plots of the concentration of suspended solids against the percent mass in the solid phase, $c_{(s)}/c_T$. The data during 1985 show a nearly linear relationship between the two variables for each of the metals, whereas during 1989 the relationship is much more complex. A linear relationship is consistent with a system in which there is a relatively localized source of particulates and associated metal, in equilibrium with the surrounding water column. As these particulates are diluted, and if they remain in equilibrium with the surrounding water column, the ratio $c_{(s)}/c_T$ will decrease proportionately. The plot of the 1989 data does not lend itself to any clear-cut interpretation; however, it seems likely that the source of particulate metal in this case is not localized. It is also noteworthy that the $c_{(s)}/c_T$ values during 1989 are generally much higher than during 1985, reaching values as high as 0.3, 0.7, and 0.9 for copper, cadmium, and zinc, respectively. This indicates a source of these metals during 1989 characterized by a much higher percentage of mass in the solid phase, as compared to 1985. A strong, sustained source with a high percentage of particulate metal could lead to observed K_d^a 's well above equilibrium values.

The overwhelming environmental factor differentiating the two data years is that 1985 was merely a below-average flow year, whereas 1989 was the third consecutive year of drought conditions in California [Palmer, *et al.* 1990; Anderson, *et al.* 1987]. Drought conditions greatly increase the flushing time in the South Bay, both because of the decreased freshwater inflow, and because stratification-induced mixing with Central Bay water is greatly reduced. This could account for the fact that total concentrations of zinc and copper are higher during 1989 than during 1985 (the reverse, however, is true of cadmium), but flushing time alone does not explain why the basin would experience a strong

influx of particulate metal during a drought year. In fact, this is somewhat counter-intuitive, as the influx of particulate metal due to non-point sources, particularly urban and nonurban runoff, should be greatly reduced during a drought. In addition, increased flushing time should increase the ratio of “old” to “new” metal in the water column, thus bringing the system as a whole closer to equilibrium. We have no definitive explanation for an increased influx of particulate metal in 1989 as compared to 1985. One possibility, however, is that upstream reservoirs controlling the flow can greatly reduce the receiving water for POTW discharges into Coyote Creek. This would presumably reduce the repartitioning of metals prior to release to the South Bay water column, resulting in a relatively higher percentage of metal in the solid phase.

Final Remarks

In the process of designing the numerical experiments and incorporating laboratory data into our model equations, we have encountered many limitations in the available information about trace metal partitioning under environmental conditions relevant to South Bay. A large caveat underlying all of this work is the choice of thermodynamic rate and equilibrium constants that may or may not be representative of the San Francisco Bay water column. If reaction time scales are much shorter than has been assumed, then the controlling effect of adsorption kinetics will be reduced accordingly. At equilibrium, our rate constants dictate an equilibrium partitioning of about 10^{-2} , 10^{-5} , and 10^{-3} , for copper, cadmium and zinc, respectively. If these values are very far off, and particularly if they are several orders of magnitude on the low side, then our conclusions about the state of the South Bay in 1985 and 1989 relative to equilibrium are faulty.

The equilibrium constants used in calculating the aqueous speciation are also subject to a great deal of error, with the constants for inorganic complexes being somewhat more reliable than those for organic complexes. The speciation of copper, in particular, is highly dependent on the concentration of dissolved organic ligand and the stability constant for the humate complexes. *Van den Berg, et al.* [1987], working in the Sheldt estuary, estimated log K' values between 11.8 and 14.0 for a single site model, or between 13.0 and 14.9 for a strong complexing site and between 11.5 and 12.8 for a weaker complexing site when a two-site model was used. These values are substantially higher than the value of log K' =9.2 used in our model simulations, although the effect of using a lower log K' is

ameliorated somewhat by the fact that our ligand concentrations are greater than those of *van den Berg, et al.* [1987] by 1-2 orders of magnitude. The more recent results of *Donat, et al.* [1993] using samples taken from South San Francisco Bay, however, indicate that the log K' value used in our simulations is appropriate to the weaker of two copper-complexing sites, while the stronger site had a log $K' > 13.5$. The weaker site, however, accounted for the larger fraction of dissolved copper (52-65%), as opposed to about 27% for the stronger site. In addition, however, these authors found that the conversion from dissolved organic carbon to concentration of surface sites should be closer to 10^{-8} M sites per mg C than the 10^{-6} that we have used. The net effect is that organically-complexed copper accounts for 92-98% (accounting for spatial and temporal variations in Hu) of the total dissolved copper in our simulations, as opposed to 80-92% found by *Donat, et al.* [1993]. This would, presumably, make more copper available for adsorption and change the position of our source inputs relative to equilibrium, although it is unlikely that this particular change in constants would result in a qualitative modification of our conclusions. Nonetheless, this example serves to illustrate the uncertainty inherent in many of the constants used in the model.

In this work we have not addressed possible sources of variability in K_d^a other than adsorption kinetics, and probably the most notable of these is the amount of variation in the nature of the suspended particles themselves. A very important piece of missing information is some understanding of how the composition of the suspended solids, and consequent adsorption properties, is likely to vary both spatially and temporally. While there is some evidence that the variability in the inorganic composition is not great, the organic composition may vary a great deal, especially with changes in POC brought on by algal blooms. The fact that the estuarine water column integrates so many temporal and spatial scales would suggest that particle variability should be concentrated at large spatial scales and low temporal frequencies; however, observational evidence to confirm or deny this does not currently exist. Field and laboratory work that provide values of rate constants under in situ conditions, as well as some measure of how those values are likely to vary in time and space, is clearly of utmost importance to future modeling studies and to an increased understanding of the cycling of trace metals in the Bay.

Diagnostic modeling has proven to be a useful tool in investigating the role of adsorption kinetics in South Bay, allowing us to visualize how the variability in measured values of K_d^a can be controlled by rate-controlled adsorption. Without a numerical model

it is difficult to make a connection between laboratory results and measurements made in the field, as the natural processes in estuaries are very complex, and the resulting interactions often lead to non-intuitive results. Long-term approaches to understanding environmental processes may well benefit from the synergism in using numerical experimentation in conjunction with field work and laboratory experimentation.

References

- Anderson, S., K.L. Markham, W. F. Shelton, L. F. Trujillo, and D. A. Grillo, 1987: Water Resources Data, California, Water Year 1985, *U.S. Geological Survey Water-Data Report CA-85-2*, vol. 2, 352 pp.
- Balistreri, L. S. and J. W. Murray, 1983: Metal-solid interactions in the marine environment: estimating apparent equilibrium binding constants, *Geochimica et Cosmochimica Acta*, vol. 47, pp. 1091-1098.
- Balistreri, L. S. and J. W. Murray, 1984: Marine scavenging: Trace metal adsorption by interfacial sediment from MANOP site H, *Geochimica et Cosmochimica Acta*, vol. 48, pp. 921-929.
- Baptista, A.M., Solution of advection-dominated transport by Eulerian-Lagrangian methods using the backwards method of characteristics, Ph.D. Dissertation, Massachusetts Institute of Technology, Cambridge, Mass, 1987.
- Brewer, P. G., 1975: in *Chemical Oceanography*, vol. 1, J. P. Riley and G. Skirrow, Eds., Academic, New York.
- Cabaniss, S. E. and M. S. Shuman, 1988: Copper binding by dissolved organic matter: I. Suwannee River fulvic acid equilibria, *Geochimica et Cosmochimica Acta*, vol. 52, pp. 185-193.
- Cheng, R. T. and J. W. Gartner, 1984: Tides, tidal and residual currents in San Francisco Bay California- results of measurements, 1979-1980, *U.S. Geological Survey Water Resources Investigations Report 84-4339*.
- Comans, R. N. J. and C. P. J. van Dijk, 1988: Role of complexation processes in cadmium mobilization during estuarine mixing, *Nature*, vol. 336, pp. 151-154.
- Conomos, T. J., 1979: Properties and circulation of San Francisco Bay waters, In: *San Francisco Bay: The Urbanized Estuary* (T.J. Conomos, ed), Pacific Division of the American Association for the Advancement of Science, San Francisco, pp. 47-84.

- Conomos, T. J., R. E. Smith, D. H. Peterson, S. W. Hager, and L. E. Schemel, 1979: Processes affecting seasonal distributions of water properties in the San Francisco Bay estuarine system, In: *San Francisco Bay: The Urbanized Estuary* (T.J. Conomos, ed), Pacific Division of the American Association for the Advancement of Science, San Francisco, pp. 115-142.
- Davis, J. A., 1984: Complexation of trace metals by adsorbed natural organic matter, *Geochimica et Cosmochimica Acta*, vol. 48, pp. 679-691.
- Davis, J. A., A. J. Gunther, B. J. Richardson, J. M. O'Connor, R. B. Spies, E. Wyatt, E. Larson, and E. C. Meiorin, 1991: *Status and Trends Report on Pollutants in the San Francisco Estuary*, San Francisco Bay-Delta Aquatic Habitat Institute, Richmond, California.
- Donat, J. R., K. A. Lao, and K. W. Bruland, 1993: Speciation of dissolved copper and nickel in South San Francisco Bay: a multi-method approach, *Analytica Chimica Acta*, in press.
- Fisher, N. S., C. V. Nolan, and S. W. Fowler, 1991: Scavenging and retention of metals by zooplankton fecal pellets and marine snow, *Deep-Sea Research*, 38(10), pp. 1261-1275.
- Flegal, A. R., G. J. Smith, G. A. Gill, S. Sañudo-Wilhelmy, and L. C. D. Anderson, 1991: Dissolved trace element cycles in the San Francisco Bay Estuary, *Marine Chemistry*, vol. 36, pp. 329-363.
- Flegal, A. R., G. A. Gill, G. J. Smith, S. Sañudo-Wilhelmy, G. Scelfo and L. D. Anderson, 1990: Trace element cycles in the San Francisco Bay estuary: results from a preliminary study in 1989-1990, *Final Report to the State Water Resources Control Board*.
- Glegg, G. A., J. G. Titley, G. E. Millward, D. R. Glasson, and A. W. Morris, 1988: Sorption behavior of waste-generated trace metals in estuarine waters, *Wat. Sci. Tech.*, 20 (6/7), pp. 113-121.
- Gonzalez-Davila, M., and F. J. Millero, 1990: The adsorption of copper to chitin in seawater, *Geochimica et Cosmochimica Acta*, vol. 54, pp. 761-768.
- Gonzalez-Davila, M., J. M. Santana-Casiano, F. J. Millero, 1990: The adsorption of Cd(II) and Pb(II) to chitin in seawater, *Journal of Colloid and Interface Science*, 137(1), pp. 102-110.
- Gordon, R. M., 1980: Trace element concentrations in seawater and suspended particulate matter from San Francisco Bay and adjacent coastal waters. Master Thesis, Department of Biological Sciences, San Jose State University, 85 pp.

- Gunther, A. J., J. A. Davis and D. J. H. Phillips, 1987: *An Assessment of the Loading of Toxic Contaminants to the San Francisco Bay Delta*, Aquatic Habitat Institute, Richmond, CA, 330 pp.
- Hammond, D. E., C. Fuller, D. Harmon, B. Hartman, M. Korosec, L. G. Miller, R. Rea, S. Warren, W. Berelson and S. W. Hager, 1985: Benthic fluxes in San Francisco Bay, *Hydrobiologia*, vol. 129, pp. 69-90
- Honeyman, B. D. and P. H. Santschi, 1988: Metals in aquatic systems, *Environmental Science and Technology*, 22(8), pp. 862-871.
- Jannasch, H. W., B. D. Honeyman, L. S. Balistrieri and J. W. Murray, 1988: Kinetics of trace element uptake by marine particles, *Geochimica et Cosmochimica Acta*, vol. 52, pp. 567-577.
- Kornicker, W. A. and J. W. Morse, 1991: Interactions of divalent cations with the surface of pyrite, *Geochimica et Cosmochimica Acta*, vol. 55, pp. 2159-2171.
- Kuwabara, J. S., C. C. Y. Chang, J. E. Cloern, T. L. Fries, J. A. Davis and S. N. Luoma, 1989: Trace metal associations in the water column of south San Francisco Bay, California, *Estuarine, Coastal and Shelf Science*, vol. 28, pp. 307-325.
- Laxen, D. P. H., 1985: Trace metal adsorption/coprecipitation on hydrous ferric oxide under realistic conditions, *Water Research*, 19(10), pp. 1229-1236.
- Li, Y. H., L. Burkhardt and H. Teraoka, 1984: Desorption and Coagulation of trace elements during estuarine mixing, *Geochimica et Cosmochimica Acta*, vol. 48, pp. 1879-1884.
- Livingstone, A. D., 1963: *Chemical Components of Rivers and Lakes*, U.S. Geological Survey Paper No. 440G.
- Luoma, S. N. and D. J. Phillips, 1988: Distribution, variability, and impacts of trace elements in San Francisco Bay, *Marine Pollution Bulletin*, 19(9), pp. 413-425.
- Mantoura, R. F. C., A. Dickson and J. P. Riley, 1978: The complexation of metals with humic materials in natural waters, *Estuarine and Coastal Marine Science*, vol. 6, pp. 387-408.
- McKnight, D. M., G. L. Feder, E. M. Thurman, R. L. Wershaw and J. C. Westall, 1983: Complexation of copper by aquatic humic substances from different environments, *Science of the Total Environment*, vol. 28, pp. 65-76.

- Morel, F. M. M. and P. M. Gschwend, 1987: The role of colloids in the partitioning of solutes in natural waters, in: *Aquatic Surface Chemistry*, edited by W. Stumm, John Wiley and Sons, NY, 520 pp.
- Nuñez, R. H., Prediction of tidal propagation and circulation in Chilean inland seas using a frequency domain model, M.S. Thesis, Oregon State University, Corvallis, Or., 1990.
- Nyffeler, U. P., Y. H. Li and P. H. Santchi, 1984: A kinetic approach to describe trace-element distribution between particles and solution in natural aquatic systems, *Geochimica et Cosmochimica Acta*, vol. 48, pp. 1513-1522.
- Oakley, S. M., P. O. Nelson, and K. J. Williamson, 1981: Model of Trace-metal partitioning in marine sediments, *Environmental Science and Technology*, 15(4), pp. 474-480.
- Palmer, J.R., W. F. Shelton, L. F. Trujillo, and K. L. Markham, 1990: Water Resources Data California, Water Year 1989, *U. S. Geological Survey Water-Data Report CA-89-2*, vol. 2, 320 pp.
- Pankow, J. F. and S. W. McKenzie, 1991: Parameterizing the equilibrium distribution of chemicals between the dissolved, solid particulate matter, and colloidal matter compartments in aqueous systems, *Environmental Science and Technology*, 25(12), pp. 2046-2053.
- Smith, G. J. and A. R. Flegal, 1993: Silver in San Francisco Bay estuarine waters, *Estuaries*, 16(3), in press.
- Smith, R. M. and P. E. Martell, 1976: Critical Stability Constants, vol. 4, Inorganic Complexes, Plenum, New York.
- Spiker, E. C. and L. E. Schemel, 1979: Distribution and stable-isotope composition of carbon in San Francisco Bay, In: *San Francisco Bay: The Urbanized Estuary* (T.J. Conomos, ed), Pacific Division of the American Association for the Advancement of Science, San Francisco, pp. 195-212.
- Sunda, W. G. and P. J. Hanson, 1979: Chemical speciation of copper in river water, effect of total copper, pH, carbonate and dissolved organic matter. In: *Chemical Modeling In Aqueous Systems*, American Chemical Society, Washington, D. C. pp. 147-180.
- Stumm, W. and J. J. Morgan, 1981: *Aquatic Chemistry*, New York, Wiley-Interscience, 780 pp.

- Thomson, E. A., S. N. Luoma, C. E. Johansson and D. J. Cain, 1984: Comparison of sediments and organisms in identifying sources of biologically available trace metal contamination, *Water Research*, 18(6), pp. 755-765.
- Thomson-Becker, E. A. and S. N. Luoma, 1985: Temporal fluctuations in grain size, organic materials and iron concentrations in intertidal surface sediment of San Francisco Bay, *Hydrobiologia*, vol. 129, pp. 91-107.
- Truesdell, A. H., and Jones, B. F., 1974: WATEQ, a computer program for calculating chemical equilibria of natural waters, *J. Res. U. S. Geol. Surv.*, vol. 2, pp. 233-248.
- Van den Berg, C. M. G., 1984: Determination of the complexing capacity and conditional stability constants of complexes of copper(II) with natural organic ligands in seawater by cathodic stripping voltammetry of copper-catechol complex ions, *Marine Chemistry*, vol. 15, pp. 1-18.
- Van den Berg, C. M. G. and J. R. Kramer, 1979: Conditional stability constants for copper ions with ligands in natural waters, In: *Chemical Modeling In Aqueous Systems*, American Chemical Society, Washington, D. C. pp. 147-180.
- Van den Berg, C. M. G., A. G. A. Merks and E. K. Duursma, 1987: Organic complexation and its control of the dissolved concentrations of copper and zinc in the Scheldt estuary, *Estuarine, Coastal and Shelf Science*, vol. 24, pp. 785-797.
- Walters, R. A., R. T. Cheng and T. J. Conomos, 1985: Time scales of circulation and mixing processes of San Francisco Bay waters, *Hydrobiologia*, vol. 129, pp. 13-36.
- Westerink, J.J., J.J. Connor and K.D. Stolzenbach, 1988: A frequency-time domain finite element model for tidal circulation based on the least-squares harmonic analysis method, *International Journal for Numerical Methods in Fluids*, vol. 8, pp. 813-843.
- Wood, T. M. and A. M. Baptista, 1993: A model for diagnostic analysis of estuarine geochemistry, *Water Resources Research*, vol. 29(1), pp. 51-71.
- Zirino, A. and S. Yamamoto, 1972: A pH-dependent model for the chemical speciation of copper, zinc, cadmium and lead in sea water, *Limnology and Oceanography*, vol. 17, pp. 661-671.

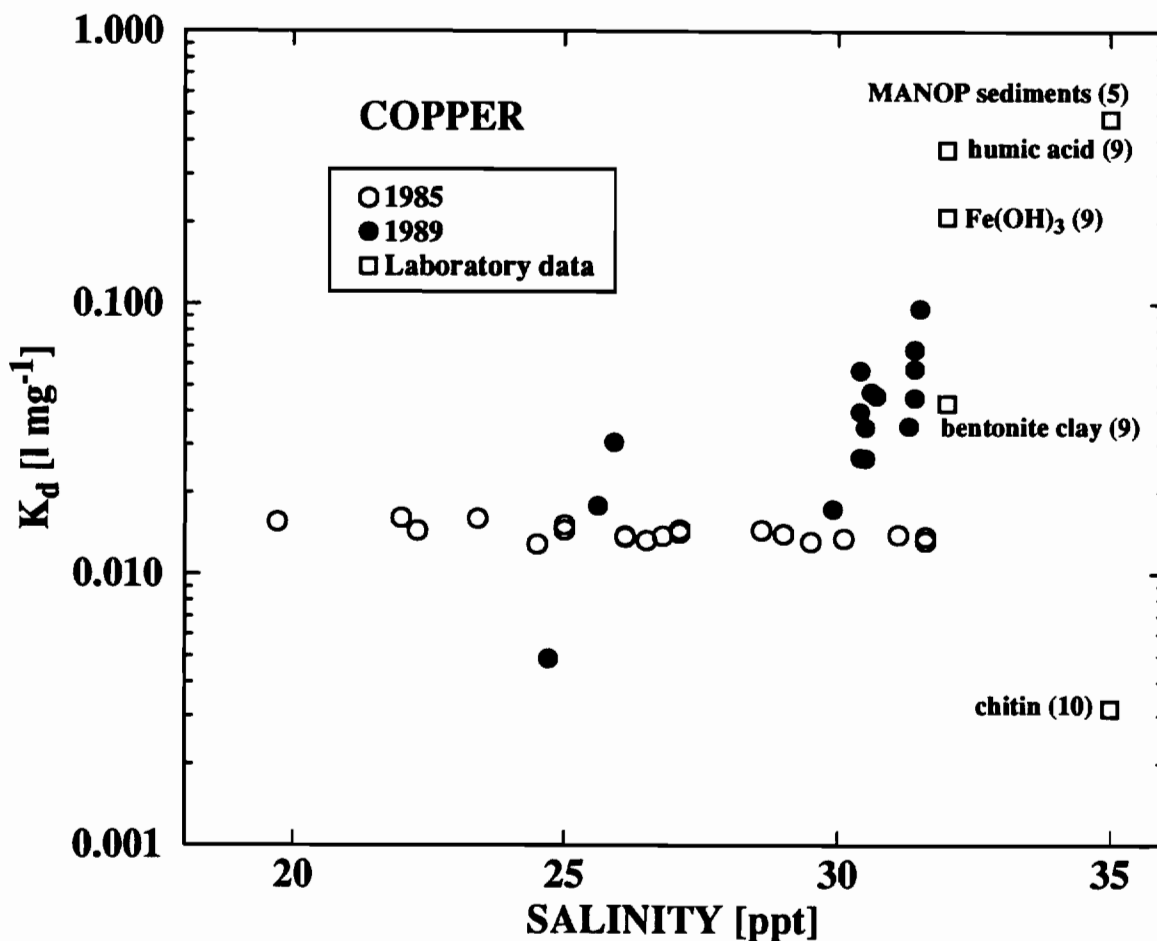


Figure 4.1. Plot of observed partition coefficient, $K_d^a = c_{(s)} / (c_{(d)} c_p)$ for 1985 and 1989 copper data. Values of $c_{(s)}$, $c_{(d)}$, and c_p for 1985 are taken from *Kuwabara, et al.* [1989]. Values of $c_{(s)}$ and $c_{(d)}$ for 1989 data are taken from *Flegal, et al.* [1990]; suspended solids data c_p are taken from *Smith and Flegal* [1993]. Some data points were eliminated from the 1989 data, either because a) c_T was not available, b) c_p was not available, or c) $c_{(d)}$ was greater than c_T . Also included in the plot are laboratory values taken from the literature, accompanied by the adsorbent material and the reference (in parentheses) from Table 4.1.

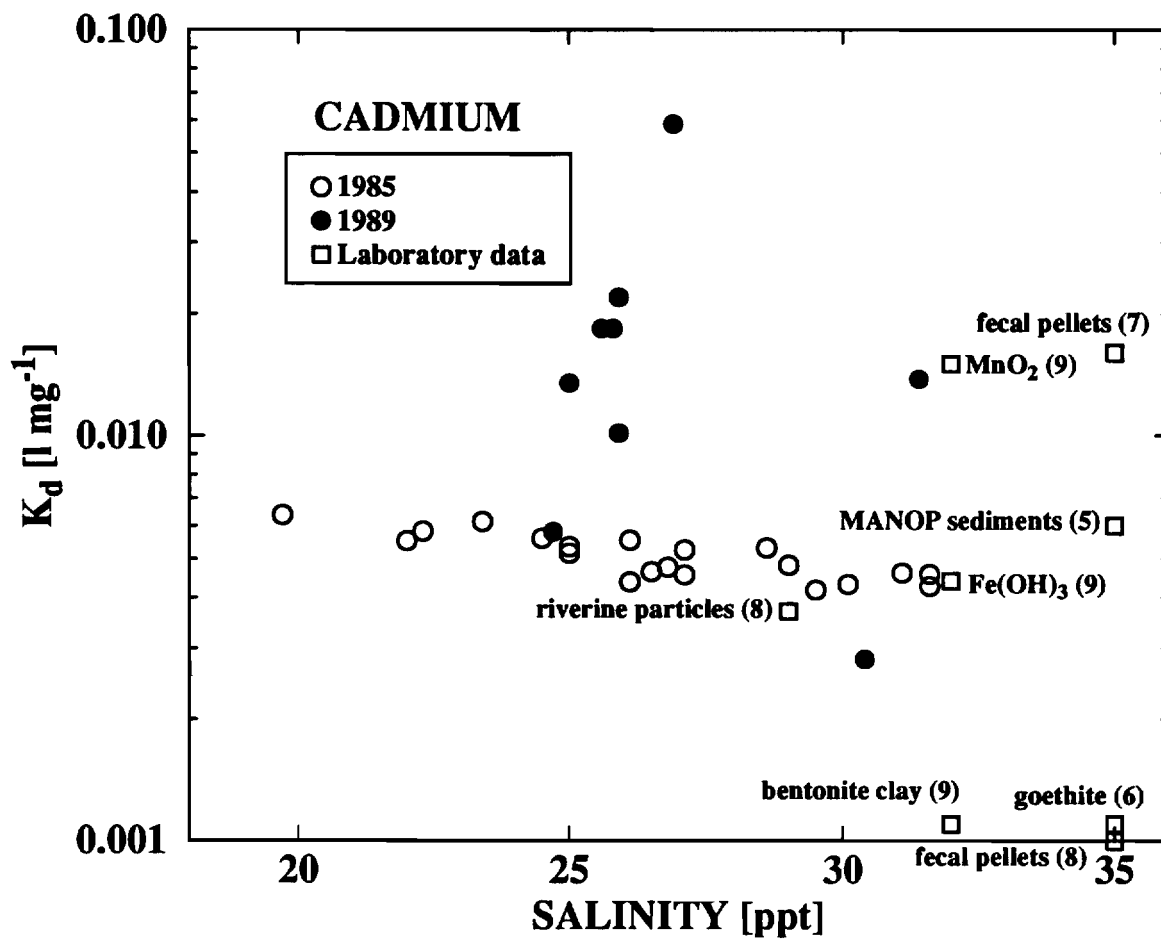


Figure 4.2. Plot of observed partition coefficient, $K_d^a = c_{(s)} / (c_{(d)} c_p)$ for 1985 and 1989 cadmium data. Dissolved Cd data have been reduced by a factor of 2 from values given in *Kuwabara, et al.* [1989], as per personal communication with J. Kuwabara. Otherwise, description as in Figure 4.1.

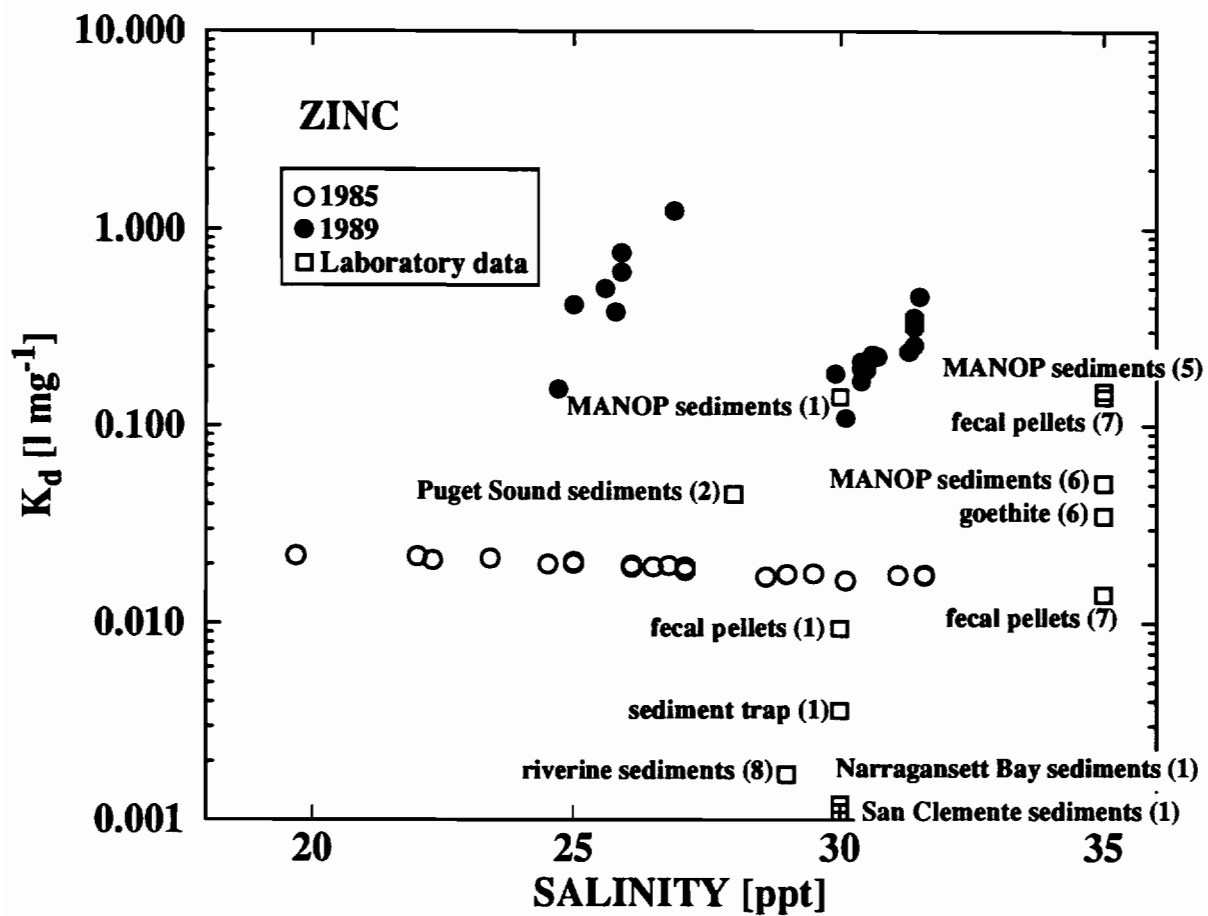


Figure 4.3. Plot of observed partition coefficient, $K_d^a = c_{(s)} / (c_{(d)} c_p)$ for 1985 and 1989 zinc data. Description as in Figure 4.1.

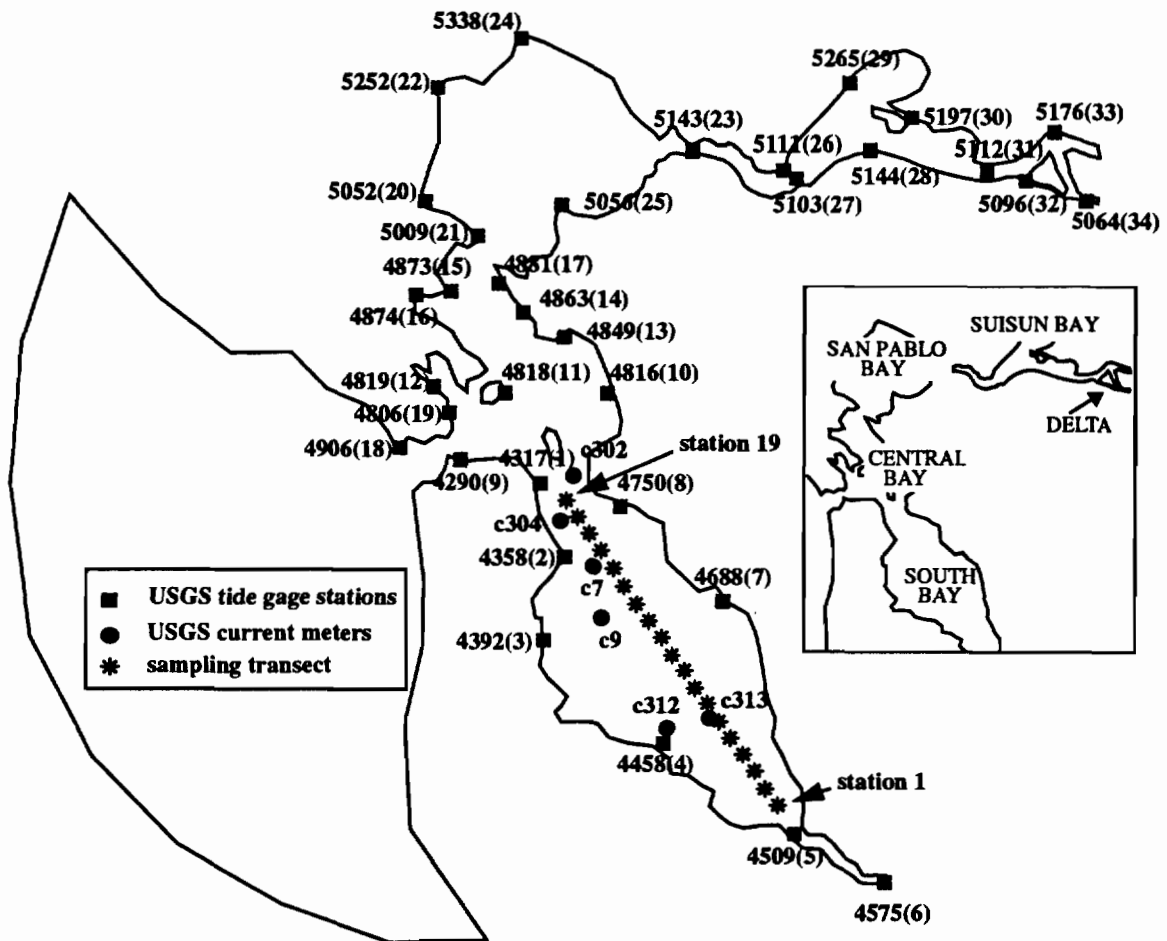


Figure 4.4. Outline of the numerical grid used in simulations. The triangular finite element grid has 1630 quadratic elements and 3709 nodes. The USGS tide gage stations at which observations are compared with the numerical data are shown as squares; the 4-digit number is the gage number as in *Cheng and Gartner* [1984], and the number in parentheses is the numbering scheme used in Figure 4.5. The USGS current meter stations where salinity comparisons were made are shown as circles and numbered as in *Cheng and Gartner* [1984]. The sampling transect for the numerical data consists of 19 stations (shown as stars), numbered from north to south.

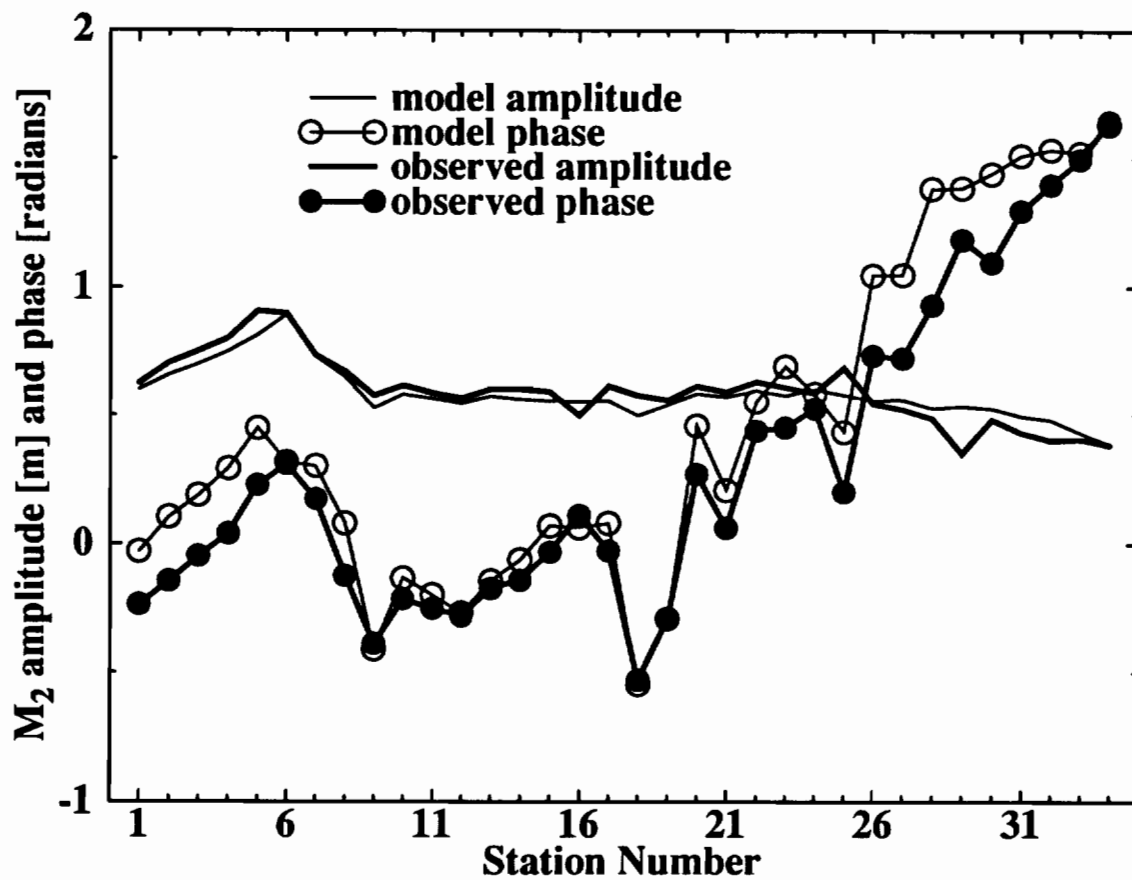


Figure 4.5. A comparison of the M_2 amplitude and phase of elevations from the TEA-NL generated circulation used in the model simulations and USGS tide gage data, at stations shown in Figure 4.4.

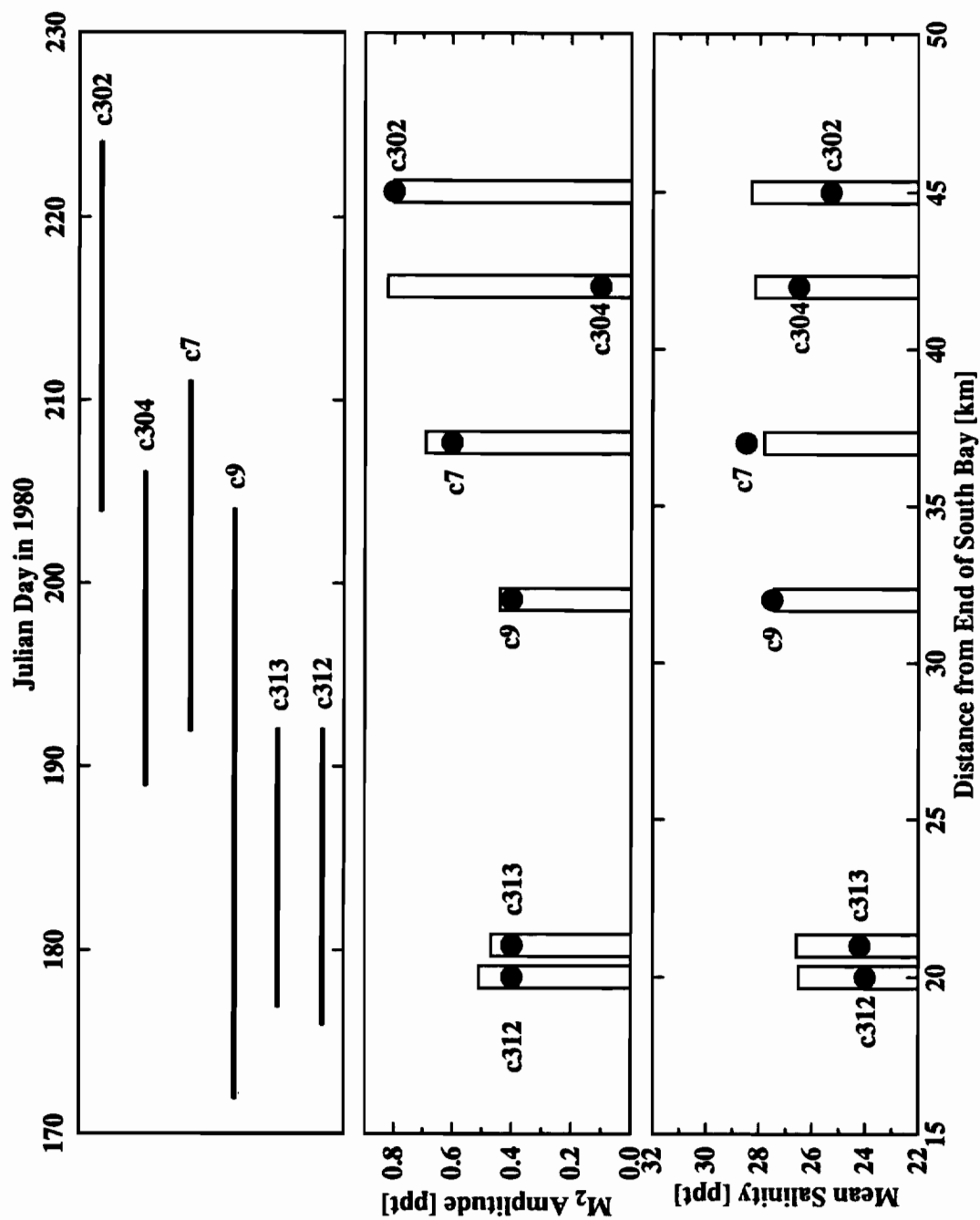


Figure 4.6. A comparison of the mean salinity and M_2 (semi-diurnal) amplitude of salinity from ELAmets and USGS salinity data, at current meter stations shown in Figure 4.4. ELAmets results are shown as a vertical bar; observed values as solid circles. Also shown is the duration of the salinity time series at each USGS station.

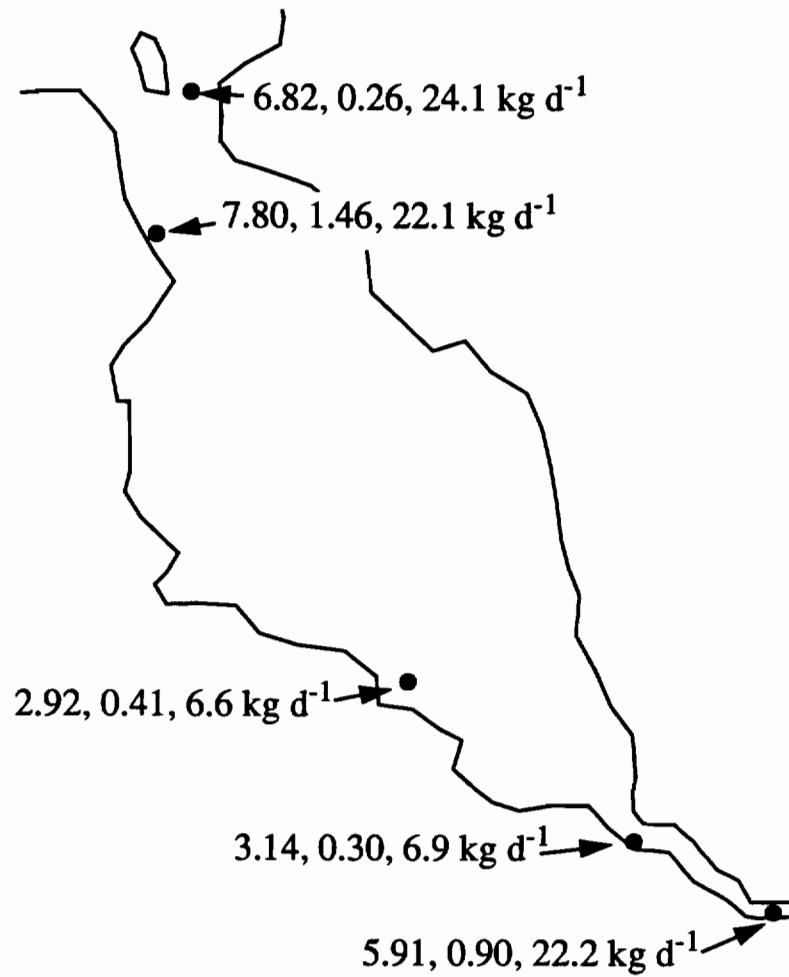


Figure 4.7. Outline of South Bay showing the locations of 5 POTWs located within the basin. The daily inputs are for Cu, Cd, and Zn, respectively.

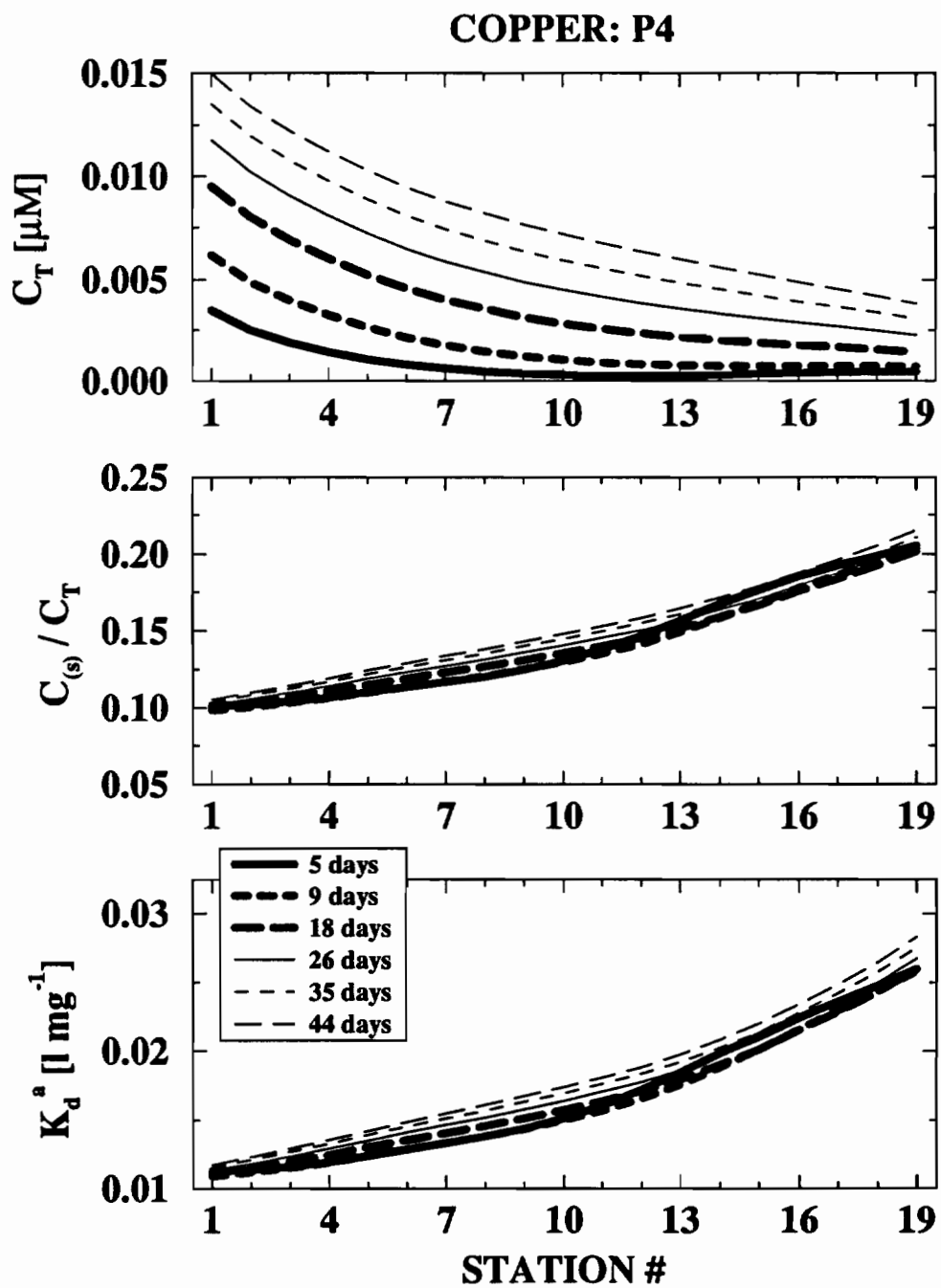


Figure 4.8. Tidally-averaged profiles of total concentration, percent mass in the solid phase, and apparent distribution coefficient for copper, experiment P4.

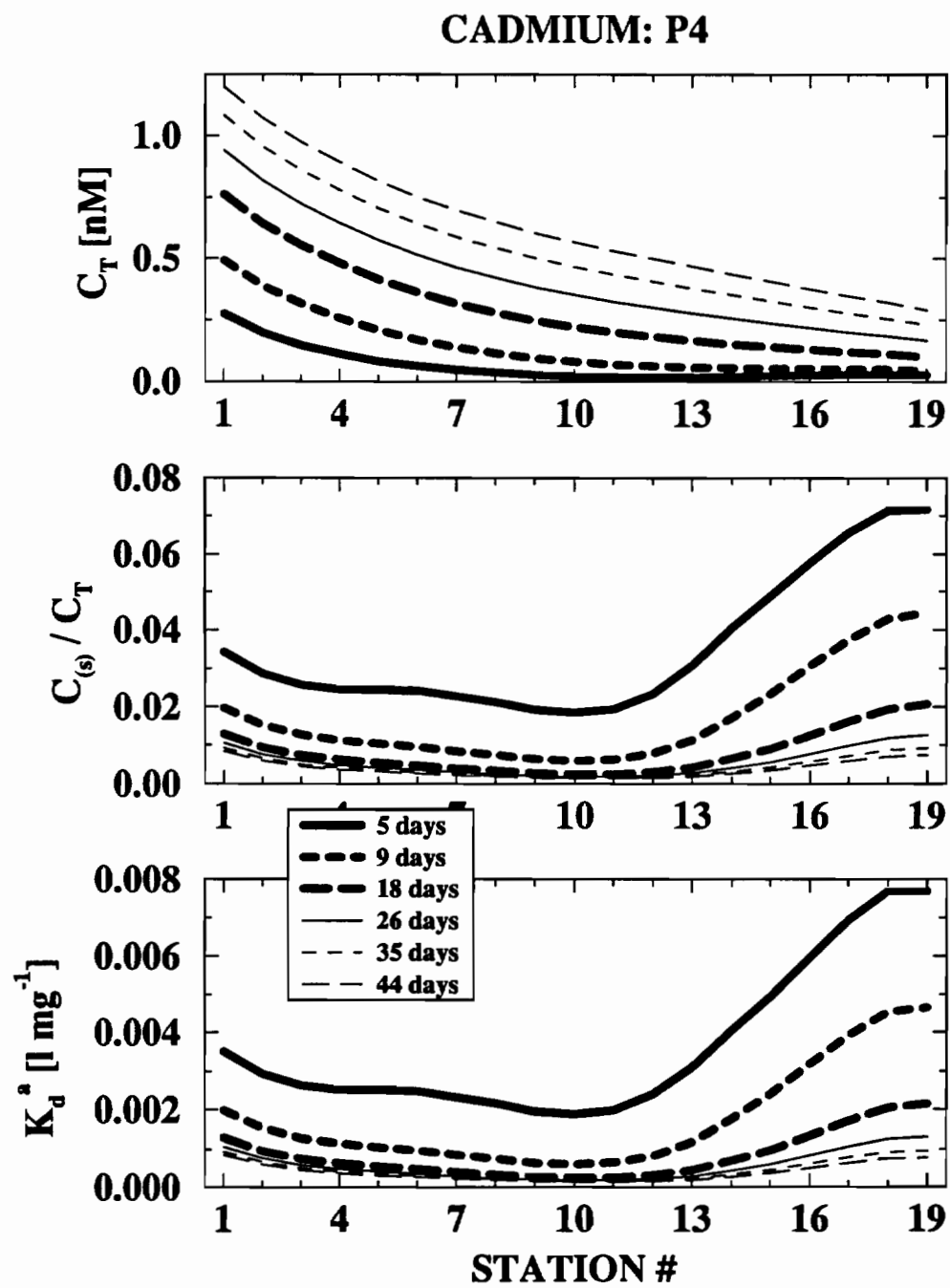


Figure 4.9. Tidally-averaged profiles of total concentration, percent mass in the solid phase, and apparent distribution coefficient for cadmium, experiment P4.

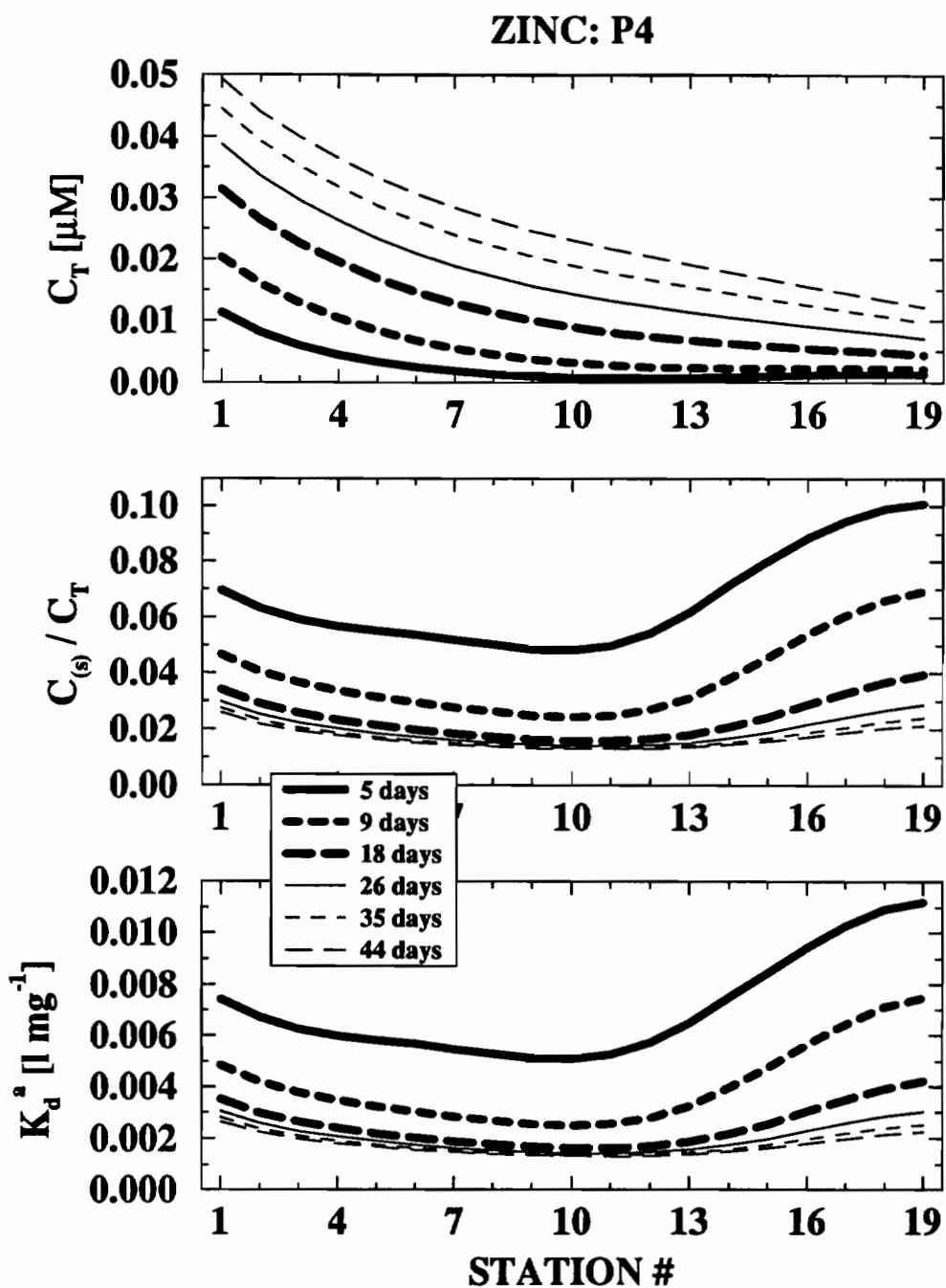


Figure 4.10. Tidally-averaged profiles of total concentration, percent mass in the solid phase, and apparent distribution coefficient for zinc, experiment P4.

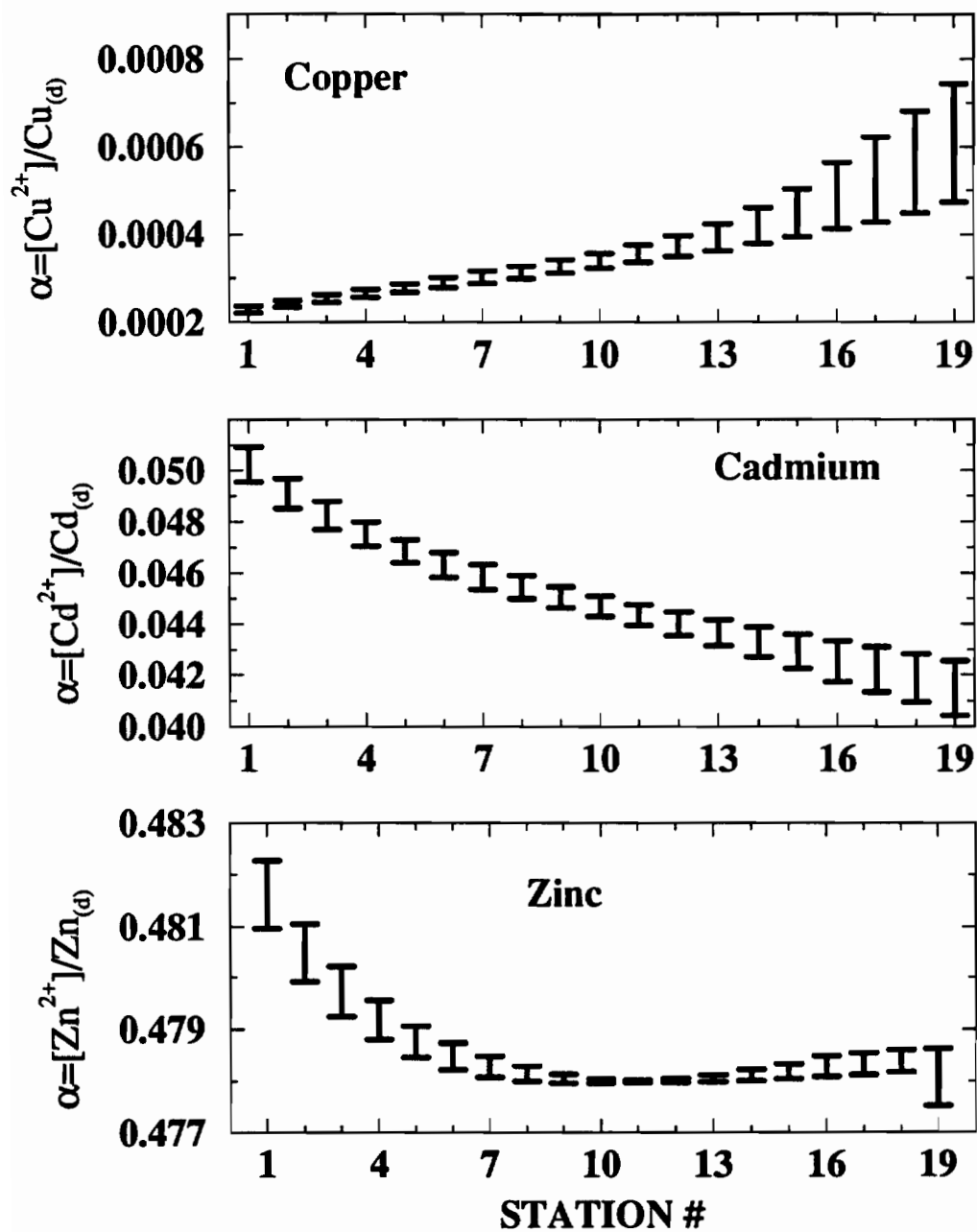


Figure 4.11. Profiles of $\alpha = C^{2+}/C_d$ for copper, cadmium and zinc, experiment P4. The bars represent the limits of tidal variability at each station.

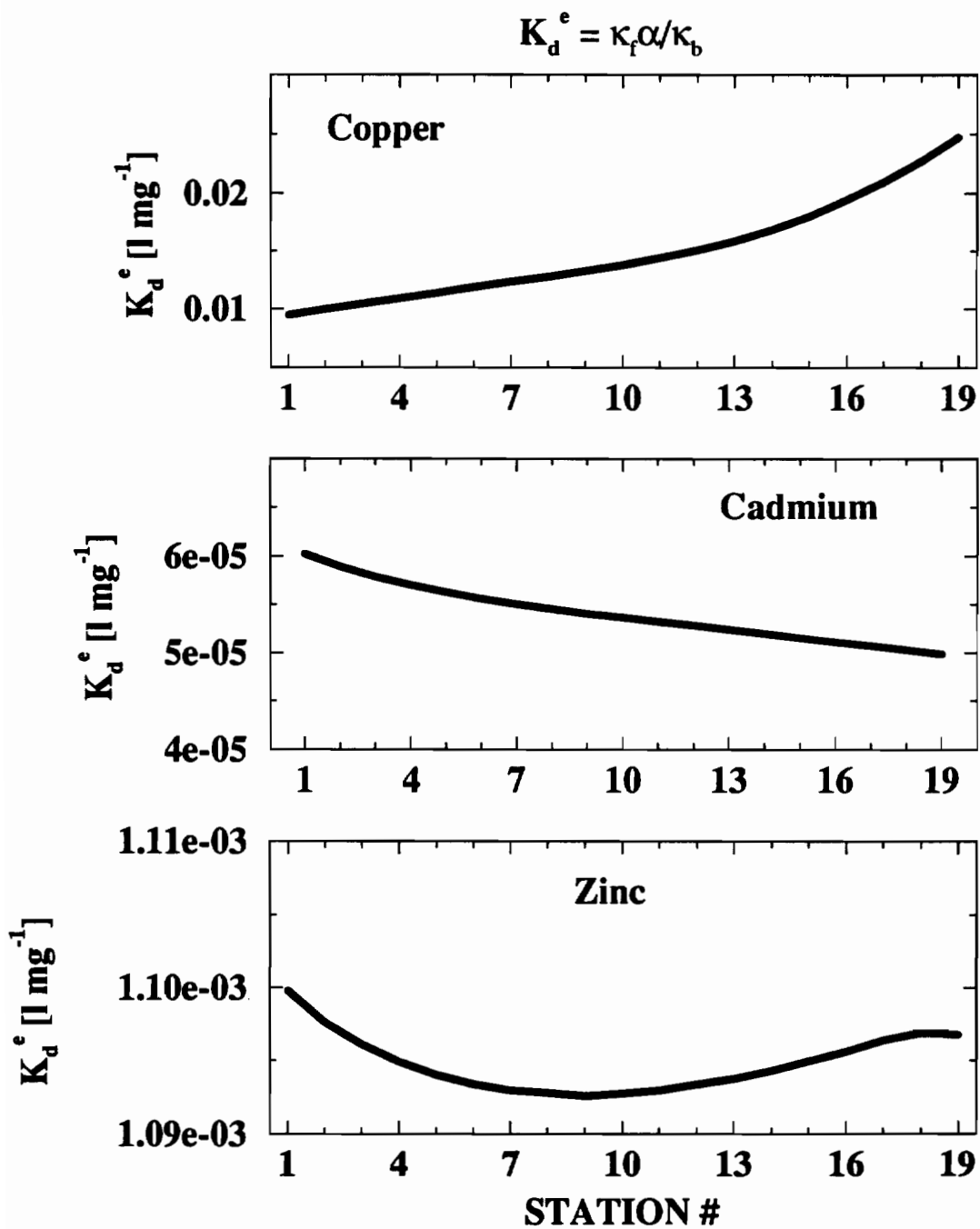


Figure 4.12. Tidally-averaged profiles of K_d^e for copper, cadmium and zinc, same conditions as experiment P4.

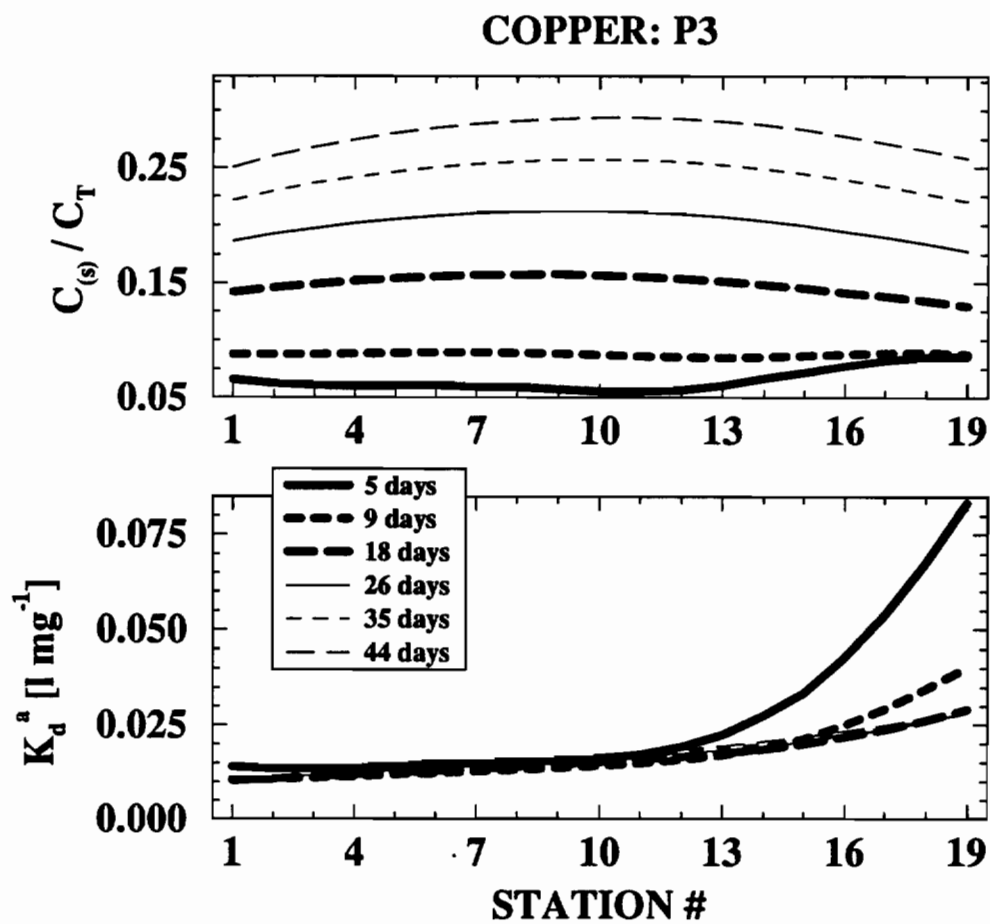


Figure 4.13. Tidally-averaged profiles of percent mass in the solid phase and apparent distribution coefficient for copper, experiment P3.

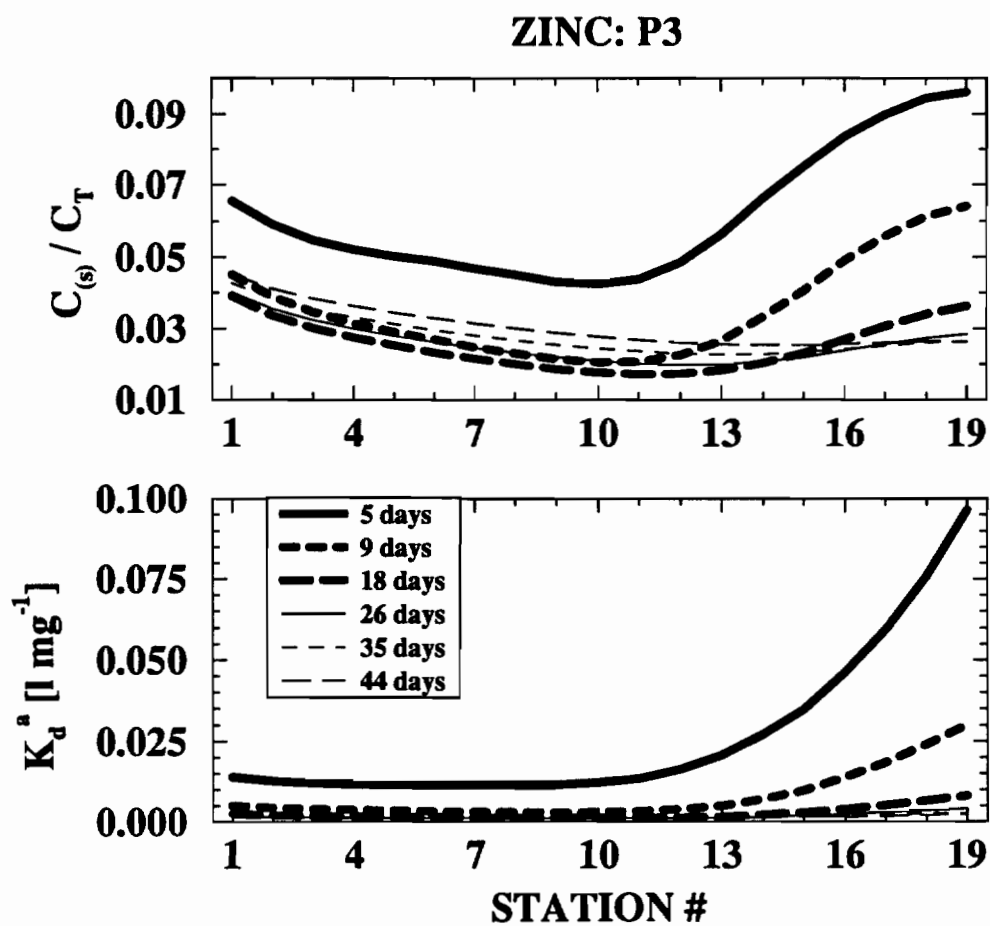


Figure 4.14. Tidally-averaged profiles of percent mass in the solid phase and apparent distribution coefficient for zinc, experiment P3.

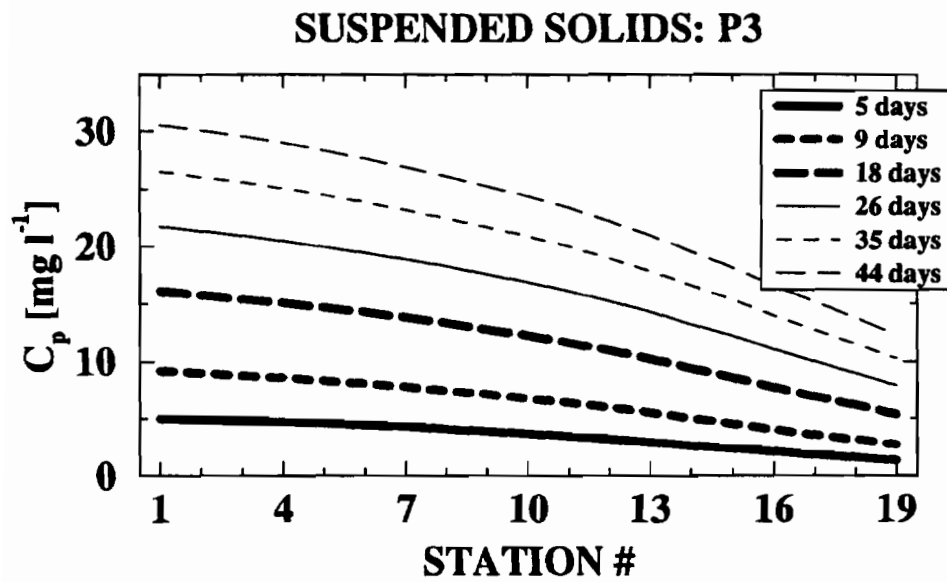


Figure 4.15. Tidally-averaged profiles of concentration of suspended solids, experiment P3.

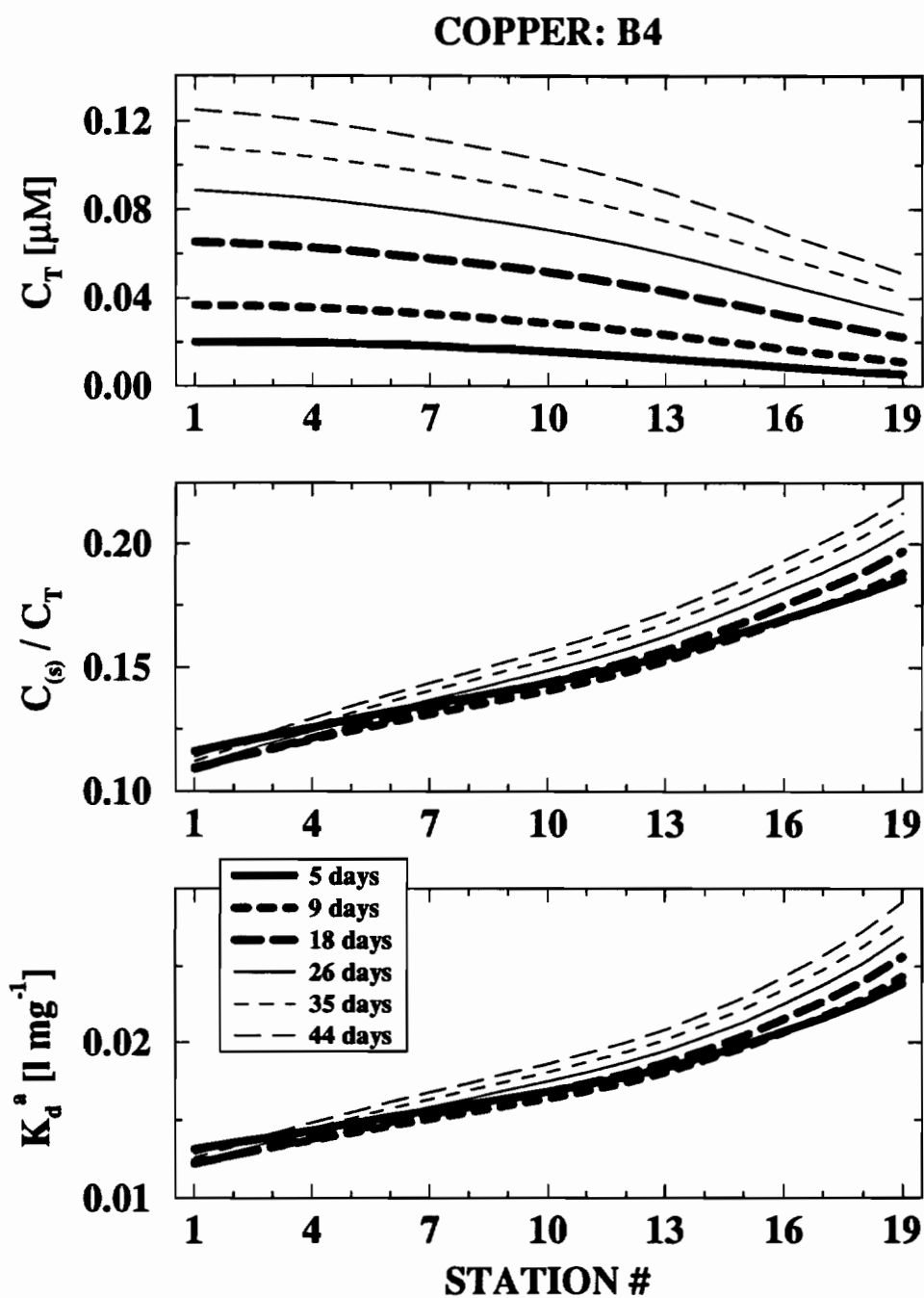


Figure 4.16. Tidally-averaged profiles of total concentration, percent mass in the solid phase, and apparent distribution coefficient for copper, experiment B4.

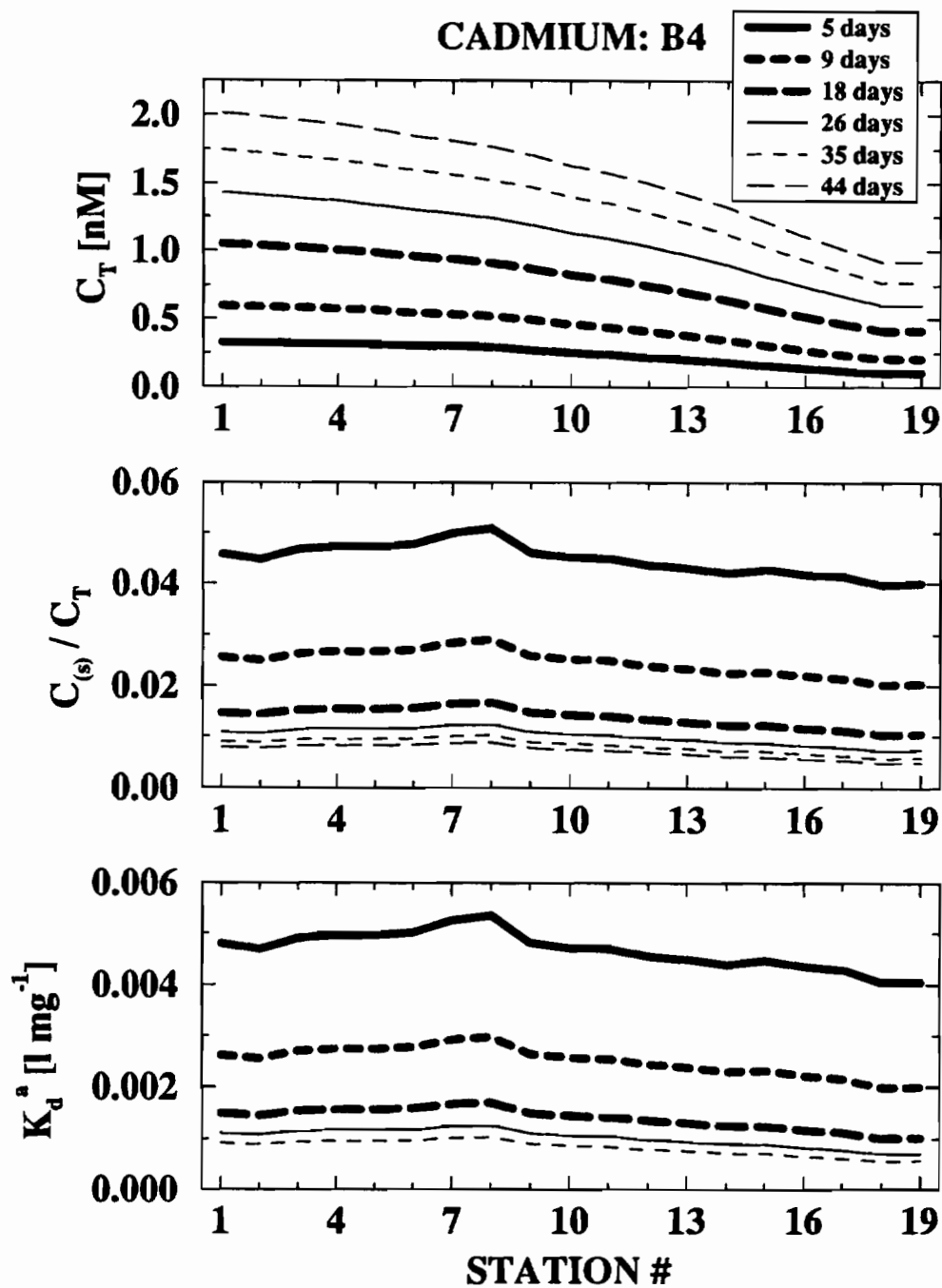


Figure 4.17. Tidally-averaged profiles of total concentration, percent mass in the solid phase, and apparent distribution coefficient for cadmium, experiment B4.

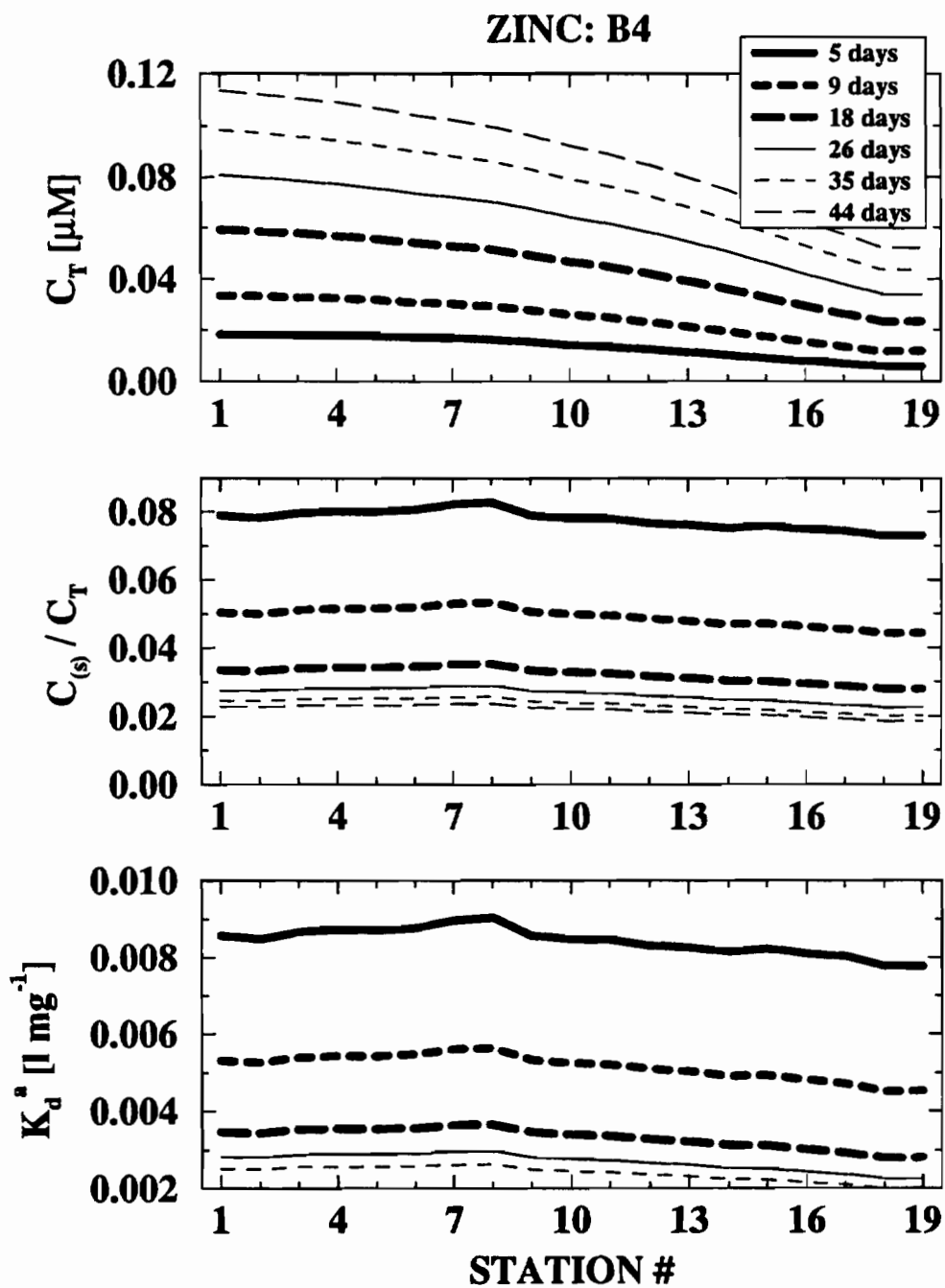


Figure 4.18. Tidally-averaged profiles of total concentration, percent mass in the solid phase, and apparent distribution coefficient for zinc, experiment B4.

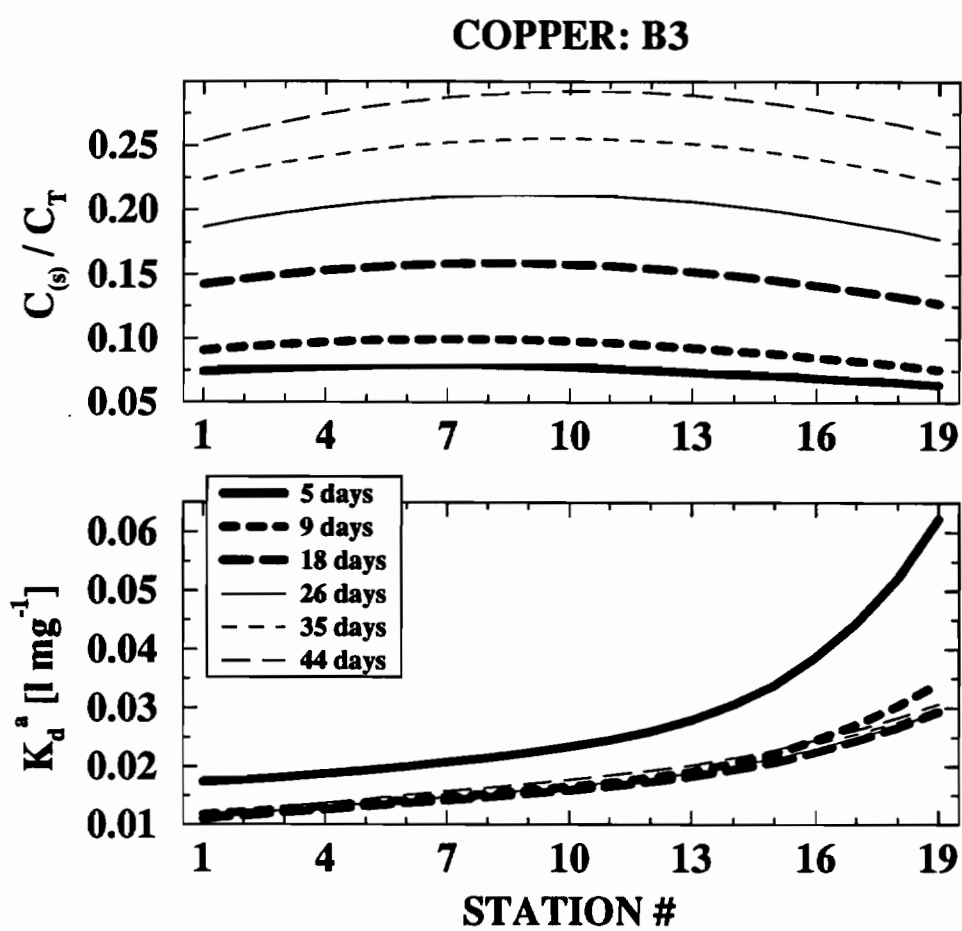


Figure 4.19. Tidally-averaged profiles of percent mass in the solid phase and apparent distribution coefficient for copper, experiment B3.

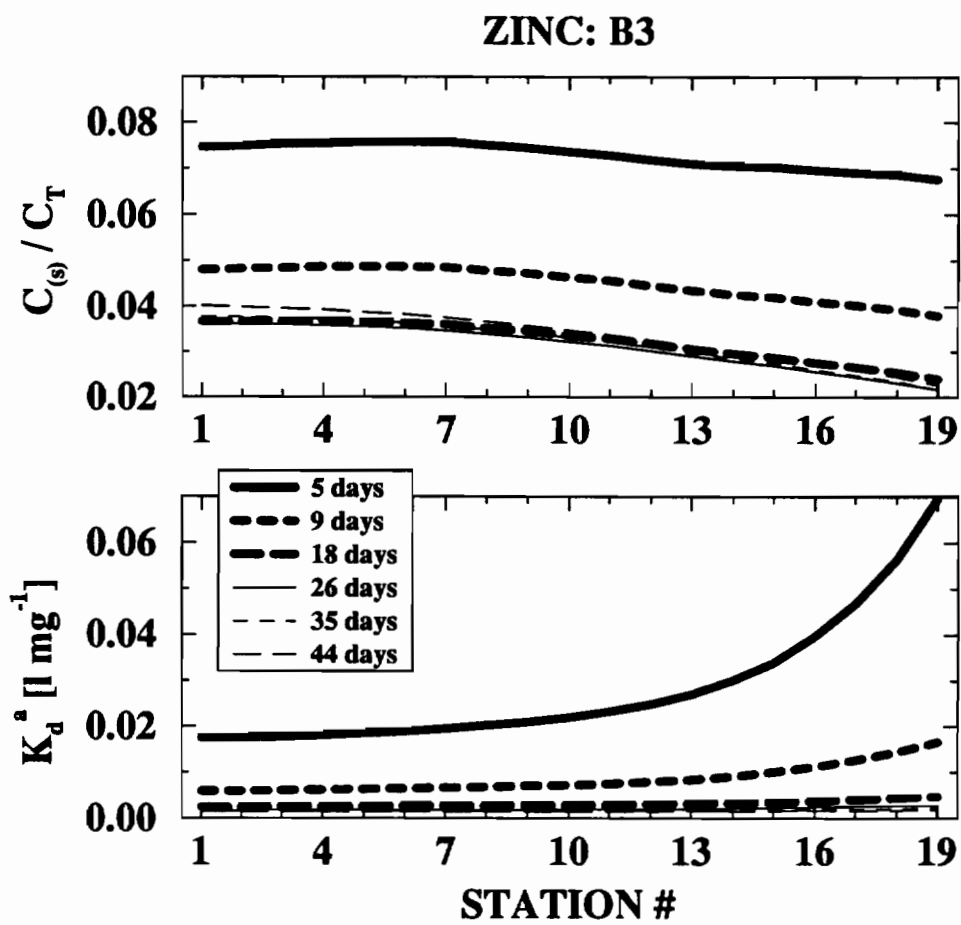


Figure 4.20. Tidally-averaged profiles of percent mass in the solid phase and apparent distribution coefficient for zinc, experiment B3.

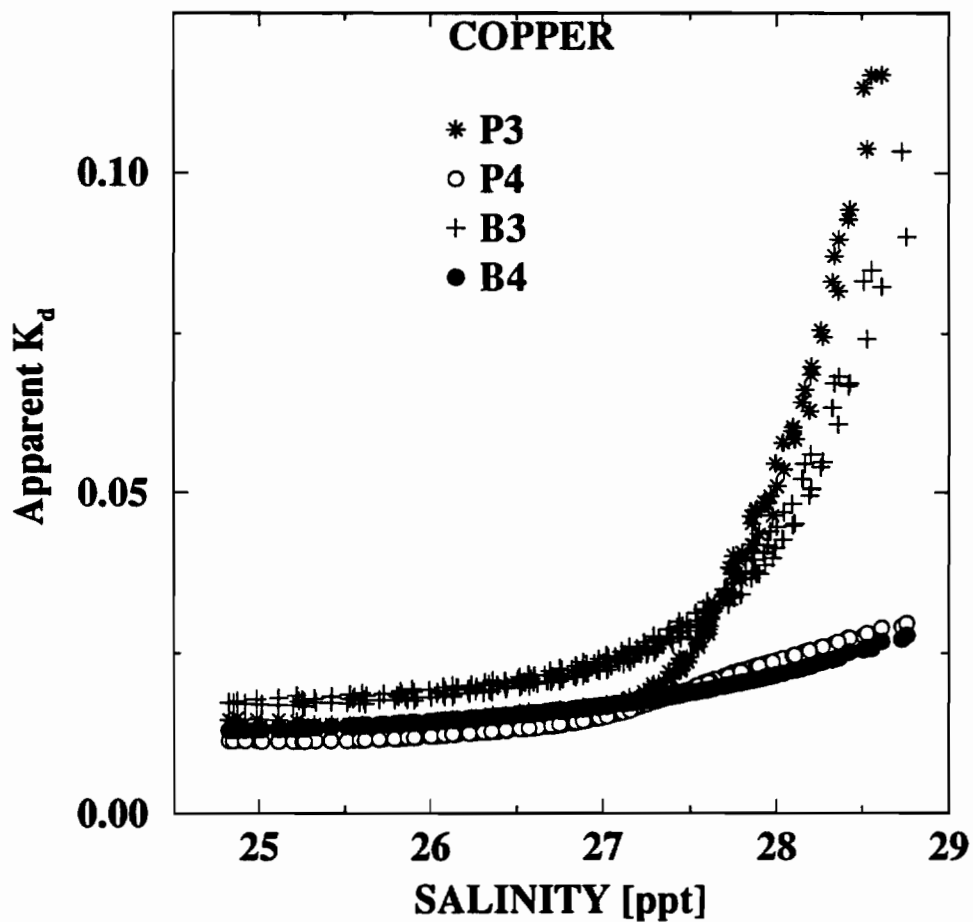


Figure 4.21. Scatterplot of apparent distribution coefficient of copper as a function of salinity. Samples were taken approximately 5 days into the simulation. Each point represents a sample at a particular station and point in time; all nineteen transect stations at a total of 12 points over the tidal cycle are represented for each experiment.

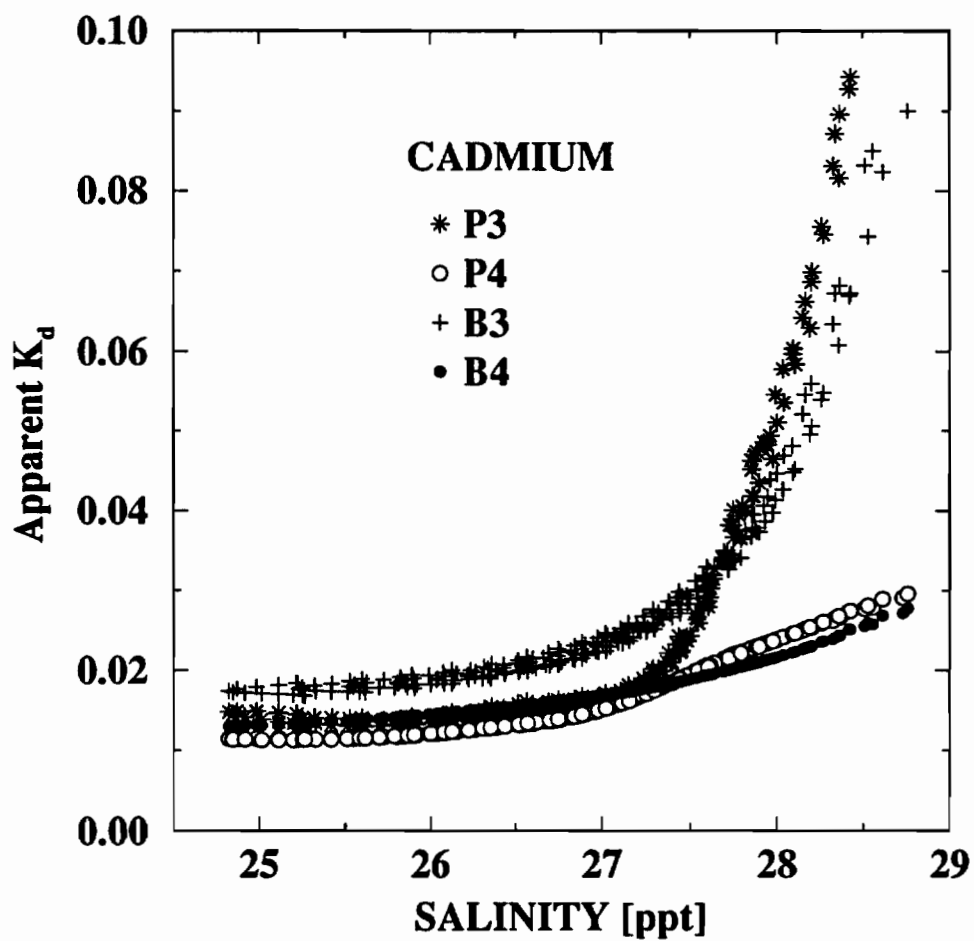


Figure 4.22. Scatterplot of apparent distribution coefficient of cadmium as a function of salinity. Explanation of points as in Figure 4.21.

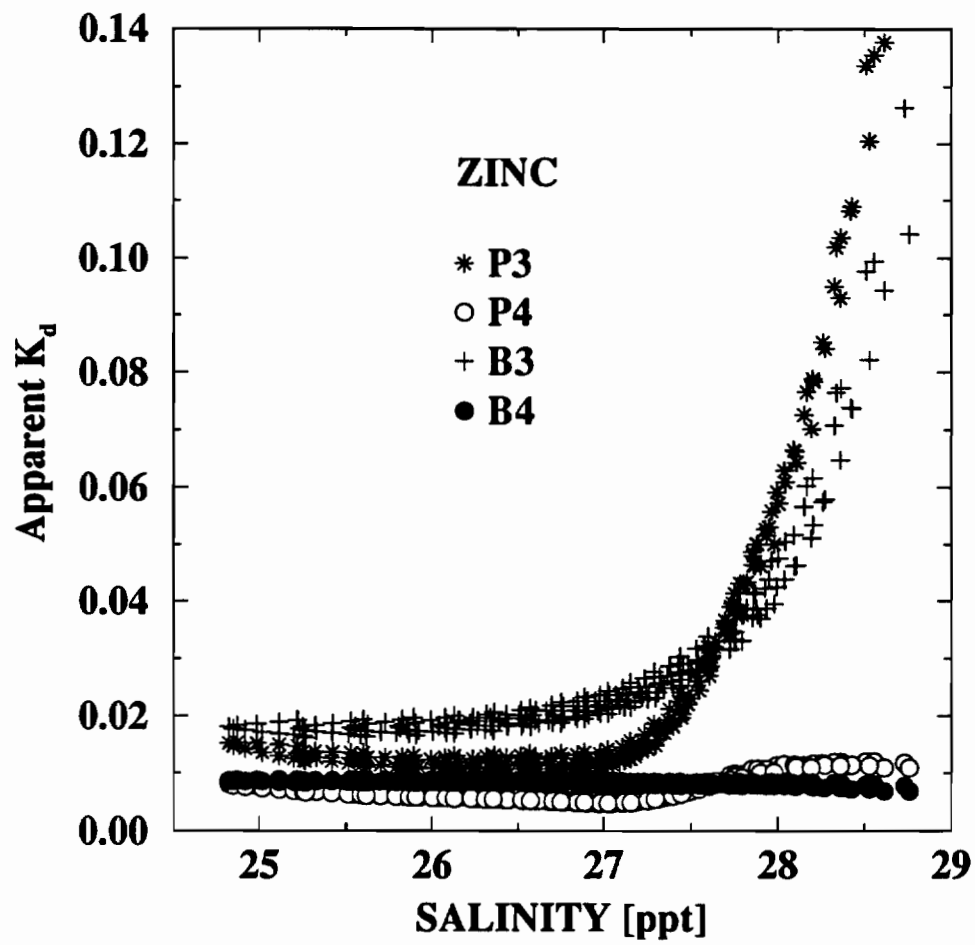


Figure 4.23. Scatterplot of apparent distribution coefficient of zinc as a function of salinity. Explanation of points as in Figure 4.21.

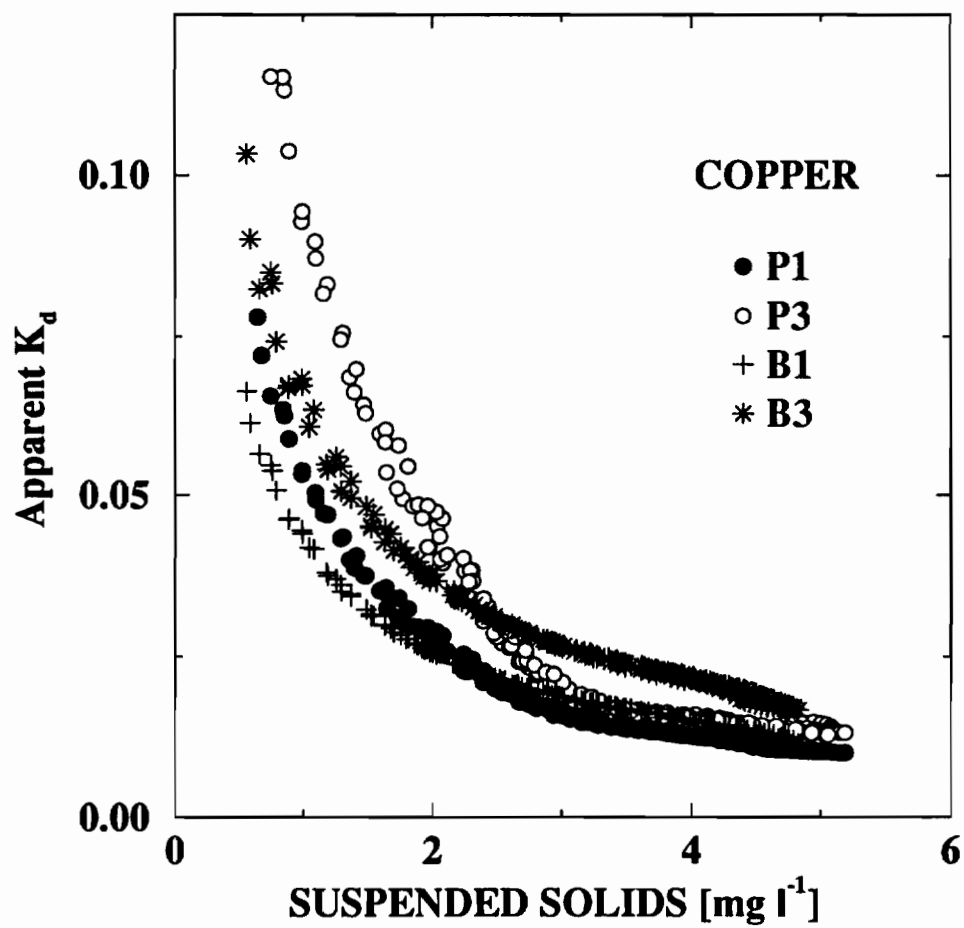


Figure 4.24. Scatterplot of apparent distribution coefficient of copper as a function of suspended solids concentration. Explanation of points as in Figure 4.21.

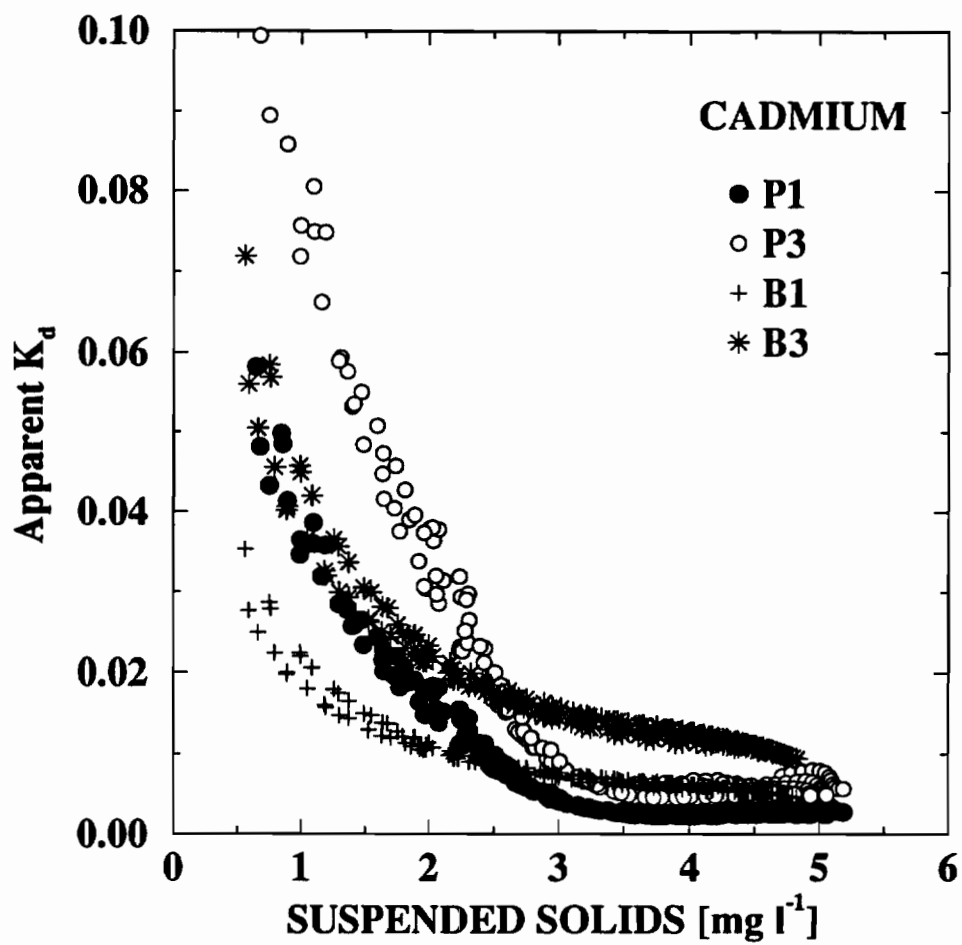


Figure 4.25. Scatterplot of apparent distribution coefficient of cadmium as a function of suspended solids concentration. Explanation of points as in Figure 4.21.

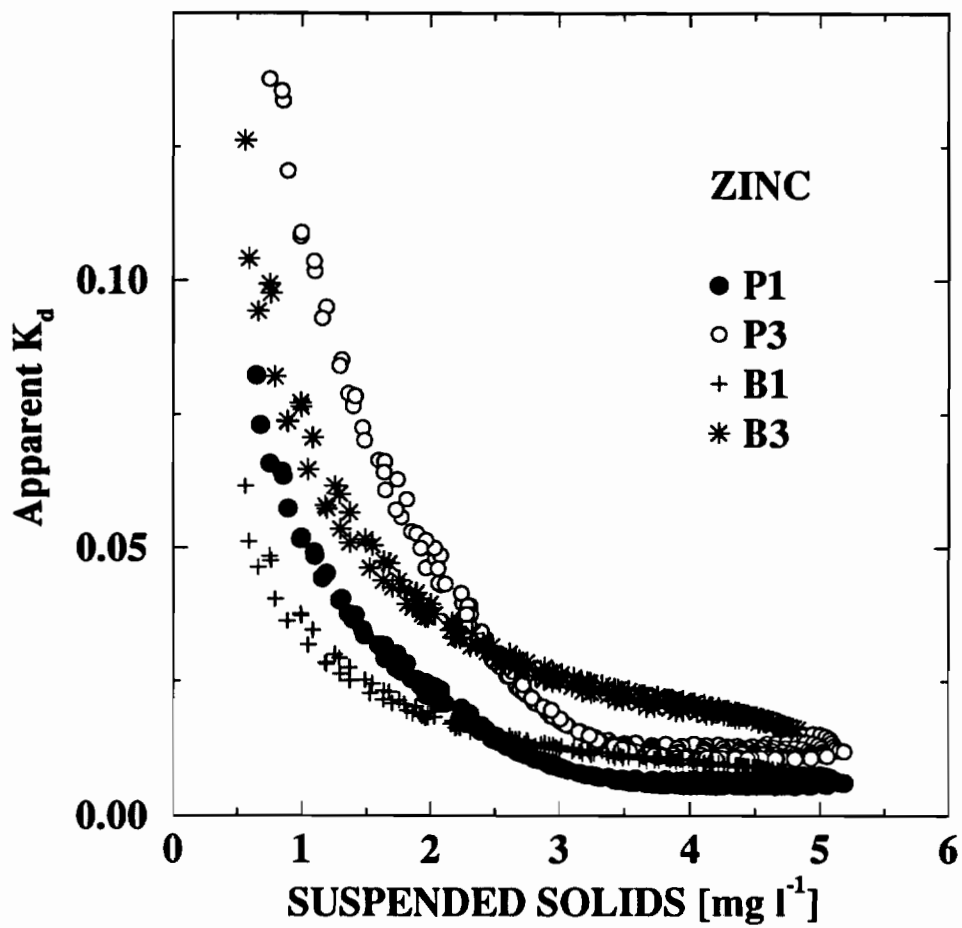


Figure 4.26. Scatterplot of apparent distribution coefficient of zinc as a function of suspended solids concentration. Explanation of points as in Figure 4.21.

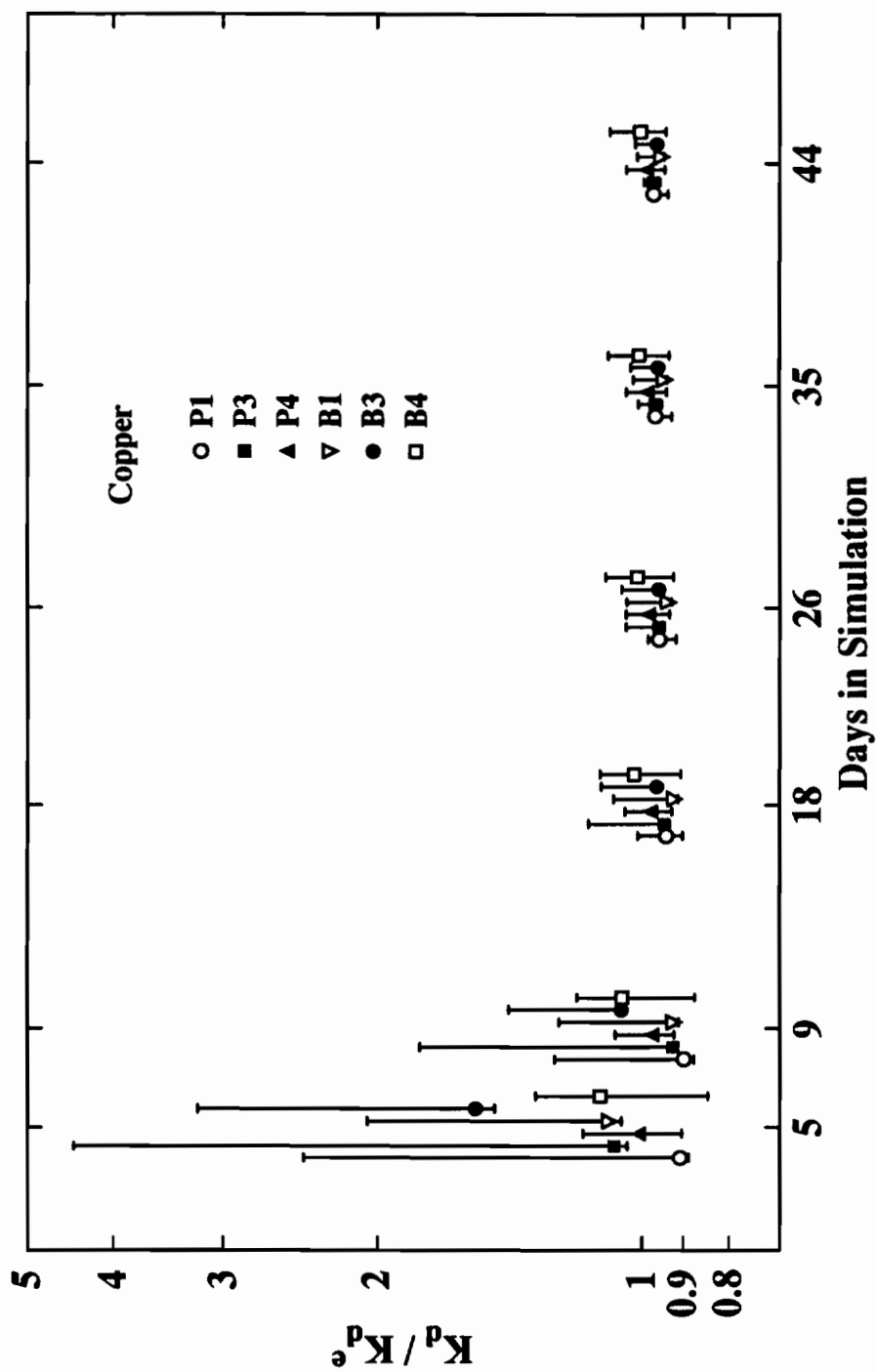


Figure 4.27. Plot of distance from equilibrium as a function of time for copper. The symbols represent tidal mean values at transect station 10; bars around the symbol represent the limit of tidal variability over the entire transect. Each experiment was sampled at 5, 9, 18, 26, 35 and 44 days, but symbols are offset for clarity in the plot.

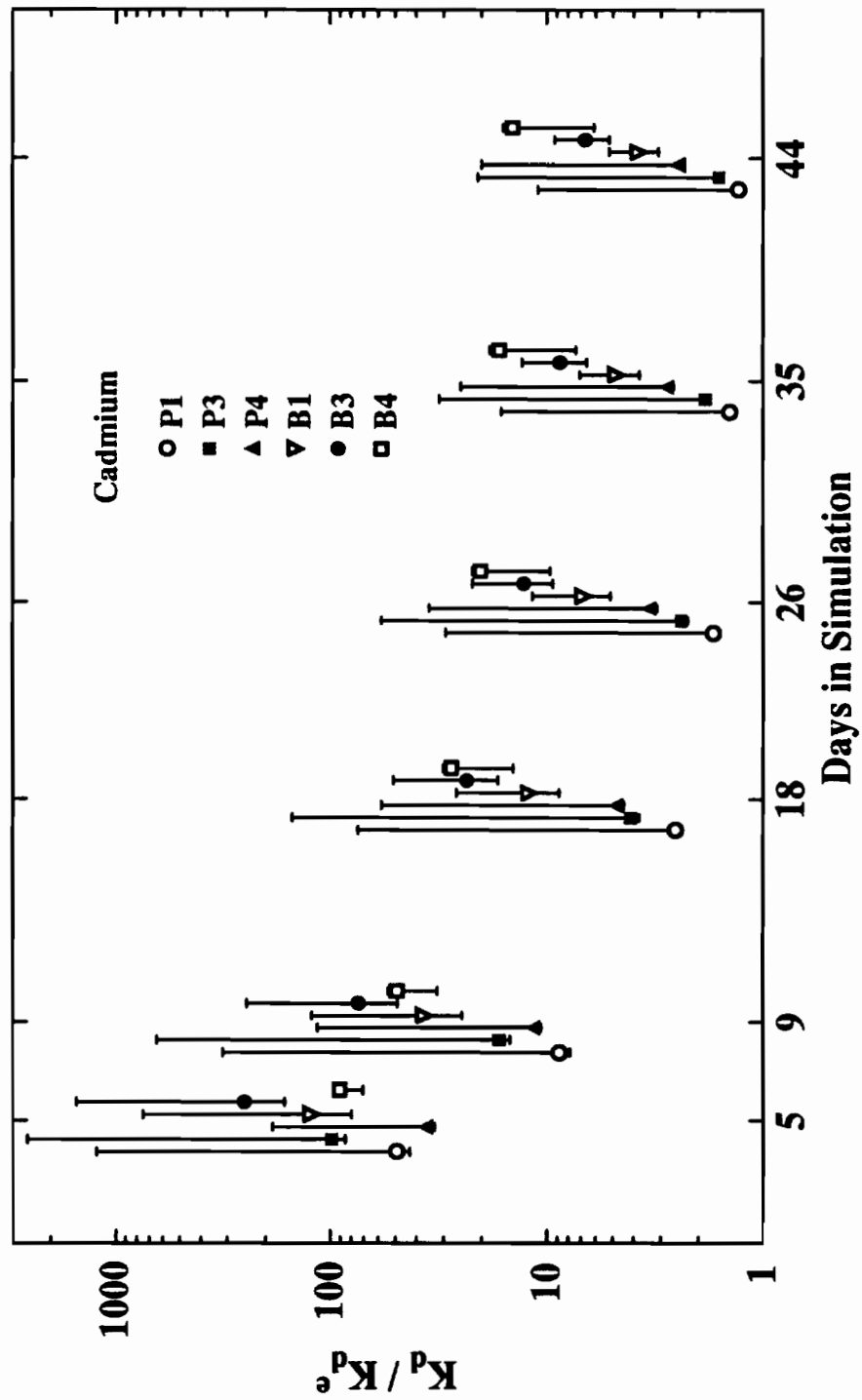


Figure 4.28. Plot of distance from equilibrium as a function of time for cadmium. Explanation as in Figure 4.27.

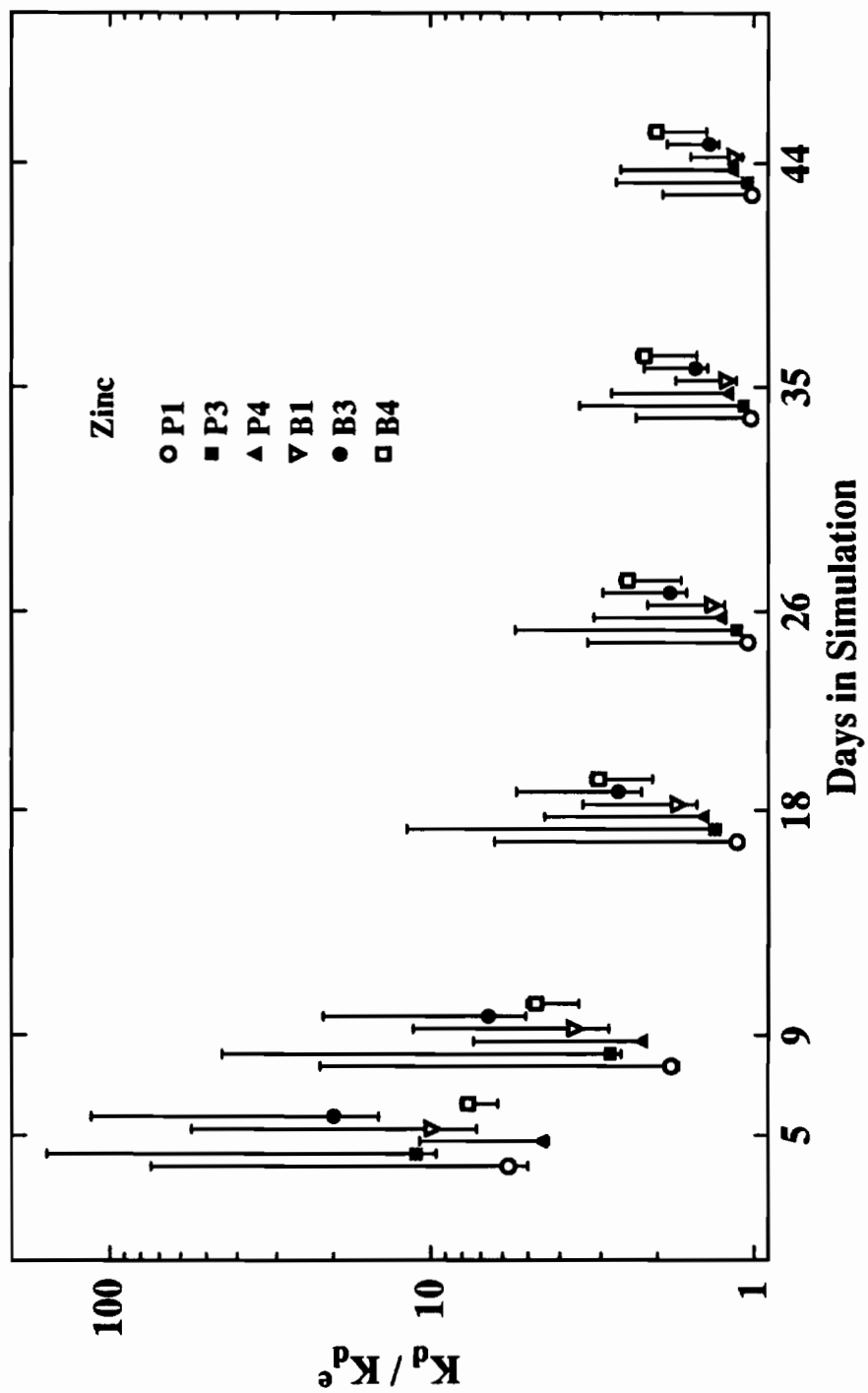


Figure 4.29. Plot of distance from equilibrium as a function of time for zinc. Explanation as in Figure 4.27.

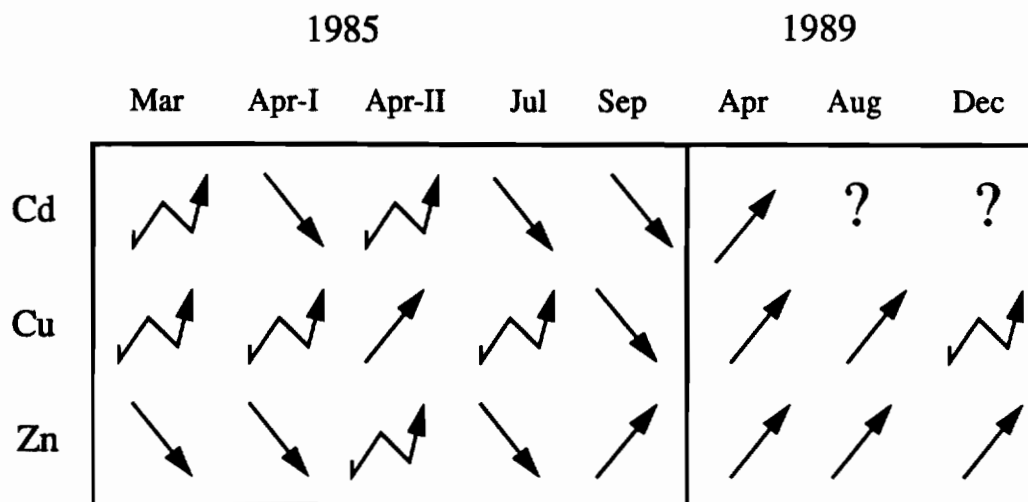


Figure 4.30. Schematic dependence of K_d^a on salinity for all cruises. The jagged arrow indicates an ambiguous relationship; the question mark indicates that there were not enough data points to make a judgement.

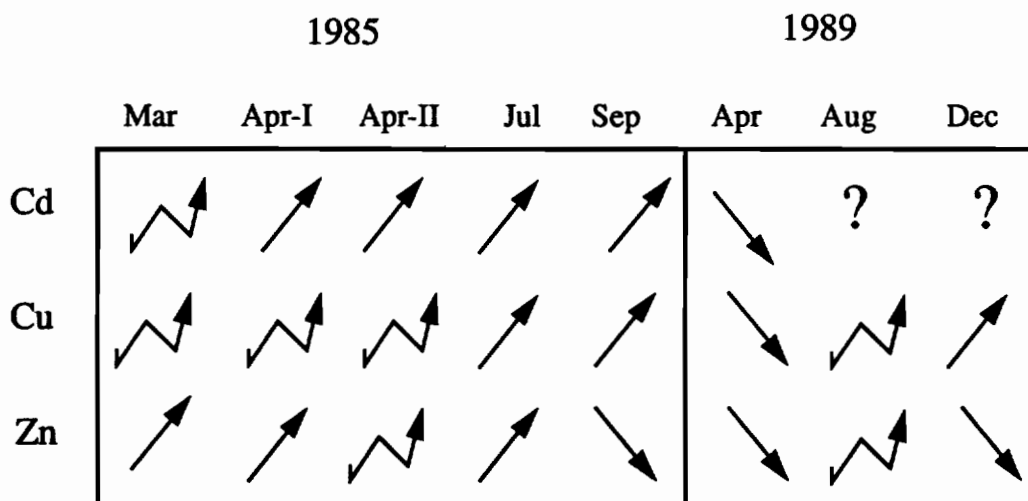


Figure 4.31. Schematic dependence of K_d^a on concentration of suspended solids for all cruises. The jagged arrow indicates an ambiguous relationship; the question mark indicates that there were not enough data points to make a judgement.

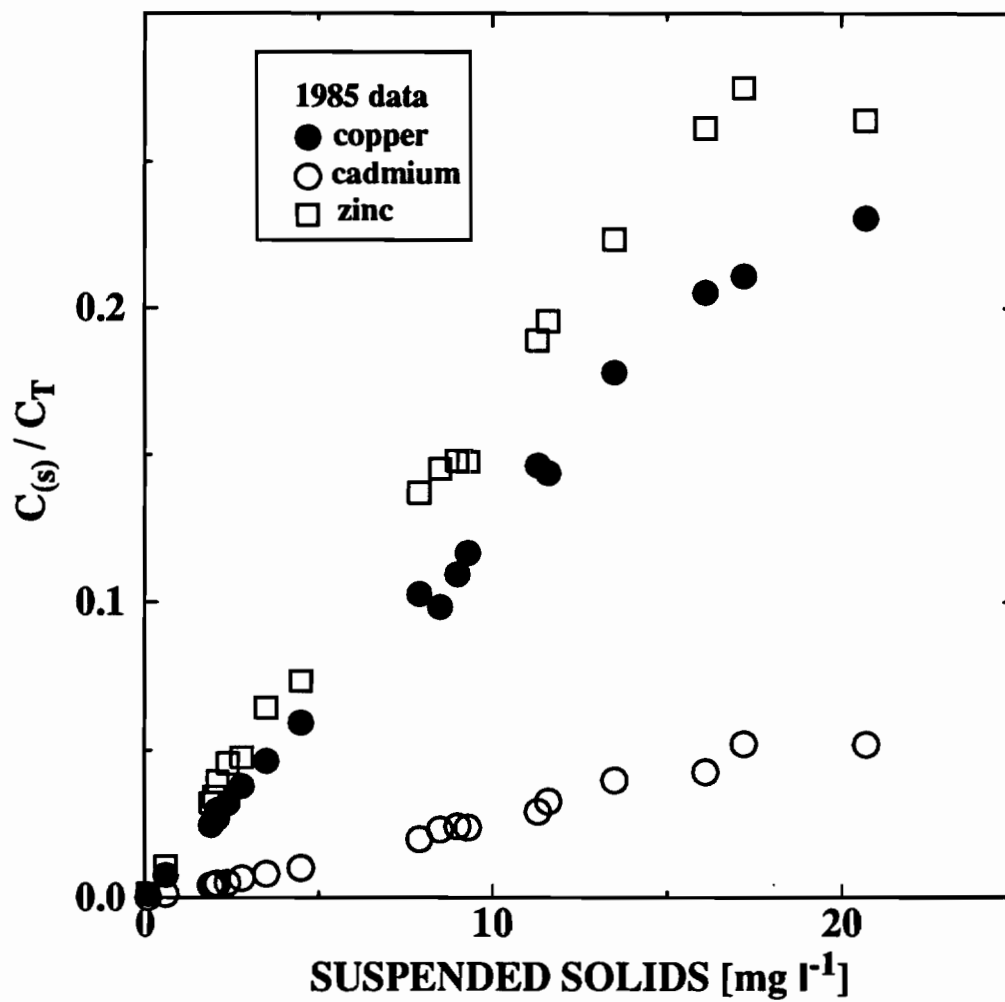


Figure 4.32. Plot of percent mass in the solid phase as a function of suspended solids concentration for 1985 data.

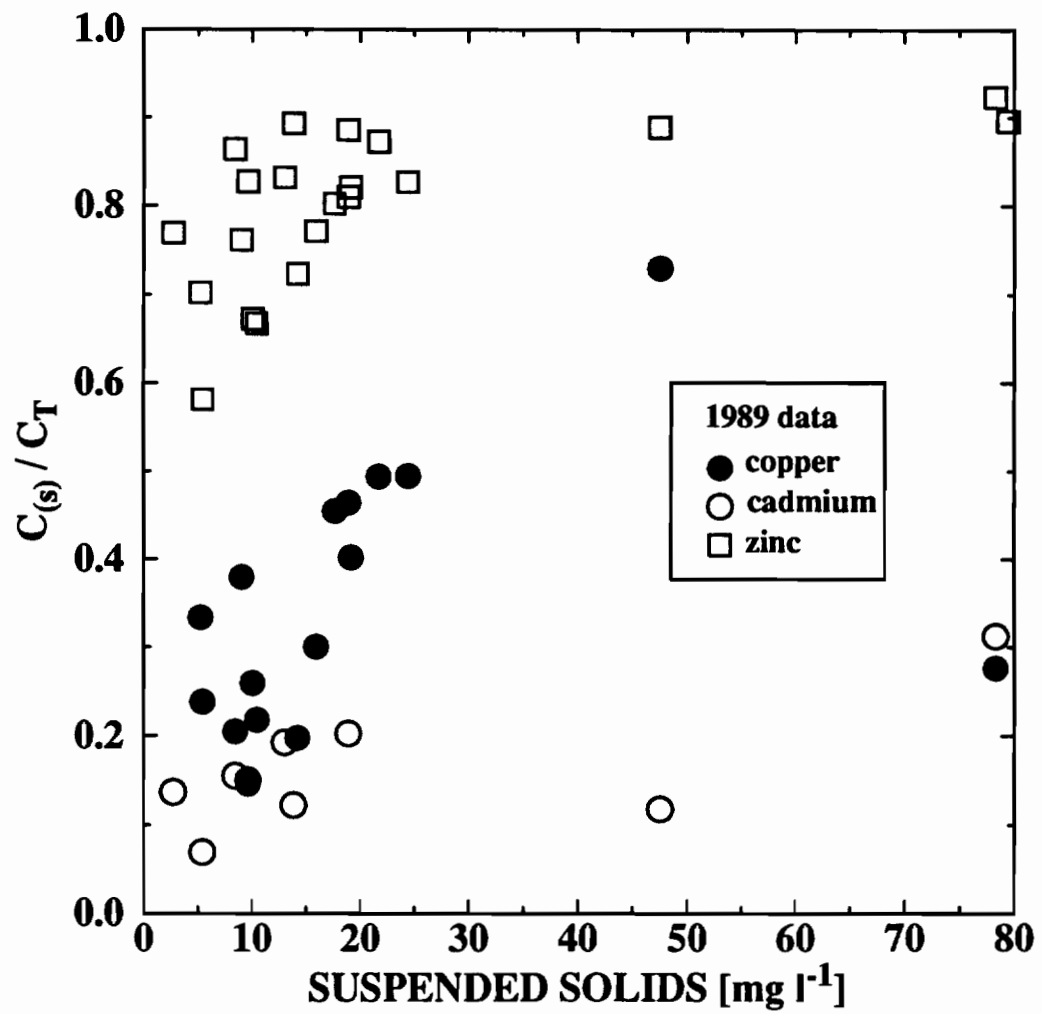


Figure 4.33. Plot of percent mass in the solid phase as a function of suspended solids concentration for 1989 data.

CHAPTER 5

User's Manual

Introduction

ELAmet is a numerical code that solves the depth-averaged advection/dispersion/transformation equation for transport of a nonconservative substance on a finite element grid. An Eulerian/Lagrangian framework is used, which decouples the advection portion of the problem from dispersion and transformation. Consequently, the time step for dispersion can be chosen independently of the time step for transformations, resulting in increased computational efficiency for the cases in which the appropriate time steps for these two portions of the problem are considerable different.

The treatment of the chemical transformations in ELAmet is general enough to accommodate many of the reactions likely to be important in determining the fate and transport of nonconservative substances in estuaries: adsorption via surface complexation or partitioning, aqueous complexation, and acid-base reactions (by considering the proton as an aqueous species). In addition, thermodynamic equilibria and rate-controlled chemical reactions can be simultaneously included, as appropriate. The examples at the end of this report show applications covering many of the possibilities in the type of reaction and the mixture of equilibria and kinetics.

Descriptions of the model are published elsewhere, in particular a detailed description of the transformation equations with some process-oriented context is found in *Wood and Baptista* [1993], along with an introduction to diagnostic application. A discussion of the solution of the transformation equations, along with a discussion of the implications of decoupling the dispersion and transformation time steps is found in *Wood and Baptista* [1992]. In this report, some information is presented which is not found elsewhere, such as the development of the elemental matrix equation used for solving dispersion. The transformation equations are presented in a different manner than elsewhere, focussing on the

way that ELAmet constructs the equations from the input information, with the intent that this will aid users in designing their input.

Potential users are encouraged to study carefully the examples provided in this report, as they have been carefully chosen to demonstrate the capabilities of ELAmet. ELAmet is a relatively flexible code, which allows it to be used in a variety of circumstances, but also puts some burden on the user to design the input information such that ELAmet constructs the correct transformation equations for the problem to be solved.

Governing Equations and Numerical Discretization

Each chemical species in the system is governed by the depth-averaged equation for conservation of mass of a passive, nonconservative tracer of the general form

$$\frac{\partial c_i}{\partial t} + \Lambda(c_i) = \Theta_i + Q_i \quad (5.1)$$

where c_i is any species concentration (mass/volume), Q_i^c represents any internal sources or sinks, Θ_i^c includes all nonconservative chemical transformation terms, and Λ is the depth-averaged advection/dispersion operator

$$\Lambda = u_k \frac{\partial}{\partial x_k} - \frac{1}{h} \frac{\partial}{\partial x_k} (D_{kj} h \frac{\partial}{\partial x_j}) . \quad (5.2)$$

In the above expression D_{kj} is the dispersion coefficient, h is the depth of the water column, and u_k is the depth-averaged velocity. Thus the $\Lambda(c_i)$ term on the left-hand-side of Equation (5.1) describes the change in mass concentration due to an imbalance between mass in and out of a control volume through hydraulic transport processes. The right-hand-side term Θ_i^c describes changes in mass concentration due to chemical transformations that convert mass of one species to mass of another; also included in this term are linear decay terms which represent a net loss of mass, and deposition/erosion terms which transfer mass to the bed sediments.

Using a variation of the Eulerian-Lagrangian methods which are well-developed for conservative tracers, ELAmet solves this compound problem by breaking the original Equation (5.1) into three simpler equations of the form:

$$u_i = \frac{dx_i}{dt}, \quad (5.3)$$

$$\frac{dc_i}{dt} = \Theta_i, \quad (5.4)$$

$$\frac{\partial c_i}{\partial t} = Q_i + \frac{1}{h} \frac{\partial}{\partial x_k} \left(D_{kj} h \frac{\partial c_i}{\partial x_j} \right). \quad (5.5)$$

The first equation is the tracking equation, which is solved once at each node for each time step. A fourth-order Runge-Kutte method is used to track backward to the intersection with the last time step along a characteristic emanating from each node. The second equation is the chemical transformation equation, which essentially solves for the speciation at each node. The third equation is the dispersion equation, which is solved using a Galerkin weighted residual statement on a finite element grid. The tracking routine that solves (5.3) is taken with minor modifications from ELA [Baptista, *et al.*, 1984]. The numerical solutions to (5.4) and (5.5) were developed for ELAmet, and are described below.

Development of Weighted Residual Statement for Dispersion

If we designate the numerical approximation to c as \hat{c} , then the residual of equation (5.5) is written (note that since this development is done for a single species, c_i , we drop the subscript i for convenience):

$$R = \frac{\partial \hat{c}}{\partial t} - \frac{1}{h} \frac{\partial}{\partial x_k} \left(D_{kj} h \frac{\partial \hat{c}}{\partial x_j} \right) - Q. \quad (5.6)$$

Applying a θ -method to discretize (5.6) in time, we get:

$$R = \hat{c}^{(n+1)} - \hat{c}^{(n)} - \theta \Delta t \left\{ \frac{1}{h} \frac{\partial}{\partial x_k} \left(D_{kj} h \frac{\partial \hat{c}}{\partial x_j} \right) + Q \right\}^{(n+1)} - (1 - \theta) \Delta t \left\{ \frac{1}{h} \frac{\partial}{\partial x_k} \left(D_{kj} h \frac{\partial \hat{c}}{\partial x_j} \right) + Q \right\}^{(n)}, \quad (5.7)$$

where the superscript $(n + 1)$ indicates the value at time step $n + 1$, and θ takes a value between 0 and 1. The weighted residual method seeks to solve an equation by minimizing the weighted integral of the residual over the domain; for this equation the weighted residual statement (WRS) derived from integrating R , properly weighted, over the numerical domain, becomes:

$$\sum_{n=1}^{N_e} \left\{ \int_{\Omega_e} w \left[\hat{c}^{(n+1)} - \hat{c}^n - \theta \Delta t \left\{ \frac{1}{h} \frac{\partial}{\partial x_k} (D_{kj} h \frac{\partial \hat{c}}{\partial x_j}) + Q \right\}^{(n+1)} - (1-\theta) \Delta t \left\{ \frac{1}{h} \frac{\partial}{\partial x_k} (D_{kj} h \frac{\partial \hat{c}}{\partial x_j}) + Q \right\}^{(n)} \right] dA_e \right\} = 0 \quad (5.8)$$

We define “pseudo-velocities” as

$$u_j^P = \frac{1}{h} \frac{\partial}{\partial x_k} (h D_{kj}) \quad (5.9)$$

and the dispersion term in (5.8) can be rewritten as

$$\frac{1}{h} \frac{\partial}{\partial x_k} (D_{kj} h \frac{\partial \hat{c}}{\partial x_j}) = u_j^P \frac{\partial \hat{c}}{\partial x_j} + D_{kj} \frac{\partial^2 \hat{c}}{\partial x_j \partial x_k}. \quad (5.10)$$

NOTE: This pseudo-velocity term has exactly the same form as the advection term in the full transport equation, and can be include in tracking, instead of carrying it in the dispersion term. This is how ELAmet was written originally, but problems arose. At the time, these problems were believed to be due to large pseudo-velocities perpendicular to the boundary. Therefore, the pseudo-velocity term has been moved to the dispersion equation in the current version of ELAmet.

The weighted integral of the second-order derivative is reduced by an integration by parts as follows:

$$\begin{aligned} \int_{\Omega_e} w \left(D_{kj} \frac{\partial^2 \hat{c}}{\partial x_j \partial x_k} \right) dA_e &= \int_{\Gamma_e} w D_{kj} \frac{\partial \hat{c}}{\partial x_j} \cdot \hat{n} dS_e - \int_{\Omega_e} \frac{\partial \hat{c}}{\partial x_j} \frac{\partial}{\partial x_k} (w D_{kj}) dA_e \\ &= \int_{\Gamma_e} w D_{kj} \frac{\partial \hat{c}}{\partial x_j} \cdot \hat{n} dS_e - \int_{\Omega_e} \left(D_{kj} \frac{\partial \hat{c}}{\partial x_j} \frac{\partial w}{\partial x_k} + w \frac{\partial \hat{c}}{\partial x_j} \frac{\partial D_{kj}}{\partial x_k} \right) dA_e \end{aligned} \quad (5.11)$$

Substituting expressions (5.10) and (5.11) back into the WRS yields:

$$\sum_{n=1}^{N_e} \left\{ \int_{\Omega_e} [w \hat{c}^{(n+1)} - w \hat{c}^n - \theta \Delta t \Psi^{(n+1)} - (1-\theta) \Delta t \Psi^{(n)}] dA_e - \int_{\Gamma_e} w [\theta \Delta t \Theta^{(n+1)} + (1-\theta) \Delta t \Theta^{(n)}] dS_e \right\} = 0 \quad (5.12)$$

where

$$\Psi = w u_j^p \frac{\partial \hat{c}}{\partial x_j} - D_{kj} \frac{\partial w}{\partial x_k} \frac{\partial \hat{c}}{\partial x_j} - w \frac{\partial D_{kj}}{\partial x_k} \frac{\partial \hat{c}}{\partial x_j} + Q$$

$$\Theta = D_{kj} \frac{\partial \hat{c}}{\partial x_j} \cdot \hat{n}$$
(5.13)

In a manner consistent with the finite element formulation, over each element the values of variables are approximated by the sum of 6 quadratic shape functions weighted by the corresponding nodal values:

$$\hat{c}^{(n+1)} = \sum_{m=1}^6 \phi_m \tilde{c}_m^{(n+1)} = \underline{\phi} \underline{c}^{(n+1)}$$

$$w = \sum_{m=1}^6 \phi_m = \underline{\phi}^T$$

$$D_{kj} = \sum_{m=1}^6 \phi_m \tilde{D}_{kjm} = \underline{\phi} \underline{D}_{kj}$$
(5.14)

These expressions are substituted into the WRS (5.12), and the resulting global matrix equation to be solved for \underline{c} is:

$$\sum_{n=1}^{N_t} \left(\int_{\Omega_e} (M_1 - \theta \Delta t (M_2 + M_3)) dA_e \right) \underline{c}^{(n+1)} = \int_{\Omega_e} (L_1 + (1 - \theta) \Delta t (L_2 + L_3)) dA_e + \int_{\Gamma_e} \underline{B} dS_e$$
(5.15)

where the elemental matrices are:

$$\underline{M}_1 = \underline{\phi}^T \underline{\phi} = \begin{bmatrix} \phi_1 \phi_1 & \dots & \phi_1 \phi_6 \\ \dots & & \dots \\ \phi_6 \phi_1 & \dots & \phi_6 \phi_6 \end{bmatrix}$$
(5.16)

$$\underline{M}_2 = -D_{kj} \frac{\partial \underline{\phi}^T}{\partial x_k} \frac{\partial \underline{\phi}}{\partial x_j} = \begin{bmatrix} \frac{\partial \phi_1}{\partial x_i} \frac{\partial \phi_1}{\partial x_j} & \dots & \frac{\partial \phi_1}{\partial x_i} \frac{\partial \phi_6}{\partial x_j} \\ -D_{kj} \frac{\partial \phi_1}{\partial x_i} \frac{\partial \phi_1}{\partial x_j} & \dots & -D_{kj} \frac{\partial \phi_1}{\partial x_i} \frac{\partial \phi_6}{\partial x_j} \\ \dots & & \dots \\ \frac{\partial \phi_6}{\partial x_i} \frac{\partial \phi_1}{\partial x_j} & \dots & \frac{\partial \phi_6}{\partial x_i} \frac{\partial \phi_6}{\partial x_j} \\ -D_{kj} \frac{\partial \phi_6}{\partial x_i} \frac{\partial \phi_1}{\partial x_j} & \dots & -D_{kj} \frac{\partial \phi_6}{\partial x_i} \frac{\partial \phi_6}{\partial x_j} \end{bmatrix}$$
(5.17)

$$\underline{M}_3 = \left(u_j^P - \frac{\partial D_{kj}}{\partial x_k} \right) \underline{\phi}^T \frac{\partial \underline{\phi}}{\partial x_j} = \begin{bmatrix} \left(u_j^P - \frac{\partial D_{kj}}{\partial x_k} \right) \phi_1 \frac{\partial \phi_1}{\partial x_j} & \cdots & \left(u_j^P - \frac{\partial D_{kj}}{\partial x_k} \right) \phi_1 \frac{\partial \phi_6}{\partial x_j} \\ \cdots & \cdots & \cdots \\ \left(u_j^P - \frac{\partial D_{kj}}{\partial x_k} \right) \phi_6 \frac{\partial \phi_1}{\partial x_j} & \cdots & \left(u_j^P - \frac{\partial D_{kj}}{\partial x_k} \right) \phi_6 \frac{\partial \phi_6}{\partial x_j} \end{bmatrix} \quad (5.18)$$

$$\underline{L}_1 = \underline{\phi}^T (\hat{c}^{(n)} + \theta \Delta t Q^{(n+1)} + (1-\theta) \Delta t Q^{(n)}) = \begin{bmatrix} \phi_1 (\hat{c}^{(n)} + \theta \Delta t Q^{(n+1)} + (1-\theta) \Delta t Q^{(n)}) \\ \cdots \\ \phi_6 (\hat{c}^{(n)} + \theta \Delta t Q^{(n+1)} + (1-\theta) \Delta t Q^{(n)}) \end{bmatrix} \quad (5.19)$$

$$\underline{L}_2 = \underline{\phi}^T \left\{ \left(u_j^P - \frac{\partial D_{kj}}{\partial x_k} \right) \frac{\partial \hat{c}}{\partial x_j} \right\}^{(n)} = \begin{bmatrix} \phi_1 \left\{ \left(u_j^P - \frac{\partial D_{kj}}{\partial x_k} \right) \frac{\partial \hat{c}}{\partial x_j} \right\}^{(n)} \\ \cdots \\ \phi_6 \left\{ \left(u_j^P - \frac{\partial D_{kj}}{\partial x_k} \right) \frac{\partial \hat{c}}{\partial x_j} \right\}^{(n)} \end{bmatrix} \quad (5.20)$$

$$\underline{L}_3 = \left(\frac{\partial \underline{\phi}^T}{\partial x_k} \right) \left\{ D_{kj} \frac{\partial \hat{c}}{\partial x_j} \right\}^{(n)} = \begin{bmatrix} \frac{\partial}{\partial x_k} (\phi_1) \left\{ D_{kj} \frac{\partial \hat{c}}{\partial x_j} \right\}^{(n)} \\ \cdots \\ \frac{\partial}{\partial x_k} (\phi_6) \left\{ D_{kj} \frac{\partial \hat{c}}{\partial x_j} \right\}^{(n)} \end{bmatrix} \quad (5.21)$$

$$\underline{B} = \left[(\theta \Delta t (D_{kj} \frac{\partial \hat{c}}{\partial x_j} \cdot \hat{n})^{(n+1)}) + (1-\theta) \Delta t (D_{kj} \frac{\partial \hat{c}}{\partial x_j} \cdot \hat{n})^{(n)} \right] \underline{\phi}^T = F \underline{\phi}^T = \begin{bmatrix} F \phi_1 \\ \cdots \\ F \phi_6 \end{bmatrix} \quad (5.22)$$

NOTE: When the pseudo-velocities were moved into the dispersion equation, the gradients of D_{kj} cancel each other in equations (5.18) and (5.20). The integrals \underline{M}_3 and \underline{L}_2 reduce to:

$$\underline{M}_3 = \left(\frac{D_{kj} \partial h}{h \partial x_k} \right) \underline{\phi}^T \frac{\partial \underline{\phi}}{\partial x_j}, \quad (5.23)$$

$$\underline{L}_2 = \underline{\phi}^T \left\{ \left(\frac{D_{kj} \partial h}{h \partial x_k} \right) \frac{\partial \hat{c}}{\partial x_j} \right\}^{(n)}. \quad (5.24)$$

In practice, there is the additional problem that since the pseudo-velocities are time-dependent, the mass matrix would have to be inverted at every time step for this formulation. In order to avoid this, integrals \underline{M}_3 and \underline{L}_2 were “turned off”, and replaced with a single RHS integral of the form:

$$\underline{L}_4 = \underline{\phi}^T \left\{ \theta \Delta t \left(\frac{D_{kj} \partial h}{h \partial x_k} \right)^{(n+1)} + (1 - \theta) \Delta t \left(\frac{D_{kj} \partial h}{h \partial x_k} \right)^{(n)} \right\} \left(\frac{\partial \hat{c}}{\partial x_j} \right)^{(n)}, \quad (5.25)$$

resulting in a modified version of (5.15):

$$\sum_{n=1}^{N_e} \left(\int_{\Omega_e} \{ \underline{M}_1 - \theta \Delta t \underline{M}_2 \} dA_e \right) \underline{\epsilon}^{(n+1)} = \int_{\Omega_e} (\underline{L}_1 + \underline{L}_4 + (1 - \theta) \Delta t \underline{L}_3) dA_e + \int_{\Gamma_e} \underline{B} dS_e \quad (5.26)$$

Development of Transformation Equations

In order to understand how the transformation equations are constructed, it is necessary to first understand how all of the various species making up the chemical system in ELAmet are grouped. The grouping has 3 tiers, as indicated in Figure 5.1. First, since ELAmet allows for both chemical equilibrium and rate-controlled reactions, the species in the system must be divided into primary variables and secondary variables, the former being those species participating in rate-controlled kinetics, and the latter being those species that are considered to be in thermodynamic equilibrium with each other. This first grouping follows the stated rule, with the caveat that even if the system is not governed by any rate-controlled reactions, there is still one set of primary variables with a 1 to 1 correspondence to dependent secondary components, as described below. At the next tier the primary system and secondary system are divided into components and derived species; component species being the fundamental units, or “building blocks” from which the derived species are constructed. The components themselves are then divided into dependent and independent components; dependent components are those for which the time-

dependent concentration is part of the solution to the problem; independent component concentrations are supplied to the model at each time step.

All the species in ELAmet are stored in the model in a pre-defined way, as indi-

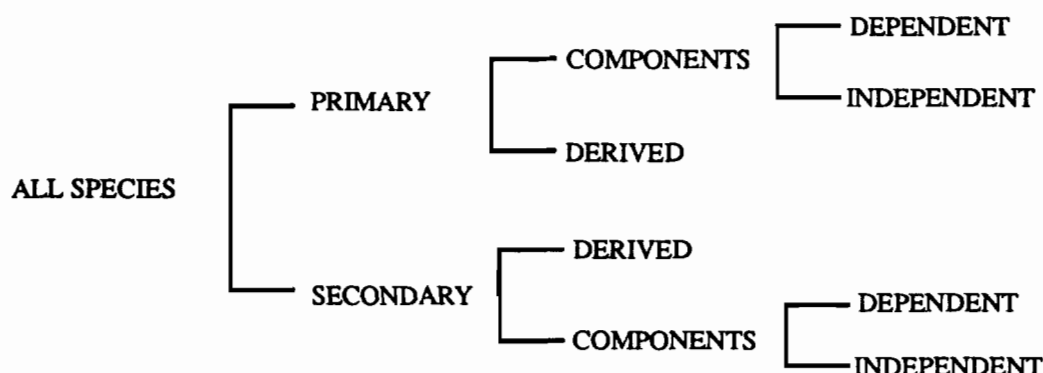


Figure 5.1. Schematic of the grouping of different types of species in ELAmet.

cated in Figure 5.2. This grouping, in combination with the order in which the species information is read into the model, defines the number assigned to each species. As indicated, $nsv1$, $nsv2$, and $nsv3$ are the numbers of secondary dependent components, independent components, and derived species, respectively. The first group of primary derived species, numbering $npv1$ which must also equal $nsv1$, are defined by the following correspondence:

$$\begin{aligned} \text{total concentration of sec. ind. comp.} &\leftrightarrow \text{primary derived species} \\ c_{(T)j} &\leftrightarrow \bar{c}_j \quad j = 1, nsv1 = 1, npv1 \end{aligned} \quad (5.27)$$

Therefore, there will always be at least $npv1$ primary variables. If there are additional primary variables, the number of primary independent components is $npv2$, and the number of additional primary derived species is $npv3$.

Figure 5.2 also indicates the functional difference between derived and component species, which is that each derived species is associated with a mass action equation if it is in the “fast” system, and a kinetic rate equation if it is in the “slow” system. A component species in either the “fast” or “slow” system is associated with a mass balance equation.

The next two sections describe how the input information is used to construct the various equations that are used to solve for the speciation in the secondary system and the

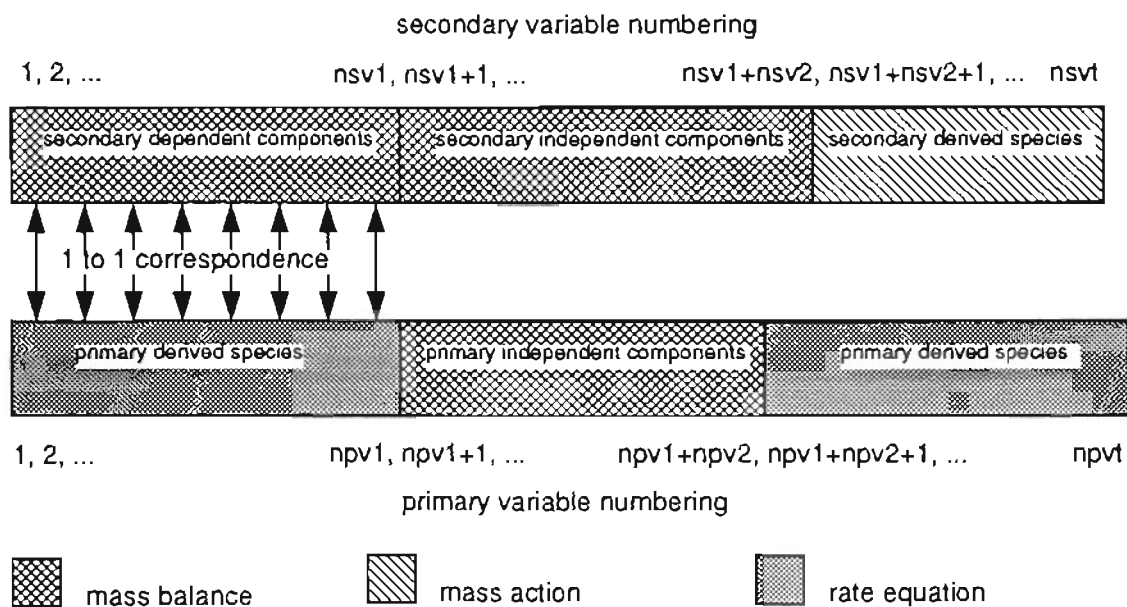
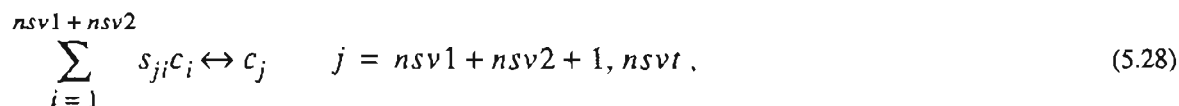


Figure 5.2. Schematic depiction of the order in which species are stored in ELAmet, with an indication of the type of equation used to solve for each type of species.

primary system. The connection between the two is provided by the first $nsv1$ species, as the first set of primary derived species provides the total concentration for the secondary dependent components. Therefore, ELAmet iterates between these two systems until the speciation converges on a solution which is acceptable within the prescribed relative error.

Secondary Equations

ELAmet assumes all secondary derived species are formed through a “fast” reaction of the form:



where s_{ji} is the stoichiometric coefficient of the i^{th} component in the j^{th} derived species, and $nsvt=nsv1+nsv2+nsv3$. From this assumed form of the reaction, and using the stoichiometric coefficients input to ELAmet for each derived species, a mass action equation is constructed for these variables:

$$c_j = K_j \prod_{i=1}^{nsv1+nsv2} c_i^{s_{ji}} . \quad (5.29)$$

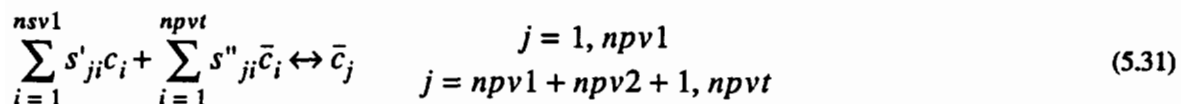
The stoichiometric information is also used to construct the mass balance equation for each secondary component (dependent and independent):

$$c_{(T)j} = \sum_{i=nsv1+nsv2+1}^{nsvt} s_{kj} c_k + c_j \quad j = 1, nsv1 + nsv2 . \quad (5.30)$$

The system of equations constituted by (5.29) and (5.30) is solved using a Newton-Raphson method [Wood and Baptista, 1992].

Primary Equations

ELAmet assumes that each primary derived species is formed through a “slow” reaction involving secondary and/or primary components that is of the form:



where s'_{ji} is the stoichiometric coefficient of the i^{th} secondary dependent component in the j^{th} primary derived species, and s''_{ji} is the stoichiometric coefficient of the i^{th} primary component in the j^{th} primary derived species. The first set of derived species may or may not be associated with a reaction of this form, and ELAmet uses the additional constraint that $c_{(T)j} = \bar{c}_j$ for the first $npv1$ primary species.

ELAmet constructs the rate equation for each species \bar{c}_j in a stepwise fashion. The first step is to place the source terms in the equation for the product species, i.e.

$$\frac{d\bar{c}_j}{dt} = \lambda_j \quad , \quad \lambda_j = \kappa_j^{(f)} \left(\prod_{i=1}^{nsv1} c_i^{s'_{ji}} \prod_{i=1}^{npvt} \bar{c}_i^{s''_{ji}} \right) - \kappa_j^{(b)} \bar{c}_j \quad (5.32)$$

where $\kappa_j^{(f)}$ and $\kappa_j^{(b)}$ are the forward and backward rate constant for the reaction forming the j^{th} primary species, respectively. The values of these rate constants can be zero (but do not have to be) for the first set of primary derived species.

The term indicated in (5.32) appears as a sink term in the equation for each primary derived species that participates in the reaction as a reactant. Therefore, the next step is to cycle through the reactants in (5.31) and place this term as a sink in the corresponding equation (this does not apply to independent components, since they are associated with a mass balance equation). The resulting equation for each of the primary derived species is of the form:

$$\frac{d\bar{c}_j}{dt} = \lambda_j - s''_{kj}\lambda_k. \quad (5.33)$$

In addition, since the first $nsvl$ secondary variables are each associated with a primary variable, the first $npvl$ primary variables may have another term in the corresponding rate equation:

$$\frac{d\bar{c}_j}{dt} = \lambda_j - s''_{kj}\lambda_k - s'_{mj}\lambda_m. \quad (5.34)$$

The final step is to cycle through all derived species and insert linear decay terms and depositional fluxes. Nonzero linear decay or deposition for secondary derived species must be inserted in the primary equations for the corresponding totals. Thus the final form of the rate equations for the primary derived species is :

$$\frac{d\bar{c}_j}{dt} = \lambda_j - s''_{kj}\lambda_k - s'_{mj}\lambda_m - \kappa_j\bar{c}_j - F_j = \Lambda_j. \quad (5.35)$$

where κ_j and F_j are the linear decay constant and the depositional flux term for the j^{th} primary derived species, respectively.

If we now apply a θ -method to discretize Equation (5.35) in time, the result is:

$$\bar{c}_j^{(n+1)} = \bar{c}_j^{(n)} + \theta\Delta t \{ \lambda_j - s''_{kj}\lambda_k - s'_{mj}\lambda_m - \kappa_j\bar{c}_j - F_j \}^{(n+1)} + (1 - \theta)\Delta t\Lambda_j^{(n)}. \quad (5.36)$$

Since the λ_j terms in Equation (5.35) can be nonlinear, it is necessary to linearize them before solving the system of equations. This is done by making the term linear in a single (arbitrary) primary variable, c_i , and computing a coefficient to this linear term using values at the last iteration, i.e.:

$$\lambda_j^{(n+1)} = \kappa_j^{(f)} \left[\left(\left(\prod_{i=1}^{nsv1} c_i^{s'ji} \right) \prod_{i=1}^{npvt} \bar{c}_i^{s''ji} \right) \bar{c}_i^{(s''ji-1)} \right]^{(n')} \bar{c}_i^{(n+1)} - \kappa_j^{(b)} \bar{c}_j^{(n+1)} \quad (5.37)$$

$$\lambda_j^{(n+1)} = \lambda_j' \bar{c}_i^{(n+1)} - \kappa_j^{(b)} \bar{c}_j^{(n+1)} \quad i \neq i'$$

In Equation (5.37) the superscript (n') refers to the value at the last iteration. When all the unknowns are brought to the LHS, the most general form of the resulting equation is:

$$\theta \Delta t \{ (\kappa_j^{(b)} + \kappa_j) \bar{c}_j^{(n+1)} - \lambda_j' \bar{c}_i^{(n+1)} + s''_{kj} (\lambda_k' \bar{c}_i^{(n+1)} - \kappa_k^{(b)} \bar{c}_k^{(n+1)}) + s'_{mj} (\lambda_m' \bar{c}_i^{(n+1)} - \kappa_m^{(b)} \bar{c}_m^{(n+1)}) \} + \bar{c}_j^{(n+1)} + F_j^{(n+1)} = \bar{c}_j^{(n)} + (1 - \theta) \Delta t \Lambda_j^{(n)} \quad (5.38)$$

To complete the system of equations, a set of mass balance equations is needed for each of the primary independent components:

$$\bar{c}_{(T)j} = \sum_{k=1}^{npvt} s''_{jk} \bar{c}_k \quad j = npv + 1, npv1 + npv2 \quad (5.39)$$

The entire system of primary equations is solved in ELAm_{et} using a sparse matrix solver known as Y12M [Zlatev, *et al.*, 1981].

Description of Input Files

The recommended 3-step procedure for designing the chemical system for input to ELAm_{et} is as follows:

Step 1. Group all species in the system into primary variables (those that participate in slow reactions) and secondary variables (those that participate in fast reactions), keeping in mind that, at the very least, there will be the same number of primary variables as there are secondary dependent components, since the first set of primary variables is the total mass concentrations of the secondary dependent components.

Step 2. Having grouped all of the species into the categories above, it is best to list them in the order that they will be read into ELAm_{et}, and assign numbers according to the scheme that ELAm_{et} uses (refer to Figure 5.2). The numbering is important, because the components making up the derived species are defined by their numbers, for input to ELAm_{et}.

Step 3. Gather all of the necessary input information for each species. Input information for each species is determined by the type of variable it is, and this information is summarized in Table 5.1. Note that while initial conditions are essential where they are indicated, as are stability constants and rate constants (even if zero), other information on boundary conditions, internal sources and sinks, and deposition / erosion fluxes are only needed if they apply to the problem at hand. The total mass at each node must be supplied on a time-dependent basis for independent species unless the species can be considered to have a steady-state total mass distribution, in which case the initial conditions are applied at all subsequent times in the simulation. The format for all input files is discussed in this section .

Description of the “.min” file

Table 5.1. Summary of Required Input Information

variable type	A	B	C	D	E	F	G
secondary dep. comp.	×						
secondary indep. comp.	×				×		
secondary derived species				×		×	
primary composite species		×	×				×
primary indep. comp.	×				×		
primary derived species	×	×	×	×			×

A: initial conditions; B: boundary conditions; C: internal sources / sinks; D: deposition / erosion fluxes; E: total mass at each node; F: stability constant; G: rate constants

Table 5.2 shown below is a template for the first input file to ELAmet, which gives the program the run parameters, and the names of other input files to look for. As currently configured, ELAmet assumes that this file has a name with the structure “#####%.min”, where “#####” represents the 5-character alphanumeric grid descriptor, and “%%” is a 2-character alphanumeric run descriptor. It was found that the construction and subsequent modification of this file was aided by breaking the information at logical points with “dummy” lines. In Table 5.2 these lines are shown as a series of stars, i.e. ‘*****’, but the user can substitute any alphanumerics. Comments indicating the type of information that follows might be useful, for example. The program expects these lines to be there, so some type of dummy line must be supplied where indicated.

The user is responsible for choosing a consistent set of units, since ELAmet does not make any assumption about the units used. This means, for example, that if velocity is in m s^{-1} , then the dispersion coefficient should be given in $\text{m}^2 \text{s}^{-1}$. If concentrations are Molar, then all stability constants and rate constants must also be in terms of Molar concentrations, and at boundary nodes where concentration is specified, it must be specified in terms of Molar concentrations. Boundary fluxes must also be consistent: if Molar concentrations are used, then boundary fluxes must be supplied in units of $U \cdot C$, where U has units consistent with those being used for velocity, and C is in moles l^{-1} . If, however, units of concentration are mass m^{-3} , then boundary fluxes would be in units of $\text{mass s}^{-1} \text{m}^{-2}$, and all stability and rate constants would need to be consistent with this concentration convention. Since chemical literature is almost exclusively in terms of molar concentrations, this is the convention used in the examples presented, and the user is strongly encouraged to use this convention as well.

The description of the variables in the template follows. (any variable name in quotes indicates that the line is read in as an alphanumeric):

“grid”	a 5-character alphanumeric grid descriptor
“run”	a 2-character alphanumeric run descriptor
eps	the relative error for tracking
dtmin	minimum time step used in tracking
nts	number of time steps in the run
time0	begin time of the run
dt	dispersion time step
theta	value of θ (0 to 1) used in time discretization
isttr	time step at which to start tracking
ifeet	0: do not save feet information from tracking; 1: save feet information from tracking (or read in old feet information)

irptr	in the case that feet values will be repeated, the number of time steps in the repeat cycle (if feet values are not repeated, this is a dummy variable)
“feetfile”	name of file containing feet information, or file to which feet information should be written
epsilon	relative error for the chemical transformations
nperts	number of chemical transformation time steps per dispersion time step
ivel	0: read in time-dependent velocities; 1: velocities are steady-state; 2: compute velocities from frequency-domain information (TEA-NL output); only ivel=2 option is currently active
idisp	0: read in time-dependent values for each node; 1: read in steady-state value for each node; 2: compute from a prescribed function; 3: dispersion is time- and space- independent; all options except idisp=2 are currently active
ibd	0: read in time-dependent boundary conditions; 1: boundary conditions are steady-state
disp1	time- and space-independent dispersion coefficient: D_{xx} ; if idisp \neq 3 this is a dummy variable
disp2	time- and space-independent dispersion coefficient: D_{yy} ; if idisp \neq 3 this is a dummy variable
disp3	time- and space-independent dispersion coefficient: $D_{xy}=D_{yx}$; if idisp \neq 3 this is a dummy variable
nsto	number of time steps for which a complete concentration field will be saved
nst(nsto)	array containing the time steps for which a complete concentration field will be saved (there must be nsto values); dummy line if nsto=0
nrefsamp	number of sampled nodes at which a time series of concentration will be saved

ntsamp sampling interval in number of time steps (sampling always starts at the first time step, skipping the initial conditions)

jref(nrefsamp) sampled nodes; dummy line if nrefsamp=0

“pts_file” name of file to which concentration time series at sampled nodes will be written; dummy line if nrefsamp=0

itq type of quadrature used (currently only Gaussian is operative)

nqp number of quadrature points (currently only 7 is operative)

hcor correction to depth at MLLW

nsv1 number of dependent secondary components

Next 3 lines repeated nsv1 times:

“sfile_sta” name of file containing initial values

isout 0: do not write out concentration field for this species; 1: do write out concentration field for this species

“sfile_cnc” name of file to which concentration field for this variable will be written (this is a dummy variable if isout=0)

nsv2 number of independent secondary components

Next 5 lines repeated nsv2 times:

“sfile_sta” name of file containing initial values

istot 0: nodal values for this dependent variable are time-dependent; 1: nodal values for this dependent variable are time-independent

“sfile_tot” if istot=1, name of file from which time-dependent nodal values will be read; otherwise, this is a dummy variable

isout 0: do not write out concentration field for this species; 1: do write out concentration field for this species

“sfile_cnc” if isout=1, name of file to which concentration field for this variable will be written; otherwise, this is a dummy variable

nsv3 number of derived secondary variables

Next 4 lines repeated nsv3 times:

isdep 0: no deposition associated with this species; 1: nodal values of deposition are time-independent; 2: nodal values of deposition are time-dependent

“sfile_dep” name of file containing time-dependent or time-independent nodal deposition values; if isdep=0, this is a dummy variable

isout 0: do not write out concentration field for this species; 1: do write out concentration field for this species

“sfile_cnc” name of file to which concentration field for this variable will be written (this is a dummy variable if isout=0)

*From * to ** repeated for k=1,nsv3:*

*

i1 number of secondary component species making up the kth secondary derived species

Next line repeated i1 times:

j, sdvmbe(k,j) j is the number of the derived species; sdvmbe is the stoichiometric coefficient of the derived species in the component species

keq stability constant for the kth derived species

sdvdec linear decay constant for the kth derived species

**

npv1 number of dependent primary component species; must be equal to nsv1

Table 5.2. Template of “.min” File

line #	variable
1	“grid”
2	“run”
3	eps, dtmin
4	nts, time0, dt, alpha
5	isttr, ifeet, irptr
6	“feetfile”
7	epsilon, nperts
8	ivel, idisp, ibd
9	disp1, disp2, disp3
10	nsto
11	nst(i),i=1,nsto
12	nrefsamp, ntsamp
13	jref(i),i=1,nrefsamp
14	“pts_file”
15	itq, nqp
16	hcor
17	*****
18	nsv1
&	“sfile_sta”
	isout
&&	“sfile_cnc”

	nsv2
%	“sfile_sta”
	istot
	“sfile_tot”
	isout
%%	“sfile_cnc”

	nsv3
@	isdep
	“sfile_dep”
	isout
@@	“sfile_cnc”

@	i
^	j, sdvmbc(k,j)
	keq
@@	sdvdec

	npv1
&	jbd
	“pfile_bnd”
	ipout
	“pfile_cnc”
	isrc
&&	“pfile_src”

Table 5.2. con’t.

line #	variable

	npv2
!	“pfile_sta”
	iptot
	“pfile_tot”
	ipout
!!	“pfile_cnc”

	npv3
#	“pfile_sta”
	jbd
	“pfile_bnd”
	ipout
	“pfile_cnc”
	isrc
	“pfile_src”
	ipdep
##	“pfile_dep”

~	i1
+	j, s3(j,k)
	i2
-	j, s4(j,k)
	forwrd, bakwrd
~~	pdvdec

\$	i1
+	j, s3(j,k)
	i2
-	j, s4(j,k)
	forwrd, bakwrd
\$\$	pdvdec
	key:
	repeat & to && nsv1 times
	repeat % to %% nsv2 times
	repeat @ to @@ nsv3 times
	repeat ^ i times
	repeat ! to !! npv2 times
	repeat # to ## npv3 times
	repeat ~ to ~~ npv1 times
	repeat + i1 times
	repeat - i2 times
	repeat \$ to \$\$ npv3 times

Next 6 lines repeated npv1 times:

- jbd** 0: no concentration boundary conditions applied for this species; 1: concentration boundary conditions are time-independent; 2: concentration boundary conditions are time-dependent
- “pfile_bnd”** name of file containing concentration boundary conditions
- ipout** 0: do not write out concentration field for this species; 1: do write out concentration field for this species
- “pfile_cnc”** name of file to which concentration field for this variable will be written (this is a dummy variable if isout=0)
- isrc** 0: no internal source for this species; 1: nodal values of internal source for this species are time-independent; 2: nodal values of internal source for this species are time-dependent
- “pfile_src”** name of file containing nodal values of time-dependent or time-independent source
- npv2** number of independent primary component species

Next 5 lines repeated npv2 times:

- “pfile_sta”** name of file containing initial values
- iptot** 0: nodal values for this dependent variable are time-dependent; 1: nodal values for this dependent variable are time-independent
- “pfile_tot”** if istot=1, name of file from which time-dependent nodal values will be read; otherwise, this is a dummy variable
- ipout** 0: do not write out concentration field for this species; 1: do write out concentration field for this species
- “pfile_cnc”** name of file to which concentration field for this variable will be written (this is a dummy variable if isout=0)

npv3 number of derived primary species

Next 9 lines repeated npv3 times:

“pfile_sta” name of file containing initial values

jbd 0: no concentration boundary conditions applied for this species; 1: concentration boundary conditions are time-independent; 2: concentration boundary conditions are time-dependent

“pfile_bnd” name of file containing concentration boundary conditions

ipout 0: do not write out concentration field for this species; 1: do write out concentration field for this species

“pfile_cnc” name of file to which concentration field for this variable will be written (this is a dummy variable if isout=0)

isrc 0: no internal source for this species; 1: nodal values of internal source for this species are time-independent; 2: nodal values of internal source for this species are time-dependent

“pfile_src” name of file containing nodal values of time-dependent or time-independent source

ipdep 0: no deposition associated with this species; 1: nodal values of deposition are time-independent; 2: nodal values of deposition are time-dependent

“pfile_dep” name of file containing time-dependent or time-independent nodal deposition values; if isdep=0, this is a dummy variable

From & to && repeated for $k=1,npv1$ and $k=npv1+npv2+1,npv3$:

&

i1 number of secondary component species making up the k^{th} primary derived species

Next line repeated i1 times:

$j, s3(j,k)$ number of the secondary component species; stoichiometric coefficient of the secondary component species in the k^{th} primary derived species

$i2$ number of primary component species making up the k^{th} primary derived species

Next line repeated $i2$ times:

$j, s4(j,k)$ number of the primary component species; stoichiometric coefficient of the primary component species in the k^{th} primary derived species

forwrđ forward rate constant for the k^{th} primary derived species

bakwrđ backward rate constant for the k^{th} primary derived species

pđvdec decay constant for the k^{th} primary derived species

&&

Format of Other Input Files

boundary file:

line 1 time

line 2 ncbp: number of boundary nodes where concentration is applied

next ncbp lines node #, concentration value

next line nfbp: number of boundary elements where flux conditions are applied

next nfbp lines middle node # of boundary element, normal flux perpendicular to element, positive into the domain, negative out of domain

initial conditions file:

line 1 time

next nnd lines node #, concentration value (nnd=number of nodes in grid)

Flow Field Input

ELAmet is currently configured to accept only a flow field generated by TEA-NL [Westerink, et al. 1988], in the standard “.tou” format. However, the convention used in ELAmet is that when computing the x and y components of velocity the phases are added, not subtracted, so care must be taken to ensure that the correct convention is used.

File Unit Numbers

The following unit numbers are currently reserved for specific files in ELAmet:

unit 1	“feetfile”; remains OPEN
unit 3	“sfile_sta”, “sfile_dep”, “pfile_sta”, “pfile_dep”; CLOSED after initialization
unit 4	“flowfile”; CLOSED after initialization (ELAmet currently configured for frequency-domain TEA-NL output, so frequency information is only read in once)
unit 7	“.min” file; CLOSED after initialization
unit 10	“pts_file”; remains OPEN
units 11-40	reserved for “sfile_cnc”; remains OPEN; however, only as many units are needed as there are secondary variables
units 41-?	reserved for “pfile_cnc”; remains OPEN; however, only as many units are needed as there are primary variables

Currently, the unit numbers on files containing time-dependent independent variable information that must be kept OPEN and read at every time step are set high enough to cause a compile-time error. This is because there have been problems in the past, when many species are used, with running out of unit numbers. If the unit numbers of files to be read in at every time step are needed, then care will be required in designing the system, and hardcoding the unit numbers such that there are no conflicts.

Running ELAmet

ELAmet takes 3 command-line arguments: the 5-character alphanumeric grid descriptor, the 2-character alphanumeric flow descriptor (currently a TEANL file), and the 2-character alphanumeric run descriptor. These arguments allow the program to find the “.min” file and the “.tou” file. For example, if the name of the input file is “test111.min” and the name of the flow file is “test110.tou”, then the command line for running the model would be: “elamet test1 10 11”.

The only changes to the code itself, before compiling, are: 1) in “param.com” file, designate the number of nodes, number of boundary nodes, number of elements, number of frequencies, and maximum number of species; 2) in “tracking.f” edit all PARAMETER statements to match the number of nodes, elements, and boundary nodes in “param.com”.

Output File Description

The output files containing the complete concentration field information have the “.cnc” format. These are binary files. The first line is an integer code, “22”. The second line is the number of nodes in the grid. The third line is the number of time steps the file contains. The fourth line contains the time of the first concentration field written out. The fifth line contains the concentration field itself. The last two lines are repeated for every time step at which the concentration was written out.

The only other output file is the “.pts” file, which, if used, is an ASCII file containing one line for each time step in the simulation. The first column is the time, and the rest of the columns contain the concentrations of each of the independent variables (secondary variables first, then primary variables) at each node specified, in the order in which the nodes were specified. In the case that many species are involved, specifying more than one or two nodes will result in a very large “.pts” file, since each of the independent species concentrations are written out for each node.

Example Applications

The following example applications are provided to demonstrate the use of ELAmet for several systems. The examples were chosen to demonstrate different aspects of the model. For the 1D simulations, a 10 km by 200 m grid is used, such that the domain can be considered 1-dimensional in x . A uniform velocity of 0.02 m s^{-1} flows through the domain in the positive x direction. Thus “upstream” refers to the boundary located at $x = 0$, and “downstream” refers to the boundary at $x = 10 \text{ km}$.

1D Carbonate System

This system contains only equilibrium speciation. This system demonstrates the use of ELAmet to solve a simplified carbonate system. This system is constructed such

that the single component species is the hydroxide ion, and the resulting mass balance equation is that for Alkalinity. Therefore the boundary condition, which is applied in terms of $[OH^-]_T$, is the condition of upstream Alkalinity, and Alkalinity is conserved throughout the domain. The system is initially at 2.4×10^{-3} M Alk, which is close to an oceanic value, and the upstream boundary condition applied is 10^{-3} M Alk, which is close to an average riverine value. Table 5.3 lists the equations making up this system, and the input file, called "test111.min", is listed in Table 5.4. Note that in Table 5.4, concentration units have been converted to μM .

A profile of the concentration of the species included in this system along the

Table 5.3. Equations for Carbonate System

Secondary Variables

Dependent Components:

species #	Equation
-----------	----------

1	$[OH^-]_T = [HCO_3^-] + 2[CO_3^{2-}] + [OH^-] - [H^+] = Alk$
---	--

Independent Components: None

Derived Species

species #	Equation	K	ref
2	$[HCO_3^-] = K[OH^-]$	$10^{2.97}$	a
3	$[CO_3^{2-}] = K[OH^-]^2$	$10^{7.7} \text{ M}^{-1}$	a
4	$[H^+] = K[OH^-]^{-1}$	$10^{-13.75} \text{ M}^2$	b

^a Stumm and Morgan (1982), Tables 4.7-4.9, seawater at 19ppt chlorinity and 20° C.

^b Ion product of water, corrected to $I=0.7$ M using the Davies equation.

length of the domain after 50 time steps, at which time a boundary condition moving by advection only will have intruded 3.6 km into the domain, is shown in Figure 5.3. This figure demonstrates that pH varies from about 8 to 8.3 from the "riverine" to "ocean" end of the domain, and for these pH's $[HCO_3^-]$ clearly dominates the alkalinity. However, the stability constants for this example have been chosen to correspond to high salinities, and therefore it is of interest to know the range in alkalinity over which this approximation is adequate. To demonstrate this, we plot in Figure 5.4 the ELAmet results with the results of a calculation made with the salinity-dependent expressions for the carbonate stability constants found in *Mook and Koene* [1975]. To do this, it was assumed that "riverine" water of salinity 0 ppt and 10^{-3} M Alk mixes conservatively with "ocean" water of salinity 35

ppt and 2.4×10^{-3} M Alk. Figure 5.4 shows that the use of the carbonate stability constants in Table 5.3 should really be restricted to about 1.8×10^{-3} to 2.4×10^{-3} M Alk. This demonstrates some of the problems which will be encountered in applying ELAmet to highly dynamic estuarine situations in which the salinity can vary a great deal.

NOTE: ELAmet can be hardcoded to handle stability constants which depend in some defined way on one or more species in the system. However, this has to be done specifically for the particular system under consideration. The subroutine "fkeq.f" can be used in this way (otherwise, this routine is a "do-nothing" routine). This is, for example, where activity corrections to thermodynamic constants could logically be made. However, since altering "fkeq.f" involves changing the code, it should only be done if absolutely necessary, and with EXTREME CARE.

Table 5.4 Test111.min		22	*****	46	1
line #	entry	23	0	47	1 -1
<hr/>		24	*****	48	0.018
1	test1	25	3	49	0.0
2	11	26	0	50	*****
3	0.001, 1.	27	xxxxxxxxxxxxxxx	51	1
4	50, 0.0, 3600.0, 1.	28	1	52	1
5	1, 1, 1	29	test111.HCO3.cnc	53	test111.Alk.bnd
6	test110.feet	30	0	54	1
7	0.00001 1	31	xxxxxxxxxxxxxxx	55	test111.Alk.cnc
8	2, 3, 1	32	1	56	0
9	10., 10., 0.	33	test111.CO3.cnc	57	xxxxxxxxxxxxxxx
10	1	34	0	58	*****
11	50	35	xxxxxxxxxxxxxxx	59	0
12	0, 1	36	1	60	*****
13	0	37	test111.H.cnc	61	0
14	xxxxxxx	38	*****	62	*****
15	1, 7	39	1	63	1
16	1.	40	1 1	64	1 1
17	*****	41	933.3	65	0
18	1	42	0.0	66	0.0, 0.0
19	test112.Alk.sta	43	1	67	0.0
20	1	44	1 2		
21	test111.OH.cnc	45	50.12		

ID Copper System

The next system demonstrates the use of a larger set of species, and independent components. This system involves the aqueous speciation of copper, under oceanic condi-

tions (as defined by salinity and Alkalinity), and varying concentrations of dissolved organic ligand, denoted as $[Hu]$. The conversion from mg l^{-1} to moles of available ligand sites per liter is taken to be 10^{-6} moles ligand sites per mg humic material [McKnight, et al., 1983; Davis, 1984]. Therefore, the upstream boundary condition placed on $[Hu]$ is $2.5 \mu\text{M}$, corresponding to 2.5 mg l^{-1} of dissolved humic material. The concentration of SO_4^{2-} is held constant throughout the domain at $28.2 \times 10^3 \mu\text{M}$, corresponding to a salinity of 35 ppt; the alkalinity is held constant throughout the domain at $2.4 \times 10^3 \mu\text{M}$, corresponding to average oceanic conditions. The total copper concentration is held constant at $0.09 \mu\text{M}$. The input file for this system is given in Table 5.5, and the governing equations in Table 5.6.

Again the simulation is run for 50 1-hour time steps, at which point there is a relatively smooth transition from the initial condition in $[Hu]$ at the downstream boundary to the upstream condition. Concentration profiles for the copper species, in terms of percent total copper at this point in the simulation, are shown in Figure 5.5. These profiles show that as the upstream boundary is approached, organically-complexed copper dominates the speciation by more than 99%. Figure 5.6 further illustrates how the distribution of mass between the two dominant copper species is controlled by the concentration of humic material along the domain. The control of copper speciation by dissolved organic ligands has been documented [van den Berg, 1984; van den Berg, et al., 1987].

1D Zinc System

In this example system, equilibrium aqueous speciation is mixed with adsorption kinetics. The equations for the system are given in Table 5.7, and the input file is listed in Table 5.8. The concentration of dissolved humic material and the major seawater ions SO_4^{2-} and Cl^- are as in the last example. The total concentration of metal is held constant throughout the domain at $.003 \mu\text{M}$. In addition, this example uses the concentration of total suspended solids, $[TSS]$, which is held constant throughout the domain at 50 mg l^{-1} . Note that there is an inconsistency in the units of the mass balance equation for $[TSS]$, since all other concentrations are in μM . This inconsistency would be eliminated if, for example, the weight of suspended solids were converted to moles of surface sites per liter,

Table 5.5. Test112.min		49	1	100	0.0
line #	entry	50	test112.CuCO3.cnc	101	2
		51	0	102	1 1
1	test1	52	xxxxxxxxxxxx	103	2 1
2	12	53	1	104	1.66e3
3	0.001,1	54	test112.CuOH.cnc	105	0.0
4	50, 0.0, 3600., 1.	55	0	106	1
5	1, 1, 1	56	xxxxxxxxxxxx	107	3 1
6	test110.feet	57	1	108	933.3
7	0.00001 1	58	test112.Cu(OH)2.cnc	109	0.0
8	2, 3, 1	59	0	110	1
9	10., 10., 0.	60	xxxxxxxxxxxx	111	3 2
10	1	61	1	112	50.12
11	50	62	test112.CuHu.cnc	113	1
12	0, 1	63	0	114	3 -1
13	0	64	xxxxxxxxxxxx	115	0.018
14	xxxxxxxxxxxx	65	1	116	0.0
15	1, 7	66	test112.HCO3.cnc	117	*****
16	1.	67	0	118	2
17	*****	68	xxxxxxxxxxxx	119	1
18	2	69	1	120	test112.CuT.bnd
19	test112.Cu.sta	70	test112.CO3.cnc	121	1
20	1	71	0	122	test112.CuT.cnc
21	test112.Cu.cnc	72	xxxxxxxxxxxx	123	0
22	test112.Hu.sta	73	1	124	xxxxxxxxxxxx
23	1	74	test112.H.cnc	125	1
24	test112.Hu.cnc	75	*****	126	test112.HuT.bnd
25	*****	76	2	127	1
26	2	77	1 1	128	test112.HuT.cnc
27	test112.OH.sta	78	4 1	129	0
28	0	79	2.e-5	130	xxxxxxxxxxxx
29	xxxxxxxxxxxx	80	0.0	131	*****
30	1	81	2	132	0
31	test112.OH.cnc	82	1 1	133	*****
32	test112.SO4.sta	83	3 1	134	0
33	0	84	4.7e-2	135	*****
34	xxxxxxxxxxxx	85	0.0	136	1
35	1	86	2	137	1 1
36	test112.SO4.cnc	87	1 1	138	0
37	*****	88	3 2	139	0.0, 0.0
38	9	89	28.2	140	0.0
39	0	90	0.0	141	1
40	xxxxxxxxxxxx	91	2	142	2 1
41	1	92	1 1	143	0
42	test112.CuSO4.cnc	93	3 1	144	0.0, 0.0
43	0	94	0.98	145	0.0
44	xxxxxxxxxxxx	95	0.0	146	0
45	1	96	2	147	*****
46	test112.CuHCO3.cnc	97	1 1		
47	0	98	3 2		
48	xxxxxxxxxxxx	99	0.11		

Table 5.6. Equations for Copper System

Secondary Variables

Dependent Components:

species #	Equation
1	$[Cu^{2+}]_T = [CuSO_4] + [CuHCO_3^+] + [CuCO_3] + [CuOH^+] + [Cu(OH)_2] + [CuHu]$
2	$[Hu]_T = [Hu] + [CuHu]$

Independent Components:

3	$[OH^-]_T = [HCO_3^-] + 2[CO_3^{2-}] + [OH^-] - [H^+] + 2[CuCO_3] + [CuOH^+] + 2[Cu(OH)_2] + [CuHCO_3^+]$
4	$[SO_4^{2-}]_T = [CuSO_4] + [SO_4^{2-}]$

Derived Species

species #	Equation	K	ref
5	$[CuSO_4] = K[Cu^{2+}][SO_4^{2-}]$	$10^{1.3} M^{-1}$	b
6	$[CuHCO_3^+] = K[Cu^{2+}][OH^-]$	$10^{1.7} \times 10^{2.97} M^{-1}$	a,b
7	$[CuCO_3] = K[Cu^{2+}][OH^-]^2$	$10^{5.75} \times 10^{7.7} M^{-2}$	a,c
8	$[CuOH^+] = K[Cu^{2+}][OH^-]$	$10^{5.99} M^{-1}$	c
9	$[Cu(OH)_2] = K[Cu^{2+}][OH^-]^2$	$10^{11.04} M^{-2}$	c
10	$[CuHu] = K[Cu^{2+}][Hu]$	$10^{9.22} M^{-1}$	b
11	$[HCO_3^-] = K[OH^-]$	$10^{2.97}$	a
12	$[CO_3^{2-}] = K[OH^-]^2$	$10^{7.7} M^{-1}$	a
13	$[H^+] = K[OH^-]^{-1}$	$10^{-14} M^2$	

^a Stumm and Morgan (1982), Tables 4.7-4.9, seawater at 19ppt chlorinity and 20° C.

^b Mantoura, et al. (1978)

^c Sunda and Hanson (1979)

which implies specifically the surface complexation mechanism for adsorption. However, it is common, especially for “natural” particles, for distribution coefficients and rate constants to be quoted in terms of $l\ mg^{-1}$, and in such cases the use of mass of *TSS* instead of moles of surface sites is not only more convenient, but likely more accurate if a good conversion to surface sites per kg solid is not available. The way that this situation should be handled is to use units for suspended solids concentration that will assure that the mass balance is highly dominated by $[TSS]$, as indicated in Table 5.7, so that the solid-phase metal species will not significantly deplete the available mass of suspended solids, which would be unphysical. In this example, since $[TSS]_T$ is $50\ mg\ l^{-1}$, and $[Zn]_T$ is $.003\ \mu M$,

is it clear that the concentration of $[Zn_{(s)}]$ will never significantly alter the mass balance of suspended solids.

The purpose of this example, in addition to demonstrating the use of mixed equilibrium- and kinetically-controlled reactions, is to demonstrate an important point about the use of the first *nsvl* species in the secondary system and the first *npvl* species in the primary system. This example was run twice; as indicated in Table 5.7 the first run specified that the rate of adsorption would be proportional to the concentration of total dissolved zinc, and in the second (alternate) run the rate of adsorption was specified to be proportional to only the uncomplexed Zn^{2+} ion. Referring to Table 5.8, this is done by specifying a primary component in the first case, and a secondary component in the second case. This distinction is important, since literature values of rate constants are often quoted in terms of total dissolved metal, but the most important adsorbing metal species, especially if the surface complexation model is employed, is usually presumed to be the uncomplexed metal ion. Therefore care must be taken in understanding the precise equation being used for the adsorption, and whether it is consistent with the rate constants being supplied.

This simulation was again run for 50 1-hour time steps. Figure 5.7 shows the profile of concentrations when the rate of adsorption is proportional to total dissolved metal, and Figure 5.8 shows the profile of concentrations when the rate of adsorption is proportional to the uncomplexed metal ion. It is clear that the proportion of the total mass of metal that is partitioned to the solid phase is significantly different in these two cases. This is further illustrated in Figure 5.9, where the measured distribution coefficient, defined as $[Zn(s)] / ([TSS][Zn^{2+}]_T)$ along the transect is plotted for both cases. Near the downstream boundary, representing conditions that have had the longest time to equilibrate, the measured distribution coefficients differ by a factor of 3.

This effect is even more important for a system in which the uncomplexed metal ion makes up a much smaller proportion of the total dissolved metal, as illustrated by the cadmium system. The species and corresponding equations for this system are given in Table 5.7. At a time 50 hours into the simulation, the concentration profiles are as shown in Figure 5.10 and Figure 5.11, for an adsorption rate proportional to total dissolved metal, and uncomplexed metal ion, respectively. For the cadmium system, a far greater proportion of the dissolved metal is found in aqueous complexes with the chloride ion. As seen in

Figure 5.12, this results in more than an order of magnitude of difference in the distribution coefficient between the case of adsorption proportional to total dissolved metal, and the case of adsorption proportional to the uncomplexed metal ion.

1D Tin System

Table 5.7. Equations for Zinc System

Secondary Variables

Dependent Components:

species #	Equation
1	$[Zn^{2+}]_T = [ZnCl^+] + [ZnSO_4] + [ZnHu] + [Zn_{(s)}]$
2	$[Cl^-]_T = [Cl^-] + [ZnCl^+]$
3	$[SO_4^{2-}]_T = [ZnSO_4] + [SO_4^{2-}]$
4	$[Hu]_T = [Hu] + [ZnHu]$
5	$[TSS]_T = [TSS] + [Zn_{(s)}] \approx [TSS]$

Independent Components: None

Derived Species:

species #	Equation	K	ref
6	$[ZnCl^+] = K [Zn^{2+}] [Cl^-]$	$10^{0.11} M^{-1}$	a
7	$[ZnSO_4] = K [Zn^{2+}] [SO_4^{2-}]$	$10^{1.3} M^{-1}$	a
8	$[ZnHu] = [Zn^{2+}] [Hu]$	$10^{4.8} M^{-1}$	b

Primary Variables

Derived Species:

species #	Equation	κ_f	κ_b	ref
6	$[Zn(s)]_t = \kappa_f [Zn^{2+}] [TSS] - \kappa_b [Zn(s)]$	$10^{-4.6} l mg^{-1} hr^{-1}$	$10^{-1.6} hr^{-1} c$	c
6 (alt)	$[Zn(s)]_t = \kappa_f [Zn^{2+}]_T [TSS] - \kappa_b [Zn(s)]$	$10^{-4.6} l mg^{-1} hr^{-1}$	$10^{-1.6} hr^{-1} c$	c

^a Smith and Martell (1976)

^b Mantoura, et al. (1978)

^c Nyfeller, et al. (1984)

$[\]_t$ denotes derivative w.r.t. time

This system demonstrates the use of secondary dependent components that are controlled by kinetically-controlled reactions in the primary system. The equations for the system are given in Table 5.4, and the input file is listed in Table 5.10. What is actually

Table 5.8. Test114.min		49	test114.ZnHu.cnc	100	*****
line #	entry	50	*****	101	1
1	test1	51	2	102	test114.Zn(s).sta
2	14	52	1 1	103	1
3	0.001, 1.	53	2 1	104	test114.Zn(s).bnd
4	50, 0.0, 3600.0, 1.	54	1.29e-6	105	1
5	1, 1, 1	55	0.0	106	test114.Zn(s).cnc
6	test110.feet	56	2	107	0
7	0.00001	57	1 1	108	xxxxxxxxxxxxxxxxxxx
8	2, 3, 1	58	3 1	109	0
9	10., 10., 0.	59	2.0e-5	110	xxxxxxxxxxxxxxxxxxx
10	1	60	0.0	111	*****
11	50	61	2	112	0
12	0, 1	62	1 1	113	0
13	0	63	4 1	114	0.0, 0.0
14	xxxxxxx	64	6.31e-2	115	0.0
15	1, 7	65	0.0	116	0
16	1.	66	*****	117	0
17	*****	67	5	118	0.0, 0.0
18	5	68	1	119	0.0
19	test114.ZnT.sta	69	test114.ZnT.bnd	120	0
20	1	70	1	121	0
21	test114.Zn.cnc	71	test114.ZnT.cnc	122	0.0, 0.0
22	test113.CIT.sta	72	0	123	0.0
23	1	73	xxxxxxxxxxxxxxxxxxx	124	0
24	test114.Cl.cnc	74	1	125	0
25	test112.SO4T.sta	75	test113.CIT.bnd	126	0.0, 0.0
26	1	76	1	127	0.0
27	test114.SO4.cnc	77	test114.CIT.cnc	128	0
28	test112.HuT.sta	78	0	129	0
29	1	79	xxxxxxxxxxxxxxxxxxx	130	0.0, 0.0
30	test114.Hu.sta	80	1	131	0.0
31	test114.TSSST.sta	81	test112.SO4T.bnd	132	*****
32	1	82	1	133	1
33	test114.TSS.cnc	83	test114.SO4T.cnc	134	1 1
34	*****	84	0	135	1
35	0	85	xxxxxxxxxxxxxxxxxxx	136	5 1
36	*****	86	1	137	1.17e-7, 8.1e-7
37	3	87	test112.HuT.bnd	138	0.0
38	0	88	1		
39	xxxxxxxxxxxxxxxxxxx	89	test114.HuT.cnc		for alternate run:
40	1	90	0	line #	entry
41	test114.ZnCl.cnc	91	xxxxxxxxxxxxxxxxxxx	133	0
42	0	92	1	134	2
43	xxxxxxxxxxxxxxxxxxx	93	test114.TSST.bnd	135	1 1
44	1	94	1	136	5 1
45	test114.ZnSO4.cnc	95	test114.TSST.cnc	137	1.17e-7, 8.1e-7
46	0	96	0	138	0.0
47	xxxxxxxxxxxxxxxxxxx	97	xxxxxxxxxxxxxxxxxxx		
48	1	98	*****		
		99	0		

Table 5.9. Equations for Cadmium System

Secondary Variables				
Dependent Components:				
species #	Equation			
1	$[Cd^{2+}]_T = [Cd^{2+}] + [CdCl^+] + [CdCl_2] + [CdCl_3] + [CdSO_4] + [CdHCO_3^+]$			
2	$[Cl^-]_T = [Cl^-] + [CdCl^+] + 2[CdCl_2] + 3[CdCl_3]$			
3	$[SO_4^{2-}]_T = [SO_4^{2-}] + [CdSO_4]$			
4	$[OH^-]_T = [OH^-] + [HCO_3^-] + [CdHCO_3^+] + 2[CO_3^{2-}] - [H^+]$			
5	$TSS_T = [TSS] + [Cd_{(s)}] \approx [TSS]$			
Independent Components: None				
Derived Species:				
species #	Equation	K		ref
6	$[CdCl^+] = K[Cd^{2+}][Cl^-]$	$10^{1.35} M^{-1}$		a
7	$[CdCl_2] = K[Cd^{2+}][Cl^-]^2$	$10^{1.7} M^{-2}$		a
8	$[CdCl_3] = K[Cd^{2+}][Cl^-]^3$	$10^{1.5} M^{-3}$		a
9	$[CdSO_4] = K[Cd^{2+}][SO_4^{2-}]$	$10^{1.3} M^{-1}$		b
10	$[CdHCO_3^+] = K[Cd^{2+}][OH^-]$	$10^{1.3} \times 10^{2.97} M^{-1}$		b
11	$[HCO_3^-] = K[OH^-]$	$10^{2.97}$		c
12	$[CO_3^{2-}] = K[OH^-]^2$	$10^{7.7} M^{-1}$		c
13	$[H^+] = K[OH^-]^{-1}$	$10^{-14} M^2$		c
Primary Variables				
Derived Species:				
species #	Equation	κ_f	κ_b	ref
6	$[Cd(s)]_t = \kappa_f[Cd^{2+}][TSS] - \kappa_b[Cd(s)]$	$10^{-3.9} \text{ l mg}^{-1} \text{ hr}^{-1}$	$10^{-1.9} \text{ hr}^{-1}$	d
6 (alt)	$[Cd(s)]_t = \kappa_f[Cd^{2+}]_T[TSS] - \kappa_b[Cd(s)]$	$10^{-3.9} \text{ l mg}^{-1} \text{ hr}^{-1}$	$10^{-1.9} \text{ hr}^{-1}$	d
<p>^a Smith and Martell (1976)</p> <p>^b Mantoura, et al. (1978)</p> <p>^c Stumm and Morgan (1982), Tables 4.7-4.9; seawater at 19ppt chlorinity and 20°C</p> <p>^d Nyfeller, et al. (1984)</p> <p>$[\]_t$ denotes derivative w.r.t. time</p>				

Table 5.10. Equations for Tin System

Secondary Variables

Dependent Components:

species #	Equation
1	$[SnBu]_T = [SnBu]$
2	$[SnBu_2]_T = [SnBu_2] + [SnBu_2(s)]$
3	$[SnBu_3]_T = [SnBu_3] + [SnBu_3(s)]$
4	$[SnBu_3^{II}]_T = [SnBu_3^{II}] + [SnBu_3^{II}(s)]$

Independent Components: None

Derived Species:

species #	Equation	K	ref
5	$[SnBu_2(s)] = K [SnBu_2]$	2.	a
6	$[SnBu_3^I(s)] = K [SnBu_3^I]$	6.	a
7	$[SnBu_3^{II}(s)] = K [SnBu_3^{II}]$	6.	a

Primary Variables

Derived Species:

species #	Equation	κ_f	κ_b	κ	ref
1	$[SnBu]_t = \kappa_f [Sn^{2+}] [Bu] - \kappa_b [SnBu]$	0.0	0.0		a
2	$[SnBu_2]_t = \kappa_f [SnBu] [Bu] - \kappa_b [SnBu_2]$	0.0	0.04 d ⁻¹		a
3	$[SnBu_3^I]_t = \kappa_f [SnBu_2] [Bu] - \kappa_b [SnBu_3^I] - \kappa [SnBu_3^I]$	0.0	0.08 d ⁻¹	0.075 d ⁻¹	a
4	$[SnBu_3^{II}]_t = \kappa_f [SnBu_2] [Bu] - \kappa_b [SnBu_3^{II}] - \kappa [SnBu_3^{II}]$	0.0	0.08 d ⁻¹	0.075 d ⁻¹	a

Independent Components:

species #	Equation
5	$[Bu]_T = [Bu] + [SnBu] + 2 [SnBu_2] + 3 [SnBu_3^I] + 3 [SnBu_3^{II}]$

^a Adelman, et al. (1990)[]_t denotes derivative w.r.t. time

being simulated in this case is the simultaneous debutylation and decay of an initial amount of tributyltin (TBT). We use experimental data from *Adelman, et al.* [1990], who found that of an initial mass of tributyltin, two-thirds would be expected to degrade through dibutyltin (DBT), which subsequently degraded to monobutyltin (MBT), while one-third would be expected to degrade directly to MBT. In addition, TBT had a volatile loss with a decay rate of 0.075 d^{-1} . It was also found that DBT and TBT partitioned to the sediments with a distribution coefficient of 2×10^{-2} and $6 \times 10^{-2} \text{ l mg}^{-1}$, respectively. For the purpose of this example, $[TSS]$ is held constant at 100 mg l^{-1} , and incorporated into the distribution coefficient, which results in the nondimensional values as shown in Table 5.4.

In order to accommodate the two different routes of degradation of TBT, the original mass of $10^{-3} \mu\text{M}$ was split up into two distinct species: $[SnBu_3^I]$ with an initial concentration of $0.33 \times 10^{-3} \mu\text{M}$ and $[SnBu_3^{II}]$ with an initial concentration of $0.66 \times 10^{-3} \mu\text{M}$. These two TBT species subsequently degraded through two different pathways, as indicated by the equations in Table 5.10.

For this simulation, units have been changed to be consistent with rate constants in terms of inverse days, rather than hours. The uniform velocity field applied is 100 m d^{-1} , and the simulation was run for 100 1-day time steps, so that the upstream boundary condition has had a chance to pass through the entire domain. The concentration profiles at this point are shown in Figure 5.13. Because of the nonzero decay constants, all TBT species decrease with distance from the upstream boundary, which also equates to time in the domain. All DBT species initially increase, since mass is being transferred from TBT species to DBT species, but DBT species eventually start to decrease as well as mass is transferred to the MBT species. The MBT species initially increases, and then stabilizes, as there is no mechanism for removal of mass once it is deposited in MBT.

San Francisco Bay

This example does not cover any special cases that have not been covered above, but it demonstrates the use of ELAmet with a relatively large number of species as applied to a more realistic problem. All of the equations and values of rate and stability constants have been covered in the examples above, so all of the species in the system are listed in Table 5.12, without the corresponding equations. A list of the input file is given in Table 5.13.

Table 5.11. Test116.min		38	test116.DBT(s).cnc	78	xxxxxxxxxxxxxxx
line #	entry	39	0	79	1
1	test1	40	xxxxxxxxxxxxxxx	80	test116.TBTIT.bnd
2	16	41	1	81	1
3	0.001, 1.	42	test116.TBTI(s).cnc	82	test116.TBTIT.cnc
4	100, 0.0, 1.0, 1.	43	0	83	0
5	1, 1, 1	44	xxxxxxxxxxxxxxx	84	xxxxxxxxxxxxxxx
6	test116.feet	45	1	85	*****
7	0.00001 1	46	test116.TBTII(s).cnc	86	1
8	2, 3, 1	47	*****	87	test116.BuT.sta
9	10., 10., 0.	48	1	88	0
10	1	49	2 1	89	xxxxxxxxxxxxxxx
11	100	50	2.	90	1
12	0, 1	51	0.0	91	test116.Bu.cnc
13	0	52	1	92	*****
14	xxxxxxx	53	3 1	93	0
15	1, 7	54	6.	94	*****
16	1.	55	1	95	0
17	*****	56	4 1	96	0
18	4	57	6.	97	0.0 0.0
19	test116.MBTT.sta	58	0.0	98	0.0
20	1	59	*****	99	0
21	test116.MBT.cnc	60	4	100	2
22	test116.DBTT.sta	61	1	101	1 1
23	1	62	test116.MBTT.bnd	102	5 1
24	test116.DBT.cnc	63	1	103	0.0 0.04
25	test116.TBTIT.sta	64	test116.MBTT.cnc	104	0.0
26	1	65	0	105	0
27	test116.TBTI.cnc	66	xxxxxxxxxxxxxxx	106	2
28	test116.TBTIIT.sta	67	1	107	2 1
29	1	68	test116.DBTT.bnd	108	5 1
30	test116.TBTII.cnc	69	1	109	0.0 0.08
31	*****	70	test116.DBTT.cnc	110	0.075
32	0	71	0	111	0
33	*****	72	xxxxxxxxxxxxxxx	112	2
34	3	73	1	113	3 1
35	0	74	test116.TBTIT.bnd	114	5 1
36	xxxxxxxxxxxxxxx	75	1	115	0.0 0.08
37	1	76	test116.TBTIT.cnc	116	0.075
		77	0	117	*****

Concentrations of the major seawater ions were determined by applying salinity boundary conditions of 20 ppt at the southernmost end of the bay, 35 ppt at the ocean boundary, and 0 ppt at the Delta outflow. The concentration of dissolved organic ligand was determined by applying a boundary condition of 4.4 mg C l⁻¹ at the southernmost end of the Bay, resulting in an *Hu* concentration that decreases with salinity northward along the length of the Bay. The concentration of the carbonate ion is determined by applying

alkalinity boundary conditions of 10^{-3} M at the Delta outflow, 2.4×10^{-3} M at the ocean boundary, and 1.8×10^{-3} M at the southernmost end of the Bay (reflecting the same mix of fresh- and seawater as the salinity). Initial conditions for CO_3^{2-} , Cl^- , SO_4^{2-} , and Hu were obtained from conservative runs with the indicated boundary conditions.

Suspended solids were modeled as coming primarily from a benthic source distributed over the entire South Bay; the strength of this source was adjusted to give reasonable TSS values in the water column over the length of the simulation. Initial conditions for suspended solids concentration were zero over the entire Bay.

Sources for the metals in this case were obtained from values for the six largest Publicly Owned Treatment Works that empty into the Bay, as compiled in *Gunther, et al.* [1987]. Each treatment plant was treated as having a Gaussian shape, with an amplitude calculated to give the appropriate mass input when integrated over the surrounding grid. The input is assumed to be distributed such that 20% of the metal is in the solid phase and 80% is in the dissolved phase. The locations of the five POTWs that empty directly into South Bay are shown in Figure 5.14; one POTW located in North Bay is not shown. The boundary conditions applied to the metals are conditions of zero concentration at the ocean boundary and at the Delta outflow (the latter is not realistic, since this outflow is a major source of some metals, but this run was intended to specifically look at the input due to the sewage treatment plants). Initial conditions for the metals were taken to be zero.

Figure 5.16, Figure 5.17, and Figure 5.18 present profiles of concentration of the various species along the transect defined in Figure 5.15 after running the simulation for 44 days. The decrease in total metal levels northward along the transect reflects the concentration of sources in the south of the Bay, and the dilution of metal levels northward. In this simulation, South Bay does not exhibit a great deal of variation in salinity, dissolved organic ligands, or suspended solids, so the relative proportions of the various metal species does not change a great deal along the transect. In Figure 5.19 is plotted the transect of apparent distribution coefficient for each metal, defined as $[Me_{(s)}] / ([TSS] [Me^{2+}]_T)$. In Figure 5.20 this quantity is divided by the apparent distribution coefficient that would be measured at equilibrium, defined as $(\kappa_f [Me^{2+}]) / (\kappa_b [Me^{2+}]_T)$. This illustrates the effects of including adsorption kinetics in this system; the measured K_d value is increased by about a factor of 2 and a factor of 10, respectively, for zinc and cadmium, relative to the value at equilibrium. Copper, however, due to its much more rapid adjustment to equilibrium, is essentially at equilibrium. In practice, the

absolute differences, at least for copper and zinc, are so small as to be well within the range of variability expected in this quantity due to other errors, the most obvious being the inaccuracy in knowing the rate constants of adsorption. It is interesting to note, however, that the kinetics causes the apparent distribution coefficient to increase with increasing salinity, which is counter to laboratory results that show partitioning decreasing with increasing salinity [Comans and van Dijk, 1988; Gonzalez-Davila, et al. 1990; Li, et al., 1984]. This is usually attributed to the competition of complexing aqueous ligands for the adsorbate.

Table 5.12. Species in San Francisco Bay System

Secondary Variables		Primary Variables	
Dependent Components:		Derived Species:	
number	species	number	species
1	Cu^{2+}	1	Cu_T
2	Cd^{2+}	2	Cd_T
3	Zn^{2+}	3	Zn_T
4	Cl^-	4	Cl_T
5	SO_4^{2-}	5	SO_{4T}
6	OH^-	6	Alk
7	Hu	7	Hu_T
8	TSS	8	TSS_T
Independent Components: none		Independent Components: none	
Derived Species:		Derived Species:	
number	species	number	species
9	$CuCO_3$	9	$Cu_{(s)}$
10	$CuHu$	10	$Cd_{(s)}$
11	$CdCl^+$	11	$Zn_{(s)}$
12	$CdCl_2$		
13	$CdCl_3^-$		
14	$CdSO_4$		
15	$ZnCl^+$		
16	$ZnSO_4$		
17	$ZnHu$		
18	HCO_3^-		
19	CO_3^{2-}		

Table 5.13. Sfba472.min							
line #	entry						
1	sfba4	69	1	140	0.0	211	sfba463.Zn(s).sta
2	72	70	sfba472.CdSO4.cnc	141	1	212	1
3	0.001, 1.	71	0	142	6, 2	213	sfba463.Zn(s).bnd
4	4000., 0, 3726.2, 1.	72	xxxxxxxxxxxxxxxx	143	50.12	214	1
5	1, 1, 12	73	1	144	0.0	215	sfba472.Zn(s).cnc
6	sfba443.feet	74	sfba472.ZnCl.cnc	145	*****	216	1
7	0.0005, 1	75	0	146	8	217	sfba472.Zn(s).src
8	2, 3, 1	76	xxxxxxxxxxxxxxxx	147	1	218	0
9	200., 200., 0.	77	1	148	sfba460.CuT.bnd	219	xxxxxxxxxxxxxxxx
10	0	78	sfba472.ZnSO4.cnc	149	1	220	*****
11	xxxxxxx	79	0	150	sfba472.CuT.cnc	221	1
12	0	80	xxxxxxxxxxxxxxxx	151	1	222	1, 1
13	xxxxxxx	81	1	152	sfba472.CuT.src	223	0
14	xxxxxxx	82	sfba472.ZnHu.cnc	153	1	224	0.0, 0.0
15	1, 7	83	0	154	sfba460.CdT.bnd	225	0.0
16	1.	84	xxxxxxxxxxxxxxxx	155	1	226	1
17	*****	85	1	156	sfba472.CdT.cnc	227	2, 1
18	8	86	sfba472.HCO3.cnc	157	1	228	0
19	sfba472.CuT.sta	87	0	158	sfba472.ZnT.src	229	0.0, 0.0
20	1	88	xxxxxxxxxxxxxxxx	159	1	230	0.0
21	sfba472.Cu.cnc	89	1	160	sfba460.CIT.bnd	231	1
22	sfba472.CdT.sta	90	sfba472.CO3.cnc	161	1	232	3, 1
23	1	91	*****	162	sfba472.CIT.cnc	233	0
24	sfba472.Cd.cnc	92	2	163	0	234	0.0, 0.0
25	sfba472.ZnT.sta	93	1, 1	164	xxxxxxxxxxxxxxxx	235	0.0
26	1	94	6, 2	165	1	236	1
27	sfba472.Zn.cnc	95	28.18	166	sfba460.SO4T.bnd	237	4, 1
28	sfba472.CIT.sta	96	0.0	167	1	238	0
29	1	97	2	168	sfba472.SO4T.cnc	239	0.0, 0.0
30	sfba472.Cl.cnc	98	1, 1	169	0	240	0.0
31	sfba472.SO4T.sta	99	7, 1	170	xxxxxxxxxxxxxxxx	241	1
32	1	100	1.64e3	171	1	242	5, 1
33	sfba472.SO4.cnc	101	0.0	172	sfba460.Alk.bnd	243	0
34	sfba472.Alk.sta	102	2	173	1	244	0.0, 0.0
35	1	103	2, 1	174	sfba472.Alk.cnc	245	0.0
36	sfba472.OH.cnc	104	4, 1	175	0	246	1
37	sfba472.HuT.sta	105	22.39e-6	176	xxxxxxxxxxxxxxxx	247	6, 1
38	1	106	0.0	177	1	248	0
39	sfba472.Hu.cnc	107	2	178	sfba460.HuT.bnd	249	0.0, 0.0
40	sfba472.TSST.sta	108	2, 1	179	1	250	0.0
41	1	109	4, 2	180	sfba472.HuT.cnc	251	1
42	sfba472.TSS.cnc	110	50.12e-12	181	0	252	7, 1
43	*****	111	0.0	182	xxxxxxxxxxxxxxxx	253	0
44	0	112	2	183	1	254	0.0, 0.0
45	*****	113	2, 1	184	sfba460.TSST.bnd	255	0.0
46	11	114	4, 3	185	1	256	1
47	0	115	31.62e-18	186	sfba472.TSST.cnc	257	8, 1
48	xxxxxxxxxxxxxxxx	116	0.0	187	1	258	0
49	1	117	2	188	sfba472.TSST.src	259	0.0, 0.0
50	sfba472.CuCO3.cnc	118	2, 1	189	*****	260	0.0
51	0	119	5, 1	190	0	261	*****
52	xxxxxxxxxxxxxxxx	120	20.43e-6	191	*****	262	1
53	1	121	0.0	192	3	263	1, 1
54	sfba472.CuHu.cnc	122	2	193	sfba463.Cu(s).sta	264	1
55	0	123	3, 1	194	1	265	8, 1
56	xxxxxxxxxxxxxxxx	124	4, 1	195	sfba463.Cu(s).bnd	266	5.3e-7, 1.2e-5
57	1	125	1.29e-6	196	1	267	0.0
58	sfba472.CdCl.cnc	126	0.0	197	sfba472.Cu(s).cnc	268	1
59	0	127	2	198	1	269	2, 1
60	xxxxxxxxxxxxxxxx	128	3, 1	199	sfba472.Cu(s).src	270	1
61	1	129	5, 1	200	0	271	8, 1
62	sfba472.CdCl2.cnc	130	20.43e-6	201	xxxxxxxxxxxxxxxx	272	1.4e-11, 1.2e-5
63	0	131	0.0	202	sfba463.Cd(s).sta	273	0.0
64	xxxxxxxxxxxxxxxx	132	2	203	1	274	1
65	1	133	3, 1	204	sfba463.Cd(s).bnd	275	3, 1
66	sfba472.CdCl3.cnc	134	7, 1	205	1	276	1
67	0	135	0.0653	206	sfba472.Cd(s).cnc	277	8, 1
68	xxxxxxxxxxxxxxxx	136	0.0	207	1	278	1.6e-11, 6.9e-6
		137	1	208	sfba472.Cd(s).src	279	0.0
		138	6, 1	209	0		
		139	9.33e2	210	xxxxxxxxxxxxxxxx		

References

- Adelman, D., K. R. Hinga and M. E. Q. Pilson, 1990: Biogeochemistry of butyltins in an enclosed marine ecosystem, *Environmental Science and Technology*, 24(7), pp. 1027-1032.
- Baptista, A.M., Solution of advection-dominated transport by Eulerian-Lagrangian methods using the backwards method of characteristics, Ph.D. Dissertation, Massachusetts Institute of Technology, Cambridge, Mass, 1987.
- Comans, R. N. J. and C. P. J. van Dijk, 1988: Role of complexation processes in cadmium mobilization during estuarine mixing, *Nature*, vol. 336, pp. 151-154.
- Davis, J. A., 1984: Complexation of trace metals by adsorbed natural organic matter, *Geochimica et Cosmochimica Acta*, vol. 48, pp. 679-691.
- Gonzalez-Davila, M., J. M. Santana-Casiano, F. J. Millero, 1990: The adsorption of Cd(II) and Pb(II) to chitin in seawater, *Journal of Colloid and Interface Science*, 137(1), pp. 102-110.
- Gunther, A. J., J. A. Davis and D. J. H. Phillips, 1987: *An Assessment of the Loading of Toxic Contaminants to the San Francisco Bay Delta*, Aquatic Habitat Institute, Richmond, CA, 330 pp.
- Li, Y. H., L. Burkhardt and H. Teraoka, 1984: Desorption and Coagulation of trace elements during estuarine mixing, *Geochimica et Cosmochimica Acta*, vol. 48, pp. 1879-1884.
- McKnight, D. M., G. L. Feder, E. M. Thurman, R. L. Wershaw and J. C. Westall, 1983: Complexation of copper by aquatic humic substances from different environments, *Science of the Total Environment*, vol. 28, pp. 65-76.
- Mook, W. G. and B. K. S. Koene, 1975: Chemistry of dissolved inorganic carbon in estuarine and coastal brackish waters, *Estuarine and Coastal Marine Science*, vol. 3, pp. 325-336.
- Van den Berg, C. M. G., 1984: Determination of the complexing capacity and conditional stability constants of complexes of copper(II) with natural organic ligands in seawater by cathodic stripping voltammetry of copper-catechol complex ions, *Marine Chemistry*, vol. 15, pp. 1-18.
- Van den Berg, C. M. G., A. G. A. Merks and E. K. Duursma, 1987: Organic complexation and its control of the dissolved concentrations of copper and zinc in the Scheldt estuary, *Estuarine, Coastal and Shelf Science*, vol. 24, pp. 785-797.

- Westerink, J.J., J.J. Connor and K.D. Stolzenbach, 1988: A frequency-time domain finite element model for tidal circulation based on the least-squares harmonic analysis method, *International Journal for Numerical Methods in Fluids*, vol. 8, pp. 813-843.
- Wood, T. M. and A. M. Baptista, Modeling the pathways of nonconservative substances in estuaries, in *Estuarine and Coastal Modeling, proceedings of the 2nd International conference*, edited by M.L. Spaulding et al., pp. 280-291, 1992.
- Wood, T. M. and A. M. Baptista, 1993: A model for diagnostic analysis of estuarine geochemistry, *Water Resources Research*, vol. 29(1), pp. 51-71.
- Zlatev, Z. , J. Wasniewski, and K. Schaumburg, 1981: Y12M: Solution of large and sparse systems of linear algebraic equations (Lecture notes in computer science 121). Berlin, NY: Springer-Verlag.

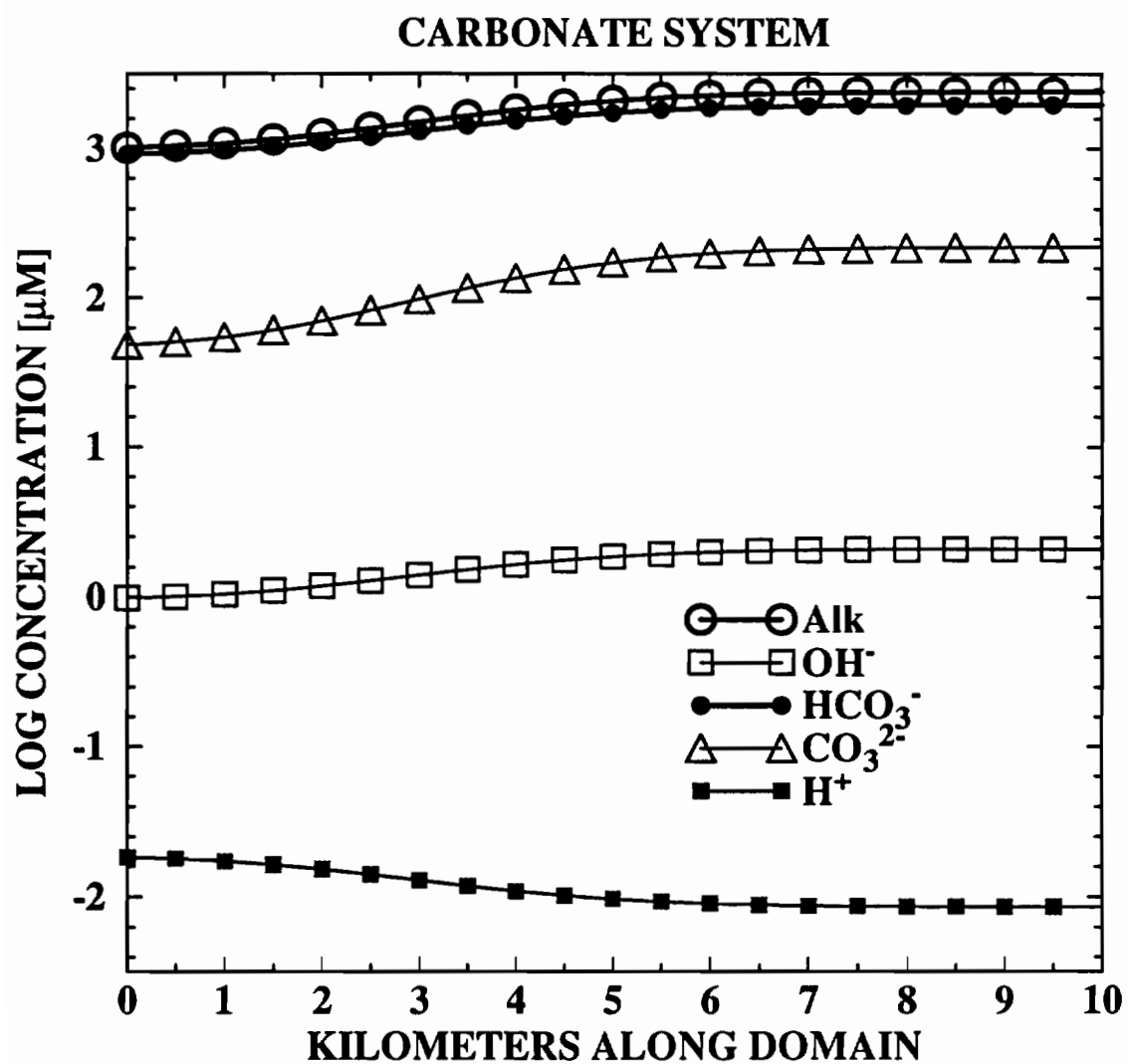


Figure 5.3. Profile of concentration along the 1-dimensional domain for the carbonate system after 50 1-hour time steps.

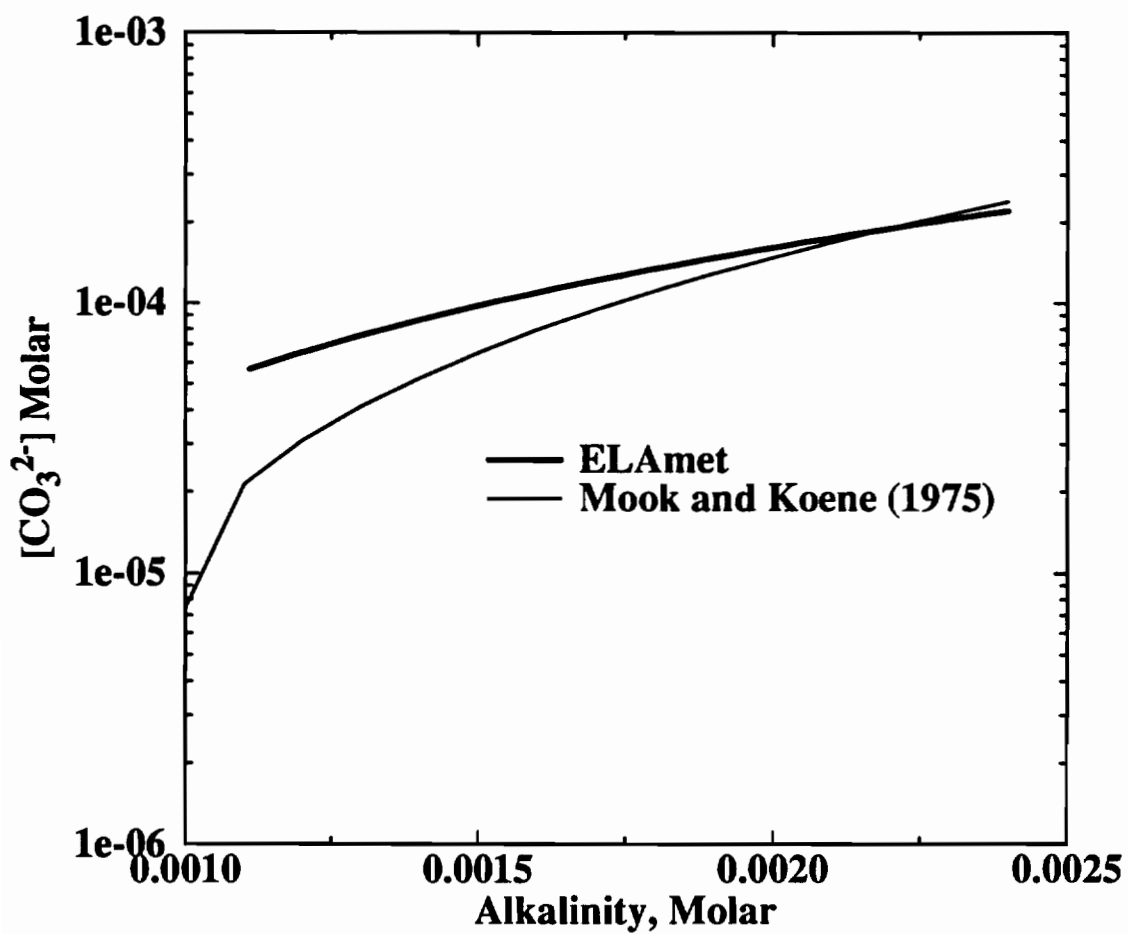


Figure 5.4. Comparison of the concentration of $[CO_3^{2-}]$ using the single-valued constants as in the ELAmet carbonate example with concentration computed using the salinity-dependent constants given in *Mook and Koene* [1975].

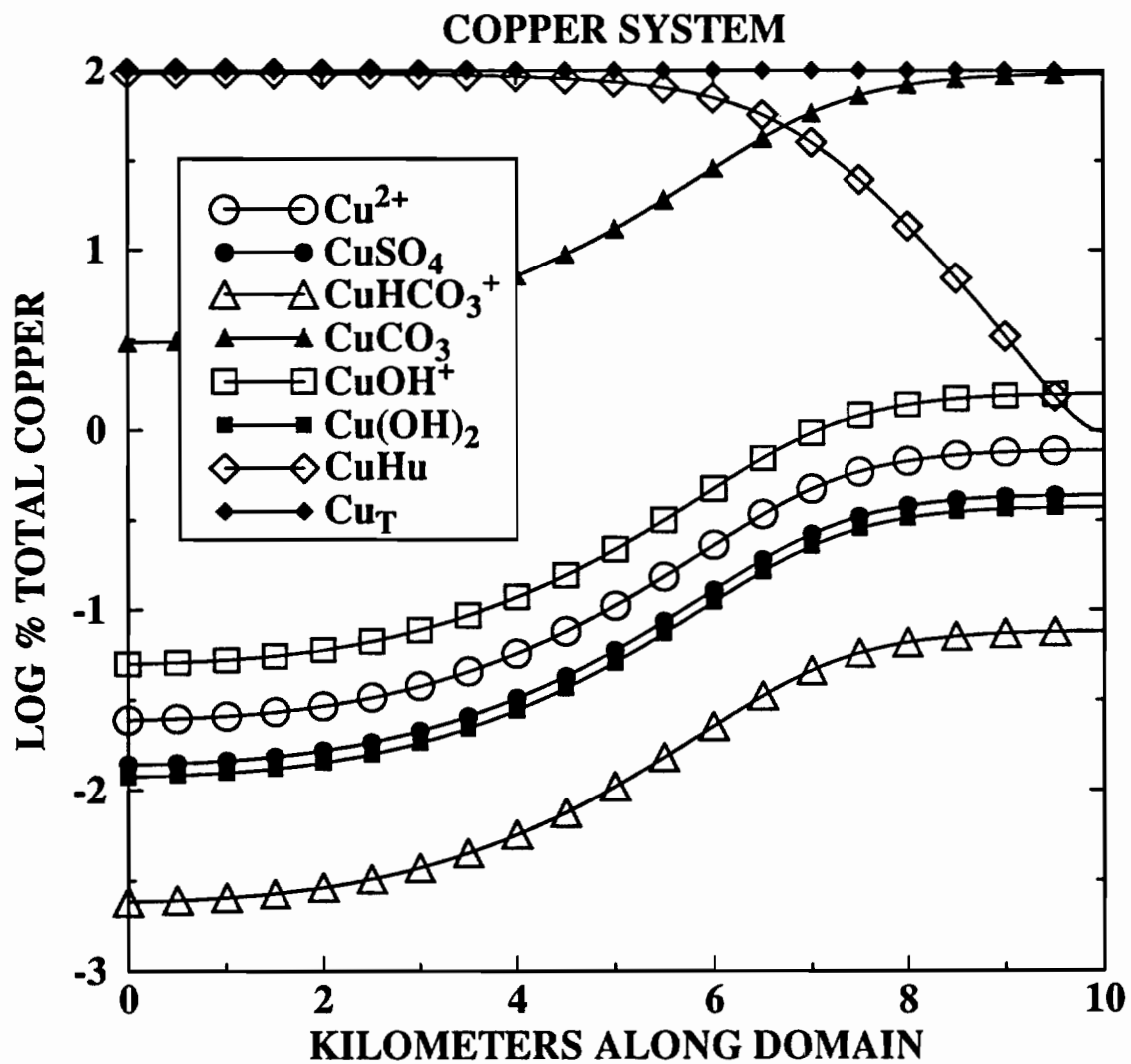


Figure 5.5. Profile of concentration along the 1-dimensional domain for the copper system after 50 1-hour time steps.

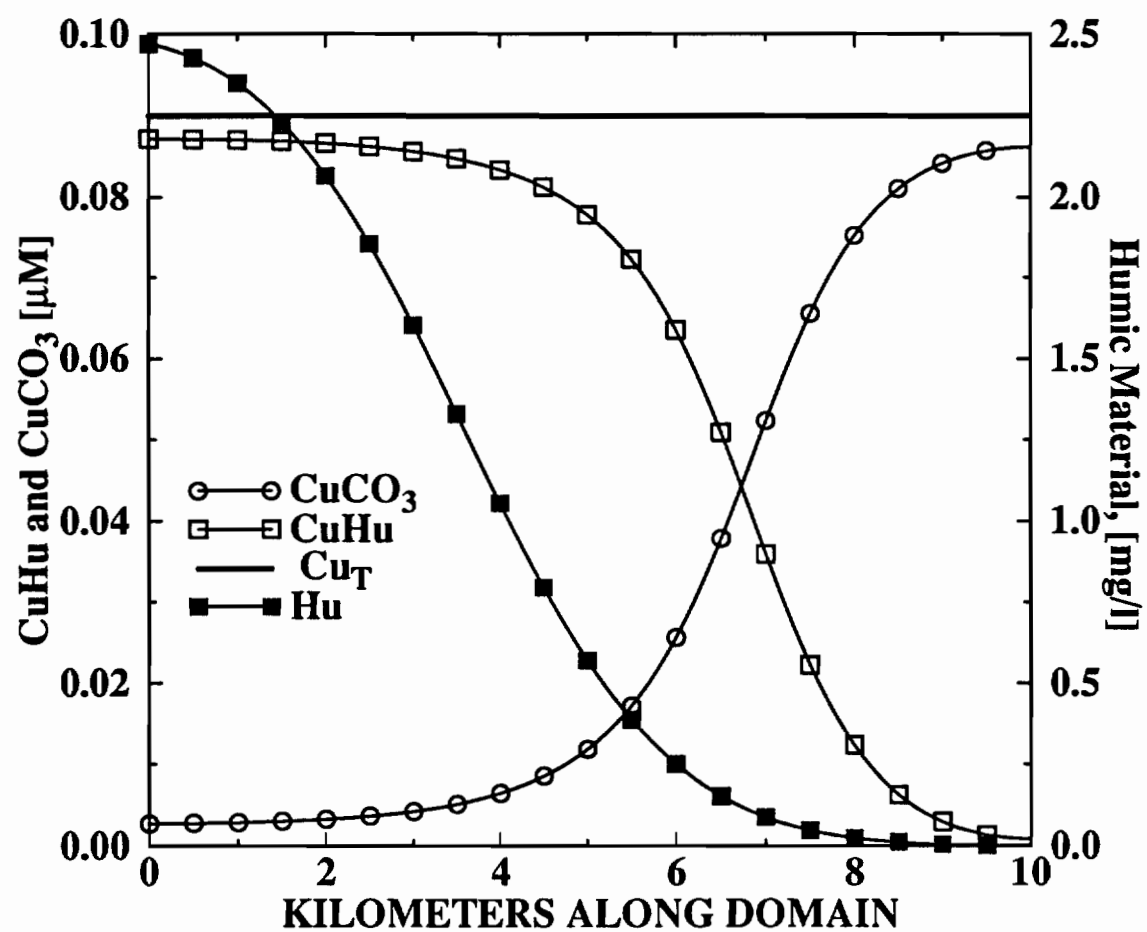


Figure 5.6. Profiles of concentration of the dominant copper species, showing the exchange of mass between $CuCO_3$ and $CuHu$ with increasing concentration of humic material.

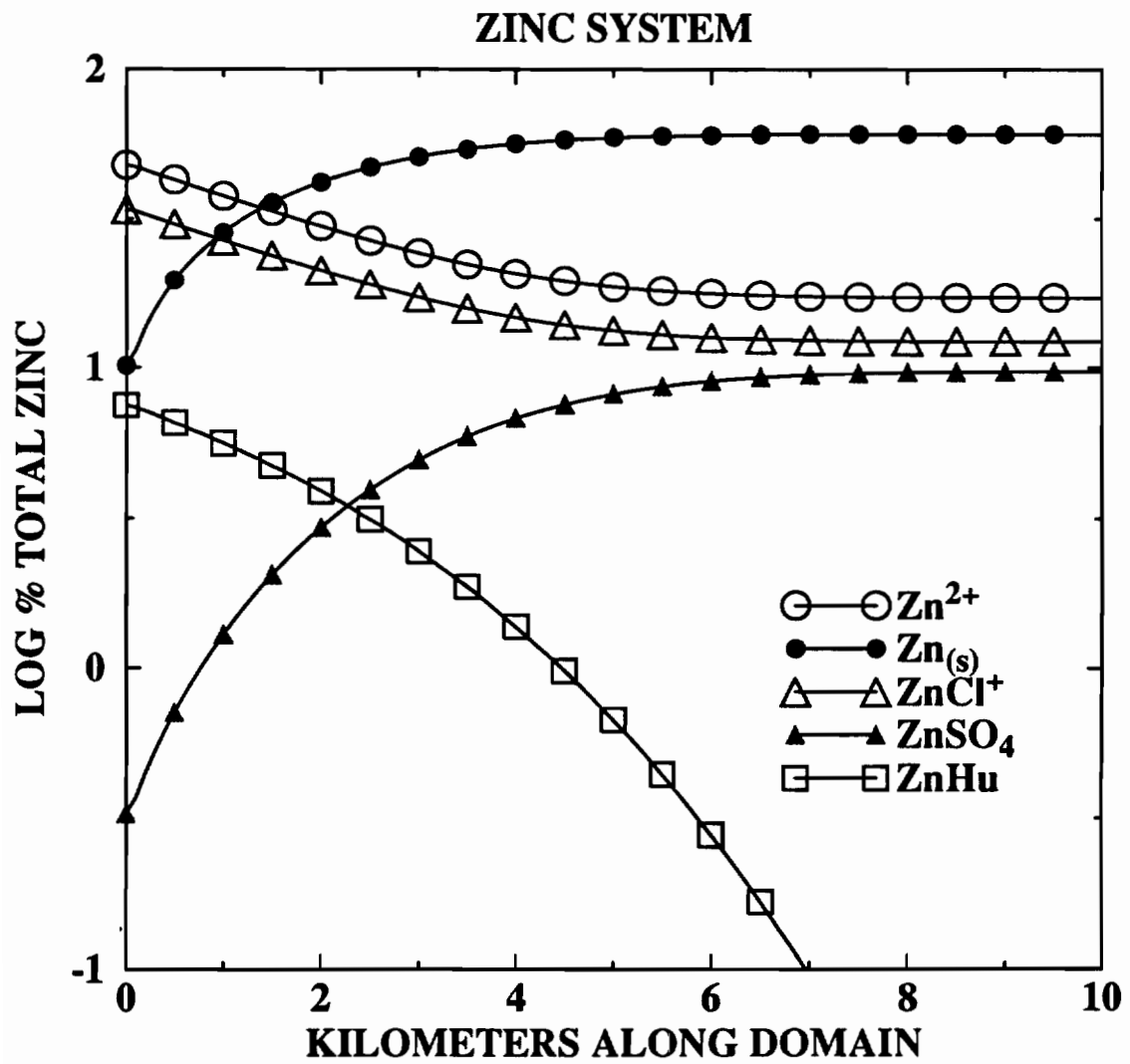


Figure 5.7. Profile of concentration along the 1-dimensional domain for the zinc system after 50 1-hour time steps; adsorption rate proportional to Zn_T .

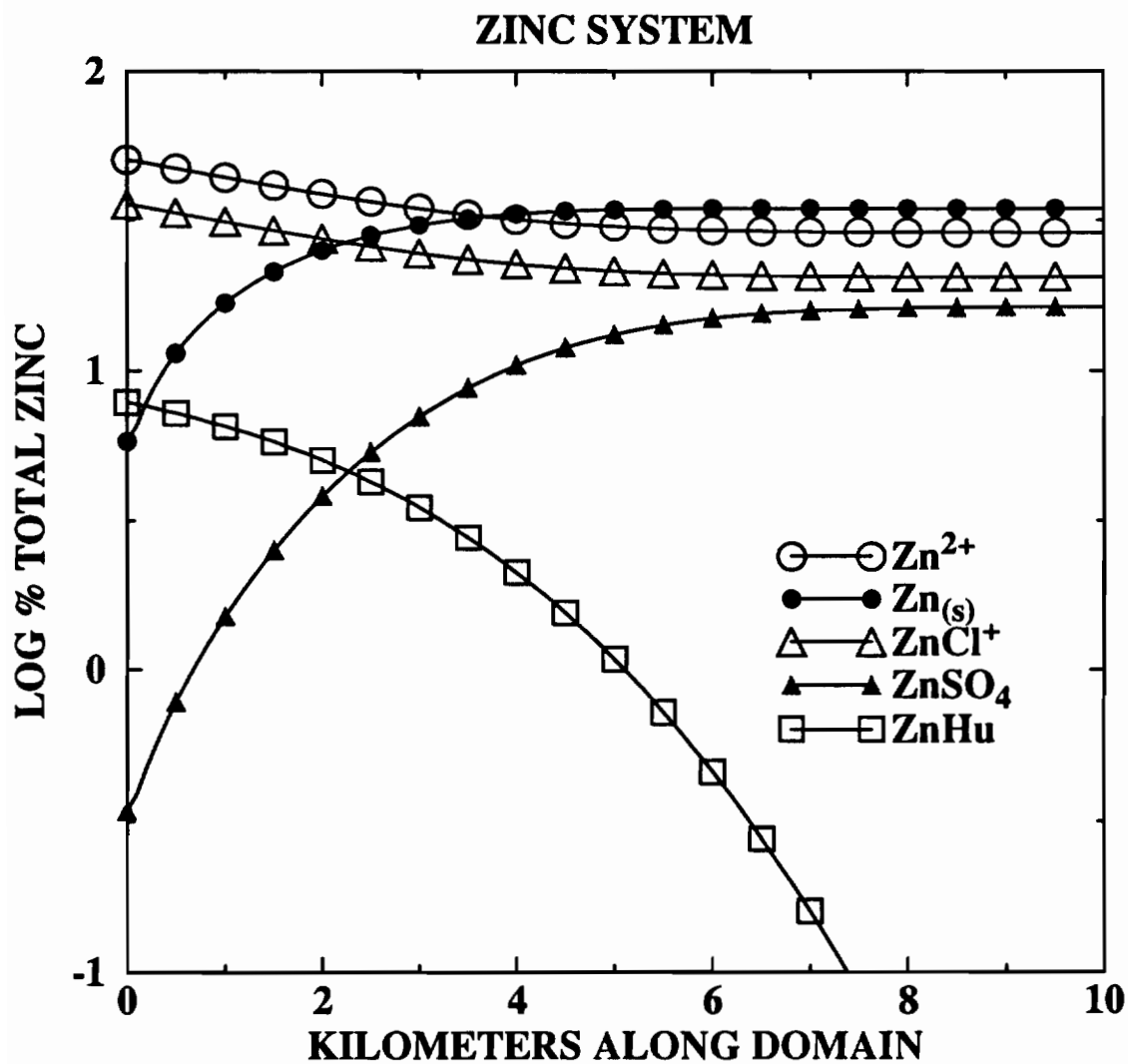


Figure 5.8. Profile of concentration along the 1-dimensional domain for the zinc system after 50 1-hour time steps; adsorption rate proportional to $[Zn^{2+}]$.

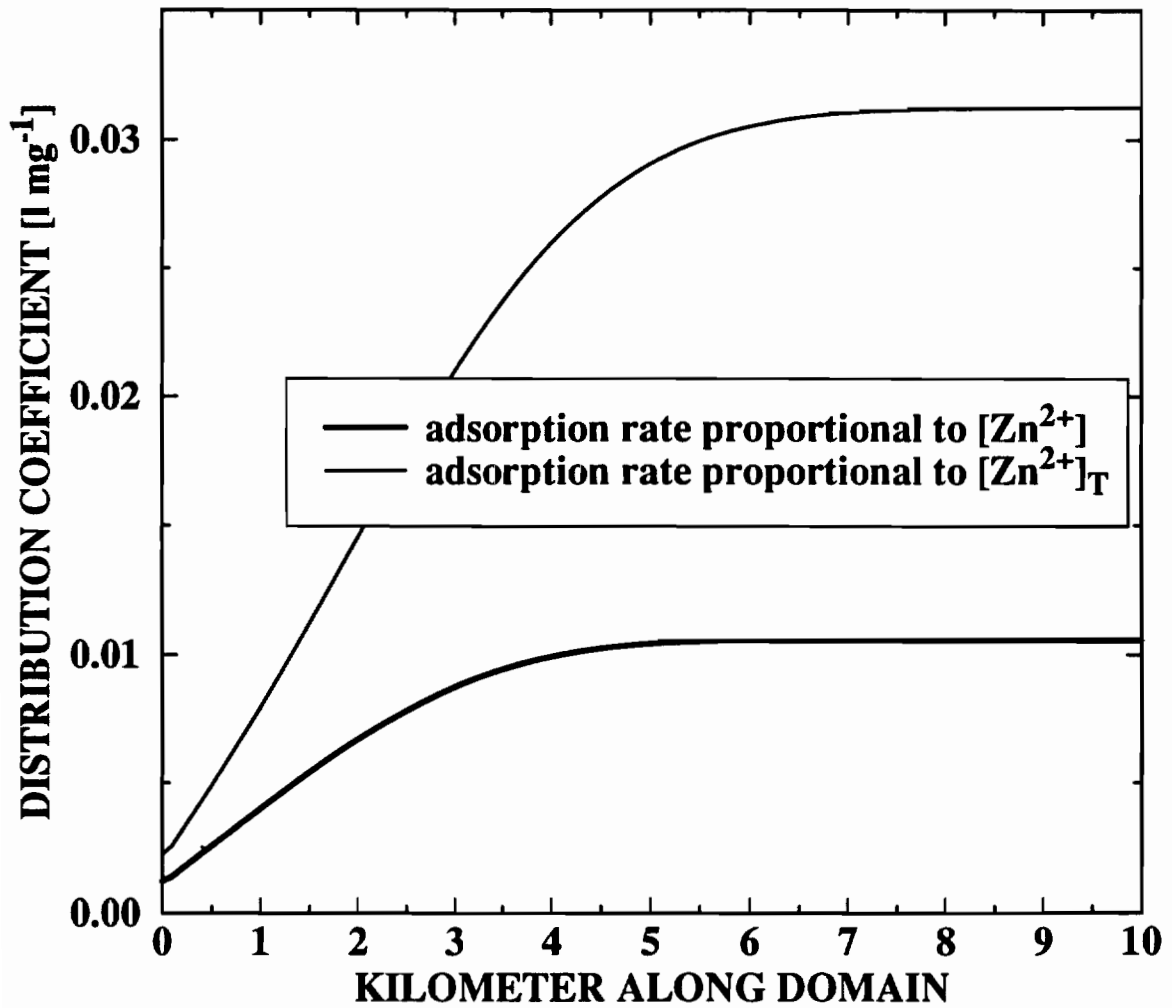


Figure 5.9. Profile of measured distribution coefficient along the domain, defined as $[Zn_{(s)}] / ([TSS] [Zn^{2+}])$, for the two different adsorption rates depicted in Figure 5.7 and Figure 5.8.

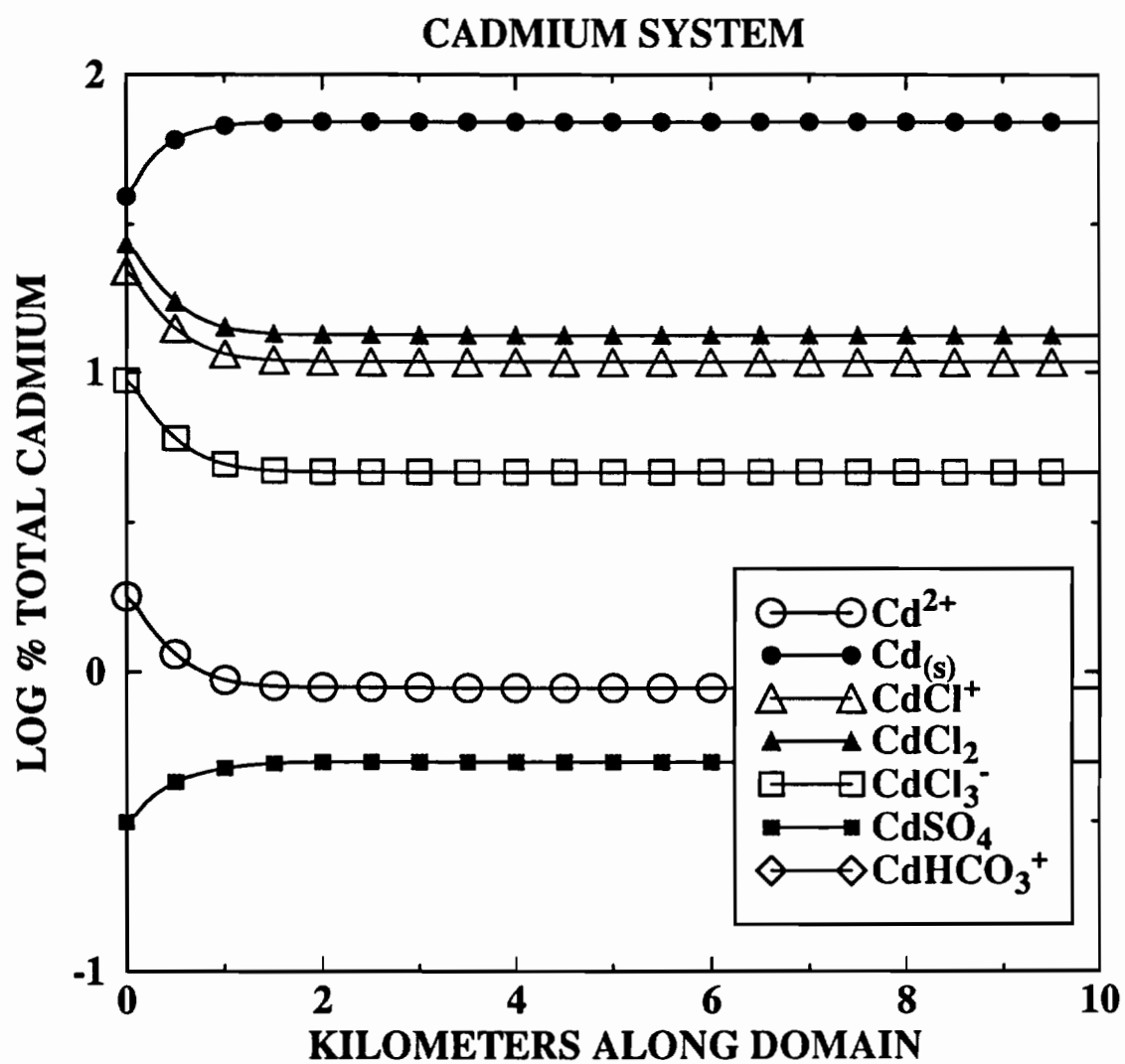


Figure 5.10. Profile of concentration along the 1-dimensional domain for the cadmium system after 50 1-hour time steps; adsorption rate proportional to Cd_T .

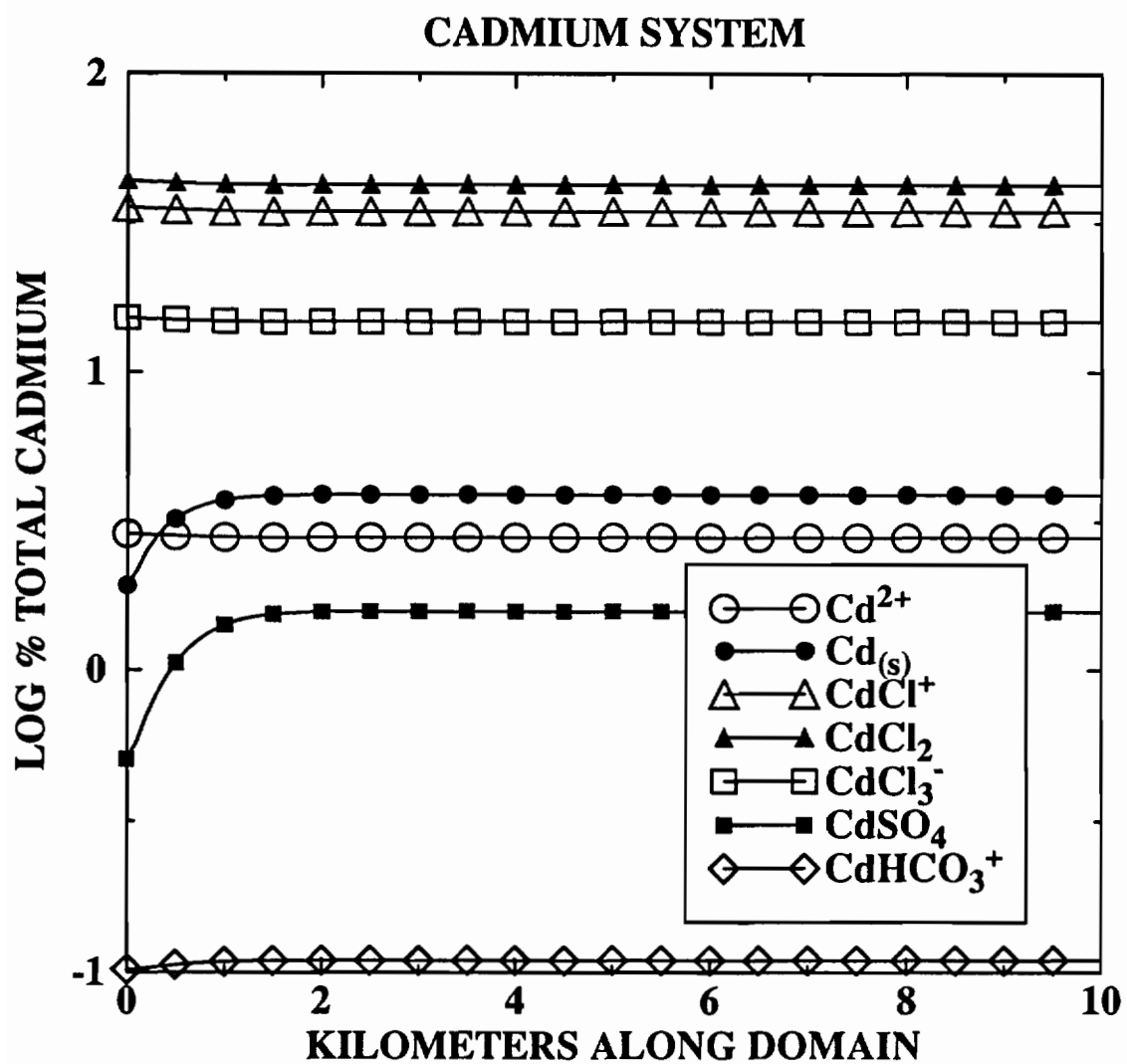


Figure 5.11. Profile of concentration along the 1-dimensional domain for the cadmium system after 50 1-hour time steps; adsorption rate proportional to $[\text{Cd}^{2+}]$.

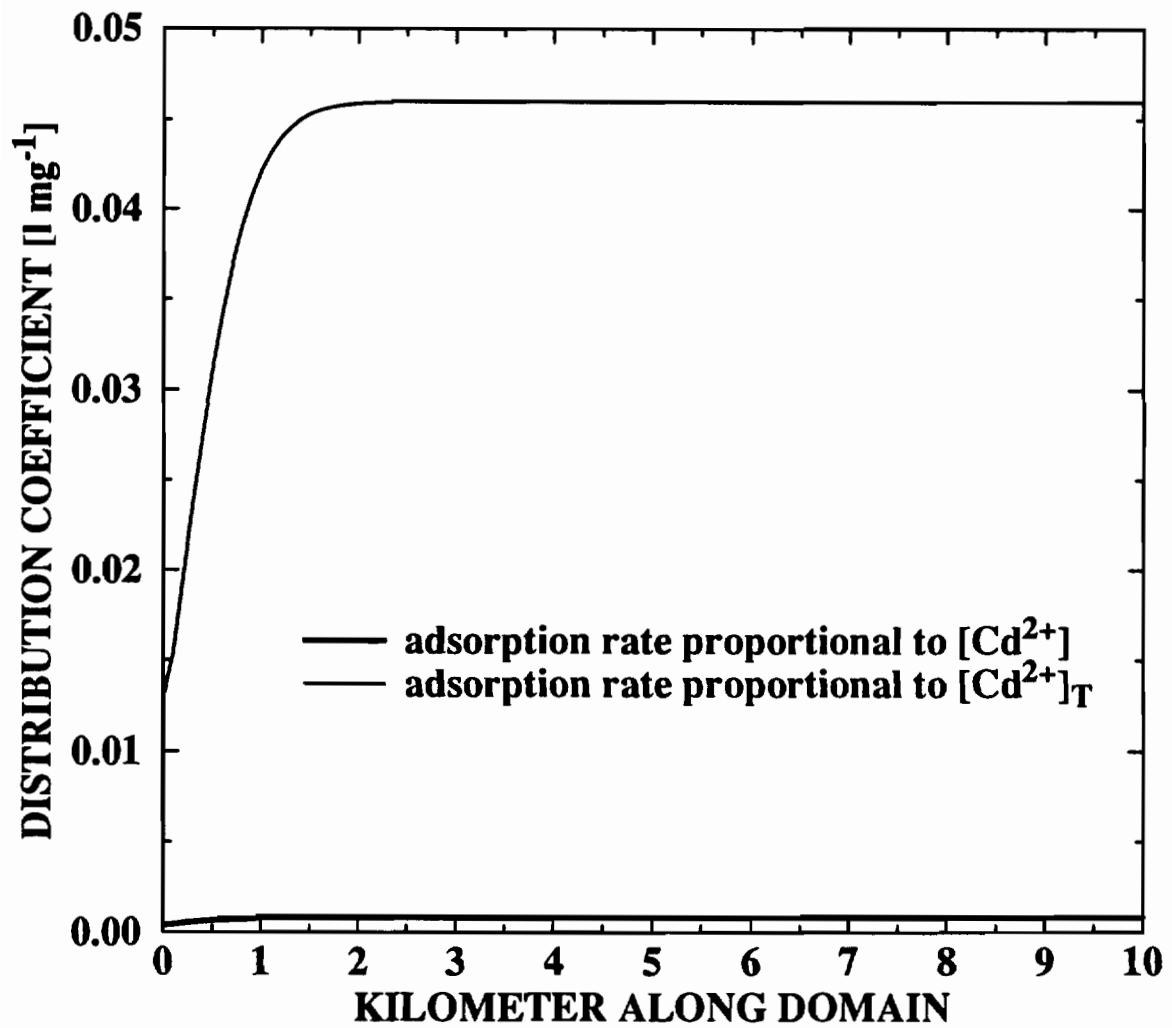


Figure 5.12. Profile of measured distribution coefficient along the domain, defined as $[Cd_{(s)}] / ([TSS] [Cd^{2+}])$, for the two different adsorption rates depicted in Figure 5.10 and Figure 5.11.

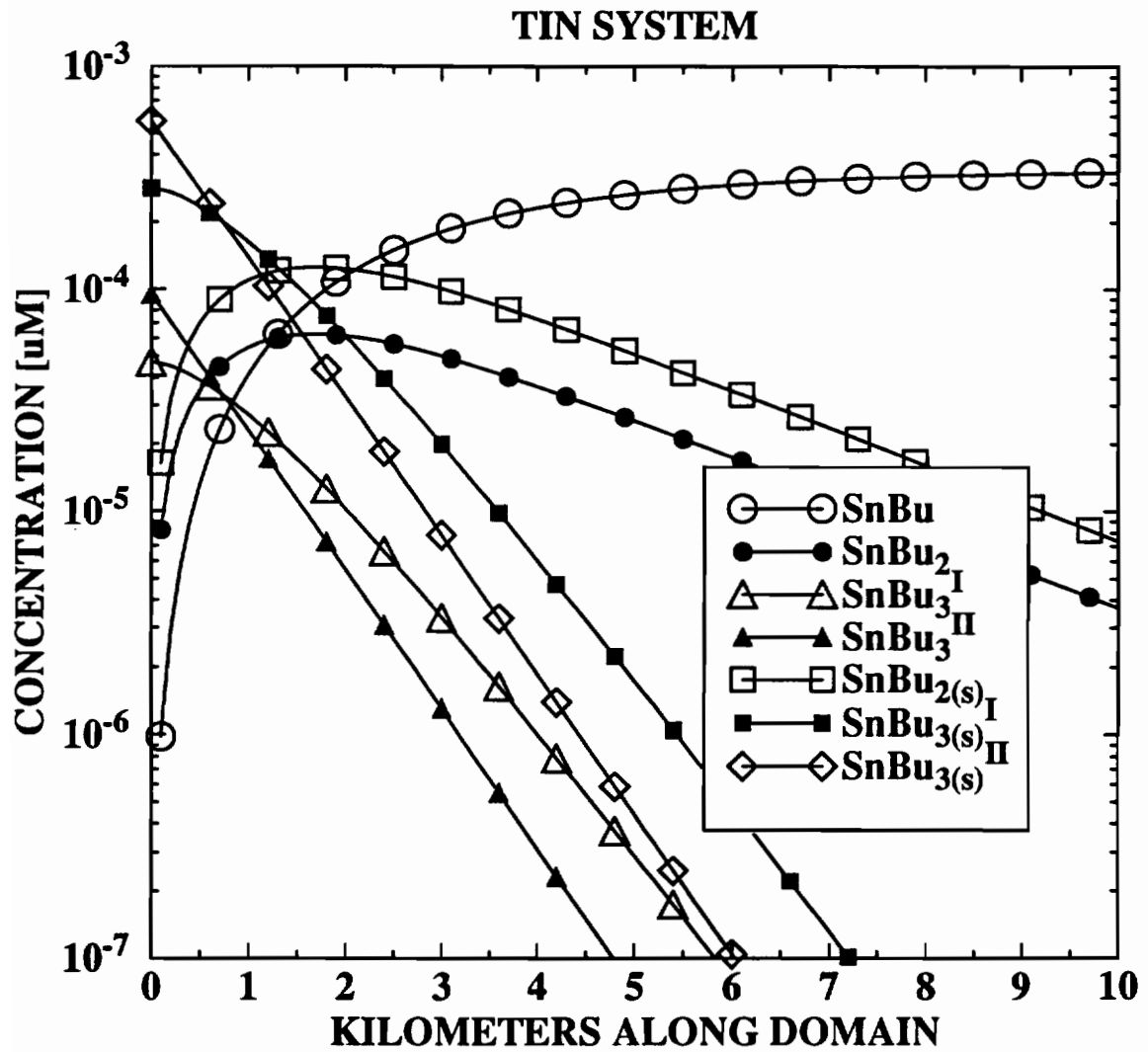


Figure 5.13. Profile of concentration along the 1-dimensional domain for the tin system after 100 1-day time steps.

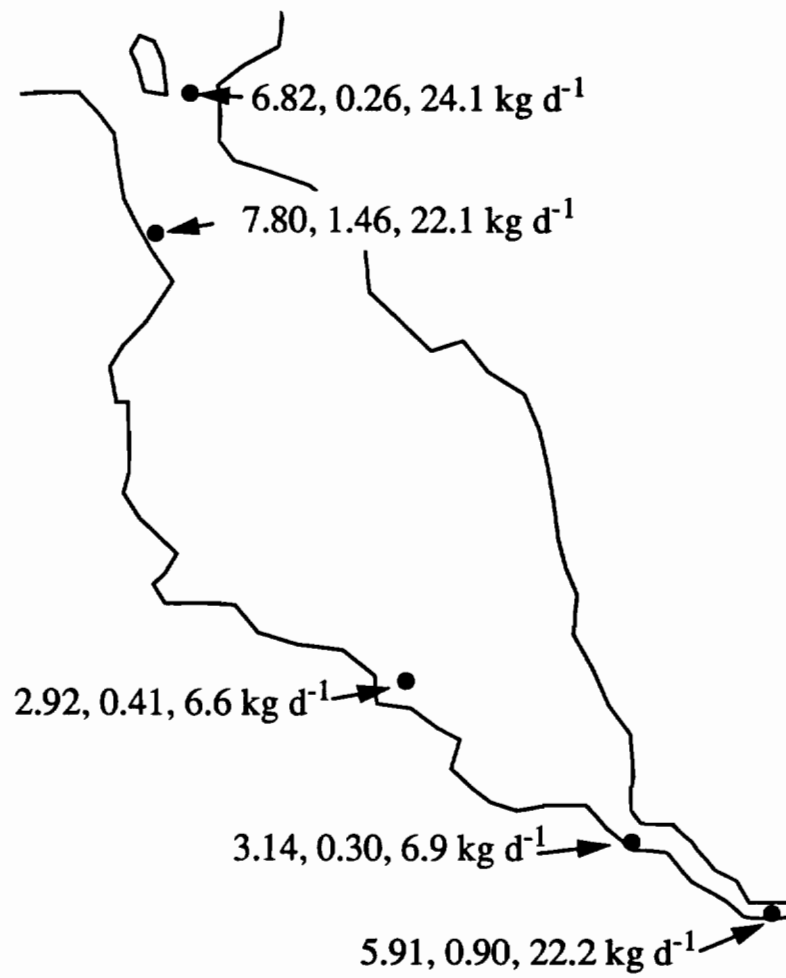


Figure 5.14. Location of five POTWs used as point sources.

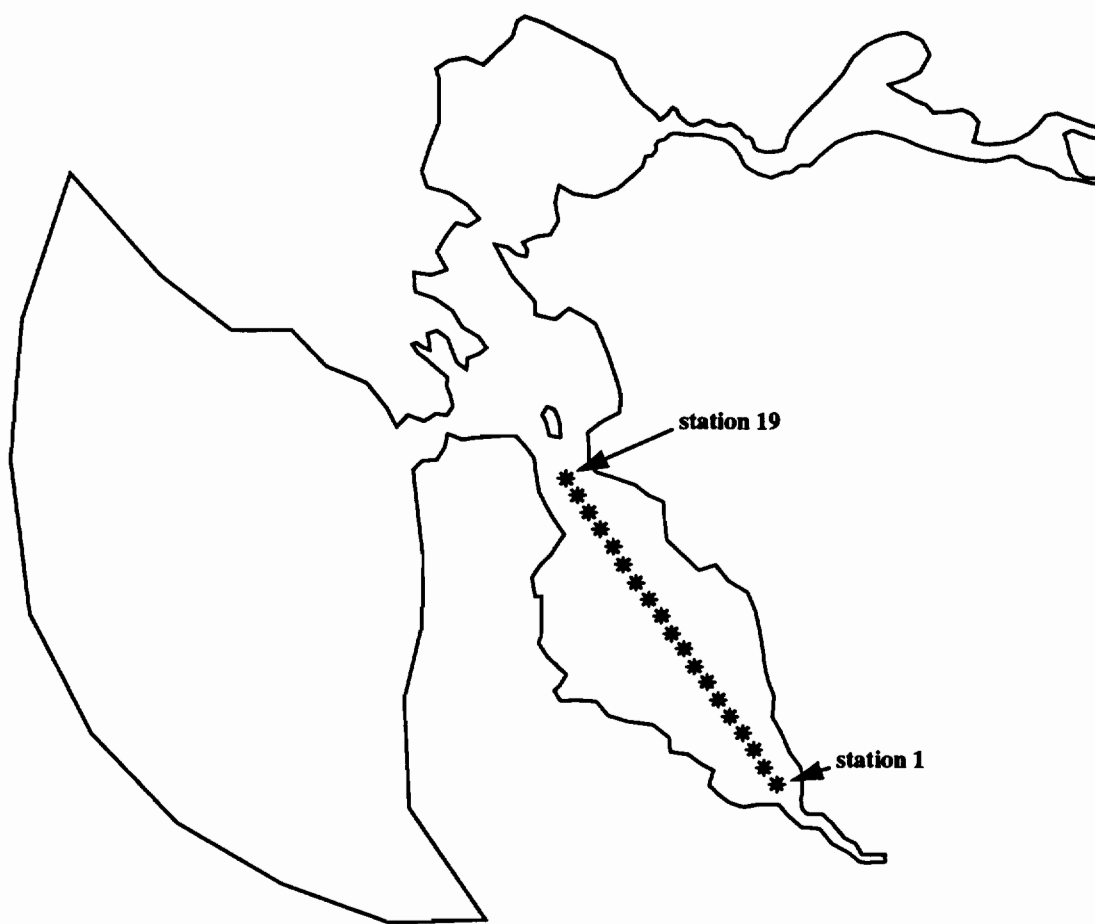


Figure 5.15. Outline of the numerical grid used in San Francisco Bay simulations, with sampling transect (19 stations).

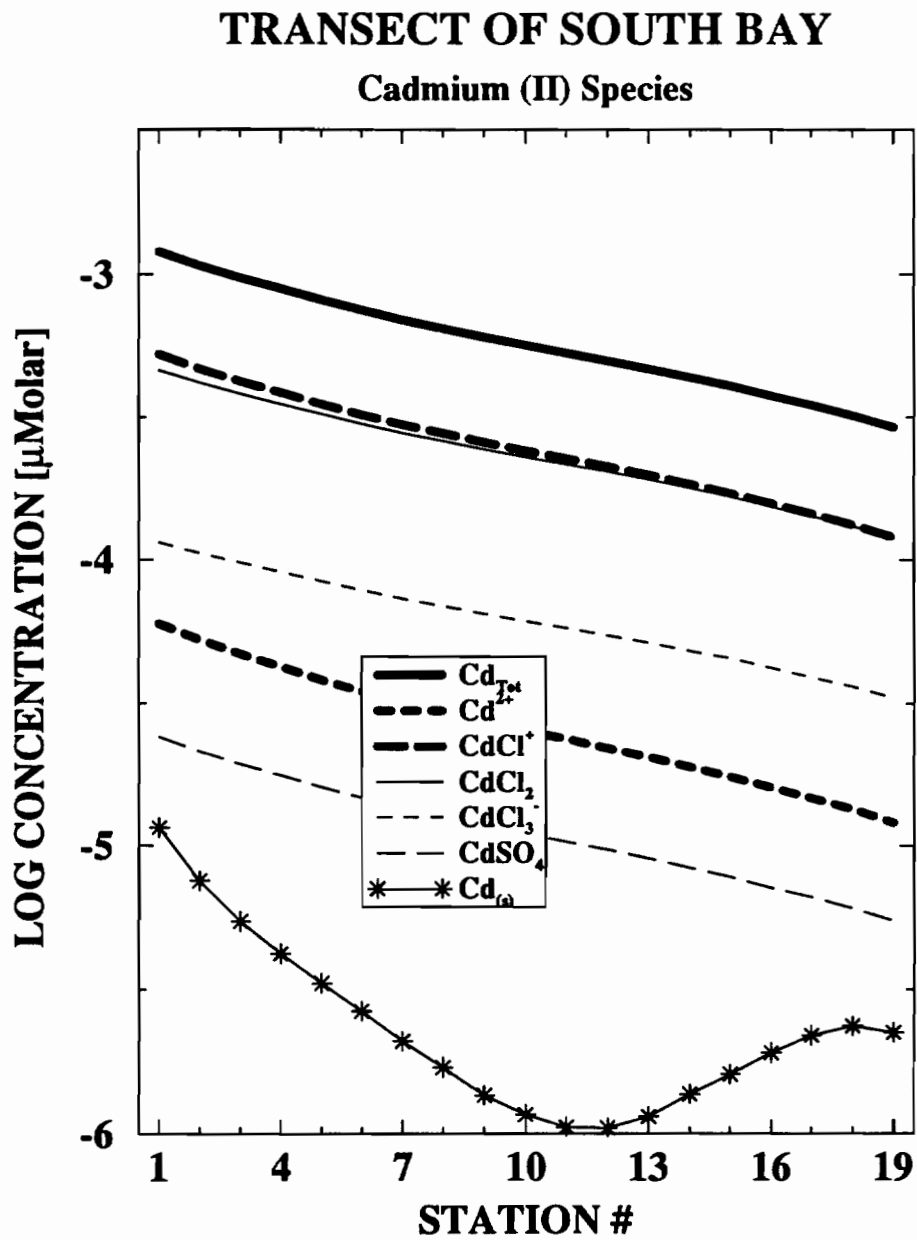


Figure 5.16. Profile along the transect shown in Figure 5.15 of Cd(II) species.

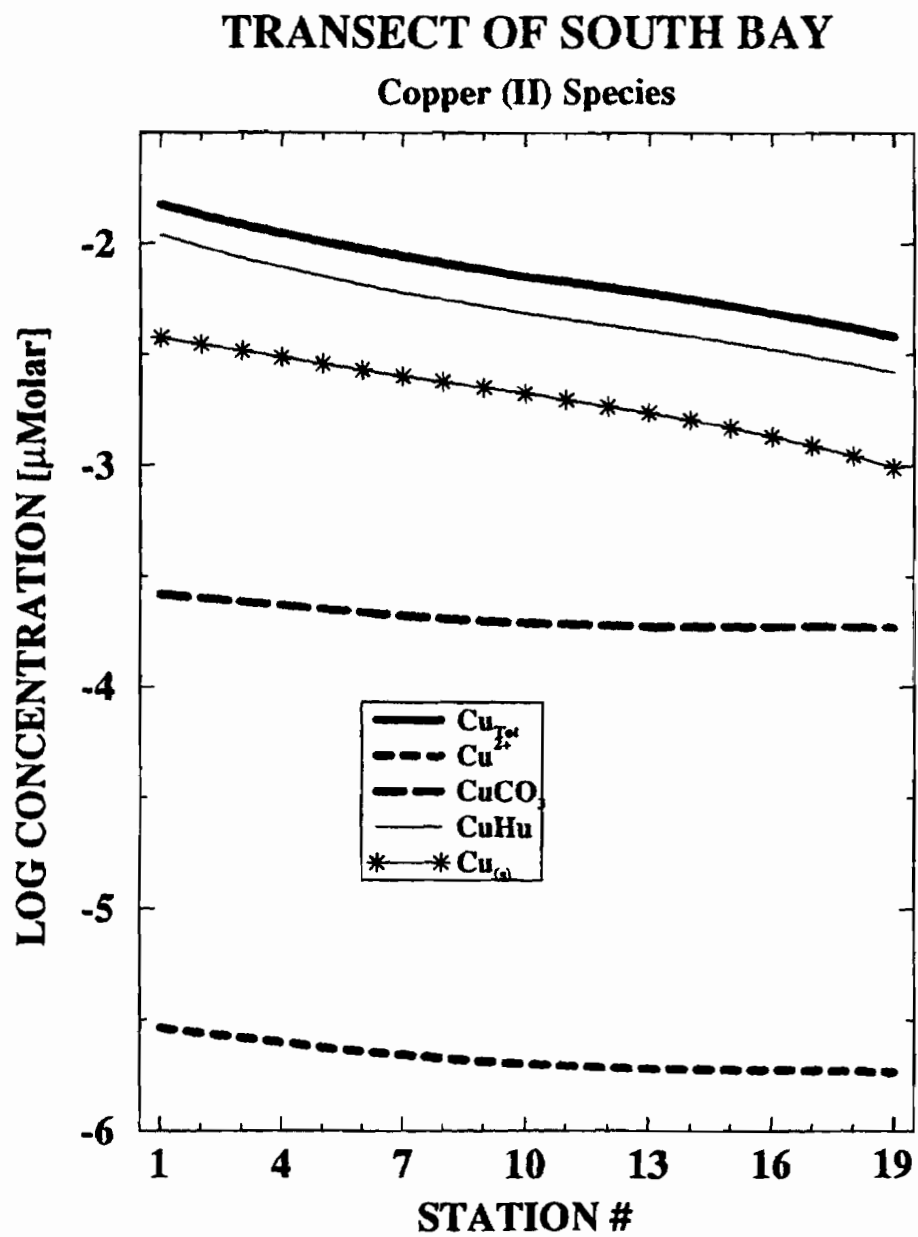


Figure 5.17. Profile along the transect shown in Figure 5.15 of Cu(II) species.

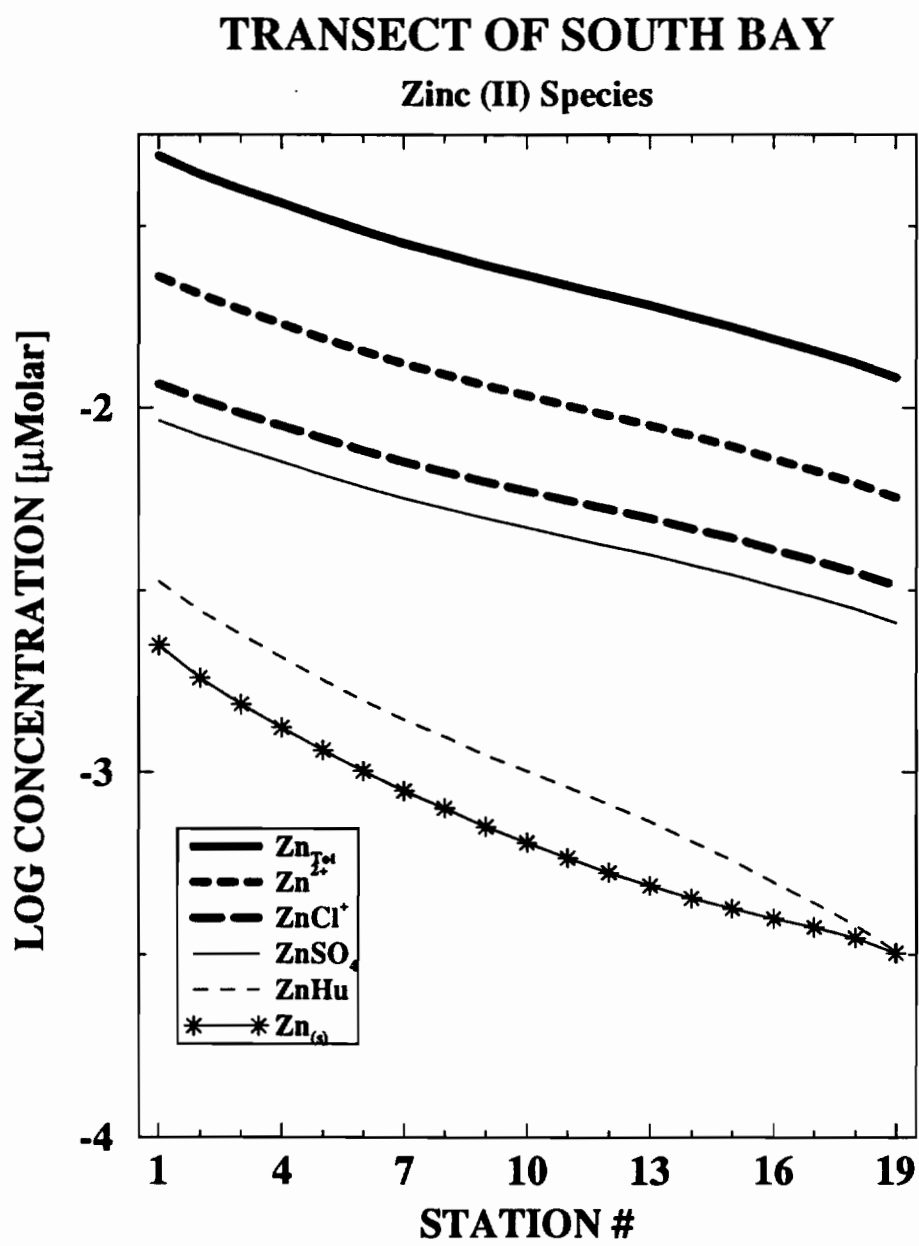


Figure 5.18. Profile along the transect shown in Figure 5.15 of Zn(II) species..

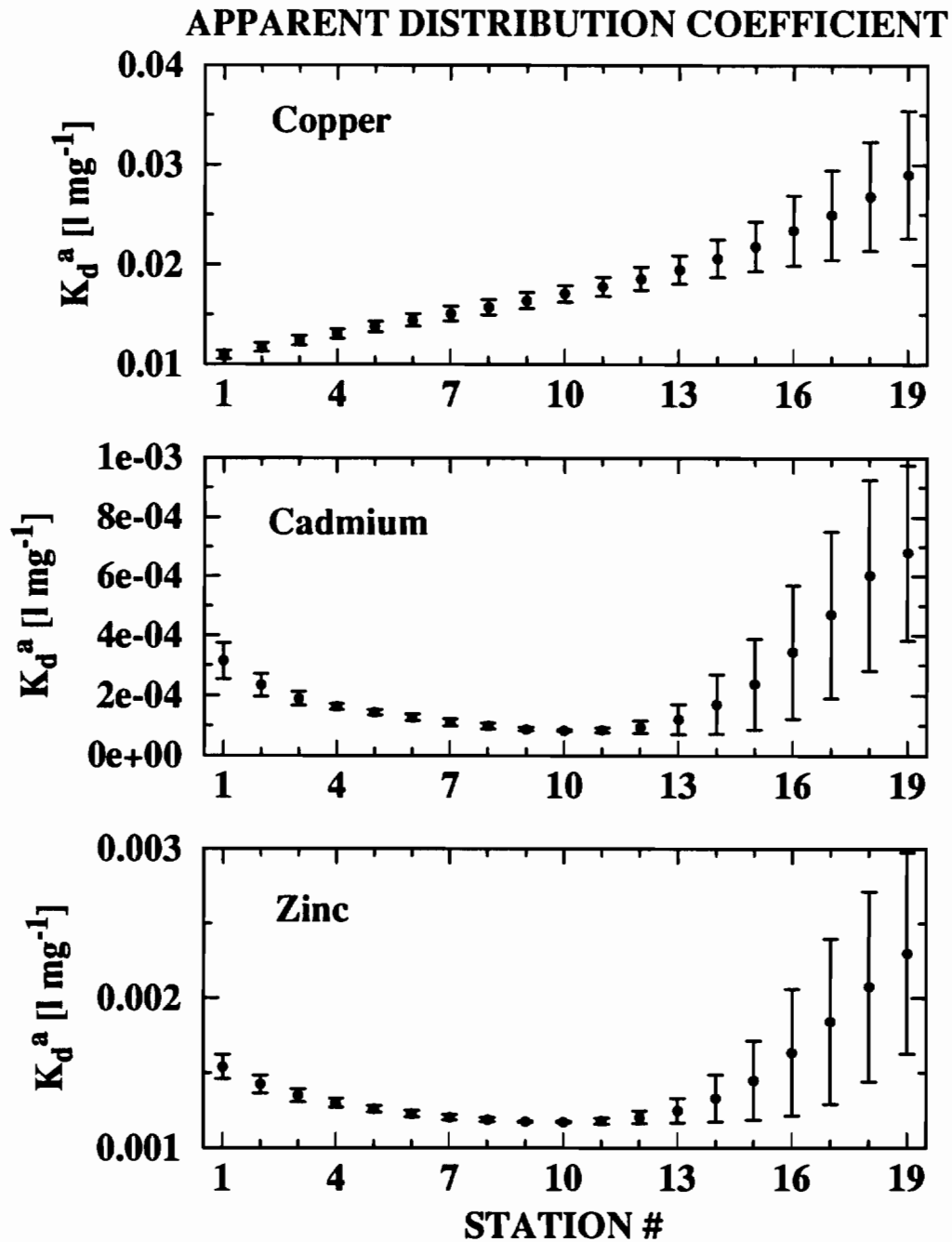


Figure 5.19. Profile along the transect shown in Figure 5.15 of apparent distribution coefficient. The bars represent the maximum extent of tidal variability; the symbol represents the tidally-averaged value.

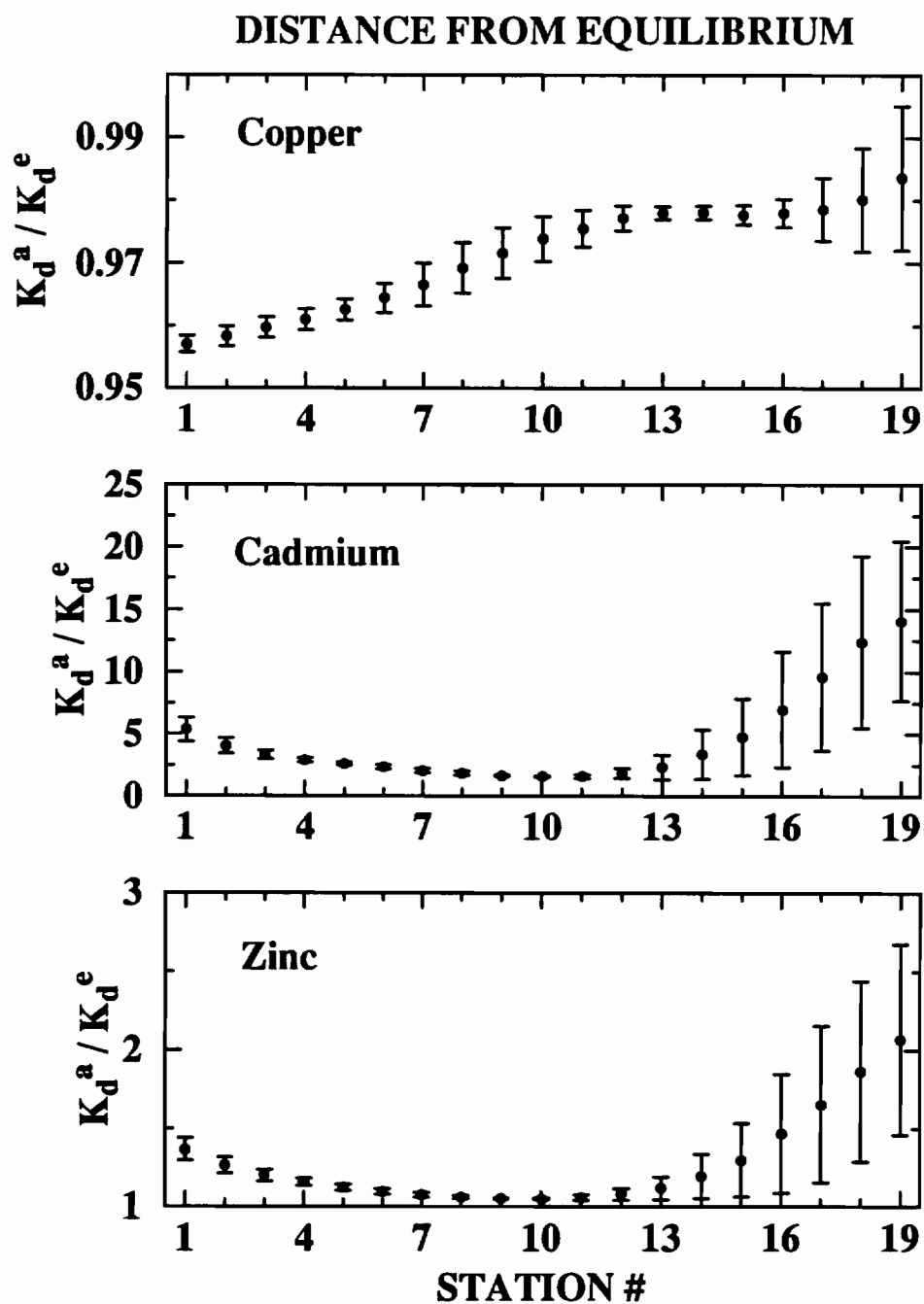


Figure 5.20. Profile along the transect shown in Figure 5.15 of departure from equilibrium as measured by the apparent distribution coefficient normalized by the distribution coefficient at equilibrium. The bars represent the maximum extent of tidal variability; the symbol represents the tidally-averaged value.

CHAPTER 6

Conclusions

Contributions

The development and application of ELAmet has established the feasibility of incorporating relatively sophisticated chemical transformation equations into surface water transport models. Because equilibria and kinetics are solved simultaneously, it is now possible to combine, for example, aqueous speciation with adsorption kinetics. However, other types of chemical behavior can now be modeled with very little modification—biologically-mediated and oxidation/reduction reactions, for example. The feasibility of generating simulations that cover months and even years has also been established, aided in large part by the fact that the model splits the total advection/dispersion/transformation problem into parts, and uses a computational time step appropriate to each individual portion of the problem.

The preliminary application of ELAmet to a simplified, synthetic estuary indicates that mixing plots generated from concentration vs. salinity data should be more closely scrutinized, especially if quantitative calculations about end-member characteristics are to be made from the observed data. These mixing plots may occupy a 2-dimensional region in the concentration/salinity plane, which is not well-represented by sparse field sampling. In cases where mixing plots have been used to estimate fluxes between the land margins and the oceans, this could lead to significant errors in the calculations of geochemical cycles.

The use of ELAmet in South San Francisco Bay has established that adsorption kinetics can be an important component in the understanding of the partitioning observed between the aqueous and solid phases in the Bay. The results suggest that adsorption kinetics can control the basin-scale variability in ways that are not predictable based on recognized relationships between partitioning and other environmental parameters such as salinity and the concentration of suspended solids. The use of ELAmet in this circum-

stance has established the need for further laboratory work. It is especially important to obtain measurements under environmentally relevant conditions of thermodynamic rate constants. Much of the laboratory experimentation on partitioning between the aqueous and solid phases has emphasized measurements at equilibrium, and partitioning to “pure” phases; however, this work has pointed out a need for measurements of rate constants for kinetically-controlled adsorption to “natural” particles. An important component of future field work should lead to some quantitative estimate of particle variability at a range of temporal and spatial scales.

Overall, this work has provided the proof-of-concept of diagnostic modeling. Numerical models can play a significant role in the study of complex natural systems. However, if they are to fulfill their potential as research tools, in many cases it is their diagnostic rather than prognostic function that should be emphasized.

Directions for Further Research

As is to be expected, the work comprising this thesis opened up more new questions than it answered, and pointed out several avenues that should be pursued in future research. There is an obvious need for further technical improvement in the numerical transport model. While ELAmet represents a significant achievement in the advancement of surface water quality models, there are many more improvements to be made. The most important is the extension of the model to three dimensions, as nearly all natural systems are influenced by 3-dimensional dynamics. This was found to be the case even in South San Francisco Bay, an embayment with very little vertical stratification, as we found that it was impossible to simulate the appropriate mixing time scales under high flow conditions (Chapter 4). Also important is the three dimensional nature of the sediment bed layer, which must be described in detail to accurately model the deposition to the bed layer and possible subsequent re-entry into the water column of some elements. The existence of a high-density near-bed suspension is a primary determining factor in the deposition and resuspension of sediments. The vertical description of the bed sediments also determines the extent to which elements are transformed in reduced sediment layers before being re-introduced to the water column.

Several possible directions that future applications of diagnostic modeling might take have emerged. I have become intrigued by two possibilities in particular that remain

largely unexplored. The first is the use of diagnostic modeling in a proactive manner to help in the optimization of field surveys. We know that a multitude of temporal and spatial scales are involved in estuarine processes. Diagnostic modeling has a great potential for highlighting the scales at which most of the variability, i.e. the strongest signal, is likely to be found, and consequently the sampling interval required to resolve those scales.

The second possibility has to do specifically with temporal sampling, which is generally not done on short time scales (days and less) due to the time limitations in laboratory analysis and the lack of in situ instrumentation for that purpose. However, if these obstacles are overcome at some point in the future, our limited experience with ELAmet has pointed to some interesting applications of “spectral fingerprinting”; i.e., the deduction of a trace material’s chemical behavior through its Eulerian variability in concentration, especially as contrasted with a known conservative substance such as salinity.

The application of this model to a real system such as San Francisco Bay has also served to point out that in many ways models can easily get ahead of the experimentally-derived constants that are needed as input parameters. While I believe that there is still a great deal of useful application of diagnostic modeling to be done in spite of this recognition, the usefulness of numerical models will only be improved as further laboratory experimentation is done to obtain better model parameters.

VITA

The author was born and raised in Lisle, New York. After graduating from Whitney Point Central High School, she attended Union College in Schenectady, where she received a very good liberal arts education. She majored in Mechanical Engineering, but was not excited by the job opportunities that were available upon graduating. So, after graduating with a B.S. in the spring of 1982, rather than getting a job doing engineering she took a year to travel after being awarded a Thomas J. Watson fellowship. Most of this year was spent in Spain and Colombia, where the author became quite proficient in Spanish and gained a wider perspective on life and world affairs.

Upon returning to the United States the author decided to enter graduate school at M.I.T. in Cambridge, Massachusetts as part of the Joint Program with the Woods Hole Oceanographic Institution. At M.I.T. she received a rigorous training in geophysical fluid dynamics, not to mention getting to spend a large part of the year on Cape Cod.

After receiving an S.M. degree in Physical Oceanography in 1987, she went to work as a Research Associate for a group of meteorologists at Atmospheric and Environmental Research in Cambridge. Here she learned a great deal about large-scale air-sea interactions, and the earth-atmosphere angular momentum budget [*Gutzler and Wood, 1989; Rosen, Salstein and Wood, 1988*]. The AER tuition reimbursement program was also responsible for giving the author her first exposure to environmental chemistry, through a course at M.I.T. taught by Phil Gschwend.

After a couple of years the lure of the Ph.D. was too great to be resisted. The author had a feeling that she really wanted to work in an interdisciplinary department on a problem with environmental applications, and that was in large part what brought her to the Pacific Northwest and the Oregon Graduate Institute of Science & Technology (then the Oregon Graduate Center). She moved to Beaverton, Oregon with her husband Scott Hahn in 1989. At OGI the author worked on constructing and implementing a model for estuarine geochemistry, under the primary direction of Antonio Baptista, which was the basis for this dissertation.

After graduating in the spring of 1993, the author hopes to regain some perspective on life through such activities as playing with her 1-year-old, riding her bike, planting her garden, and reading some novels. Employment will surely come soon enough.

Publications

- Wood, T. M. and A. M. Baptista, 1992: A Model for Diagnostic Analysis of Estuarine Geochemistry, *Water Resources Research*, 29(1), pp. 51-71.
- Wood, T. M. and A. M. Baptista, 1992: Modeling the Pathways of Nonconservative Substances in Estuaries, in *Estuarine and Coastal Modeling, Proceedings of the 2nd International Conference*, edited by M. L. Spaulding et al., ASCE, New York, pp. 280-291.
- Gutzler, D. S. and T. M. Wood, 1989: Structure of Large-Scale Convective Anomalies over Tropical Oceans, *Journal of Climate*, 3(4), pp. 483-496.
- Rosen, R. D., D. A. Salstein, D. A. and T. M. Wood, 1988: Discrepancies in the Earth-Atmosphere Angular Momentum Budget, *Journal of Geophysical Research*, 95(B1), pp. 265-279.